Nanoparticle-based delivery and activation of platinum (IV) prodrugs and dsRNA for cancer chemotherapy

PhD Thesis

To obtain the Doctor of Philosophy degree in *Applied Chemistry and Polymeric Materials* at the University of the Basque Country (EHU/UPV)

by

AMAIA GARAIKOETXEA ARGUINZONIZ

Donostia, 2017

Thesis Supervisor: Prof. Juan C. Mareque Rivas (Theranostic Nanomedicine Laboratory, CIC biomaGUNE)

University Tutor: Prof. Mª Angeles Garralda Hualde (Department of Applied Chemistry, Faculty of Chemistry, University of the Basque Country)

Table of Contents

Resumen

El cáncer es sin duda un alarmante problema sanitario a nivel global; las estimaciones prevén una tendencia alarmantemente creciente tanto para la tasa de incidencia como para las muertes relacionadas con el cáncer. Las actuales opciones terapéuticas combinan abordajes quirúrgicos y radiación con la administración sistémica de fármacos quimioterapéuticos. A pesar de los avances que se han hecho en las últimas décadas, los efectos secundarios vinculados a los fármacos anti-cancerígenos tradicionales siguen siendo una preocupación principal junto con la pérdida de eficacia terapéutica y el desarrollo de mecanismos de resistencia.

Los compuestos a base de platino, especialmente el cisplatino, son probablemente los fármacos quimioterápicos más comúnmente utilizados. Eficaz para el tratamiento de una amplia variedad de tipos de cáncer, los fármacos de platino se unen al ADN produciendo una distorsión de la doble hélice que provoca a la muerte celular programada. Junto con el cisplatino, hay otros dos fármacos de platino (II) con aprobación mundial, y tres más sólo aprobados en ciertos países. Más recientemente, los profármacos del platino (IV) también han ganado gran interés ya que permiten el suministro de un compuesto inerte que una vez dentro de las células cancerosas es capaz de producir especies citotóxicas de platino (II). Aunque ningún nuevo compuesto ha alcanzado la aprobación de la FDA en los últimos años, sigue habiendo extensa investigación en esta área que sostiene una gran promesa en la mejora de los tratamientos quimioterápicos.

Además de la quimioterapia, el uso del propio sistema inmunológico del cuerpo para combatir el cáncer también ha surgido como una alternativa alentadora contra esta enfermedad. La denominada inmunoterapia ha atraído gran atención y una amplia variedad de herramientas, incluyendo anticuerpos, vacunas o agonistas de receptores TLR, ya han sido descritas para explotar este enfoque.

Resumen

A pesar del gran número de avances que se han hecho en el desarrollo de agentes quimioterápicos e inmunoterapéuticos más seguros y eficaces, todavía hay que superar importantes desventajas. La mayoría de los enfoques inmunoterapéuticos implican costosos procedimientos que limitan su aplicabilidad. Los fármacos de quimioterapia más sofisticados, por otra parte, todavía carecen de la selectividad necesaria y producen graves efectos secundarios tales como toxicidad sistémica y quimiorresistencia.

Los recientes adelantos en nanotecnología podrían ser la clave para lograr un tratamiento más seguro y eficaz contra el cáncer, superando los principales problemas relacionados con las terapias tradicionales. La posibilidad de utilizar nanopartículas para transportar los fármacos directamente a los tumores u otras áreas de interés permite una mayor selectividad con dosis más bajas y efectos secundarios reducidos. El uso de nanopartículas como vehículos de transporte de fármacos es, de hecho, el foco principal de este trabajo.

Gracias a la vasculatura caótica y la falta de drenaje linfático efectivo de los tumores, se pueden diseñar nanopartículas de tamaños y formas específicas para lograr una acumulación selectiva en el tumor a través de transporte pasivo basado en el efecto de permeabilización y retención mejorada. Además, las extraordinarias propiedades fisicoquímicas de las nanopartículas permiten la integración de diferentes modalidades de imagen para el seguimiento tanto *in vitro* como *in vivo* de los sistemas administrados.

Tanto las nanopartículas como los agentes terapéuticos empleados durante la tesis fueron seleccionados teniendo en cuenta la trayectoria y la experiencia previa del grupo. Como vehículos de transporte se han empleado nanopartículas de oro y de óxido de hierro, ambas caracterizadas por su biocompatibilidad y baja toxicidad. Además ambas preparaciones permiten la fácil incorporación de gran variedad ligandos en la superficie para así poder elegir la estrategia más adecuada para anclar el agente quimioterápico. Asimismo, aunque el principal objetivo de este trabajo ha sido el desarrollo de vehículos de transporte, tanto las nanopartículas de oro como las de

oxido de hierro ofrecen también la posibilidad se empeladas como agentes de contraste en diferentes modalidades de imagen molecular (resonancia magnética, rayos X, imagen óptica, etc.) y pueden también actuar como agente terapéuticos debido a su habilidad de generar suficiente calor como para dañar células de cáncer bajo un estímulo externo como luz o un campo magnético.

Debido a la amplia experiencia del grupo en la síntesis de complejos de platino y su importancia como fármacos contra el cáncer, esta tesis describe la preparación y varios compuestos de platino con potencial citotóxico para su transporte a través nanopartículas. Sin embargo, el lugar de emplear fármacos de platino (II), la investigación se ha centrado en el uso de profármacos de platino (IV) que permiten el transporte de un modo inerte así como la posibilidad de usar los ligandos axiales para su funcionalización o anclaje.

Por otro lado, se ha seleccionado el poly(I:C), un análogo sintético de ARN muy conocido por si capacidad inmunoestimuladora. La investigación para su uso en inmunoterapia y la creación vacunas contra en cáncer es muy extensa pero a pesar de actual principalmente como activador del sistema inmune, también se ha demostrado que es capaz de inducir muerte celular a través de diferentes mecanismos. Esta doble funcionalidad resulta de gran interés ya que permitiría el use de un mismo compuesto para atacar el cáncer desde los dos enfoques, quimioterapia e inmunoterapia. Mediante el uso de nanopartículas como vehículo de transporte, se pretende en este caso promover su actividad como agente quimioterápico.

Esta tesis está estructurada en cuatro secciones principales, una introducción general y tres capítulos experimentales, cada uno enfocado en el desarrollo de un vehículo basado en nanopartículas para el transporte de un agente anticancerígeno y la evaluación de su eficacia.

El capítulo inicial tiene como objetivo ofrecer una visión general del cáncer como principal motivación de esta investigación; partiendo de conceptos generales, se

describen los enfoques terapéuticos hacia la enfermedad así como estrategias más avanzadas que implican el uso de profármacos basados en platino y agentes inmunoterapéuticos entre otros. Siendo el uso de nanopartículas la base de esta trabajo, este capítulo también introduce la nanotecnología y su aplicación para el tratamiento del cáncer, haciendo hincapié en el use de nanopartículas para el transporte de fármacos y profármacos. También se describen las funcionalidades adicionales que ofrece el uso de nanopartículas tanto en el ámbito de imagen como su uso intrínsecamente terapéutico y como la combinación de todas ellas permite el desarrollo de nanosistemas teranósticos que integran funcionalidades diagnósticas y terapéuticas en una sola plataforma.

A pesar de que cada uno de los tres capítulos experimentales se centra en el desarrollo de un nanovehículo de transporte y su uso en conjunto con un fármaco o compuesto anticancerígeno particular, los tres capítulos siguen un esquema similar. El trabajo parte de la síntesis y caracterización de las nanopartículas que se van a usar en cada caso, para obtener un sistema soluble en agua y biocompatible que además permita la interacción con el compuesto de interés. La incorporación del compuesto activo se lleva a cabo a través de diferentes estrategias y una vez formado el sistema, se estudia la funcionalidad *in vitro* usando líneas celulares de cáncer. Además, en todos los casos se añade un componente fluorescente al sistema de transporte para comprobar que es internalizado por las diferentes células cancerígenas.

Finalmente, a pesar de que no ha sido posible en todos los casos, una vez comprobada la funcionalidad *in vitro* del sistema, se traslada a estudios de eficacia terapéutica *in vivo* con un modelo tumoral de ratón. Para poder ver la biodistribución y la posible acumulación de las nanopartículas en el tumor, el marcaje radioactivo permite su seguimiento mediante técnicas de imagen nuclear altamente sensibles.

- El **capítulo 2** describe la preparación de nanopartículas de oro revestidas con polietilenimina (PEI) y su aplicabilidad en el transporte de un agonista de TLR bien conocido, poly(I:C). Aunque el poly(I:C) es más comúnmente utilizado para

la inmunoestimulación, este trabajo tiene como objetivo promover sus propiedades quimioterapéuticas a través del transporte con la nanopartícula.

- Extendiendo la aplicabilidad de las nanopartículas de oro revestidos con PEI, el **capítulo 3** se enfoca en el polímero cargado positivamente situado en la superficie de las nanopartículas, el PEI. Este trabajo se basa en la utilización de una estrategia novedosa basada en interacciones de esfera externa entre el polímero y un complejo de platino para administrar y activar un profármaco de platino (IV) en tres líneas celulares de cáncer diferentes.

  Este trabajo fue además publicado a lo largo de la tesis bajo el título *"Enhanced cancer cell killing of a Pt(IV) prodrug promoted by outer-sphere coordination with polyethyleneimines"* (A. Garaikoetxea Arguinzoniz, N. Gómez Blanco, P. Ansorena Legarra and J. C. Mareque-Rivas, *Dalton Trans.*, **2015**, *44*, 7135.)

- Finalmente, el **capítulo 4** ilustra el uso de una estrategia covalente para cargar un profármaco de platino (IV) en micelas de óxido de hierro. Los ligandos axiales del complejo permiten su incorporación a un fosfolípido PEGilado utilizado posteriormente para la formación de las micelas. Una estrategia de radiomarcaje libre de quelatos permitió el uso de técnicas de imagen nuclear para el seguimiento de la biodistribución *in vivo* del sistema en un modelo de tumor de ratón. Además, este capítulo también describe la eficacia terapéutica *in vivo* del sistema en el mismo modelo tumoral de ratón.

Summary

Cancer is undoubtedly a major health problem worldwide; the estimates indicate an alarmingly increasing trend for both the incidence rate and cancer related deaths. Current therapeutic options combine surgical and radiation approaches with the systemic administration of chemotherapeutic drugs. Platinum based compounds, especially cisplatin, are the most commonly used chemotherapeutic drugs. Efficient for the treatment of a wide variety of cancer types, platinum based drugs bind to DNA producing a distortion of the double helix that leads to programmed cell death. More recently, platinum (IV) prodrugs have also gained great interest as they allow the delivery of an inert compound that once inside the cancer cells is able to render cytotoxic platinum (II) species. Besides chemotherapy, the use of the body's own immune system to fight cancer has also emerged as an encouraging alternative against cancer. The so called immunotherapy is attracting major attention and a wide variety of tools including antibodies, vaccines or Toll-like receptor agonists have already been reported for exploiting this approach. Despite important advances that have been made over the last decades in the development of effective chemotherapeutic and immunotherapeutic agents, significant downsides and limitations still need to be overcome.

Recent advances in nanotechnology might hold the key to achieving a safer and more efficient cancer treatment. The possibility of using nanoparticles to direct the drugs to the tumours or other areas of interest allows improved selectivity with lower doses and reduced side effects. On the basis of the leaky vasculature and lack of effective lymphatic drainage of tumours, nanoparticles of specific sizes and shapes can be designed to achieve a selective tumour accumulation. This thesis has focused on the use of gold and iron oxide based nanoparticles as delivery vehicles for two different therapeutic cargos, a platinum (IV) prodrug and the synthetic dsRNA poly(I:C).

Low molecular weight polyethyleneimine (LMW-PEI) coated gold nanoparticles, PEI-AuNPs have been explored in chapters 2 and 3 for the delivery and enhancement of

the cytotoxicity of both a platinum (IV) prodrug and poly(I:C). The use of PEI not only allows the easy preparation of the aqueous nanoparticles, but also plays a major role in the interactions with both cargos; being a well-known transfection agent this positively charged polymer electrolyte can interact with the negatively charged dsRNA. Moreover, it can also be used to promote outer-sphere interactions with the platinum prodrugs. This versatile and simple system is able to effectively deliver both cytotoxic agents and achieve an enhanced cancer cell death in different relevant cell lines.

Aiming for enhancing the therapeutic efficacy of the platinum (IV) prodrug, iron oxide-filled micelles have also been explored as delivery vehicles. The PEGylated phospholipids forming part of the micelle structure can be modified to covalently attach the prodrug. Chapter 4 focuses on the use of this platinum-modified micelle construct as a proof-of-concept study against an aggressive murine melanoma model.

In summary two different nanoparticle-based delivery vehicles have been prepared and characterized during this thesis. Their functionality and effectiveness has been explored for the delivery of two relevant cargos, a cisplatin platinum (IV) prodrug and a well known dsRNA. PEI-coated AuNPs have demonstrated to be very versatile, allowing the delivery of different agents, but at the same time specific as only the cytotoxic effect of poly(I:C) is promoted rather than its most commonly used immunostimulatory activity. Moreover, the platinum-modified IONP micelles have also been tested *in vivo* for the treatment of a very aggressive tumour model and proved to be efficient in delaying tumour growth and more importantly improving survival rates of treated animals. The importance of the results obtained is not in the improved anticancer effect, but also in the simple design and versatility of the constructs which opens up a myriad of possibilities towards cancer theranostics and combinational therapy approaches.

1

Cancer Nanotechnology:

Nanoparticle-based drug delivery vehicles

1.1. Cancer: current perspective and treatments

According to data from the World Health Organization (WHO) cancer is still one of the leading causes of death globally. Only in 2012 14 million new cancer cases were diagnosed and caused over 8 million deaths. Moreover, cancer incidence is expected to rise by up to 70% over the next two decades.[1] This multifunctional disease originates when the natural cycle of cell growth and division breaks down and cells start to proliferate in an uncontrolled way (Figure 1). The abnormal cancer cells do not die when they should; instead they keep proliferating and generate abnormal cell masses called tumours.

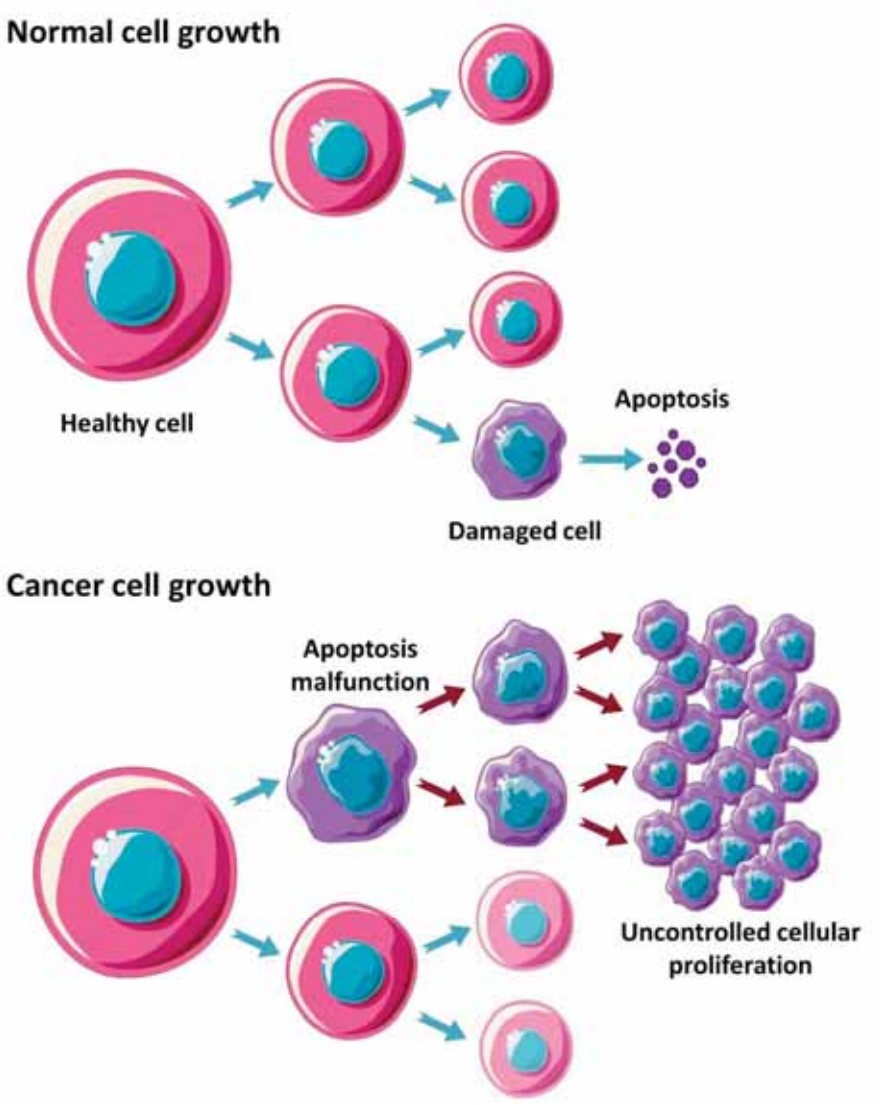

Figure 1. Schematics of the difference between the natural cell cycle and the malfunction of cancer cells leading to uncontrolled proliferation.

As these malignant tumours keep growing they spread and invade nearby tissues. Moreover, some cancer cells can break off and disseminate through blood or the lymphatic stream spreading to other parts of the body. This process by which cancer spreads from the primary tumour to another site in the body is called metastasis and once it occurs the cancer becomes harder to control.[2,3]

Although there are over one hundred types of cancer, usually named according to the organ to cell type of origin, some particular types have a higher incidence or a higher rate of mortality. Prostate cancer for instance is the most common type of cancer in men among Europe, and the second worldwide with an estimated 1.1 million new cases in 2012 (Figure 2).[1]

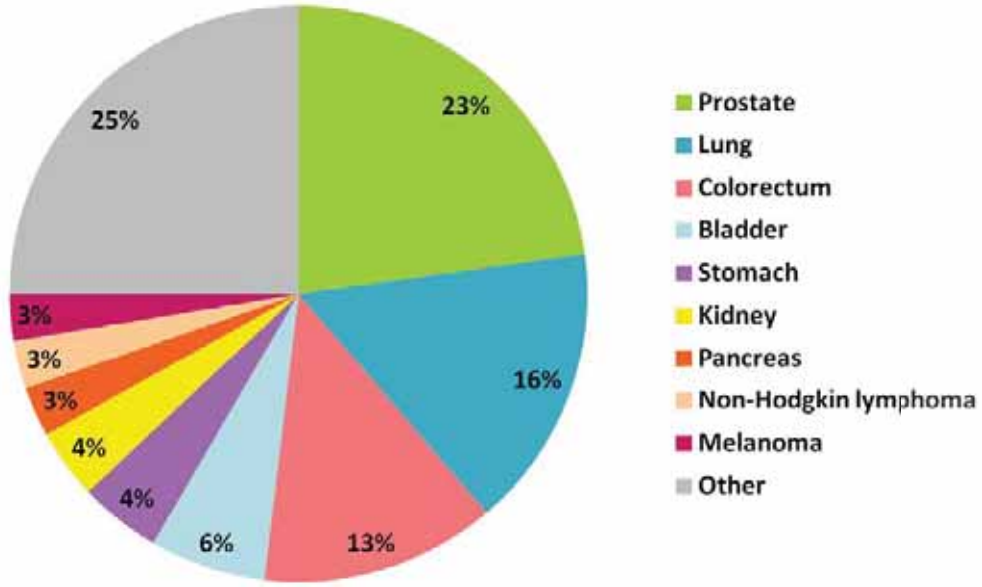

Figure 2. Estimated cancer incidence proportions in men in Europe for 2012.[1]

Despite not being as common as prostate or breast cancers, melanoma skin cancer incidence has alarmingly increased in the last decades (Figure 3), with over 230000 new cases diagnosed in 2012. Melanoma is the most aggressive form of skin cancer, and even though it mostly affects fair-skinned populations, it still represents the sixth most commonly diagnosed type of cancer.[4] Additional problems associated with melanoma include its evolution, the inefficacy of current treatments, and that it is highly prone to disseminations, with around 30% of cases developing metastasis.[5]

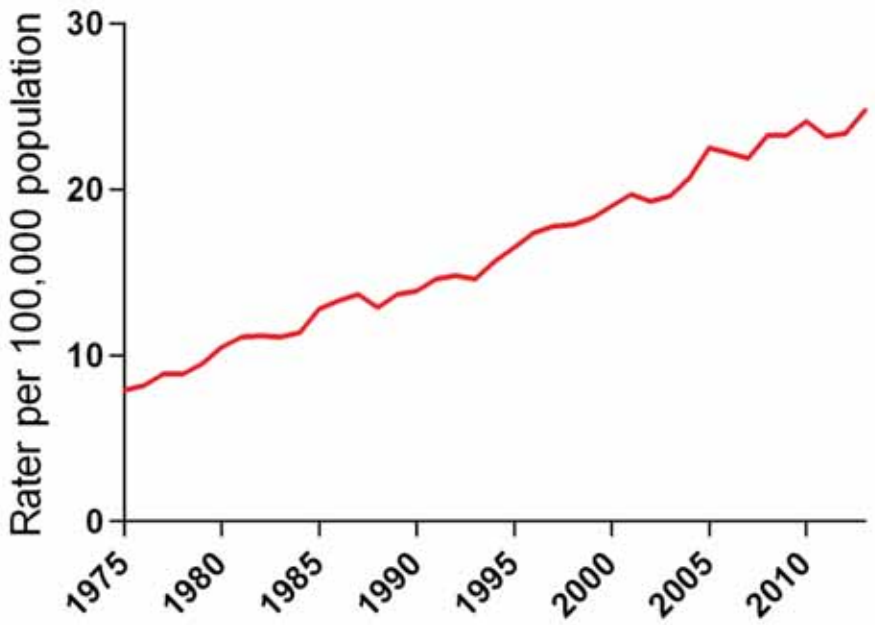

Figure 3. Melanoma skin cancer incidence rate in the US (1975-2013).[6]

Either due to a worryingly high global incidence in the case of prostate cancer or the alarming increase and the highly metastatic nature of melanoma, research to develop new and more efficient cancer treatments has attracted major interest over the last decades.

Current therapeutic options mainly involve local treatments, based on surgery and/or radiation. For the case of solid and localized tumours surgery is usually the first option, but it is useless for blood cancers and many cases where the cancer has already spread. The use of ionizing radiation to treat solid tumours is also a very common approach in clinics.[7] Although radiation with a high energy photon beam is the most extended treatment modality, alternative treatment options such as proton[8] or neutron[9] beams are gaining interest due to their higher efficacy in treating tumours where other forms of radiation are inefficient. Nevertheless, while surgery and radiotherapy are the primary treatments of choice for local and non-metastatic cancers, the use of additional anticancer therapies such as chemotherapy and biological therapies is often needed.

1.1.1. Chemotherapy

In spite of the interest gained by the alternative therapies, chemotherapy is undoubtedly the most common approach usually in combination with surgical and radiation therapies. Chemotherapy constitutes a systemic therapy for cancers, based in the intravenous administration of one or more anticancer drugs, which most commonly interfere with the cell cycle resulting in cell death. The potential of chemical drugs for cancer treatment dates back to World War I and II, where soldiers exposed to mustard gas were found to develop lymphoid aplasia.[10] As a result of these findings, a nitrogen mustard derivative (Figure 4) was the first drug to be clinically tested and found to be effective against lymphoma.[11] Closer in time, researchers also discovered the potential use of a folic acid derivative in leukaemia treatment.[12,13] Remarkably, one of these folate analogues, methotrexate (Figure 4), is still commonly used to treat cancer.

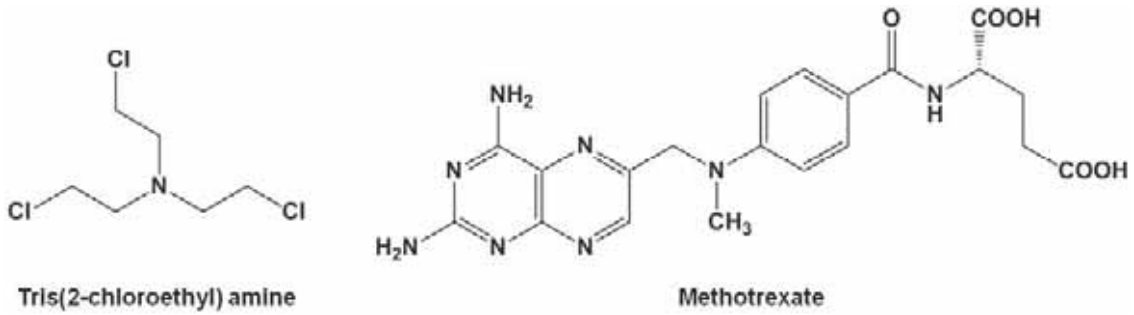

Figure 4. Chemical structures of the nitrogen mustard derivative tris(2-chloroethyl) amine and the folate derivative anticancer drug methotrexate.

These two findings were fundamental for the development of modern chemotherapy, however, it took over a decade to find out the mechanisms of action they had in common, which involved their ability to interact with DNA and damage it resulting in cell death. The approach of DNA targeting for cancer treatment was the base for the development of a wide range of chemotherapeutic drugs, but it was Rosenberg's accidental discovery of anticancer properties of cisplatin in the 1960s that resulted in a major landmark in the history of successful anticancer drugs.[14]

1.1.1.1. Platinum-based anticancer drugs

Since its serendipitous discovery as an anticancer agent in the 1960s cisplatin (cis-diamminedichloroplatinum (II)) has been very successfully used for the treatment of testicular cancer and has shown good efficacy towards other types of cancer such as ovarian, bladder, head and neck and cervical cancer.[15–17] Due to its major role in cancer chemotherapy, the mechanism of action behind the anticancer activity of this drug has been widely investigated. The generalized mechanism (illustrated in Figure 5) suggests that the neutral cisplatin molecule is first intracellularly activated by the aquation of one of the two chloride groups; this dissociation is indeed facilitated inside the cell due to the low chloride concentrations inside the cell.[18] The activated platinum is then able to bind to nucleotide bases in DNA.[19] Experimental results indicate that the binding occurs at the nucleophilic N7 position of the imidazole ring of purine bases (guanine (G) and to a less extent adenine (A)). Cross-linking occurs through the displacement of the remaining chloride ligand, typically binding to another G. Despite most interactions occurring within adjacent bases (intrastrand cross-links), adducts involving bases in opposite DNA strand can also be present (interstrand cross-links). [20]

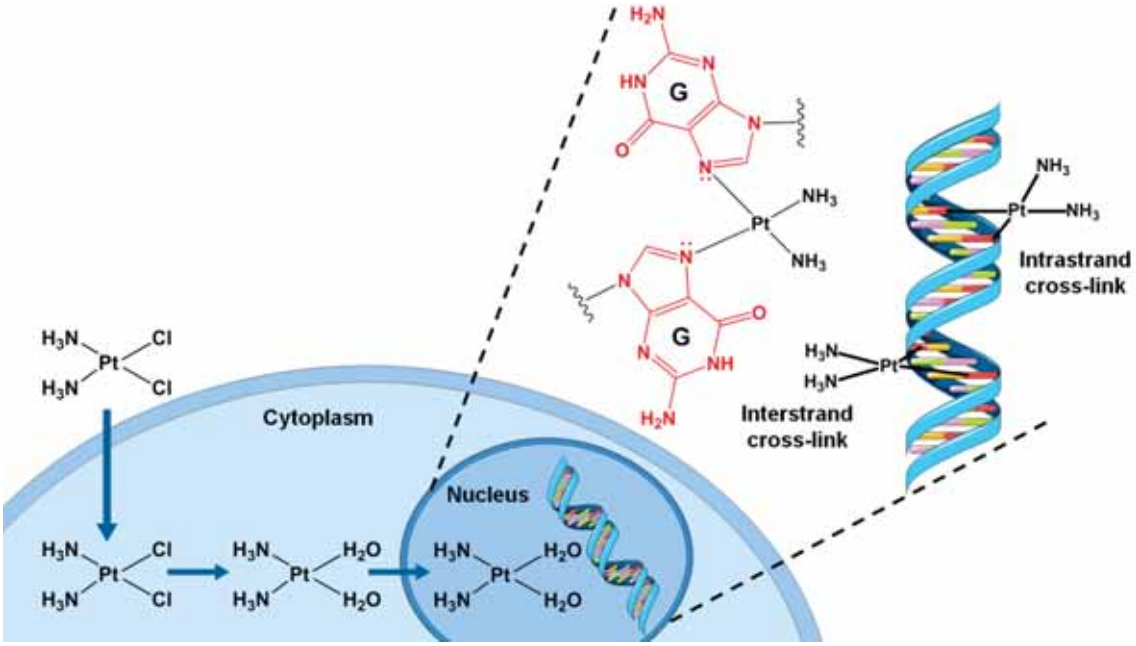

Figure 5. Schematic of the mechanism of action of cisplatin; initiated by uptake across the cell membrane, followed by the aquation process in the cytoplasm and binding to the guanine bases on the DNA strands to form intra and/or interstrand cross-links in the nucleus.

X-ray crystallography and nuclear magnetic resonance studies of cisplatin-DNA adducts also provided a better understanding of the mechanisms behind the anticancer activity. In essence, these studies showed that the formation of the cross-links causes significant distortion of the double helical structure of DNA. This distortion interferes with DNA replication and triggers cellular responses that generally result in apoptotic cell death.[21]

The success and clinical impact of cisplatin however, comes with a cost as it is notoriously toxic to the kidneys and gastrointestinal tract and many patients develop cisplatin resistance. These issues led to the development of less toxic but active alternative platinum drugs. As a result, nowadays three platinum-based anticancer agents are approved worldwide for cancer treatment, cisplatin, carboplatin and oxaliplatin; in addition, other three platinum derivative anticancer drugs are approved in specific countries, nedaplatin (Japan), heptaplatin (Korea) and lobaplatin (China) (Figure 6). The success of carboplatin is based on the presence of a more stable leaving group, which significantly lowers the toxicity. Since its approval in 1989, carboplatin has become indeed the standard chemotherapy treatment for ovarian cancer in most countries.[22] On the other hand, the importance of oxaliplatin relied on its ability to overcome cisplatin resistance and is now a front line chemotherapeutic for colon cancer.[23]

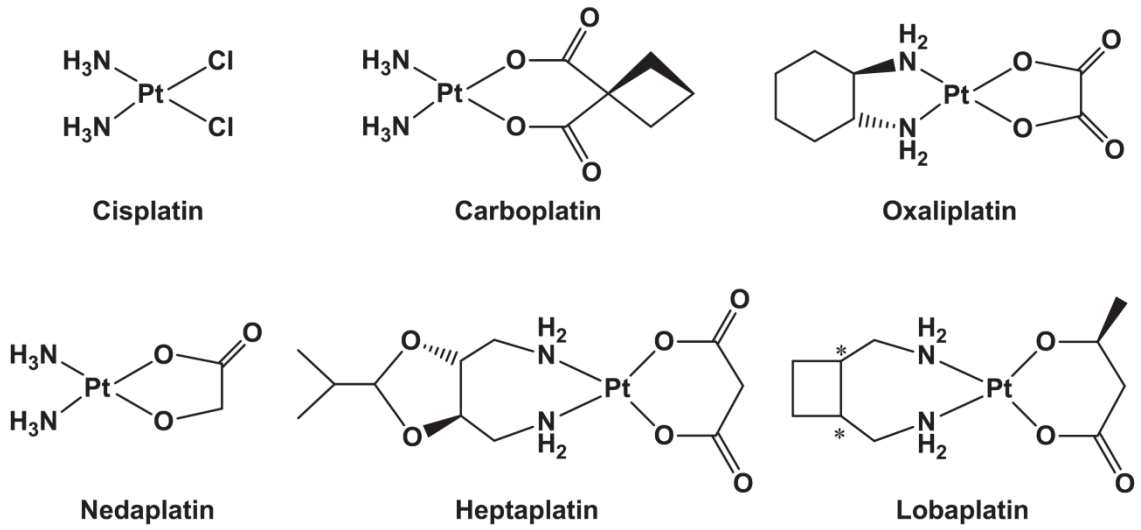

Figure 6. Chemical structures of platinum based anticancer drugs approved for clinical use in cancer treatment.

In spite of the extensive use of these drugs, it has been over a decade since a platinum based drug has reached global approval for cancer treatment. Nevertheless, the search for more effective and safer platinum compounds has remained a very active field in the last decades. According to the SciFinder tool over 4700 compounds with the general formula *cis*-PtA_2X_2 have been reported, reflecting the diversity of complex perturbations introduced to the general framework that approved platinum drugs share.[19] The wide variety of approaches include the incorporation of targeting units such as carbohydrates that target glucose receptors, steroid derivatives to target various steroid receptors over-expressed in cancer cells, or the use of folate and peptide based targeting. In addition, many other platinum derivatives such as polynuclear species and non-covalently binding platinum compounds have also been intensively studied.[19] Besides cisplatin and all the aforementioned platinum (II) species, platinum (IV) complexes are also known to have anticancer potential since the initial discovery of cisplatin;[24] however, it was only recently that considerable research efforts have been focussed on such compounds.

1.1.1.2. Prodrugs: new approach in chemotherapeutics

Unlike the aforementioned platinum (II) species, platinum (IV) complexes generally exhibit a low spin d^6 octahedral geometry (Figure 7), rendering a higher inertness to the coordination sphere. Platinum (IV) complexes are more resistant to ligand substitution reactions than their square planar platinum (II) counterparts. Prepared through oxidative addition of the platinum (II) precursor, platinum (IV) complexes gain two axial ligands that can be further modified to confer improved properties such as lipophilicity, redox stability or improved cellular uptake to potentially overcome the unwanted side effects and resistance exhibited by traditional platinum (II) drugs.

The prodrug concept is based on the general assumption that the more chemically inert platinum (IV) agents will only be activated inside the cells, where cellular reducing agents such as ascorbic acid or glutathione will produce a reductive elimination of the two axial ligands liberating the active platinum (II) species.[25]

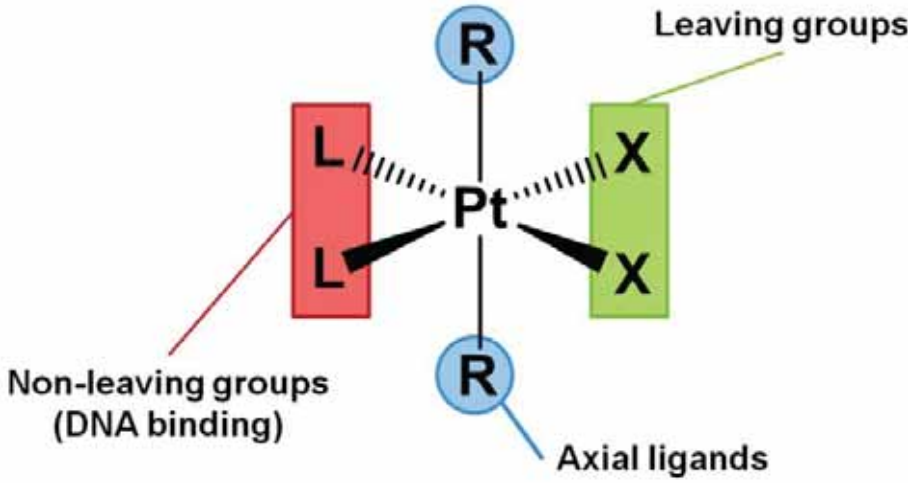

Figure 7. General structure of platinum (IV) prodrugs.

Different platinum (IV) anticancer prodrugs have undergone clinical trials (Figure 8), but the most promising one so far has been satraplatin, which reached advanced phase III clinical trials, but was finally not approved by the FDA due to the lack of overall survival improvement.[26] Since the axial ligands are released upon intracellular reduction, the use of biologically active molecules in the axial positions has prompted the research for "dual action" platinum (IV) complexes.

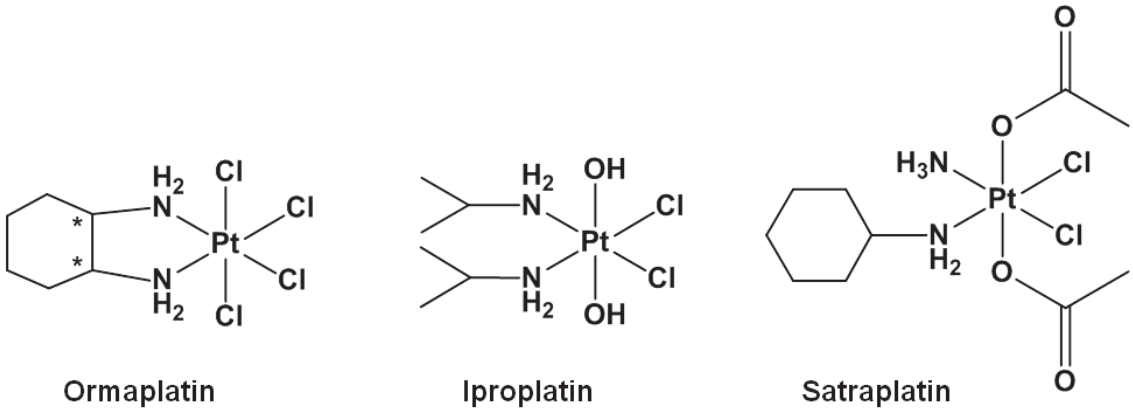

Figure 8. Chemical structures of platinum (IV) prodrugs that have undergone clinical trials.

In the many attempts to prepare such dually active agents, different approaches have been reported. Ethacraplatin and mitaplatin are two of the most notable examples of cisplatin platinum (IV) derivatives engineered to implement a dual therapeutic effect

(Figure 9). Ethacraplatin has ethacrynic acid axial ligands over a cisplatin scaffold, which upon release inhibit glutathione-S-transferase in a bid to overcome cisplatin resistance.[27,28] Mitaplatin on the other hand was reported to be able to selectively kill cancer cells over healthy fibroblasts thanks to the combined action of cisplatin and the two dichloroacetate molecules that also act on the mitochondria promoting apoptosis.[29] Although these compounds showed promising *in vitro* results, more advanced studies and insights into the *in vivo* behaviour and efficacy are still needed as none of these complexes have been able to improve the therapeutic efficacy of cisplatin.[25]

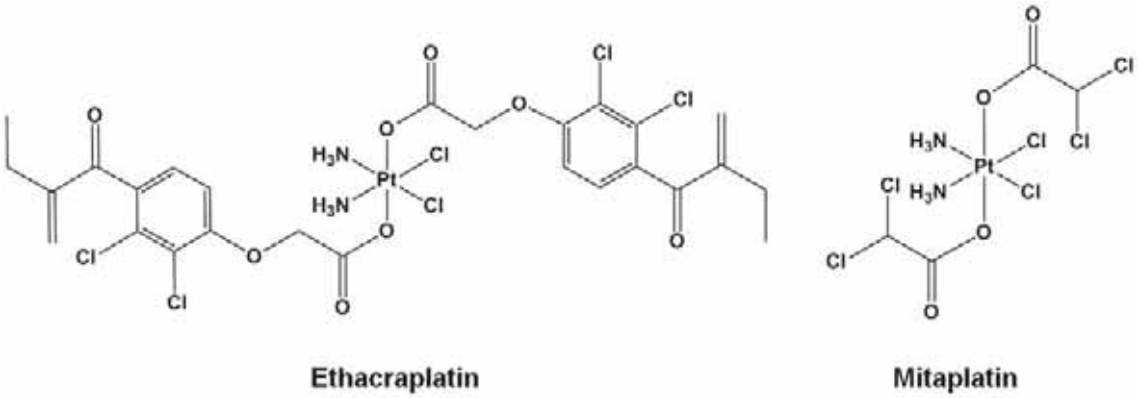

Figure 9. Chemical structures of the dually active cisplatin platinum (IV) derivatives ethacraplatin and mitaplatin.

1.1.2. Cancer immunotherapy

Over the past decades, the application of immunotherapy in cancer treatment has evolved from a promising new alternative to a consolidated option in clinics. Based on the ability of the body's own immune system to act to destroy the cancer cells, immunotherapy has attracted great interest and many efforts have been dedicated to develop efficient tools to exploit this approach (Figure 10).

Despite the immune system naturally being able to detect and destroy abnormal cells, cancerous cells often lay undetected due to a reduced expression of tumour antigens or the expression of proteins that induce immune cell inactivation. Immunotherapy focuses on stimulating the immune responses against cancer and counteracting the

signals that suppress the immune response. Many different approaches, including the use of antibodies (Abs), vaccines, immune checkpoint inhibitors, cell therapies or toll-like receptor (TLR) agonists have been developed for this aim, and various systems already have been approved to treat a variety of cancers.[30]

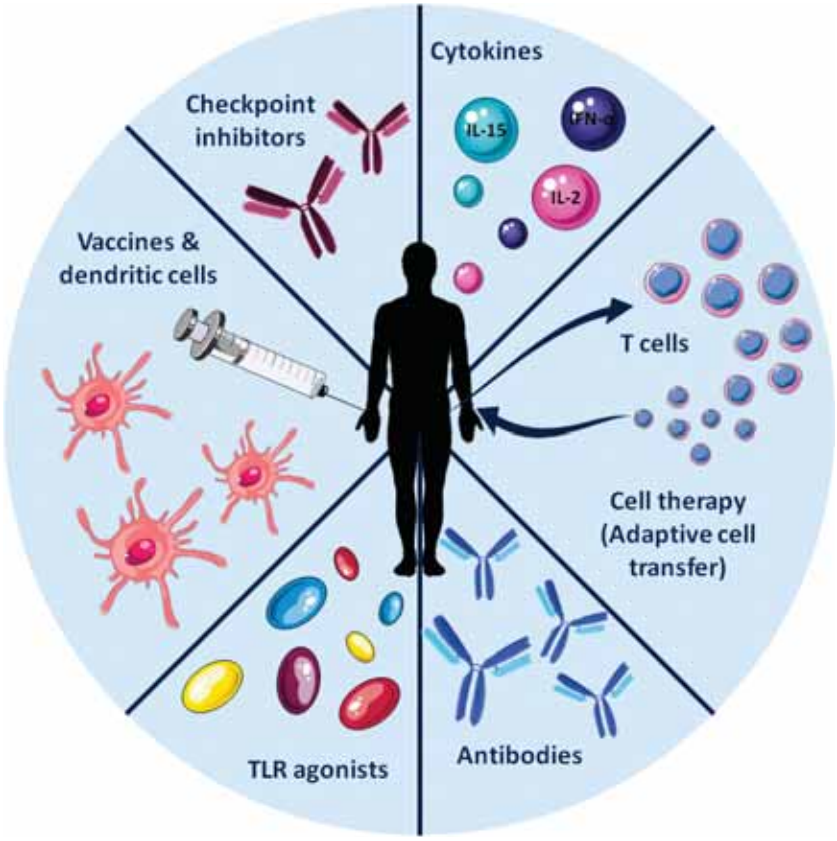

Figure 10. Summary of different anticancer immunotherapeutic approaches.

Particularly interesting for this thesis is the use of TLR agonists, which as it will be discussed later on, are not only valuable tools for immunotherapy, but can also act as chemotherapeutic drugs against cancer.[31,32] TLRs are a type of pattern recognition receptors (PRR) expressed in cells of the innate immune system to detect pathogens such as bacteria or viruses. Upon activation these receptors are able to start a signalling cascade that can produce powerful pro-inflammatory responses as well as the activation of cells of the immune system such as macrophages or natural killer (NK) cells. Thanks to important advances in the understanding and development of advanced immunotherapeutic tools to fight cancer, this approach is gaining great

significance as a single therapeutic tool, as well as in combination with the previously described strategies like radiation or chemotherapy.[33]

1.1.3. Limitations of traditional therapies

Both local and systemic anticancer therapies have great advantages and are indeed the most common clinical approaches, but they all suffer from unwanted side effects on one or another way. While immunotherapy aims at a more targeted approach to limit side effects and has a bright future ahead, many of the options still require very costly and time consuming processes such as cell manipulation and many others still have not been able to show a revolutionary clinical success. The main drawback of conventional chemotherapeutic drugs on the other hand, is their lack of selectivity, often resulting in undesired side effects like systemic toxicity and resistance to the drugs.[34] To describe de attempts to achieve targeted toxicity, the term "*Magic Bullet*" was coined on the late 19th century.[35] In spite of remaining a purely theoretical concept for many decades, the rapid growth of nanotechnology for medical applications now promises the development of such sophisticated strategies aiming to overcome the intrinsic limitations of traditional drugs and lead to more effective and safer therapies for cancer treatment.

1.2. *Nanotechnology based approaches in cancer*

Nanotechnology provides many benefits to various fields of modern medicine, but in particular is making a significant impact on cancer treatment and diagnosis. Starting from the basics, nanotechnology is the science regarding matter at the scale of 1 billionth of a metre, hence a nanometre (Figure 11).

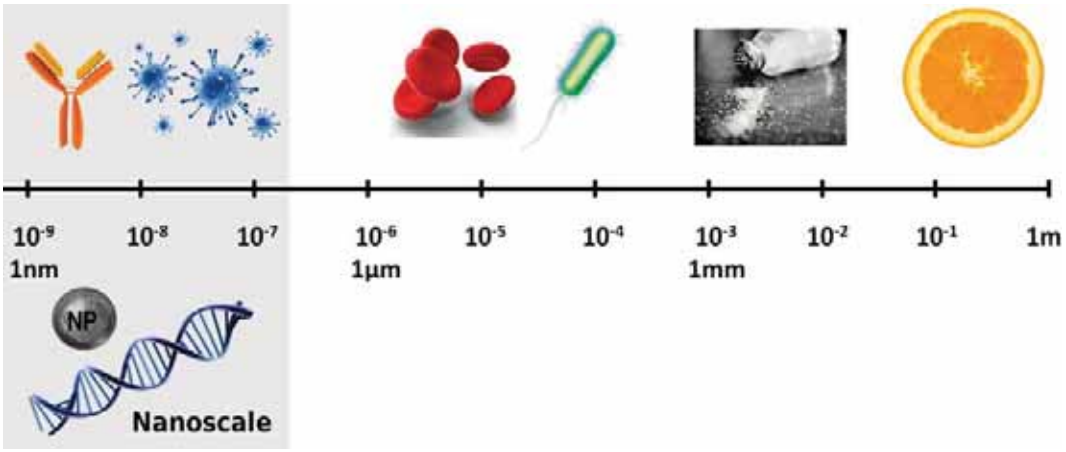

Figure 11. Illustration of different objects with sizes down to the nanoscale.

This rapidly growing research area deals with submicron moieties typically ranging from one up to several hundred nanometres in size, known as nanoparticles (NPs). Nanoparticles can be classified in two main categories depending on their composition; they can be organic or inorganic. Organic nanoparticles include liposomes, polymeric nanoparticles or carbon based materials such as carbon nanotubes or carbon dots. Inorganic nanoparticles on the other hand encompass metallic structures, based on gold or silver among others, semiconductor materials such as quantum dots or rare earth doped nanoparticles like up-converting nanoparticles (UCNPs).

The main reason for the increasing interest in nanoscale materials and their applicability in biomedicine relates to the unique properties that the nanoscale produces, providing nanomaterials with an intermediate behaviour between bulk materials and discrete molecules. This singular behaviour however, is not a recent discovery. It has been applied from ancient times in sculptures and paintings. One of

the most characteristic examples of that is the Lycurgus cup (fourth century AD), which changed from an opaque green colour to a transparent red by just shining light from the inside (Figure 12); it was later revealed that the presence of silver and gold nanocrystals was responsible for this phenomenon.

Figure 12. Images of the Lycurgus cup changing from green colour to a brilliant red when shining light from the inside.

The development of modern technology allowed not only discovering this early use of nanomaterials and understanding of their properties and science, but also led to a wide range of new possibilities in the applications of nanoscale structures, not only in biomedicine but also in many other fields ranging from electronics to agriculture. The growing interest in applying nanotechnology to cancer is largely attributable to how the exceptional features of nanoparticles readily contribute in many different aspects such as drug delivery, biosensing, image-based diagnosis and even the intrinsic therapeutic nature of some nanomaterials.[36]

1.2.1. The unique properties of nanoparticles

Among the several properties that get affected when taking a material to the nanoscale, the Lycurgus cup serves as an example to clearly illustrate how the optical

behaviour of nanomaterials greatly differs from the bulk. Two very clear exponents of this unique feature are semiconductor nanocrystals and plasmonic nanoparticles. In both cases the physical confinement of the material to nanoscale dimensions produces very particular optical properties.[37] In semiconductor nanocrystals, also known as quantum dots, the extremely small particle size causes the so called quantum confinement effect, where energy levels become discrete rather than continuous and as a result, the optical and electronic properties become strongly size dependent.[38] A decrease in particle size produces a blue shift in the optical absorption of quantum dots (Figure 13), therefore by slightly changing the size or even the composition, the absorption and fluorescence emission of quantum dots can be effectively tuned.

Figure 13. Size dependent fluorescent emission of semiconductor nanocrystals, quantum dots.

For plasmonic nanostructures, the strong light absorption is produced by the surface plasmon resonance (SPR) phenomenon. This effect was first described by Wood and is related to the collective oscillation of the conduction electrons in the surface of a nanoparticle exposed to light.[39,40] The point at which the amplitude of the oscillation reached maximum at a specific frequency is called SPR. According to Mie theory, this effect induces a strong absorption of the light that depends on particle composition, size, shape and structure among other things; when the shape of the particle is elongated for example, the SPR shifts towards higher wavelengths (Figure 14).[41]

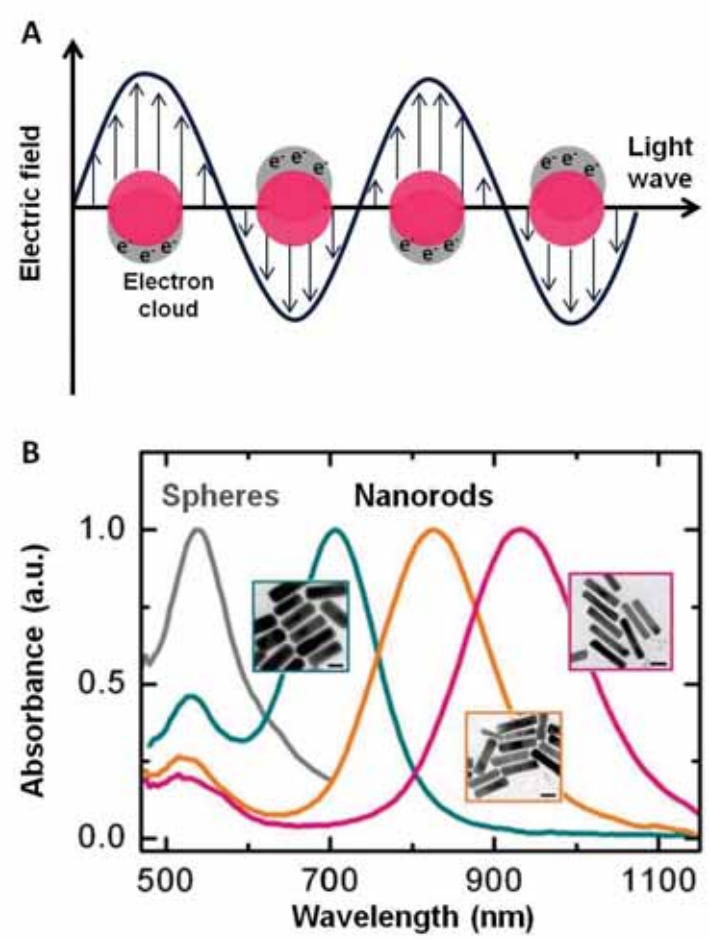

Figure 14. (**A**) SPR effect in gold nanoparticles due to the collective oscillation of surface electrons with incident light of a certain wavelength. (**B**) Shift in the absorbance spectrum from gold nanospheres to gold nanorods of increasing length. Adapted from [41]

Another very important characteristic affected by the size at the nanometre range is the magnetic behaviour of materials. The magnetic properties strongly depend on the size and morphology of the particles. In bulk state, magnetic materials are constituted of multidomains, but as particle size decreases to the micron or sub-micron range, the particles become monodomains, leading to a ferromagnetic behaviour. If size is reduced even further, the resulting nanoparticles become superparamagnetic.[42]

A very clear example of this behaviour can be observed in iron oxide nanoparticles where generally particles larger than 25 nm exhibit a ferromagnetic behaviour, hence

no need of an external magnetic field due to long relaxation times. When the particle size goes below 25 nm, the material does no longer exhibit any hysteresis effect and becomes superparamagnetic, thus an external magnetic field needs to be applied.[43]

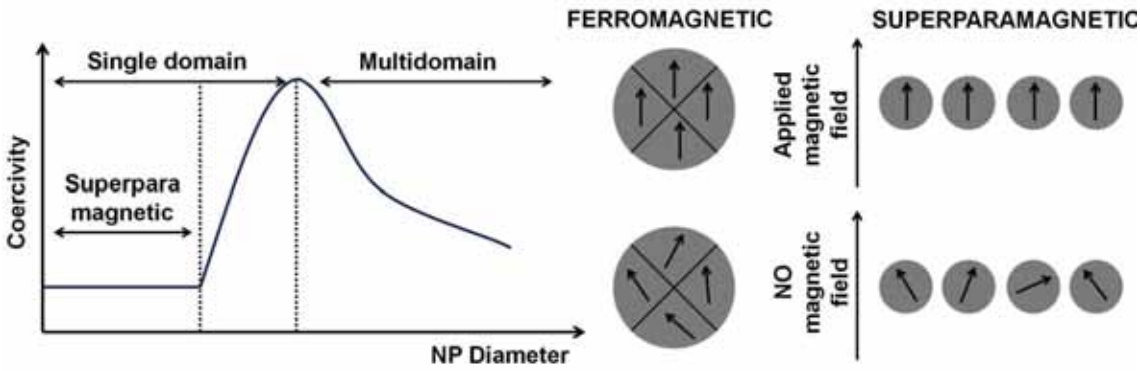

Figure 15. Size dependent magnetic behaviour of iron oxide nanoparticles.

Finally the small size of nanoparticles provides them with a large surface-to-volume ratio[44] which means that surface atoms in these particles have higher energies, effectively making nanoparticles more chemically reactive than the bulk material. This property is not only key for the development of catalytic systems, but also extremely important for surface functionalization and drug loading purposes.

All of these unique properties can provide strategic advantages over traditional molecular therapeutic approaches, with the successful application of nanomaterials to improve anticancer treatments becoming a revolutionary approach towards tackling the disease.

1.2.2. Nanoparticle-based drug delivery vehicles

Over the past decade, many efforts have been focused on the design and development of new drug delivery systems for improving cancer treatment.[36,46,47] Many of the most effective anticancer drugs being hydrophobic or poorly soluble, the use of nanoparticles as delivery vehicles can provide enhanced delivery, targeting and protection (Figure 16).

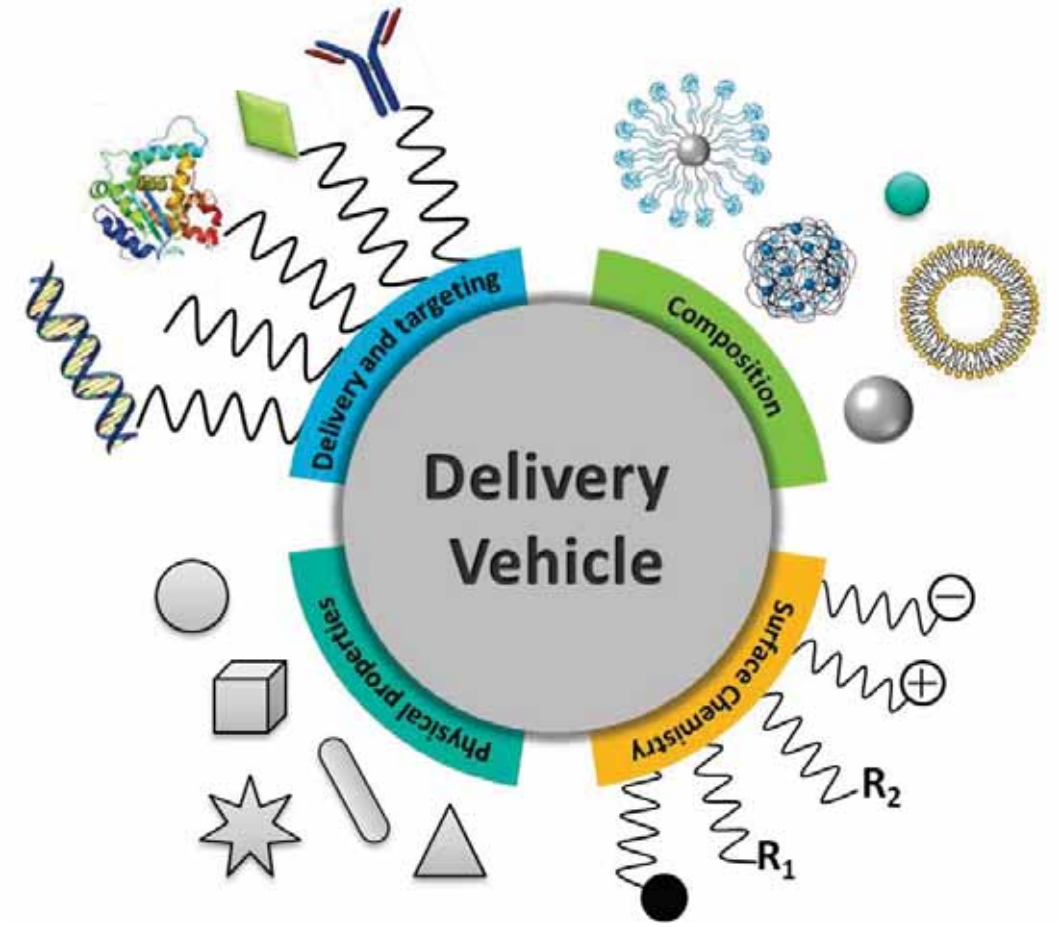

Figure 16. General features of nanoparticle based drug delivery vehicles.

Nanomaterials are available in a wide variety of compositions, ranging from micelles to polymer based nanoparticles, fluorescent quantum dots or metallic nanoparticles, each having particular properties. The shape of these nanoparticles can also influence their biological function. Based on a variety of synthetic protocols the shape and size can be tuned to obtain a myriad of structures going from spherical nanoparticles, to more complex ones like nanocubes or nanostars. Finally the surface of the nanocarrier can also be readily modified to introduce either functional groups, hydrophobic or hydrophilic ligands or targeting moieties and cargos like antibodies, small molecules, drugs or proteins depending on the specific needs.

The benefits of nanoparticle based delivery systems can be summarized in three key points. The first advantage is the possibility of overcoming the problems caused by the poor solubility and chemical stability of the traditional drugs,[48] either attaching them

to the surface of a nanoparticle or through encapsulation within a water soluble nanocarrier. This will not only protect the drug but also confer an improved pharmacokinetic profile (e.g. solubility, stability, circulating half-life). Second, the use of nanoparticles allows both passive and active targeting strategies to improve tumour accumulation. Such drug delivery systems can be rationally designed to accumulate in the tumour area taking advantage of the enhanced permeability and retention effect (EPR) or by attaching targeting moieties.[49] Third, this approach also facilitates controlled release strategies by using stimuli-responsive nanocarriers.[50,51]

Depending on the nature of the payload and the nanocarrier, three major strategies can be adopted to achieve drug loading: conjugation, encapsulation and adsorption.

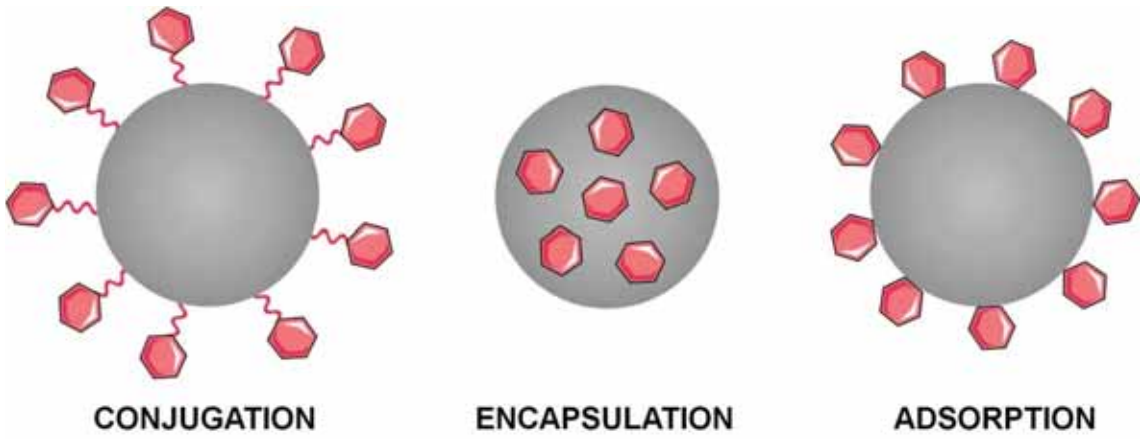

Figure 17. Schematics of the three main strategies for drug loading.

Encapsulation is most commonly applied in the case of organic nanoparticles such as liposomes or polymeric nanoparticles, which can incorporate hydrophobic cargos and deliver them in a water soluble manner.[52,53] The adsorption strategies are often based on either electrostatic or hydrophobic interactions, by which the drug can be retained and successfully delivered. An example is the electrostatic attachment of nucleic acids to positively charged nanoparticles in gene delivery systems.[54,55] The conjugation approach involves the creation of a chemical bond between the drug and the nanoparticle, usually mediated by carefully chosen ligands or linker molecules. In all

cases the delivery vectors must not only transport the payload but also be able to release it in a specific location.

The ability to selectively accumulate the nanotherapeutic system in the tumour area is a key factor towards achieving a successful and efficient treatment. Both passive and active targeting approaches have been widely reported (Figure 18).[56,57] Passive drug delivery is based on exploiting the characteristics of tumour growth, and the well described enhanced permeability and retention (EPR) effect.[58] First identified by Maeda and Matsumara in the 1980s, this phenomenon relies on the leaky vasculature and dysfunctional lymphatic drainage of tumours which allows small size nanoparticles to enter the interstitium and accumulate in the tumour.[59,60] With the aim of accomplishing an increased delivery to the tumour a variety of active targeting strategies have been developed attaching diverse moieties to the surface of nanoparticles.[61,62]

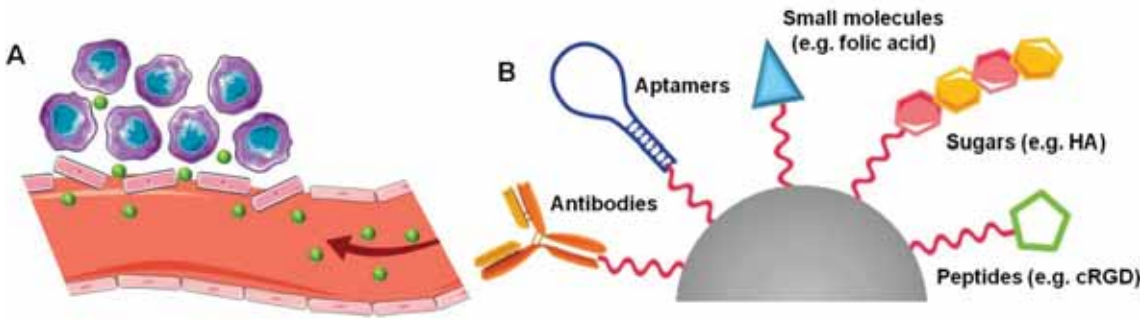

Figure 18. Schematic representation of (**A**) the EPR effect (passive targeting) and (**B**) active targeting strategies.

The most commonly used targeting moieties include monoclonal antibodies or antibody fragments, small molecules, peptides, carbohydrates or aptamers recognized by specific receptors exclusively expressed on tumour cells or those with a clear overexpression compared to healthy tissue. Wang *et al*. reported the use of an anti-epidermal growth factor receptor (EGFR) mAb (Cetuximab) as an active targeting ligand in IONPs for enhanced magnetic resonance imaging (MRI) sensitivity and thermal ablation of lung cancer *in vivo*.[63] Shi *et al*. described a dual targeting approach

based on the use of a $\alpha_v\beta_3$ integrin targeting small molecule (tetrac) and hyaluronic acid (HA); another small molecule known to have specific affinity for CD44 cells.[64] Using this dual-targeting strategy in paclitaxel loaded solid-lipid nanoparticles (SLNs) the authors reported an improved antitumour therapeutic effect in a B16F10 metastatic melanoma model. Lippard and co-workers used an aptamer targeting the prostate specific membrane antigen (PSMA) to improve the delivery of a platinum (IV) prodrug for prostate cancer treatment.[65] Despite the great number of active targeting strategies reported over the last decade, these approaches have not achieved to date breakthrough improvements in terms of therapeutic outcomes. In fact a recent literature survey by Wilhelm *et al*. on this issue indicates that the median delivery efficiency has not improved in the past decade,[66] suggesting that a more simple system based on passive accumulation of the nanoparticles in the tumour might also result in an effective cancer drug delivery system.

Beyond the possibility of selective tumour accumulation and enhanced delivery, nanoparticle based systems also provide a higher degree of control over the drug release, another essential factor in anticancer therapy. For this reason the study of different strategies that impart the ability to trigger the liberation of the drug is a key aspect. Triggers can be classified into internal or external but in either case, the exposure to the proper stimulus must produce physical or chemical changes in the delivery system drastic enough to allow the release of the drug cargo.

Internal stimuli involve changes in the microenvironment of the tumour compared to normal tissue such as pH, redox, or enzyme activity. A recent work by Cui *et al.* serves as example of internal stimuli responsive systems.[67] The authors developed a two-step stimulus responsive gold nanoparticle-based delivery vehicle for the widely known anticancer drug doxorubicin (Figure 19). The incorporation of the drug to the nanocarrier is achieved via a conjugation mechanism, using lipoic acid as a linker between the carbonyl group of the doxorubicin and the gold nanoparticle. To confer further solubility and stability, the amino group of the drug is conjugated to a PEG moiety through a carbamate bond. When the system is internalized into the cells, the acidic pH in the lysosomes triggers the first release, cleaving the hydrazone bond with

the nanoparticle. When the PEG-conjugated drug is released into the cytoplasm, the second release reaction occurs catalyzed by stearase, yielding the free doxorubicin which can then enter the nucleus and produce the anticancer effect. The use of the gold nanoparticle as a delivery vehicle not only is reported to provide solubility and protection to the drug, but also to lead to an increased uptake and efficacy thanks to the dually triggered release of the doxorubicin.

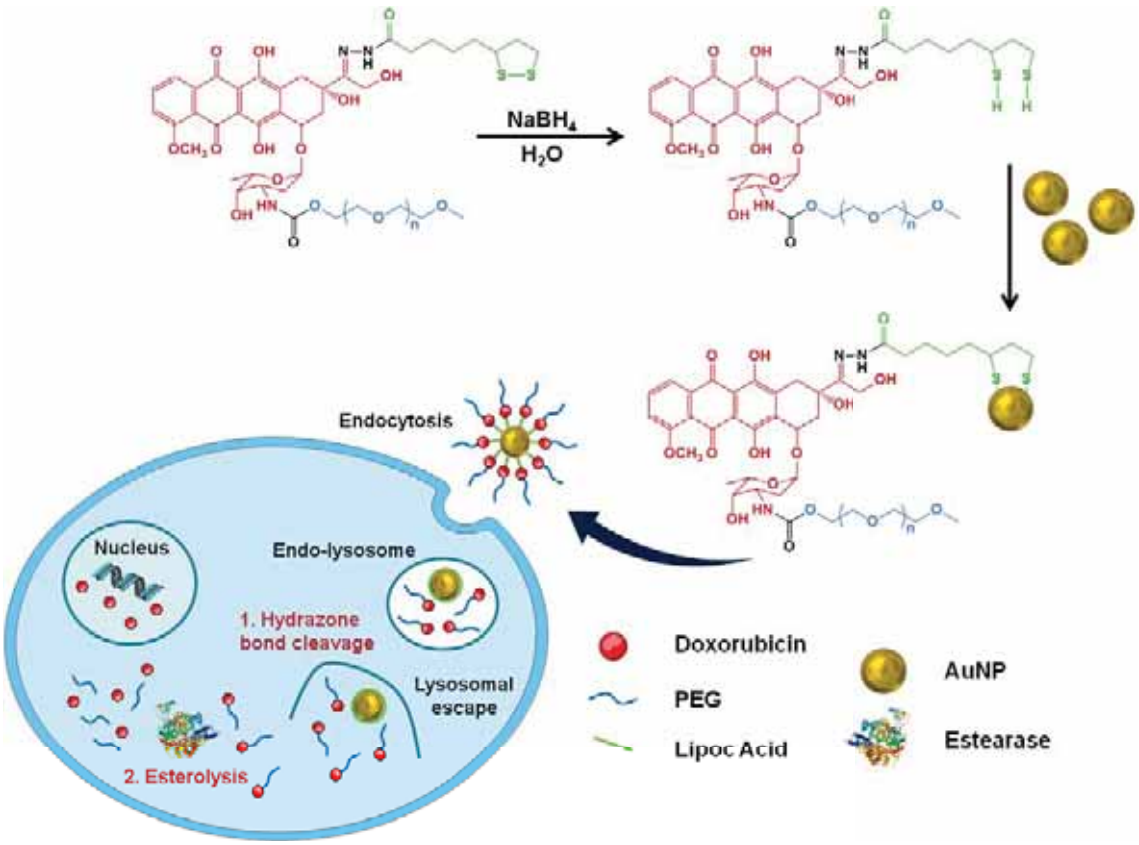

Figure 19. The structure of AuNP-NHN=Dox-mPEG and an illustration of its intracellular drug release mechanism.[67]

External stimuli on the other hand include application of magnetic fields, light irradiation or ultrasounds. The use of light for example is an effective and non-invasive approach to provide controlled release of a chemotherapeutic drug. In many cases however, high energy UV light is needed, which apart from having a low penetration depth is also harmful to healthy tissue. Therefore the use of low energy near infra red (NIR) light is preferred as an external stimulus for clinical applications. An example of NIR light triggered drug release was reported by Fedoryshin *et al*. using up converting

nanoparticles (UCNPs) for the delivery and controlled release of the chemotherapeutic agent 5-fluorouracil (Figure 20).[68] UCNPs are known for their ability to convert NIR light into high energy UV/visible radiation, which in this case is able to cleave the *o*-nitrobenzyl linker between the drug and the carrier.

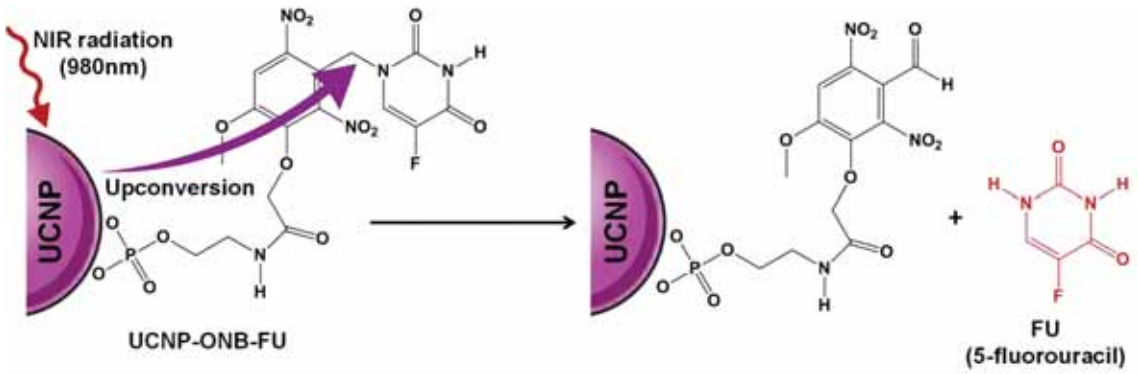

Figure 20. Schematics of the NIR triggered drug release. NIR excitation of the UCNP resulting in upconverted emission at 364 nm, used for the photo-cleavage of the ONB-FU bond and subsequent release of 5-fluorouracil from the UCNP surface.[68]

1.2.3. Beyond drug delivery: nanoparticles as multimodal imaging and intrinsically therapeutic agents.

The importance of nanoparticles goes way beyond their use as delivery vehicles for different anticancer drugs. Their unique properties also contribute to their use as imaging agents or contrast enhancers and even alternative therapeutic approaches using the intrinsic properties of the nanomaterials. Given that gold and iron oxide nanoparticles have been used during this thesis, the following sections will focus on these materials, their properties and recent advances as both imaging and intrinsically therapeutic agents for cancer.

Gold is well known to be one of the most resistant and inert metals and is this bioinert nature that makes gold an ideal material for biological applications (Figure 21). Although being mainly a non reactive material, the strong affinity of gold for thiolated compounds or disulfide groups has been well described and investigated as functionalization strategy for gold nanomaterials.[69] In addition, gold characterizes for

its ability to attenuate high energy radiation, making it a very interesting material for the development of X-ray contrast agents.[70] Significantly, gold nanostructures are also able to produce heat under the proper light irradiation conditions, serving as potentially therapeutic entities for thermal ablation of tumour tissue and cancer cells.[71]

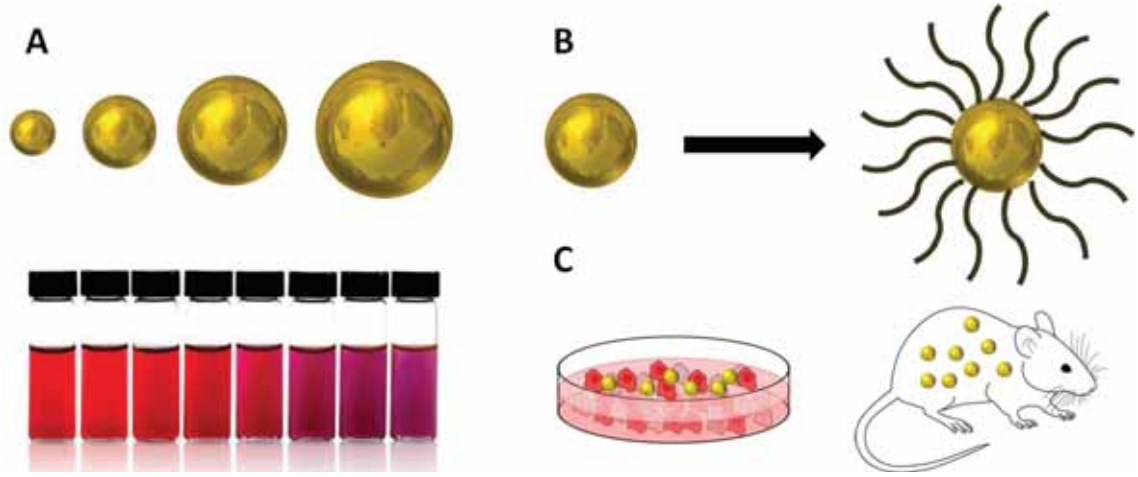

Figure 21. Advantages of AuNPs. (**A**) Tuneable size a photography showing the change in colour of increasing size AuNPs, (**B**) Straight forward functionalization. (**C**) Biocompatibility.

Iron oxide based nanoparticles (IONPs) on the other hand are abundant in nature and present in soils, natural waters, sediments and even in some living organisms such as magnetotactic bacteria.[72] Due to their magnetic nature, they have been used in many applications ranging from magnetoreception and compasses to hard disks.[73] IONPs are typically composed of maghemite (γ-Fe_2O_3) or magnetite (Fe_3O_4) and synthetic procedures nowadays allow the preparation of a wide range of shapes and sizes (Figure 22). In addition, the body's natural ability to metabolize iron renders these materials great biocompatibility.[74] IONPs have indeed been extensively studied as contrast agents for MRI, but their magnetic properties also contribute to the applicability as multifunctional platforms provided by magnetically guided drug delivery and heat based anticancer therapy.

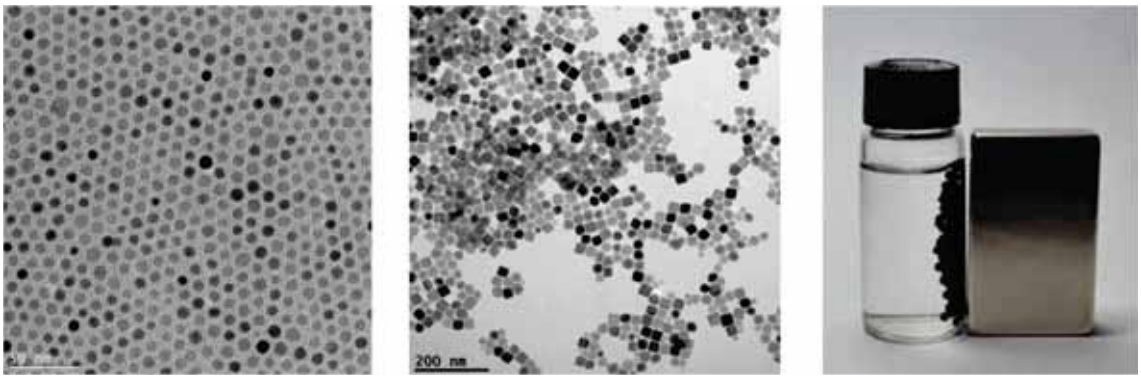

Figure 22. TEM images of iron oxide nanospheres and nanocubes developed in this thesis, representative of the tuneable size and shape. Photograph illustrating the magnetic manipulation of IONPs.

1.2.3.1. AuNPs and IONPs for biomedical and multimodal imaging

Biomedical imaging is undoubtedly one of the mail pillars of cancer clinical protocols, providing structural and functional information with minimally invasive techniques. Although it plays a major part in many aspects such as detection, screening, staging, image guided therapy and assessment of the therapeutic response, the role of imaging techniques in early-diagnosis in particular has made an enormous impact in the reduction of cancer mortality.[75]

A number of different imaging techniques are currently used in clinics, including MRI, optical imaging, ultrasound imaging, X-ray computerized tomography (CT) or nuclear techniques such as single photon emission computerized tomography (SPECT) and positron emission tomography (PET). All these modalities present their own strengths and weaknesses in terms of sensitivity, resolution and tissue depth penetration (Table 1). Nuclear imaging techniques for example exhibit a very high sensitivity but limited resolution; MRI or CT on the contrary are able to provide very high spatial resolution and accurate anatomical information, but their sensitivity is rather low. Optical imaging based on fluorescence on the other hand is routinely used for studies at the cellular level, but the scattering and low tissue penetration complicate and limit *in vivo* applications. Given that none of the individual techniques is enough to provide high resolution anatomical information with a high sensitivity, many efforts have been

focused on the development of combined approaches involving multiple imaging modalities.

Table 1. Comparison between different imaging modalities in terms of sensitivity, resolution and tissue penetration depth.

Modality	Sensitivity	Spatial resolution	Depth
CT	mM	50-200 μm	No limit
MRI	nM-μM	10-100 μm	No limit
Optical	nM	> 0.3 μm	< 10 cm
PET, SPECT	pM	1-2 mm	No limit

Functional nanomaterials have become an ideal platform to combine the strengths of various techniques and develop multimodal imaging agents able to provide precise information at the anatomical, functional and molecular level (Figure 23). The unique inherent properties of different nanomaterials and their readily modifiable surfaces allows the design of novel imaging probes with increased sensitivity, spatial and temporal resolution as well as a controlled biodistribution.[76,77]

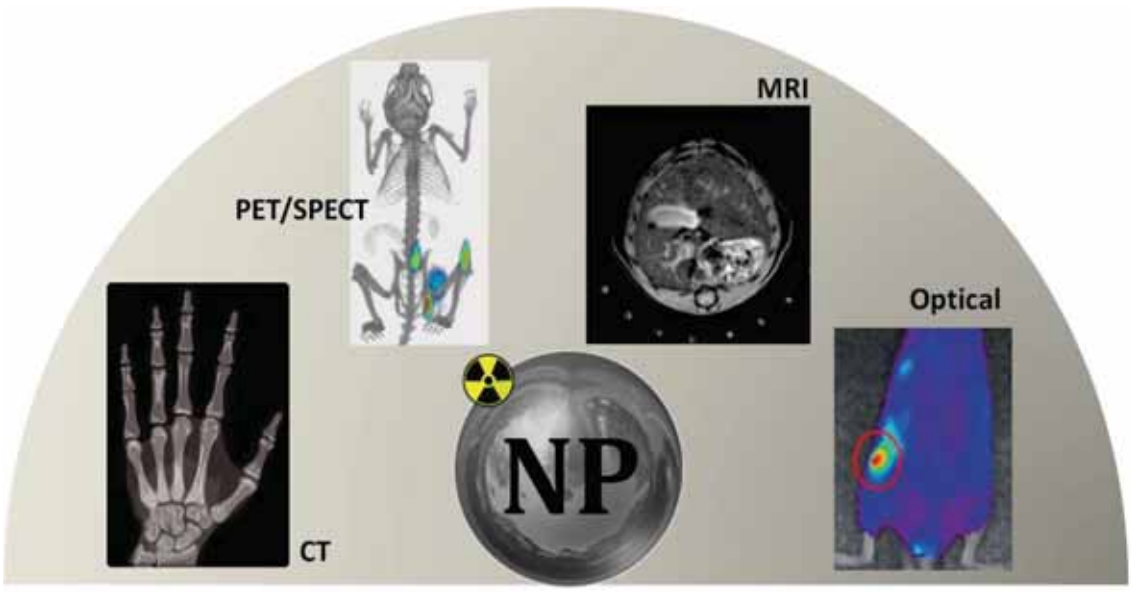

Figure 23. Representation of different imaging modalities that nanoparticles can provide towards multimodal imaging.

Gold based nanomaterials offer excellent properties for various imaging modalities; fluorescent gold nanoclusters for instance can be prepared with excitation and emission profiles tuned from the UV to the NIR regions, offering a great alternative to traditional dyes and fluorescent probes.[78–80] Not only applicable in cellular studies, gold nanoclusters have also been reported for *in vivo* optical imaging applications.[81] The ability of gold to enhance X-ray contrast on the other hand, dates back to the 1890s, when Wilhelm Roentgen took an X-ray image of his wife's hand and the gold ring on her finger produced a greater attenuation than the bones. The attenuation is dependent on the electron density, thus atomic number of the elements present in the tissue; therefore gold is able to produce a stronger contrast than the natural elements present in the body. Compared to traditional iodine based contrast agents for CT, gold nanostructures show a 2.7-fold enhancement of the mass attenuation coefficient.[82] The enhancement, however, is proportional to the amount of gold localized in a certain area. Given the low sensitivity of the technique, high doses are required to obtain sufficient contrast enhancement. For this reason, development of gold based nanostructures that combine their intrinsic properties for optical or CT imaging with more sensitive techniques such as MRI or nuclear imaging have gained great interest.

With the aim of developing dual CT/nuclear imaging nanostructures, many examples of radiolabelled AuNPs have been reported recently using radioisotopes such as ^{64}Cu or ^{89}Zr for PET[83–86] and ^{111}In, ^{123}I or ^{199}Au for SPECT.[87–89] Most of these systems rely on the attachment of external moieties like antibodies, peptides or chelators to achieve the radiolabelling. Zhao *et al.* reported a ^{64}Cu-alloyed gold nanoparticle system for combined PET/CT imaging,[90,91] which avoids the traditional chelator-based strategy to introduce a radioisotope to a nanoparticle by the direct incorporation of the copper into the nanostructure's lattice, forming ^{64}CuAuNPs. This system could be clearly detected by PET/CT in both breast and prostate cancer tumour models.

A more recent publication by Ge *et al.* described a novel combination of lanthanides and gold nanoparticles for CT/MRI dual imaging.[92] The authors report a facile synthetic method to prepare gold nanoparticles by using oleylamine not only as reducing and stabilizing agent but also as a bridge between the gold and the lanthanide ions (Figure

24). Both Gd^{3+} and Yb^{3+} are able to coordinate to the nitrogen atom on the oleylamine to form the conjugated system, which is further functionalized with PEG to achieve water solubility and biocompatibility. Gd^{3+} is a well known contrast agent for MRI, having seven unpaired electrons is able to affect the longitudinal relaxation times of the water protons in the surrounding tissue to generate positive contrast, also known as T_1 imaging. The high atomic number and electron density of both gold and ytterbium on the other hand renders a stronger attenuation of X-rays in CT imaging. The capacity of the system for dual-imaging was tested both *in vitro* and *in vivo* with tumour bearing mice confirming the applicability of this combined approach for cancer imaging.

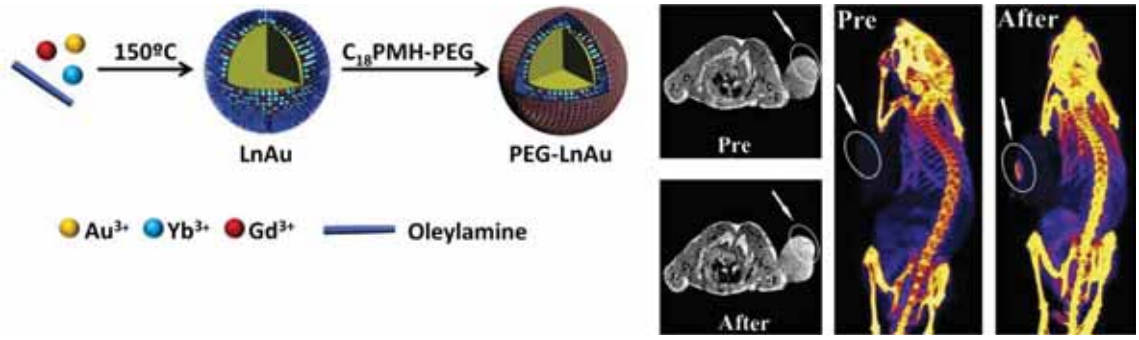

Figure 24. PEGylated lanthanide-AuNPs for CT/MRI dual imaging in tumour bearing mice (tumour region indicated with white arrows). Figure adapted from [92]

The potential of iron oxide nanoparticles to act as contrast agents for MRI was first described by Ohgushi and co-workers in 1978 for dextran-coated nanoparticles.[93] Under the magnetic field of a MRI scanner, the superparamagnetic nature of these nanoparticles induces a magnetic dipole moment that is able to perturb the magnetic relaxation of the surrounding water protons and cause a substantial shortening of their spin-spin relaxation time (T_2). This perturbation results in decreased signal intensity, hence a darkening of the area of the MR image. The efficiency of the contrast enhancement is indicated by the relaxivity coefficient (r_2), a value obtained as the gradient of the plot of R_2 ($R_2 = 1/T_2$) versus the molarity of the magnetic atoms. Both the size and the composition of the nanoparticles affect the r_2 values as shown in Figure 25; within the size range where the superparamagnetic nature of the

nanoparticles exists, the relaxivity coefficient increases with size.[94] Regarding the composition, the r_2 values can also be increased by replacing some of the Fe^{2+} ions by other transition metal ions such as Mn^{2+}, Co^{2+} or Zn^{2+} to form doped-IONPs.[95]

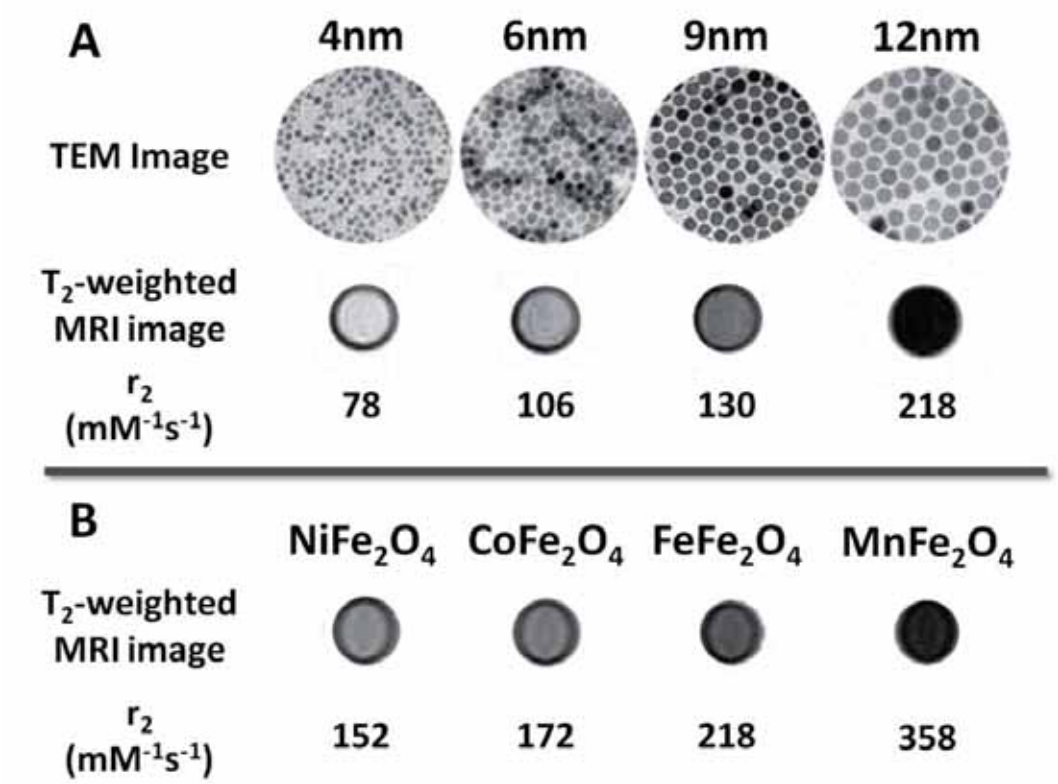

Figure 25. Changes in T_2-weighed MR contrast of IONPs depending on the size (**A**) and the introduction of doping metal ions (**B**).

Several iron oxide based nanoparticles have been approved by the FDA for MR contrast enhancement.[96] However, the low commercial interest and the lack of improvement compared to gadolinium based T_1 contrast agents caused the withdrawal of all of them from the market. Nevertheless many efforts are still focused on the development of more efficient iron oxide based contrast agents as extensive preclinical and clinical studies on the previously approved preparations already proved the excellent safety profile of these materials. New clinical trials are indeed planned for testing the iron oxide based drug Ferumoxytol, already approved for the treatment of iron deficiency, as an MR contrast agent.[97]However, as mentioned previously a single imaging modality is not able to provide sufficient information.

Taking advantage of the aforementioned intrinsic capacity of IONPs to produce T_2–weighed MR contrast, many approaches have been described to introduce additional imaging modalities including optical, nuclear or CT based imaging.[98,99] Regarding dual MRI/optical platforms the initial approach involved the use of traditional fluorescent dyes like rhodamine or Cy5.5. The latter has been particularly interesting due to its NIR fluorescence nature and therefore deeper tissue penetration.[100,101] More sophisticated alternatives have taken advantage of intrinsically fluorescent nanoparticles such as quantum dots,[102] carbon dots[103] or UCNPs.[104] A great variety of hybrid systems has been reported, using electrostatic and covalent interactions, encapsulation strategies and also core@shell structures. As an illustrative example of the wide range of possibilities to develop hybrid systems, two distinct IONP-UCNP core@shell dual imaging probes have been selected.

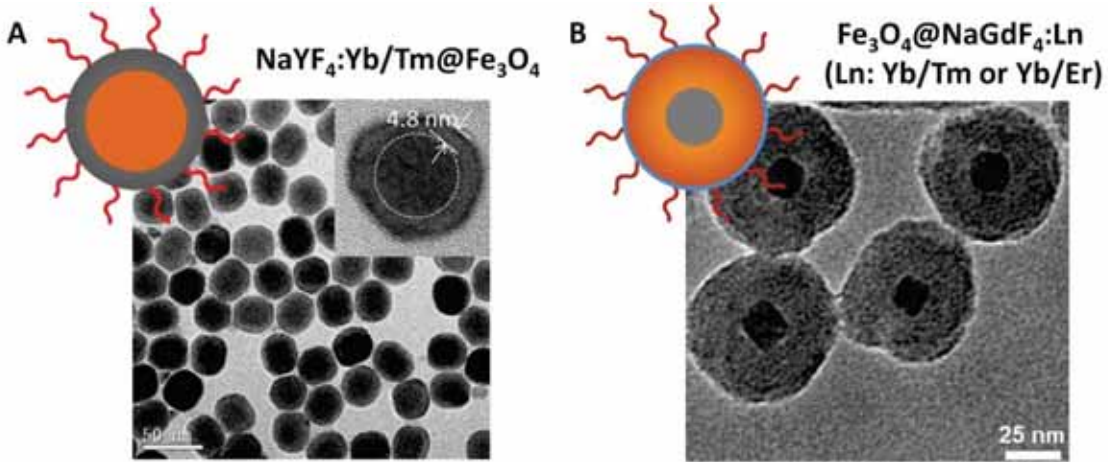

Figure 26. Schematic representation and TEM images of two relevant UCNP-IONP core@shell combinations for UCL/MRI imaging. (**A**) Nanoparticles consisting of UCNP cores with an iron oxide shell and (**B**) using IONP cores with a gadolinium based UC shell. Figure adapted from [105] and [106]

Li and co-workers reported the synthesis of NIR fluorescent UCNPs with an iron oxide shell to provide MR contrast (Figure 26A).[105] The resulting system was successfully used for *in vivo* lymph node imaging in mice using both the up-converting luminescence (UCL) at 800 nm upon excitation with a 980 nm laser and T_2 weighed MR imaging. Anker and co-workers on the other hand developed a PEGylated

Fe_3O_4@$NaGdF_4$:Yb/Er or Yb/Tm nanoconstruct able to combine UCL with both T_1 and T_2 MRI thanks to the presence of both IONPs and gadolinium ions (Figure 26B).[106] Although the system was not tested *in vivo*, the authors assessed the UCL imaging up to 1 cm deep in tissue, as well as the non-toxic nature of the nanoparticles in breast cancer cells.

The design of radiolabelled IONPs for dual nuclear-MR imaging has also been extensively exploited. Radiolabelling strategies for both PET and SPECT radioisotopes have been described including ^{11}C, ^{64}Cu, ^{67}Ga, ^{68}Ga, ^{69}Ge, ^{89}Zr, $^{*}As$, ^{99m}Tc, ^{111}In and ^{124}I.[107–118] In many cases, traditional chelating ligands such as DOTA or NOTA and radiolabelled moieties such as ^{89}Zr-DFO or ^{124}I-labelled serum albumin have been employed; more recently however direct chelator-free strategies have gained great interest. Pioneered by Chen *et al*. who reported a novel chelator-free radioarsenic labelling of IONPs for dual PET/MRI *in vivo* imaging,[114] many groups have adopted similar strategies to produce dual imaging IONP nanoconstructs. Among them, Holland and co-workers described a novel and versatile heat induced approach to radiolabel IONPs, where they demonstrate the efficacy of the process for the chelate free labelling of FDA approved IONP-based MR contrast agent Feraheme with three different radioisotopes (^{89}Zr, ^{64}Cu and ^{111}In).[109] A more recent example by Mareque-Rivas and co-workers takes advantage of the affinity of Ga^{3+} ions for magnetite to afford a direct chelator-free labelling of IONPs with ^{67}Ga or ^{68}Ga for dual SPECT/MRI or PET/MRI image tracked delivery of immunostimulatory molecules to the lymph nodes.[110]

Finally several hybrid systems that combine both gold and iron oxide nanoparticles for multimodal imaging have also been reported. Carril *et al*. synthesized gold-coated iron oxide gyconanoparticles for tri-modal imaging, combining MRI, CT and ultrasound imaging in a single platform.[119] A similar core@shell strategy as followed by Shi and co-workers, but changing the morphology of the gold coating to form a gold nanostar shell around the IONPs.[120] Further functionalization with polyethyleneimine and hyaluronic acid rendered biocompatibility to the system which was able to combine MRI and CT imaging both *in vitro* and *in vivo* using tumour

bearing mice. Gu and co-workers on the other hand selected heterostructures Au-Fe_3O_4 nanoparticles for a similar dual MRI/CT imaging approach in rabbits.[121] As a different alternative and taking advantage of the optical properties of AuNPs, Wang *et al.* made use of electrostatic interactions to adsorb fluorescent gold nanoclusters to the surface of negatively charged CTAB coated magnetic nanoparticles.[122] These gold nanoclusters presented a bright red fluorescence under 365 nm UV light and the IONPs retained their magnetic properties even after the formation of the hybrid system. The authors used this dual imaging system as a proof of concept and confirmed its biocompatibility and ability to act as a fluorescent probe in 293T cells. The potential use of these hybrid particles as T_2 contrast agents was also assessed, showing a concentration dependent enhancement of R_2 values.

1.2.3.2. Intrinsic therapeutic properties of nanoparticles

Although this aspect is not the focus of this thesis, cancer nanotechnology also exploits the inherent therapeutic properties of some nanoparticles. Both iron oxide and gold nanoparticles have the intrinsic ability to produce heat under certain conditions, which can be applied in a therapeutic approach, commonly known as hyperthermia. The exposure to elevated temperatures has been described to turn cells more sensitive to radiation and chemotherapy, serving as an adjuvant.[123] If enough heat is produced however, cells can suffer irreversible damage due to the loss of membrane integrity, DNA damage, protein denaturalization or inhibition of biochemical pathways. While a moderate rise in temperature preferentially induces apoptotic mechanisms, temperatures rising above 46 ºC produce necrotic cell death.[124] Taking advantage of both passive and active targeting strategies, heat-producing nanoparticles can selectively accumulate in the tumour area, maximizing the local effectiveness of hyperthermia while limiting the exposure and damage to the surrounding healthy tissues.

The characteristic SPR band of gold nanoparticles is not only responsible for a strong absorption, but also allows this absorbed light to then be converted into heat through a series of non-radiative processes, making gold nanomaterials ideal for light

induced heat generation or photothermal therapy (PTT).[125] A rational design of the gold nanostructures can provide a strong absorption in the NIR region – an ideal wavelength range considering the biological optical window that allows deep tissue penetration.[126] Although simple gold nanospheres do not allow such long wavelength absorption, alternative structures such as silica-gold nanoshells, gold nanorods or gold nanocages have successfully been used in cancer PTT both *in vitro* and *in vivo*.

The first extensive *in vitro* study of gold nanoparticle mediated PTT was reported by Pitsillides *et al*. who used micro and nanosize gold nanoparticles to selectively damage lymphocytes upon irradiation with a pulsed laser.[127] The same year Hirsch *et al.* published the first *in vivo* application of NIR absorbing silica-gold nanoshells for the thermal ablation of a human breast carcinoma xenograft model in mice.[128] Since then, many other examples of gold nanoshells for PTT have been reported, many including active targeting moieties to improve the selective accumulation in the tumour area.[129–133]

Despite the initial success of gold nanoshells however, AuNRs quickly gained wide interest as they can also be tuned to achieve strong NIR absorption and were found to be more efficient for light induced heat generation.[134–136] Bhatia and co-workers for instance reported the photothermal treatment of breast cancer xenograft tumour models using PEG-coated AuNRs. Compared to nanoshells, these AuNR system shows a 6-fold increase in heat generation and as shown in Figure 27, the mice treated with the PTT present a clear decrease in tumour volume as well as an extended survival rate.[136] Since then, more exotic gold structures have also been designed for PTT applications, including nanocages,[137] nanomatryoshkas,[138,139] nano-semicubes[140] or hybrid nanoparticles[92,120] among others.

Wang *et al*. for instance published a comparative study of gold nanohexapods, nanorods and nanocages for PTT.[137] Using these three NIR absorbing gold nanostructures they first evaluate the light-to-heat conversion ability of all three materials and demonstrate how the addition of a PEGylated surface to improve the biocompatibility is especially important in the case of AuNRs (Figure 28). The authors also investigate the *in vivo* biodistribution in tumour bearing mice as well as the heat

generation and PTT efficacy in terms of tumour metabolic activity and conclude that nanohexapods are the most promising structures for this biomedical application.

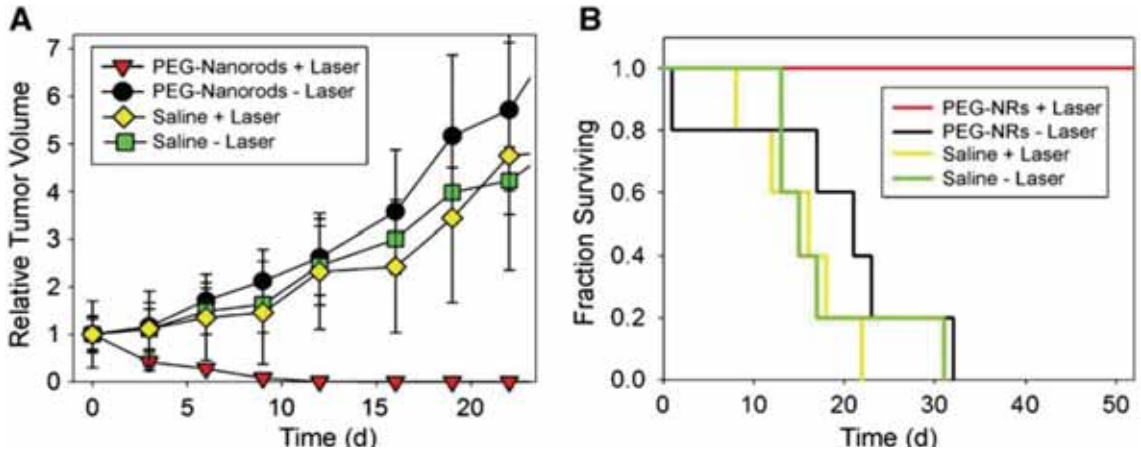

Figure 27. *In vivo* antitumour efficacy of PEG-coated AuNRs as PTT agents is a breast cancer xenograft model in terms of (**A**) tumour volume and (**B**) survival rate.[141]

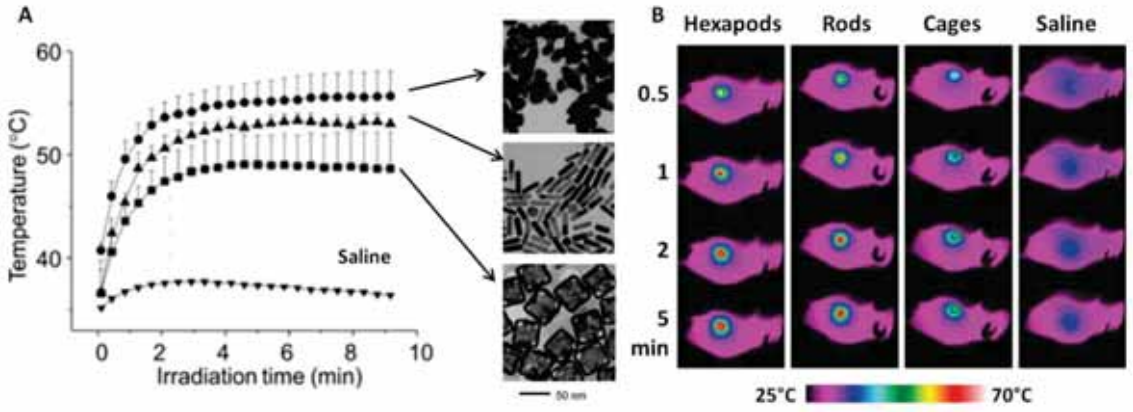

Figure 28. Comparative study of gold nanohexapods, nanorods and nanocages for PTT. (**A**) Plot of the average temperature increase of the tumour area upon irradiation (808 nm) with the PEGylated gold nanostructures and (**B**) thermographs of the tumour bearing mice receiving the treatment at different irradiation times. Adapted from [137]

Besides AuNPs, thanks to their magnetic nature IONPs also have the intrinsic ability to produce enough heat to be applicable in hyperthermia treatment. Rather than through a light induced mechanism, IONPs generate heat when subjected to an alternating magnetic field (AMF) through the Néel and Brownian relaxation processes

shown in Figure 29.[72] While the Néel relaxation is caused by the continuous reorientation of the spins of the nanoparticles under the AMF, the Brownian relaxation component relates to the friction caused by the physical rotation of the nanoparticles in the surrounding media.

Figure 29. Heating dissipation processes of IONPs under an AMF. Néel relaxation is related to the alignment and relaxation of the spins while the Brownian relaxation is determined by the rotational mobility of the nanoparticles.

Known as magnetic hyperthermia, the use of magnetic IONPs for thermal treatment was first explored by Gilchrist *et al*. in 1957 as a tool to destroy lymph node metastases in dogs.[142] However, still today some degree of controversy exists over the results due to the lack of control experiments. In spite of the debate, many groups continued this research line since its initial discovery due to the very appealing advantages of the technique. The use of an AFM presents no restrictions in tissue penetration and the selective tumour accumulation as well as the possibility of magnetic guidance of the nanoparticles allows a selective treatment with minimal damage to the surrounding tissue. In fact the first clinically applicable magnetic hyperthermia system was developed in 2004 and only a few years later European regulatory approval was obtained by MagForce® for magnetic hyperthermia based brain tumour treatment. Since then, many *in vivo* studies using animal models and even clinical trials have been carried out to study the possible application of magnetic hyperthermia in different cancer types.

Most of the current research on magnetic hyperthermia is focussed on improving the effectiveness of a nanoparticle system to generate heat under an AMF. This parameter is most commonly defined by the specific adsorption rate (SAR), the rate at which the electromagnetic energy is absorbed, and is highly dependent on the magnetic

properties, size[143] and morphology of the nanoparticles. [143] With the aim of improving the heating efficiency different strategies such as the introduction of doping metal ions,[144–146] core/shell[147] structures and the synthesis of non spherical nanoconstructs[148–150] can be adopted. Nemati *et al*. for instance recently described how a core/shell morphology can enhance the heat generation efficacy of IONPs compared to normal spherical nanoparticles of a similar size.[147] Several examples of doped compositions and anisotropic structures such as cubes,[151,152] octopods,[153] rods,[154] or prisms[150] and have also been reported over the past few years. Samia and co-workers recently published a thorough study comparing the SAR of spherical and cubic IONP as well as the effect of a zinc doped composition in both cases. As shown in Figure 30 the Zn-doped oxide nanocubes proved to be the most efficient heat producers, with a 5-fold improvement compared to undoped spherical IONPs.[152] Kanaras and co-workers on the other hand reported the application of manganese doped iron oxide nanoclusters for both MRI and magnetic hyperthermia.[146] Due to both the presence of manganese and the cluster structure, the authors achieved a greatly improved SAR compared to previously reported manganese ferrite NPs and more importantly within a safe amplitude and frequency range of the magnetic field.

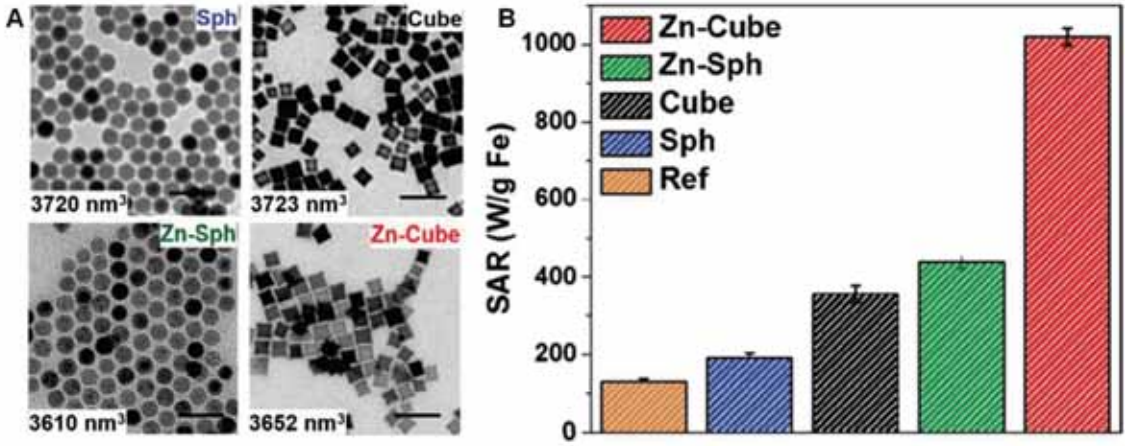

Figure 30. (**A**) TEM images of the Zn-doped and undoped spherical and cubic IONPs and (**B**) the calculated specific absorption rates (SAR) from hyperthermia measurements of all samples. Adapted from [152]

1.3 Theranostic nanomedicine for cancer

Nanotechnology offers unique opportunities towards improving cancer treatment and diagnosis. As described throughout this chapter, nanoparticles do not simply play a major role in anticancer drug delivery but can also serve as multimodal imaging platforms and even provide additional therapeutic strategies based on their intrinsic properties. The possibility of integrating all of these aspects within a single platform gave rise to the term "theranostics", first described by Warner in 2004.[155] Hence, theranostic nanomedicine refers to the integration of diagnostic and therapeutic tools in a single entity, in this case, a nanoparticle.

The research interest in theranostic nanomedicine for cancer has experienced an enormous development over the past decade, owing to the advances in both the synthesis and functionalization of nanoparticles and their applicability in diverse aspects of cancer diagnosis and treatment. One relatively early example of this type of system was reported by Medarova *et al.* in 2007, describing the preparation of multifunctional IONPs for the simultaneous targeted delivery and imaging of siRNA (Figure 31).[156] The incorporation of a NIR dye provided dual optical/MR imaging capabilities to monitor the *in vivo* antitumour therapeutic efficacy of the siRNA.

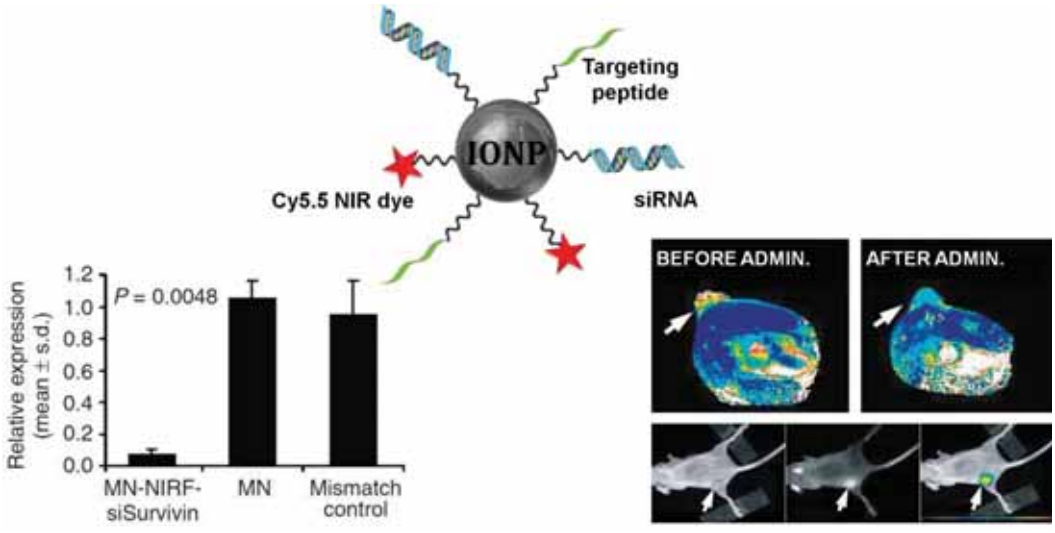

Figure 31. Schematic representation of the theranostic nanoplatform reported by Medarova *et al*. with the *in vivo* MRI (right side top) and NIR fluorescence (right side bottom) images of the treated tumour bearing mice and the effective silencing of survidin achieved with the delivery of siRNA.

Over the last few years many more reports and review articles discussing the fundamental notions of theranostic nanosystems have been published, which integrate different combinations of nanoparticles, drugs, targeting moieties, imaging modalities and therapeutic approaches.[76,157–159]

Although this thesis is not focused on the design of theranostic nanoparticles, but rather on drug delivery, all the systems developed have potential to be used as theranostic platforms and may serve as the starting point for the design of more advanced systems in the future.

1.4 Objectives of the thesis

Considering the urgent need for safer and more effective therapeutic strategies against cancer and the precedents described throughout this chapter, this PhD thesis work has mainly focussed on the development of nanoparticle based delivery vehicles for anticancer drugs. Taking advantage of the previous work and expertise of the group in preparation and functionalization of nanoparticles, the aim of this thesis has been to design and prepare different versatile nanocarriers for the delivery and enhancement of the chemotherapeutic effect of two specific anticancer agents; a cisplatin platinum (IV) prodrug and a immunostimulatory and cytotoxic agent, poly(I:C).

Although each of the following chapters describes the design, development, characterisation and testing of a different nanocarrier-drug system, the common objectives of this thesis have been:

- The synthesis and characterization of water soluble and biocompatible nanoparticle systems with appropriate surface coating for the delivery of the chemotherapeutic drugs.
- Selecting an appropriate strategy for the incorporation of the anticancer agents to each of the nanocarriers based on the possible interactions and the nature of each component.
- The addition of fluorescent moieties to the system for assessing the cellular uptake of the nanoparticles.
- Testing the functionality of the drug-loaded constructs in relevant cancer cell lines and the potential enhancement of the anticancer properties of the selected drugs.
- The radiolabelling of the nanoparticles for nuclear image based biodistribution studies in tumour bearing mice.
- *In vivo* testing of the therapeutic efficacy of the most promising constructs in a relevant mice tumour model.

1.5 References

(1) *World Cancer Report 2014*; Stewart, B. W.; Wild, C. P., Eds.; International Agency for Research on Cancer: Lyon, **2014**.

(2) World Health Organization. Cancer Fact Sheet, **2012** http://www.who.int/mediacentre/factsheets/fs297/en/ (accessed Feb 1, 2017).

(3) National Cancer Institute at the National Institutes of Health, Defining Cancer, **2013** http://www.cancer.gov/cancertopics/ cancerlibrary/what-is-cancer (accessed Feb 1, 2017).

(4) Ferlay, J.; Soerjomataram, I.; Ervik, M. GLOBOCAN **2012**, Cancer Incidence and Mortality Worldwide: IARC Cance Base http://globocan.iarc.fr (accessed Feb 1, 2017).

(5) Sandru, A.; Voinea, S.; Panaitescu, E.; Blidaru, A. *J. Med. Life* **2014**, *7*, 572.

(6) SEER Cancer Statistics Review, National Cancer Institute, Melanoma incidence rate in the US https://seer.cancer.gov/statfacts/html/melan.html (accessed Feb 1, 2017).

(7) Connell, P. P.; Hellman, S. *Cancer Res.* **2009**, *69*, 383.

(8) Olsen, D. R.; Bruland, Ø. S.; Frykholm, G.; Norderhaug, I. N. *Radiother. Oncol.* **2007**, *83*, 123.

(9) Shahri, K. K.; Motavalli, L. R.; Hakimabad, H. M. *Hell. J. Nucl. Med.* **2011**, *14*, 110.

(10) Krumbhaar, E. B.; Krumbhaar, H. D. *J. Med. Res.* **1919**, *40*, 497.

(11) Goodman, L. S.; Wintrobe, M. M. *J. Am. Med. Assoc.* **1946**, *132*, 126.

(12) Farber, S.; Diamond, L. K.; Mercer, R. D.; Sylvester, R. F.; Wolff, J. A. *N. Engl. J. Med.* **1948**, *238*, 787.

(13) Farber, S. *Blood* **1949**, *4*, 160.

(14) Rosenberg, B.; Vancamp, L.; Krigas, T. *Nature* **1965**, *205*, 698.

(15) Rosenberg, B.; VanCamp, L. *Cancer Res.* **1970**, *30*, 1799.

(16) Weiss, R. B.; Christian, M. C. *Drugs* **1993**, *46*, 360.

(17) U.S. National Library if Medicine, Cisplatin http://www.nlm.nih.gov/medlineplus/druginfo/meds/a684036.html (accessed Apr 4, 2017).

(18) Reishus, J. W.; Martin, D. S. *J. Am. Chem. Soc.* **1961**, *83*, 2457.

(19) Johnstone, T. C.; Suntharalingam, K.; Lippard, S. J. *Chem. Rev.* **2016**, *116*, 3436.

(20) Alderden, R. A.; Hall, M. D.; Hambley, T. W. *J. Chem. Educ.* **2006**, *83*, 728.

(21) Wang, D.; Lippard, S. J. *Nat. Rev. Drug Discov.* **2005**, *4*, 307.

(22) Canetta, R.; Rozencweig, M.; Carter, S. K. *Cancer Treat. Rev.* **1985**, *12*, 125.

(23) Ali, I.; Wani, W. A.; Saleem, K.; Haque, A. *Anticancer Agents Med. Chem.* **2013**, *13*, 296.

(24) Rosenberg, B.; Van Camp, L.; Trosko, J. E.; Mansour, V. H. *Nature* **1969**, *222*, 385.

(25) Gibson, D. *Dalton Trans.* **2016**, *45*, 12983.

(26) Bhargava, A.; Vaishampayan, U. N. *Expert Opin. Investig. Drugs* **2009**, *18*, 1787.

(27) Ang, W. H.; Khalaila, I.; Allardyce, C. S.; Juillerat-Jeanneret, L.; Dyson, P. J. *J. Am. Chem. Soc.* **2005**, *127*, 1382.

(28) Parker, L. J.; Italiano, L. C.; Morton, C. J.; Hancock, N. C.; Ascher, D. B.; Aitken, J. B.; Harris, H. H.; Campomanes, P.; Rothlisberger, U.; De Luca, A.; Lo Bello, M.; Ang, W. H.; Dyson, P. J.; Parker, M. W. *Chemistry* **2011**, *17*, 7806.

(29) Dhar, S.; Lippard, S. J. *Proc. Natl. Acad. Sci. U.S.A.* **2009**, *106*, 22199.

(30) Galluzzi, L.; Vacchelli, E.; Bravo-San Pedro, J.; Buqué, A.; Senovilla, L.; Baracco, E. E.; Bloy, N.; Castoldi, F.; Abastado, J.; Agostinis, P.; Apte, R. N.; Aranda, F.; Ayyoub, M.; Beckhove, P.; Blay, J. Y.; Bracci, L.; Caignard, A.; Castelli, C.; Cavallo, F.; Celis, E.; Cerundolo, V.; Clayton, A.; Colombo, M. P.; Coussens, L.; Dhodapkar, M. V.; Eggermont, A. M.; D.T., F.; Fridman, W. H.; Fucíková, J.; Gabrilovich, D. I.; Galo, J.; Garg, A.; Ghiringhelli, F.; Giaccone, G.; Kalinski, E.; Kärre, K.; Kepp, O.; Kiessling, R.; Kirkwood, J. M.; Klein, E.; Knuth, A.; Lewis, C. E.; Liblau, R.; Lotze, M. T.; Lugli, E.; Mach, J. P.; Mattei, F.; Mavilio, D.; Melero, I.; Melief, C. J.; Mittendorf, E. A.; Moretta, L.; Odunsi, A.; Okada, H.; Palucka, A. K.; Peter, M. E.; Pienta, K. J.; Porgador, A.; Predengast, G. C.; Rabinovich, G. A.; Restifo, N. P.; Rizvi, N.; Sautès-Firdman, K.; Schreiber, H.; Seliger, B.; Shiku, H.; Silva-Santos, B.; Smyth, M. J.; Speiser, D. E.; Spisek, R.; Srivastava, P. K.; Talmadge, J. E.; Tartour, E.; Van Der Burg, S. J.; Van Den Eynde, B. J.; Vile, R.; Wagner, H.; Weber, J. S.; Whiteside, T. L.; Wolchok, J. D.; Zitvogel, L.; Zou, W.; Kroemer, G. *Oncotarget* **2015**, *5*, 12472.

(31) Lu, H. *Front. Immunol.* **2014**, *5*, 3.

(32) Shi, M.; Chen, X.; Ye, K.; Yao, Y.; Li, Y. *Medicine* **2016**, *95*, e3951.

(33) Farkona, S.; Diamandis, E. P.; Blasutig, I. M. *BMC Med.* **2016**, *14,* DOI:10.1186/s12916-016-0623-5.

(34) Corrie, P. G. *Medicine* **2007**, *36*, 24.

(35) Fanciullino, R.; Ciccolini, J. *Curr. Med. Chem.* **2009**, *16*, 4361.

(36) Shi, J.; Kantoff, P. W.; Wooster, R.; Farokhzad, O. C. *Nat. Rev. Cancer* **2016**, *17*, 20.

(37) Alivisatos, A. P. *Science* **1996**, *271*, 933.

(38) Wegner, K. D.; Hildebrandt, N. *Chem. Soc. Rev.* **2015**, *44*, 4792.

(39) Wood, R. W. *Philos. Mag. Ser. 6* **1902**, *4*, 396.

(40) Wood, R. W. *Philos. Mag. Ser. 6* **1912**, *23*, 310.

(41) Li, J.; Guo, H.; Li, Z. *Photonics Res.* **2013**, *1*, 28.

(42) Colombo, M.; Carregal-Romero, S.; Casula, M. F.; Gutiérrez, L.; Morales, M. P.; Böhm, I. B.; Heverhagen, J. T.; Prosperi, D.; Parak, W. J. *Chem. Soc. Rev.* **2012**, *41*, 4306.

(43) Krishnan, K. M. *IEEE Trans. Magn.* **2010**, *46*, 2523.

(44) Doane, T. L.; Burda, C. *Chem. Soc. Rev.* **2012**, *41*, 2885.

(45) Holohan, C.; Van Schaeybroeck, S.; Longley, D. B.; Johnston, P. G. *Nat. Rev. Cancer* **2013**, *13*, 714.

(46) Wicki, A.; Witzigmann, D.; Balasubramanian, V.; Huwyler, J. *J. Control. Release* **2015**, *200*, 138.

(47) Estanqueiro, M.; Amaral, M. H.; Conceiçao, J.; Sousa Lobo, J. M. *Colloids Surf. B.* **2015**, *126*, 631.

(48) Williams, H. D.; Trevaskis, N. L.; Charman, S. A.; Shanker, R. M.; Charman, W. N.; Pouton, C. W.; Porter, C. J. H. *Pharmacol. Rev.* **2013**, *65*, 315.

(49) Kim, D. K.; Dobson, J. *J. Mater. Chem.* **2009**, *19*, 6294.

(50) Torchilin, V. *Eur. J. Pharm. Biopharm.* **2009**, *71*, 431.

(51) Jhaveri, A.; Deshpande, P.; Torchilin, V. *J. Control. Release* **2014**, *190*, 352.

(52) Malam, Y.; Loizidou, M.; Seifalian, A. M. *Trends Pharmacol. Sci.* **2009**, *30*, 592.

(53) Allen, T. M.; Cullis, P. R. *Adv. Drug Deliv. Rev.* **2013**, *65*, 36.

(54) Keles, E.; Song, Y.; Du, D.; Dong, W. J.; Lin, Y. *Biomater. Sci.* **2016**, *4*, 1291.

(55) Loh, X. J.; Lee, T. C.; Dou, Q.; Deen, G. R. *Biomater. Sci.* **2016**, *4*, 70.

(56) Yu, M. K.; Park, J.; Jon, S. *Theranostics* **2012**, *2*, 3.

(57) Pérez-Herrero, E.; Fernández-Medarde, A. *Eur. J. Pharm. Biopharm.* **2015**, *93*, 52.

(58) Bazak, R.; Houri, M.; Achy, S. El; Hussein, W.; Refaat, T. *Mol. Clin. Oncol.* **2014**, *2*, 904.

(59) Matsumura, Y.; Maeda, H. *Cancer Res.* **1986**, *46*, 6387.

(60) Maeda, H.; Matsumura, Y. *Crit. Rev. Ther. Drug Carrier Syst.* **1989**, *6*, 193.

(61) Byrne, J. D.; Betancourt, T.; Brannon-Peppas, L. *Adv. Drug Deliv. Rev.* **2008**, *60*, 1615.

(62) Friedman, A. D.; Claypool, S. E.; Liu, R. *Curr. Pharm. Des.* **2013**, *19*, 6315.

(63) Wang, Z.; Qiao, R.; Tang, N.; Lu, Z.; Wang, H.; Zhang, Z.; Xue, X.; Huang, Z.; Zhang, S.; Zhang, G.; Li, Y. *Biomaterials* **2017**, *127*, 25.

(64) Shi, S.; Zhou, M.; Li, X.; Hu, M.; Li, C.; Li, M.; Sheng, F.; Li, Z.; Wu, G.; Luo, M.; Cui, H.; Li, Z.; Fu, R.; Xiang, M.; Xu, J.; Zhang, Q.; Lu, L. *J. Control. Release* **2016**, *235*, 1.

(65) Dhar, S.; Gu, F. X.; Langer, R.; Farokhzad, O. C.; Lippard, S. J. *Proc. Natl. Acad. Sci. U.S.A.* **2008**, *105*, 17356.

(66) Wilhelm, S.; Tavares, A. J.; Dai, Q.; Ohta, S.; Audet, J.; Dvorak, H. F.; Chan, W. C. W. *Nat. Rev. Mater.* **2016**, *1*, 1.

(67) Cui, T.; Liang, J. J.; Chen, H.; Geng, D. D.; Jiao, L.; Yang, J. Y.; Qian, H.; Zhang, C.; Ding, Y. *ACS Appl. Mater. Interfaces* **2017**, *9*, 8569.

(68) Fedoryshin, L. L.; Tavares, A. J.; Petryayeva, E.; Doughan, S.; Krull, U. J. *ACS Appl. Mater. Interfaces* **2014**, *6*, 13600.

(69) Yang, X.; Yang, M.; Pang, B.; Vara, M.; Xia, Y. *Chem. Rev.* **2015**, *115*, 10410.

(70) Ahn, S.; Jung, S. Y.; Lee, S. J. *Molecules* **2013**, *18*, 5858.

(71) Huang, X.; Jain, P. K.; El-Sayed, I. H.; El-Sayed, M. A. *Lasers Med. Sci.* **2008**, *23*, 217.

(72) Lee, N.; Yoo, D.; Ling, D.; Cho, M. H.; Hyeon, T.; Cheon, J. *Chem. Rev.* **2015**, *115*, 10637.

(73) Tartaj, P.; Morales, M. P.; Gonzalez-Carreño, T.; Veintemillas-Verdaguer, S.; Serna, C. J. *Adv. Mater.* **2011**, *23*, 5243.

(74) Arami, H.; Khandhar, A.; Liggitt, D.; Krishnan, K. M. *Chem. Soc. Rev.* **2015**, *44*, 8576.

(75) Weissleder, R.; Pittet, M. J. *Nature* **2008**, *452*, 580.

(76) Lee, D. E.; Koo, H.; Sun, I. C.; Ryu, J. H.; Kim, K.; Kwon, I. C. *Chem. Soc. Rev.* **2012**, *41*, 2656.

(77) Key, J.; Leary, J. F. *Int. J. Nanomedicine* **2014**, *9*, 711.

(78) Chen, L. L.; Wang, C. W.; Yuan, Z.; Chang, H. T. *Anal. Chem.* **2015**, *87*, 216.

(79) West, A. L.; Schaeublin, N. M.; Griep, M. H.; Maurer-Gardner, E. I.; Cole, D. P.; Fakner, A. M.; Hussain, S. M.; Karna, S. P. *ACS Appl. Mater. Interfaces* **2016**, *8*, 21221.

(80) Yahia-Ammar, A.; Sierra, D.; Mérola, F.; Hildebrandt, N.; Le Guével, X. *ACS Nano* **2016**, *10*, 2591.

(81) Wu, X.; He, X.; Wang, K.; Xie, C.; Zhou, B.; Qing, Z. *Nanoscale* **2010**, *2*, 2244.

(82) Dorsey, J. F.; Sun, L.; Joh, D. Y.; Witztum, A.; Kao, G. D.; Alonso-Basanta, M.; Avery, S.; Hahn, S. M.; Al Zaki, A.; Tsourkas, A. *Transl. Cancer Res.* **2013**, *2*, 280.

(83) Xie, H.; Wang, Z. J.; Bao, A.; Goins, B.; Phillips, W. T. *Int. J. Pharm.* **2010**, *395*, 324.

(84) Karmani, L.; Labar, D.; Valembois, V.; Bouchat, V.; Nagaswaran, P. G.; Bol, A.; Gillart, J.; Levêque, P.; Bouzin, C.; Bonifazi, D.; Michiels, C.; Feron, O.; Grégoire, V.; Lucas, S.; Borght, T. Vander; Gallez, B. *Contrast Media Mol. Imaging* **2013**, *8*, 402.

(85) Tian, M.; Lu, W.; Zhang, R.; Xiong, C.; Ensor, J.; Nazario, J.; Jackson, J.; Shaw, C.; Dixon, K. A.; Miller, J.; Wright, K.; Li, C.; Gupta, S. *Mol. Imaging Biol.* **2014**, *15*, 614.

(86) Li, H.; Yu, H.; Zhu, C.; Hu, J.; Du, M.; Zhang, F.; Yang, D. *RSC Adv.* **2016**, *6*, 94160.

(87) Kao, H. W.; Lin, Y. Y.; Chen, C. C.; Chi, K. H.; Tien, D. C.; Hsia, C. C.; Lin, M. H.; Wang, H. E. *Bioorganic Med. Chem. Lett.* **2013**, *23*, 3180.

(88) Ng, Q. K. T.; Olariu, C. I.; Yaffee, M.; Taelman, V. F.; Marincek, N.; Krause, T.; Meier, L.; Walter, M. A. *Biomaterials* **2014**, *35*, 7050.

(89) Zhao, Y.; Pang, B.; Luehmann, H.; Detering, L.; Yang, X.; Sultan, D.; Harpstrite, S.; Sharma, V.; Cutler, C. S.; Xia, Y.; Liu, Y. *Adv. Healthcare Mater.* **2016**, *5*, 928.

(90) Zhao, Y.; Sultan, D.; Detering, L.; Cho, S.; Sun, G.; Pierce, R.; Wooley, K. L.; Liu, Y. *Angew. Chem. Int. Ed.* **2014**, *53*, 156.

(91) Zhao, Y.; Sultan, D.; Detering, L.; Luehmann, H.; Liu, Y. *Nanoscale* **2014**, *6*, 13501.

(92) Ge, X.; Song, Z. M.; Sun, L.; Yang, Y. F.; Shi, L.; Si, R.; Ren, W.; Qiu, X.; Wang, H. *Biomaterials* **2016**, *108*, 35.

(93) Ohgushi, M.; Nagayama, K.; Wada, A. *J. Magn. Reson.* **1978**, *29*, 599.

(94) Jun, Y. W.; Huh, Y. M.; Choi, J. S.; Lee, J. H.; Song, H. T.; Kim, S.; Yoon, S.; Kim, K. S.; Shin, J. S.; Suh, J. S.; Cheon, J. *J. Am. Chem. Soc.* **2005**, *127*, 5732.

(95) Lee, J. H.; Huh, Y. M.; Jun, Y. W.; Seo, J. W.; Jang, J. T.; Song, H. T.; Kim, S.; Cho, E. J.; Yoon, H. G.; Suh, J. S.; Cheon, J. *Nat. Med.* **2007**, *13*, 95.

(96) Min, Y.; Caster, J. M.; Eblan, M. J.; Wang, A. Z. *Chem. Rev.* **2015**, *115*, 11147.

(97) Bashir, M. R.; Bhatti, L.; Marin, D.; Nelson, R. C. *J. Magn. Reson. Imaging* **2015**, *41*, 884.

(98) Thomas, R.; Park, I. K.; Jeong, Y. Y. *Int. J. Mol. Sci.* **2013**, *14*, 15910.

(99) Shin, T. H.; Choi, Y.; Kim, S.; Cheon, J. *Chem. Soc. Rev.* **2015**, *44*, 4501.

(100) Josephson, L.; Kircher, M. F.; Mahmood, U.; Tang, Y.; Weissleder, R. *Bioconjugate Chem.* **2002**, *13*, 554.

(101) Kircher, M. F.; Mahmood, U.; King, R. S.; Kircher, M. F.; Mahmood, U.; King, R. S.; Weissleder, R.; Josephson, L. *Cancer Res.* **2003**, *63*, 8122.

(102) Fan, H. M.; Olivo, M.; Shuter, B.; Yi, J. B.; Bhuvaneswari, R.; Tan, H. R.; Xing, G. C.; Ng, C. T.; Liu, L.; Lucky, S. S.; Bay, B. H.; Ding, J. *J. Am. Chem. Soc.* **2010**, *132*, 14803.

(103) Wang, H.; Shen, J.; Li, Y.; Wei, Z.; Cao, G.; Gai, Z.; Hong, K.; Banerjee, P.; Zhou, S. *Biomater. Sci.* **2014**, *2*, 915.

(104) Shen, S.; Guo, X.; Wu, L.; Wang, M.; Wang, X.; Kong, F.; Shen, H.; Xie, M.; Ge, Y.; Jin, Y. *J. Mater. Chem. B* **2014**, *2*, 5775.

(105) Xia, A.; Gao, Y.; Zhou, J.; Li, C.; Yang, T.; Wu, D.; Wu, L.; Li, F. *Biomaterials* **2011**, *32*, 7200.

(106) Chen, H.; Qi, B.; Moore, T.; Colvin, D. C.; Crawford, T.; Gore, J. C.; Alexis, F.; Mefford, O. T.; Anker, J. N. *Small* **2014**, *10*, 160.

(107) Sharma, R.; Xu, Y.; Kim, S. W.; Schueller, M. J.; Alexoff, D.; David, S. *Nanoscale* **2013**, *5*, 7476.

(108) Lee, H.; Li, Z.; Chen, K.; Hsu, A. R.; Xu, C.; Xie, J.; Sun, S.; Chen, X. *J. Nucl. Med.* **2008**, *49*, 1371.

(109) Boros, E.; Bowen, A. M.; Josephson, L.; Holland, J. P. *Chem. Sci.* **2015**, *6*, 225.

(110) Ruiz-De-Angulo, A.; Zabaleta, A.; Gómez-Vallejo, V.; Llop, J.; Mareque-Rivas, J. C. *ACS Nano* **2016**, *10*, 1602.

(111) Kim, S. M.; Chae, M. K.; Yim, M. S.; Jeong, I. H.; Cho, J.; Lee, C.; Ryu, E. K. *Biomaterials* **2013**, *34*, 8114.

(112) Valdovinos, H. F.; Chen, F.; Lewis, C. M.; Ellison, P. A.; Luo, H.; Meyerand, M. E.; Nickles, R. J.; Cai, W. *Adv. Mater.* **2014**, *26*, 5119.

(113) Thorek, D. L. J.; Ulmert, D.; Diop, N. F. M.; Lupu, M. E.; Doran, M. G.; Huang, R.; Abou, D. S.; Larson, S. M.; Grimm, J. *Nat. Commun.* **2014**, *5*, DOI:10.1038/ncomms4097.

(114) Chen, F.; Ellison, P. A.; Lewis, C. M.; Hong, H.; Zhang, Y.; Shi, S.; Hernandez, R.; Meyerand, M. E.; Barnhart, T. E.; Cai, W. *Angew. Chem. Int. Ed.* **2013**, *52*, 13319.

(115) Gómez Blanco, N.; Jauregui-Osoro, M.; Cobaleda-Siles, M.; Maldonado, C. R.; Henriksen-Lacey, M.; Padro, D.; Clark, S.; Mareque-Rivas, J. C. *Chem. Commun.* **2012**, *48*, 4211.

(116) , R.; Glaria, A.; Varma, G.; Protti, A.; Blower, P. J. *Bioconjug. Chem.* **2011**, *22*, 455.

(117) Zeng, J.; Jia, B.; Qiao, R.; Wang, C.; Jing, L.; Wang, F.; Gao, M. *Chem. Commun.* **2014**, *50*, 2170.

(118) Park, J. C.; Yu, M. K.; An, G. Il; Park, S. Il; Oh, J.; Kim, H. J.; Kim, J. H.; Wang, E. K.; Hong, I. H.; Ha, Y. S.; Choi, T. H.; Jeong, K. S.; Chang, Y.; Welch, M. J.; Jon, S.; Yoo, J. *Small* **2010**, *6*, 2863.

(119) Carril, M.; Fernández, I.; Rodríguez, J.; García, I.; Penadés, S. *Part. Part. Syst. Charact.* **2014**, *31*, 81.

(120) Li, J.; Hu, Y.; Yang, J.; Wei, P.; Sun, W.; Shen, M.; Zhang, G.; Shi, X. *Biomaterials* **2015**, *38*, 10.

(121) Zhu, J.; Lu, Y.; Li, Y.; Jiang, J.; Cheng, L.; Liu, Z.; Guo, L.; Pan, Y.; Gu, H. *Nanoscale* **2014**, *6*, 199.

(122) Wang, C.; Yao, Y.; Song, Q. *J. Mater. Chem. C* **2015**, *3*, 5910.

(123) Hildebrandt, B. *Crit. Rev. Oncol. Hematol.* **2002**, *43*, 33.

(124) Arvizo, R.; Bhattacharyya, S.; Kudgus, R.; Giri, K.; Bhattacharya, R.; Mukherjee, P. *Chem. Soc. Rev.* **2012**, *41*, 2.

(125) Huang, X.; El-Sayed, M. a. *J. Adv. Res.* **2010**, *1*, 13.

(126) Riley, R. S.; Day, E. S. *Wiley Interdiscip. Rev. Nanomed. Nanobiotechnol.* **2017**, *e1449*.

(127) Pitsillides, C. M.; Joe, E. K.; Wei, X.; Anderson, R. R.; Lin, C. P. *Biophys. J.* **2003**, *84*, 4023.

(128) Hirsch, L. R.; Stafford, R. J.; Bankson, J. a; Sershen, S. R.; Rivera, B.; Price, R. E.; Hazle, J. D.; Halas, N. J.; West, J. L. *Proc. Natl. Acad. Sci. U.S.A.* **2003**, *100*, 13549.

(129) O'Neal, D. P.; Hirsch, L. R.; Halas, N. J.; Payne, J. D.; West, J. L. *Cancer Lett.* **2004**, *209*, 171.

(130) Loo, C.; Lin, A.; Hirsch, L. R.; Lee, M. H.; Barton, J.; Halas, N.; West, J.; Drezek, R. *Technol. Cancer Res. Treat.* **2004**, *3*, 33.

(131) Loo, C.; Lowery, A.; Halas, N.; West, J.; Drezek, R. *Nano Lett.* **2005**, *5*, 709.

(132) Liu, H.; Chen, D.; Li, L.; Liu, T.; Tan, L.; Wu, X.; Tang, F. *Angew. Chem. Int. Ed.* **2011**, *50*, 891.

(133) Carpin, L. B.; Bickford, L. R.; Agollah, G.; Yu, T. K.; Schiff, R.; Li, Y.; Drezek, R. A. *Breast Cancer Res. Treat.* **2011**, *125*, 27.

(134) Huang, X.; El-Sayed, I.; Qian, W.; El-Sayed, M. *J. Am. Chem. Soc.* **2006**, *128*, 2115.

(135) Dickerson, E. B.; Dreaden, E. C.; Huang, X.; El-Sayed, I. H.; Chu, H.; Pushpanketh, S.; McDonald, J. F.; El-Sayed, M. A. *Cancer Lett.* **2008**, *269*, 57.

(136) Von Maltzahn, G.; Park, J. H.; Agrawal, A.; Bandaru, N. K.; Das, S. K.; Sailor, M. J.; Bhatia, S. N. *Cancer Res.* **2009**, *69*, 3892.

(137) Wang, Y.; Black, K. C. L.; Luehmann, H.; Li, W.; Zhang, Y.; Cai, X.; Wan, D.; Liu, S. Y.; Li, M.; Kim, P.; Li, Z. Y.; Wang, L. V; Liu, Y.; Xia, Y. *ACS Nano* **2013**, *7*, 2068.

(138) Ayala-Orozco, C.; Urban, C.; Knight, M. W.; Urban, A. S.; Neumann, O.; Bishnoi, S. W.; Mukherjee, S.; Goodman, A. M.; Charron, H.; Mitchell, T.; Shea, M.; Roy, R.; Nanda, S.; Schiff, R.; Halas, N. J.; Joshi, A. *ACS Nano* **2014**, *8*, 6372.

(139) Ayala-Orozco, C.; Urban, C.; Bishnoi, S.; Urban, A.; Charron, H.; Mitchell, T.; Shea, M.; Nanda, S.; Schiff, R.; Halas, N.; Joshi, A. *J. Control. Release* **2014**, *191*, 90.

(140) Abo-Elfadl, M. T.; Gamal-Eldeen, A. M.; Elshafey, M. M.; Abdalla, G. M.; Ali, S. S.; Ali, M. R. K.; Zawrah, M. F. M. *J. Photochem. Photobiol. B Biol.* **2016**, *164*, 21.

(141) Von Maltzahn, G.; Park, J.; Agrawal, A.; Bandaru, N. K.; Das, S. K.; Sailor, M. J.; Bhatia, S. N. *Cancer Res.* **2009**, *69*, 3892.

(142) Gilchrist, R. K.; Medal, R.; Shorey, W. D.; Hanselman, R. C.; Parrott, J. C.; Taylor, C. B. *Ann. Surg.* **1957**, *146*, 596.

(143) Bakoglidis, K. D.; Simeonidis, K.; Sakellari, D.; Stefanou, G.; Angelakeris, M. *IEEE Trans. Magn.* **2012**, *48*, 1320.

(144) Drake, P.; Cho, H. J.; Shih, P. S.; Kao, C. H.; Lee, K. F.; Kuo, C. H.; Lin, X. Z.; Lin, Y. J. *J. Mater. Chem.* **2007**, *17*, 4914.

(145) Jang, J. T.; Nah, H.; Lee, J. H.; Moon, S. H.; Kim, M. G.; Cheon, J. *Angew. Chem. Int. Ed.* **2009**, *48*, 1234.

(146) Casula, M. F.; Conca, E.; Bakaimi, I.; Sathya, A.; Materia, M. E.; Casu, A.; Falqui, A.; Sogne, E.; Pellegrino, T.; Kanaras, A. G. *Phys. Chem. Chem. Phys.* **2016**, *18*, 16848.

(147) Nemati, Z.; Alonso, J.; Khurshid, H.; Phan, M. H.; Srikanth, H. *RSC Adv.* **2016**, *6*, 38697.

(148) Hugounenq, P.; Levy, M.; Alloyeau, D.; Dubois, E.; Ricolleau, C.; Wilhelm, C.; Gazeau, F.; Bazzi, R. *J. Phys. Chem. C.* **2012**, *116*, 15702.

(149) Xie, J.; Yan, C.; Zhang, Y.; Gu, N. *Chem. Mater.* **2013**, *25*, 3702.

(150) Wang, H.; Shrestha, T. B.; Basel, M. T.; Pyle, M.; Toledo, Y.; Konecny, a.; Thapa, P.; Ikenberry, M.; Hohn, K. L.; Chikan, V.; Troyer, D. L.; Bossmann, S. H. *J. Mater. Chem. B* **2015**, *3*, 4647.

(151) Espinosa, A.; Di Corato, R.; Kolosnjaj-Tabi, J.; Flaud, P.; Pellegrino, T.; Wilhelm, C. *ACS Nano* **2016**, *10*, 2436.

(152) Bauer, L. M.; Situ, S. F.; Griswold, M. A; Samia, A. C. S. *Nanoscale* **2016**, *8*, 8.

(153) Nemati, Z.; Alonso, J.; Martinez, L. M.; Khurshid, H.; Garaio, E.; Garcia, J. A.; Phan, M. H.; Srikanth, H. *J. Phys. Chem. C* **2016**, *120*, 8370.

(154) Das, R.; Alonso, J.; Nemati Porshokouh, Z.; Kalappattil, V.; Torres, D.; Phan, M. H.; Garaio, E.; García, J. Á.; Sanchez Llamazares, J. L.; Srikanth, H. *J. Phys. Chem. C* **2016**, *120*, 10086.

(155) Warner, S. *Sci.* **2004**, *18*, 38.

(156) Medarova, Z.; Pham, W.; Farrar, C.; Petkova, V.; Moore, A. *Nat. Med.* **2007**, *13*, 372.

(157) Li, E. K.; Kin, T.; Paik, S.; Haam, S.; Huh, Y. M.; Lee, K. *Chem. Rev.* **2015**, *115*, 327.

(158) Kunjachan, S.; Ehling, J.; Storm, G.; Kiessling, F.; Lammers, T. *Chem. Rev.* **2015**, *115*, 10907.

(159) Chen, G.; Roy, I.; Yang, C.; Prasad, P. N. *Chem. Rev.* **2016**, *116*, 2826.

2

PEI-coated AuNPs for the delivery of poly(I:C) as chemotherapeutic agent

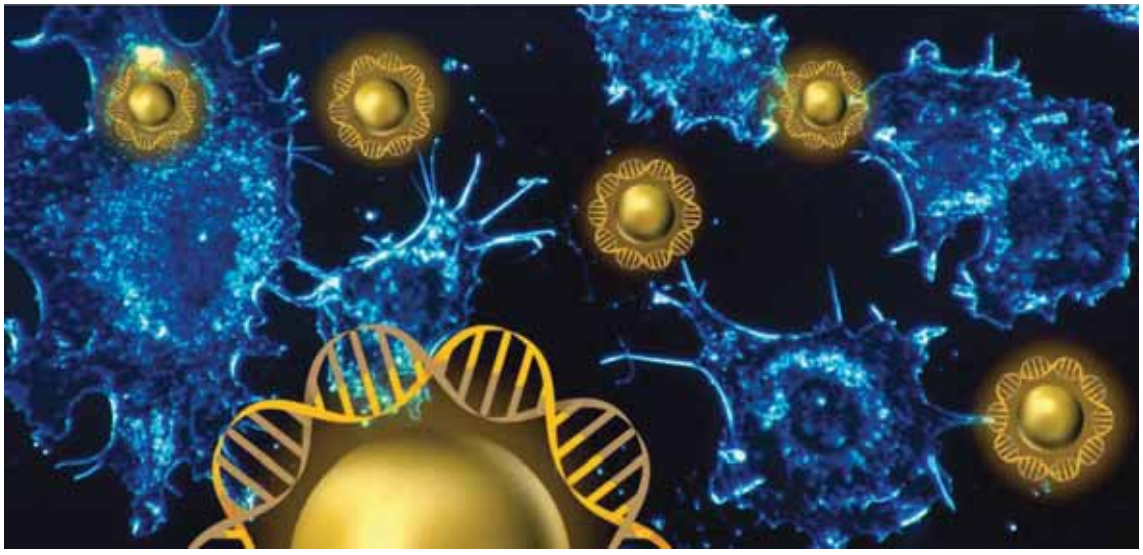

2.1 Introduction

Prostate cancer as the second most common cancer worldwide[1] represents one of the leading causes of cancer death in men in western countries. The standard treatment is androgen depletion therapy, but despite its initial efficacy, ultimately most patients die of disease progression. This is because with time the disease ceases to respond and more aggressive and chemotherapy insensitive tumours appear.[2] Therefore there is major need for finding novel molecular targets and alternative prostate cancer therapies.

As described earlier, TLR agonists are part of the toolbox currently being used in cancer immunotherapy, as they play a critical role in the early innate immune response. These receptors recognize specific molecular motifs (so-called pathogen associated molecular patterns (PAMPs)) and trigger signalling cascades that lead to the activation of the immune system.[3,4] Although TLRs are predominantly expressed in cells of the immune system, it has also been reported that various tumour cells from prostate[5] and breast cancer[6] and melanoma[7] also express TLR receptors and respond to TLR ligands. Of particular interest in this work is the TLR3 receptor, located in the endosomal membranes of cells. TLR3 not only recognizes viral RNA as PAMP, but also synthetic analogues of double stranded RNA (dsRNA).

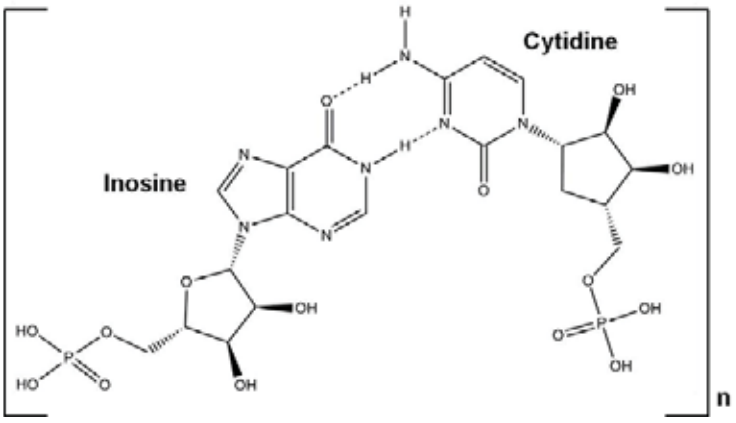

Figure 1. Chemical structure of poly(I:C)

Among synthetic dsRNA analogues polyinosinic:polycytidylic acid (poly(I:C)) (Figure 1) stands as a very promising TLR3 agonist for the development of vaccines.[8] Even though its application in immunotherapy has been studied for many years,[8–12] it is only

recently that reports show that it can provide a two-pronged mode of action against cancer due to having both direct immunogenic and anticancer properties.[13–15] Recognized not only by TLR3 receptors but also by retinoic acid inducible gene I (RIG-I) like receptors and melanoma differentiation-associated gene 5 (MDA-5), poly(I:C) can specifically activate the innate immune system by stimulating a type I interferon response, and also induce direct cancer cell death through different apoptosis-mediated mechanisms.[13,16] This versatility has prompted a great interest in the use of poly(I:C) as an anticancer agent against different solid[17,18] and even metastatic[19] tumours, and consequently in the development of effective vehicles for its targeted delivery.

Traditional delivery vectors for nucleic acids can be broadly classified as viral and non-viral; whilst viral vectors are known to be highly efficient they also suffer from major drawbacks such as immunogenicity and cytotoxicity. Able to overcome immunotoxicity, the research on non-viral vectors has seen a significant increase over the last decade. Several chemical carriers have been reported for nucleic acid transfection, including liposomes, dendrimers or polymers but among them, polyethyleneimines (PEIs) have become a “gold standard”. Characterized by a high density of amino groups, these synthetic cationic polymers promote an efficient internalization, trafficking and release of nucleic acids within cells (Figure 2).[20,21]

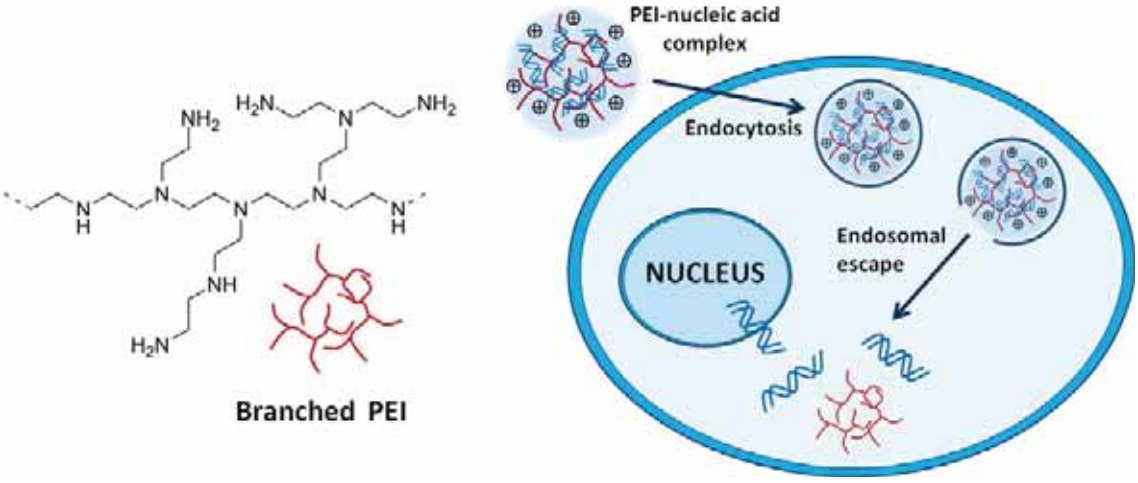

Figure 2. Generic structure of a branched PEI polymer and schematic representation of the transfection mechanism; endocytic internalization of the polyplex structure followed by endosomal escape and free trafficking of the cargo to the nucleus.

PEIs are able to condense nucleic acid molecules into polyplex structures through interactions between the positively charged polymer and the negatively charged phosphate backbone of DNA or RNA. Moreover, the highly positive charge density provided by the polymer allows not only a rapid internalization of the polyplex structure but also a proton-sponge effect mediated endosomal escape.[22] The main disadvantage of using PEIs as delivery vectors comes from their toxicity, as both the transfection efficacy and toxicity are highly dependent on their molecular weight (MW).[23]

Nanoparticle-based delivery vehicles have emerged as a promising alternative to traditional non-viral delivery vectors for nucleic acids. To achieve an effective but also safe transfection, many groups have developed nanoparticle based strategies for synthetic and natural nucleic acid fragments including the aforementioned poly(I:C). For example, targeting improved immune responses Cobaleda-Siles *et al.* took advantage of superparamagnetic iron oxide nanoparticles to selectively deliver poly(I:C) via the lymphatic system.[24] In this system, the incorporation of the poly(I:C) was achieved via non-covalent interactions with water soluble PEGylated IONP micelles, which greatly enhanced the immunostimulatory activity of the dsRNA both *in vitro* and *in vivo*. Moreover, ^{99m}Tc radiolabelling and a rhodamine labelled-PEG were introduced to enable multimodal imaging of drug delivery (Figure 3).

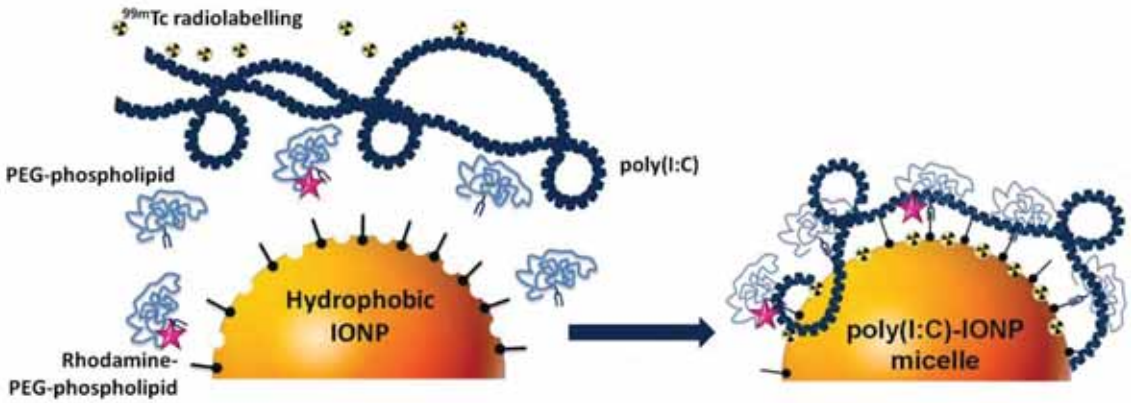

Figure 3. Structure of poly(I:C) and schematic representation of the poly(I:C) loaded IONP-micelles for the intracellular delivery and immune system activation and *in vivo* lymphatic trafficking.

Other groups have used silica based nanoparticles as delivery vehicles. For example, Colapicchioni *et al*. have recently reported a liposome-silica NP hybrid structure[25] and Ultimo *et al.* mesoposous silica nanoparticles[26] that take advantage of the direct antitumour efficacy of the poly(I:C) to kill different tumour cells. Colapicchioni *et al.* tested both PEGylated and non-PEGylated liposome-silica NPs in prostate cancer cells (PC-3) and cisplatin resistant breast cancer cells (MCF-7) and found a clear increase in the cancer cell killing ability of the nanoparticle mediated poly(I:C). Ultimo *et al*. on the other hand tested the mesoporous silica nanoparticle-poly(I:C) system in TLR3 expressing breast cancer cells (SK-BR-3), where the use of a porous nanocarrier also allows the encapsulation of an additional drug, doxorubicin in this case, prior to the functionalization with the poly(I:C). A TLR3 mediated internalization of the nanoparticles leads to an increased cytotoxicity in both the single and the dual drug loaded systems compared to poly(I:C) alone.

Finally, a very recent example by Ramani *et al.* made use of naked zinc oxide nanoparticles to deliver poly(I:C) and demonstrated its *in vivo* efficacy in a murine tumour model of melanoma. This system is based on the direct attachment of the dsRNA to the surface of intrinsically therapeutic ZnO nanoparticles.[27] In such way, the anticancer activity of the vehicle itself and the poly(I:C) could contribute to the efficacy of the treatment.

AuNPs have also been used as non-viral gene carriers.[28–30] The growing interest in the development of AuNP-based delivery vehicles is due to their relatively facile synthesis and functionalization, excellent biocompatibility and applicability for therapy and imaging. Although a wide range of surface coatings that have been described for AuNPs, the possibility of using positively charged polymers, such as PEIs, already known to promote an efficient transfection is a particularly interesting approach. Combining the ability of PEI to interact with nucleic acids with the unique advantages and features provided by AuNPs allows the development of multifunctional delivery vectors for nucleic acids. One of the first examples was reported in 2003 by Thomas *et al*. who improved the efficacy of both 2 kDa and 25 kDa PEIs to deliver plasmid DNA to mammalian cells by conjugating them to AuNPs.[31] Since then several more examples have been published for PEIs of different MWs and the delivery of both plasmid DNA

and siRNAs to diverse cells.[32–37] Song *et al*. for instance followed a one-pot synthetic procedure to prepare 25 kDa PEI-coated AuNPs (Figure 4), which then were able to enhance the intracellular delivery of a siRNA into breast cancer cells.[34]

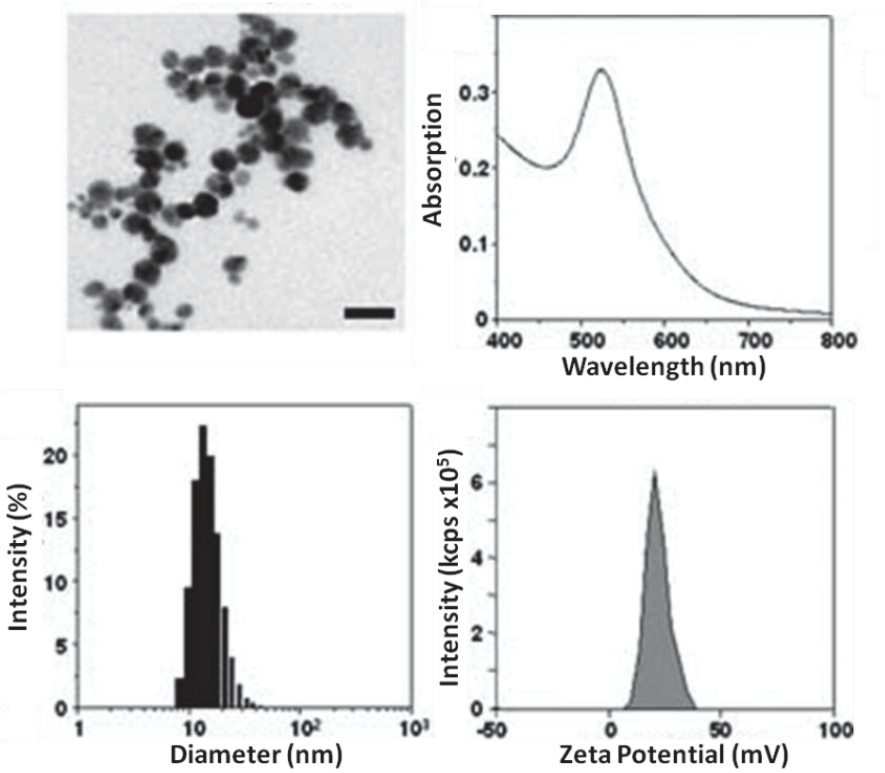

Figure 4. Characterization of the PEI-capped AuNPs by Song *et al*.; TEM image (scale bar 20nm), UV-Vis absorption spectrum, hydrodynamic size and zeta potential.

Given the known cytotoxic nature of high MW PEIs, the design of a similar system based on less toxic LMW PEI represents a very interesting challenge; therefore this chapter will focus on the development of a non-toxic LMW PEI-coated AuNP system for the efficient delivery of poly(I:C) as chemotherapeutic agent against prostate cancer cells.

2.2 Results and Discussion

2.2.1 Synthesis and characterization of PEI-coated AuNPs

The main synthetic approach for the preparation of AuNPs consists of the chemical reduction of a gold salt, typically gold tetrachloroaurate ($HAuCl_4$), in the presence of a stabilizing agent. The tendency of gold colloids to aggregate in solution make the use of capping ligands essential to control the particle size and stability of AuNPs.[38] Cationic polymers like PEIs should make excellent protective ligands as they can stabilize the nanoparticles by a combination of both steric and electrostatic effects.[39] Moreover, it has been described that polyamines can not only act as protective agents but also are able to reduce the gold salt and form stable colloids without the need of an additional reducing agent.[40] Hence, using PEI as both stabilizing and reducing agent for the preparation of AuNPs allows a facile single-step preparation of water soluble nanoparticles. Control over the AuNP size can potentially be achieved by systematically varying the initial molar ratio between both components.

PEIs are available in a wide range of molecular weights (MW) and with both linear and branched topologies. In general high MW PEIs have improved transfection efficiency but also show greater toxicity.[23] With the aim of keeping the toxicity as low as possible and the incorporation of the AuNP, this thesis work focused on using a non-toxic low MW (1.8 kDa). The PEI-coated AuNPs (PEI-AuNPs) were prepared by slightly modifying a previously reported synthesis, where high MW PEI was used.[34,41] The procedure allowed the rapid preparation of water soluble AuNPs in a single step by incubating the PEI with an aqueous solution of $HAuCl_4$ at 90 ºC for 2 h.

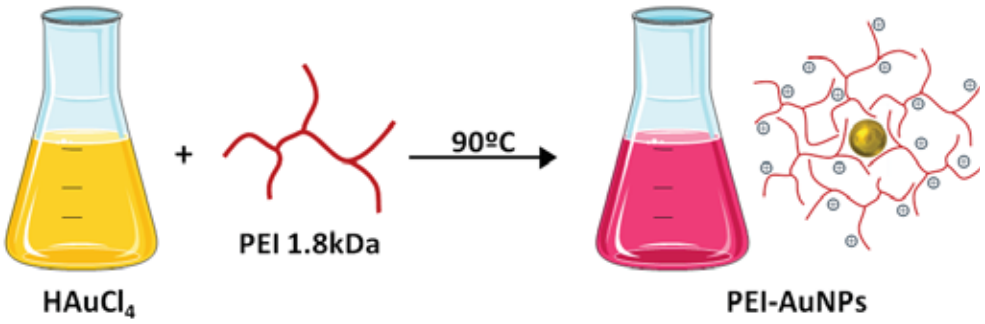

Scheme 1. One-pot synthesis of LMW PEI-coated AuNPs.

The formation of the AuNPs was monitored by recording the UV-vis absorption spectra of the reaction mixture at different time points. As it can be seen in Figure 5, the absorption band corresponding to the unreacted tetrachloroaurate salt (310 nm) initially red-shifts when the PEI is added, and as the reaction progresses the plasmon band indicating the formation of the AuNPs starts to develop at ca. 520 nm and continues to gain intensity until it reaches saturation after 2 h. It is at this point that the reaction is left to cool and the mixture is purified to remove excess reactants, rendering a stable aqueous solution of PEI-AuNPs.

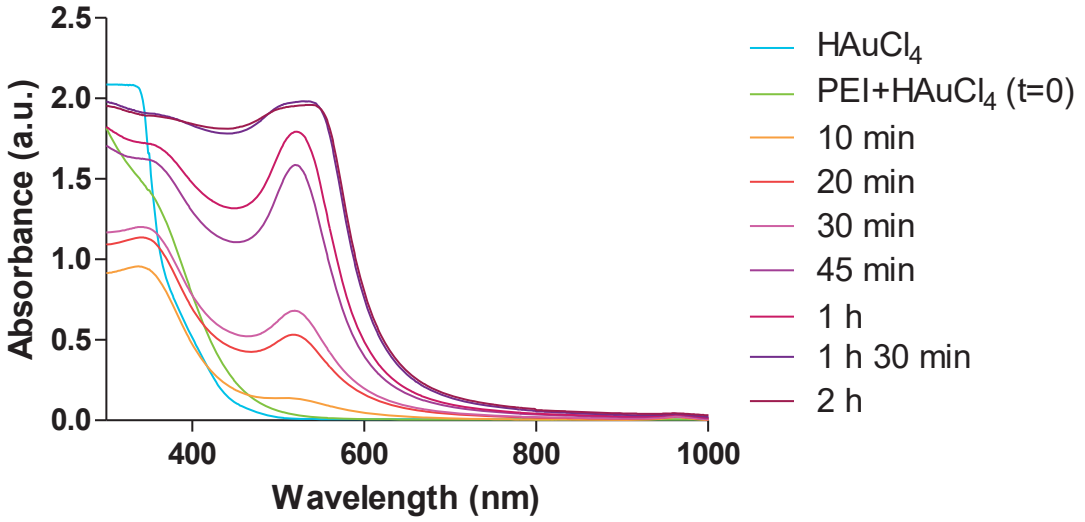

Figure 5. UV-vis spectra of the solutions of $HAuCl_4$ and 1.8 kDa PEI at different stages of the synthesis of the PEI-capped AuNPs in water.

After purification, the PEI-AuNPs were characterized to determine the size, morphology and polydispersity (Figure 6). Transmission electron microscopy (TEM) images show non-aggregated spherical AuNPs with a core diameter of 10.3 ± 1.5 nm. These results are consistent with the dynamic light scattering (DLS) measurements of the aqueous solution that indicate an average hydrodynamic diameter of 14.7 ± 0.2 nm with a relatively narrow size distribution (poly dispersity index (PdI) = 0.072 ± 0.008). As expected for spherical AuNPs of this size[42] the UV-vis spectrum of the solution shows an intense absorption band at 521 nm assignable to surface plasmon resonance. Finally, zeta potential studies confirmed the presence of the positively charged PEI on the surface of the AuNPs (zeta potential = 28.4 ± 2.0 mV).

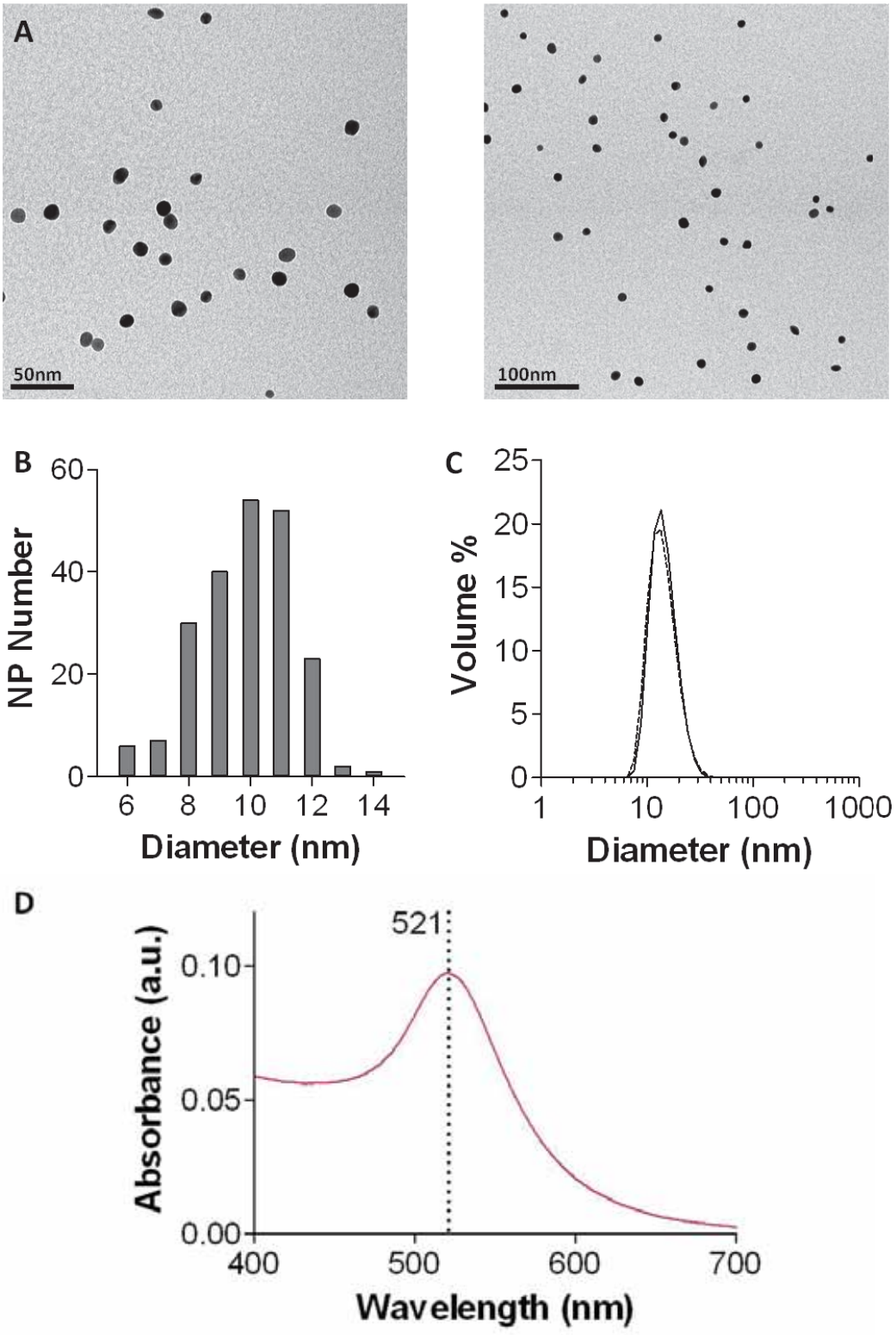

Figure 6. Characterization of PEI-AuNPs. (**A**) Representative TEM images and (**B**) size distribution histogram indicating an average diameter of 10.3 ± 1.5nm. (**C**) Hydrodynamic diameter and (**D**) UV-vis spectrum showing the surface plasmon resonance band at 521 nm.

A fluorescently labelled analogue of PEI-AuNPs was also synthesized for flow cytometry and fluorescence microscopy studies. As summarized in Scheme 2, the incorporation of the fluorophore was achieved by attaching it to the PEI prior to the preparation of the nanoparticles. The same LMW PEI used in the non-fluorescent PEI-AuNP preparations was employed for the labelling as well. The attachment of rhodamine B was achieved using standard carbodiimide chemistry (EDC/NHS) adapting a previously reported protocol.[43] After this coupling reaction, the modified PEI was used to prepare the rhodamine-labelled PEI-AuNPs as described above. The free PEI and/or fluorophore were removed in the purification step.

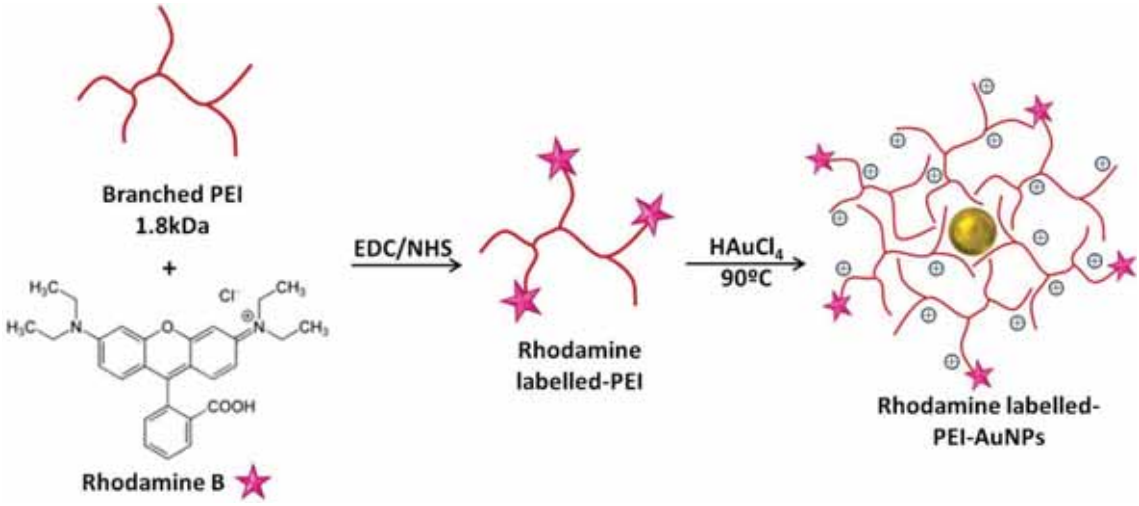

Scheme 2. Schematics of the incorporation of rhodamine B to the PEI and synthesis of rhodamine-labelled PEI-AuNPs.

The purified system was characterized by TEM, confirming that the morphology of the nanoparticles had not been altered by the incorporation of the fluorophore (Figure 7). Due to overlapping between the absorption band of rhodamine B and the plasmon band of the AuNPs the UV-vis absorption spectrum of the rhodamine-labelled PEI-AuNPs (Figure 8) was very similar to that of the PEI-AuNPs. The fluorescence spectrum on the other hand showed the distinct red emission peak due to the presence of rhodamine B, confirming the formation of Rho-PEI-AuNPs.

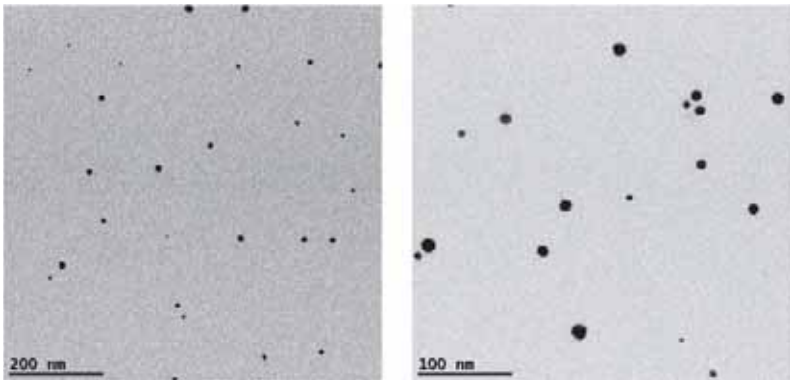

Figure 7. TEM images of the rhodamine-labelled PEI-AuNPs at different magnifications.

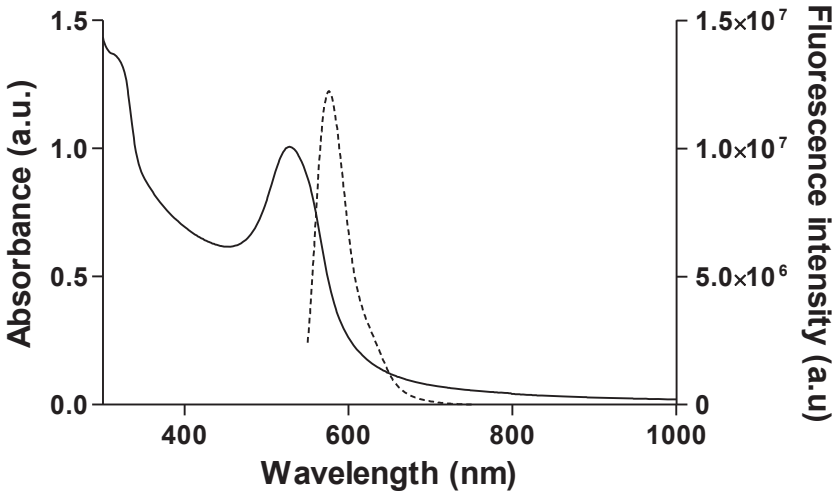

Figure 8. UV-vis absorption (continuous line) and fluorescence spectra (dashed line) of the rhodamine-labelled PEI-AuNPs.

2.2.2 Delivery of poly(I:C)

The incorporation of poly(I:C) was achieved by electrostatic interaction between the positively charged PEI on the surface of the nanoparticles and the negatively charged phosphate backbone of the dsRNA. For the preparation of PEI-AuNPs-poly(I:C) complexes, aqueous solutions of PEI-AuNPs and poly(I:C) were mixed and incubated for ca. 15 min at room temperature. The characterization of the poly(I:C) containing systems (Figure 9) reflects that the incorporation of the dsRNA does not significantly affect neither the size nor the morphology of the AuNPs. It is however clear from the zeta potential measurements that the association takes place (i.e. the surface charge became less positive after the addition of poly(I:C)) changing from 28.4 ± 2.0 mV to 18.1 ± 0.1 mV in samples with 100 μM Au and 1 μg/mL poly(I:C).

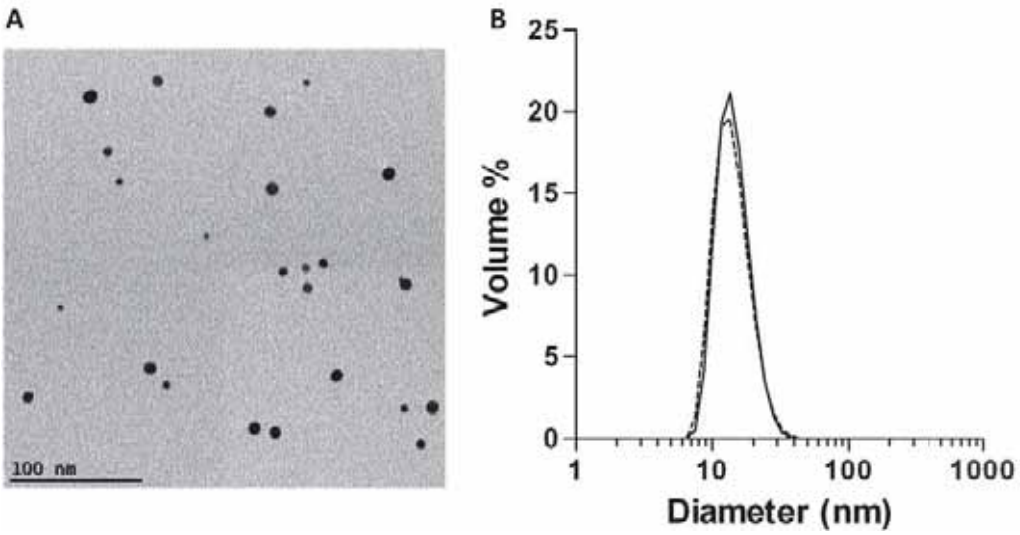

Figure 9. Hydrodynamic diameters of PEI-AuNPs (continuous line) and PEI-AuNPs-poly(I:C) (dashed line) at 100 μM Au and 1 μg/mL poly(I:C) in aqueous solution.

2.2.3 Cell culture studies

To test the cancer cell killing ability of the PEI-AuNP-poly(I:C) system, a highly aggressive human prostate cancer cell line PC-3 was selected. As described in the introduction, TLRs are not only expressed in cells of the immune system but also in many cancer cells. The expression of TLR3 in PC-3 cells was confirmed by flow cytometry (Figure 10).

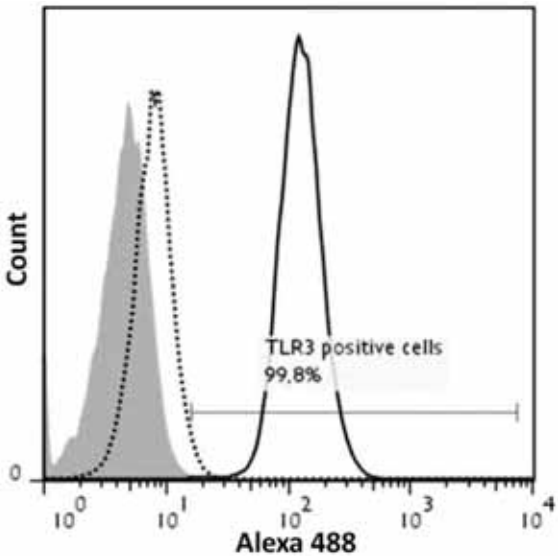

Figure 10. Flow cytometry histogram of TLR3 positive PC-3 cells (continuous line), negative control (dashed line) and non-labelled cells (grey peak).

2.2.3.1 Cellular uptake

The uptake and intracellular fate of the Rho-PEI-AuNPs in PC-3 cells was studied by flow cytometry and fluorescence microscopy. Following a 2 h of incubation with the Rho-PEI-AuNPs, flow cytometry analysis confirmed the uptake of the fluorescent nanoparticles by PC-3 cells. Live cell fluorescence microscopy showed the presence of the labelled system (red fluorescence) within the cytoplasm region of the cells (Figure 11). Then, a commercially available fluorescently labelled poly(I:C) allowed the preparation of a dual-labelled system to allow for the independent tracking of the nanoparticle delivery vehicle and its cargo. (Scheme 3)

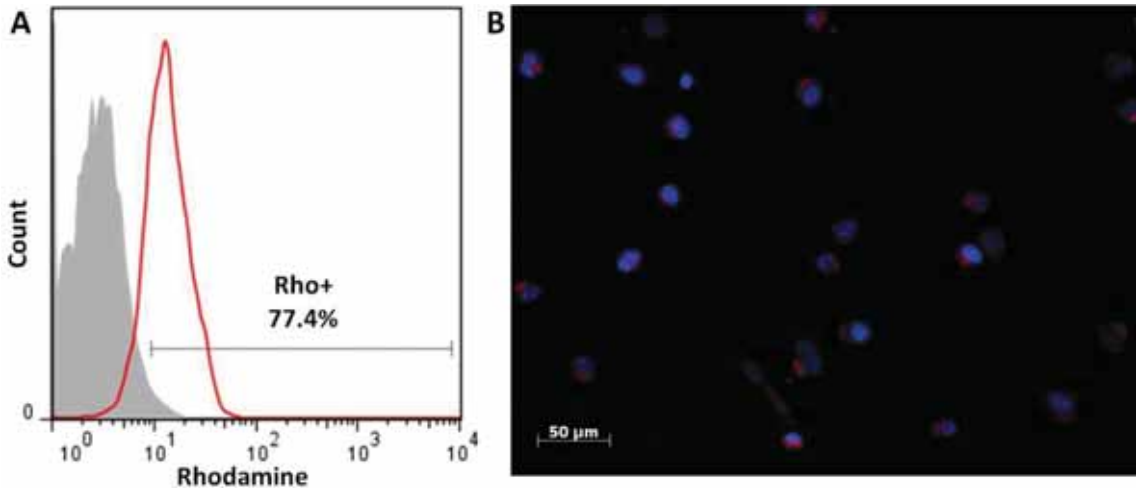

Figure 11. (**A**) Flow cytometry histogram of PC-3 cells incubated with Rho-PEI-AuNPs for 2 h (**B**) fluorescence microscopy image taken of live PC-3 cells after 2 h incubation with Rho-PEI-AuNPs (red). The nuclei are stained with Hoechst 33342 (blue).

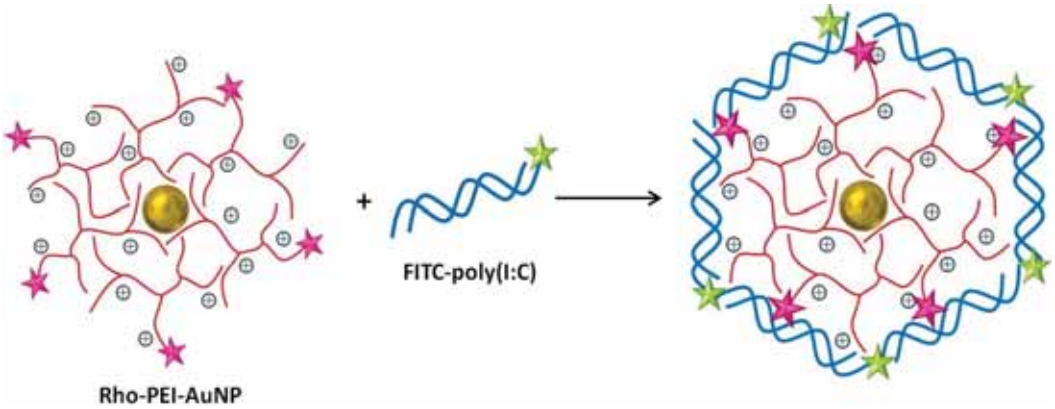

Scheme 3. Schematics of the rhodamine-labelled PEI-AuNP system conjugated with the FITC-labelled poly(I:C) used for fluorescence microscopy.

The fluorescence microscopy images of the dual-labelled system confirm the uptake of both the PEI-AuNP (shown in red) and the poly(I:C) (shown in green) after 2 h (Figure 12). Higher magnification images clearly show that although both components are successfully internalized, they separate and follow a different fate (Figure 13).

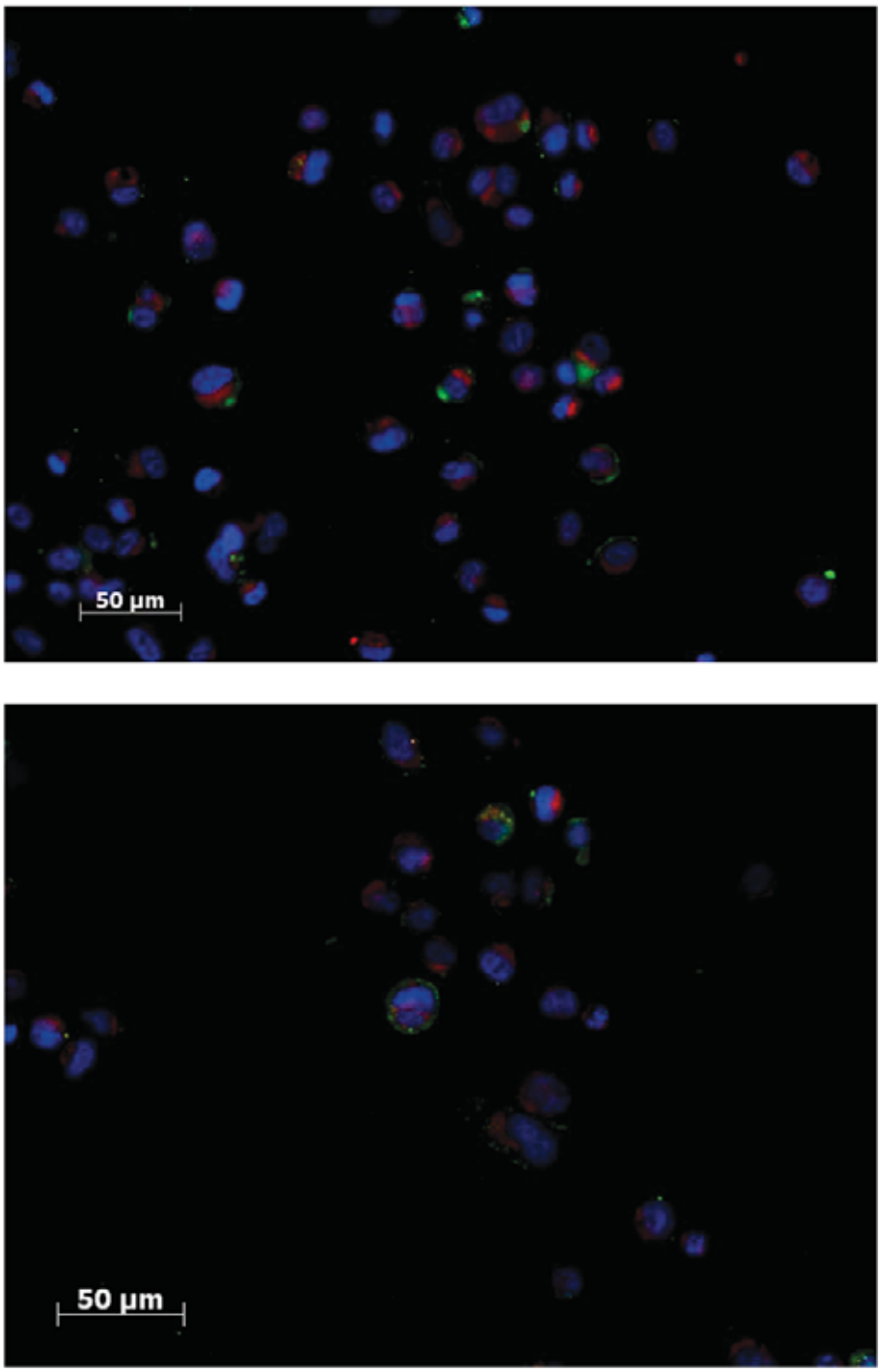

Figure 12. Fluorescence microscopy images taken of live PC-3 cells after 2 h incubation with Rho-PEI-AuNP (Red) - FITC-poly(I:C) (green) at 2 µg/mL poly(I:C). Nuclei are stained with Hoechst 33342 (blue).

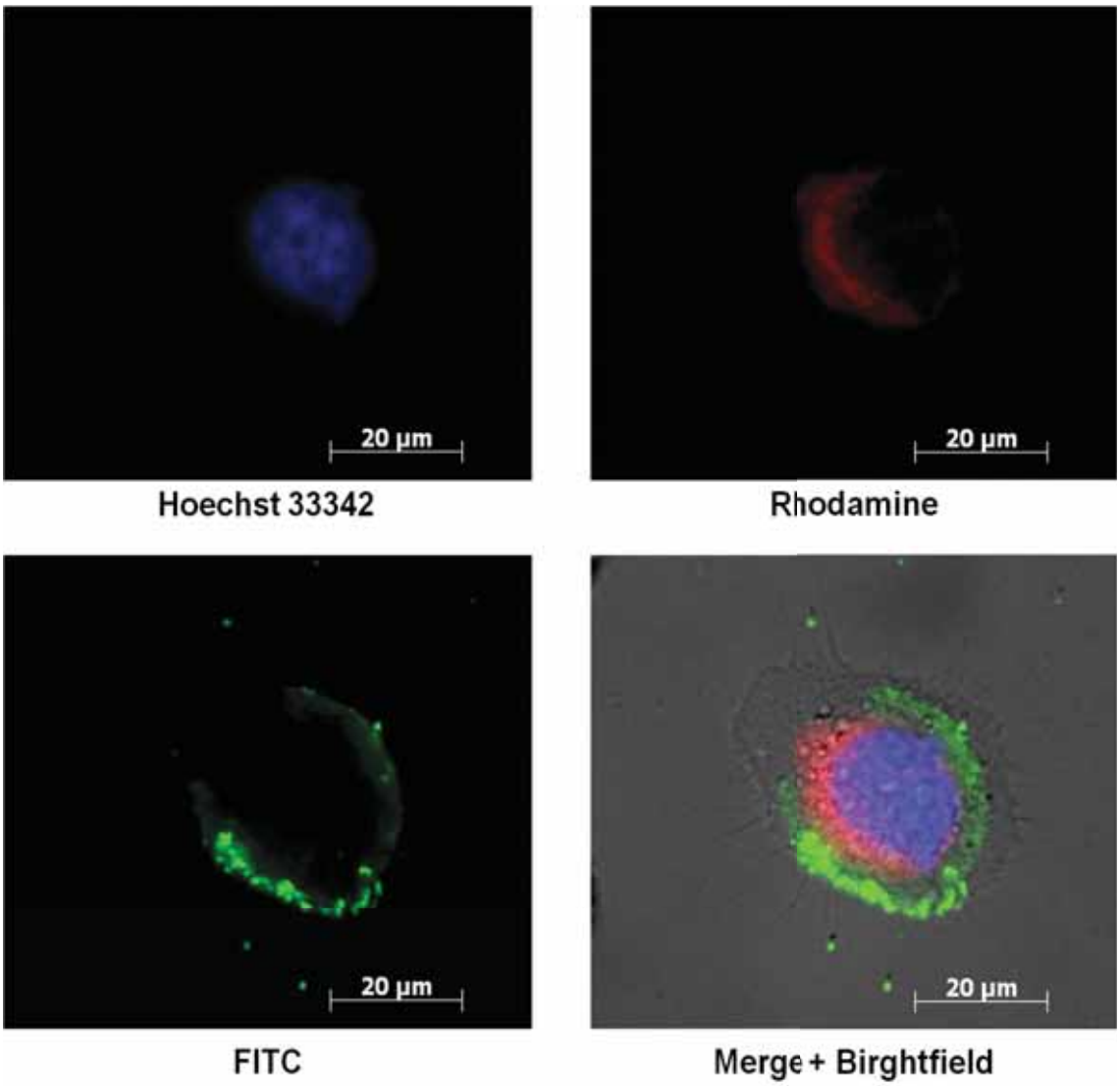

Figure 13. Uptake and trafficking of the Rho-PEI-AuNP (red) - FITC-poly(I:C) (green) system in PC-3 cells after 2 h of incubation at 2 µg/mL poly(I:C). Nuclei were stained with Hoechst 33342 (blue), PEI-AuNPs were labelled with Rhodamine B (red) and commercially available FITC labelled poly(I:C) (green) was used.

Fluorescence microscopy also show that, after 2 h incubation, in the absence of nanoparticle, no uptake of poly(I:C) was detectable; even after 24 h only weak green fluorescence was detected in the cells. Flow cytometry was used to corroborate these results and obtain more quantitative data. Figure 14 shows that after 2 h incubation only shift in fluorescence intensity between negative control and positive samples is obtained when poly(I:C) is combined with the PEI-AuNP vehicles.

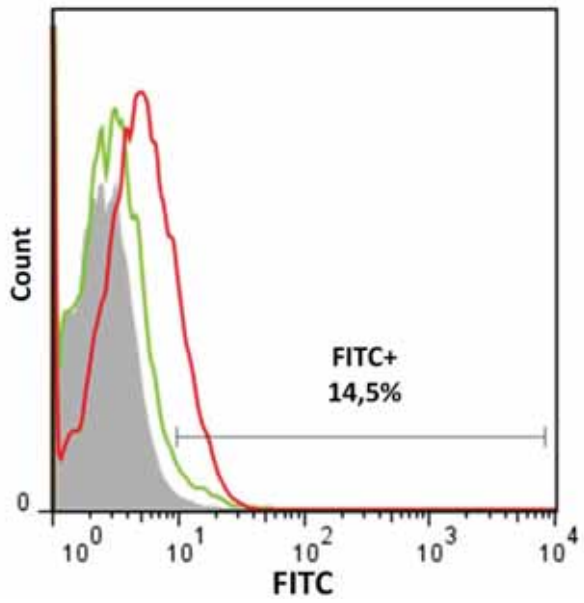

Figure 14. Flow cytometry histogram of PC-3 cells incubated with PEI-AuNP/FITC-poly(I:C) (red) or FITC-poly(I:C) (green) for 2 h at 5 μg/mL poly(I:C) concentration.

2.2.3.2 Cancer cell killing efficacy

The cytotoxicity of the PEI-AuNPs in PC-3 cells was studied first. Cell viability was determined using the MTT assay, and the results showed that almost 100% cell viability is retained up to 10 μM of gold even after 72 h incubation with the PEI-AuNPs (Figure 15); therefore this was the concentration selected for the poly(I:C) delivery studies.

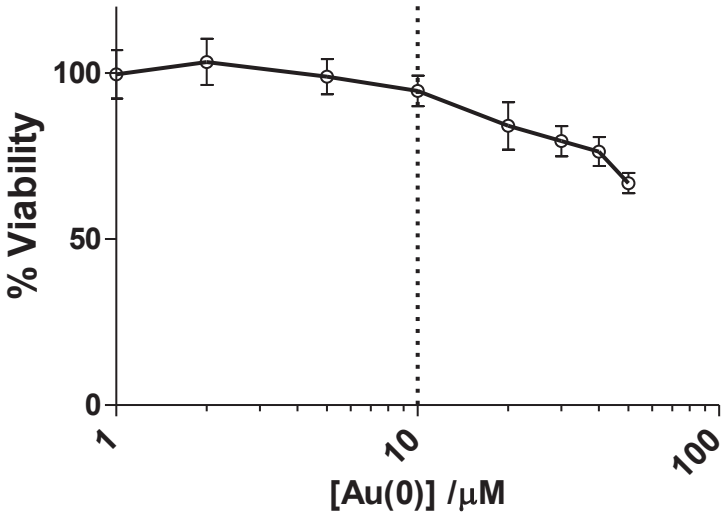

Figure 15. Cytotoxicity profile of PEI-AuNPs in PC-3 cells after 72 h incubation. Au(0) concentrations are determined from the UV-Vis spectrum.

To test the cancer cell killing ability of the PEI-AuNP-poly(I:C), a fixed PEI-AuNP concentration (10 μM gold) and three different poly(I:C) (referred as pIC in the figures below) concentrations were selected to explore the effect using different poly(I:C) to nanoparticle ratios. In all cases, the free poly(I:C) presents negligible *in vitro* cytotoxicity. When is delivered by PEI-AuNPs however, the results show that the cell-killing ability is significantly enhanced at the lowest poly(I:C) concentration (0.1 μg/mL) (Figure 16). In contrast increasing concentrations of poly(I:C) lead to less efficient systems for cancer cell killing. A possible explanation for this observation is that increasing amounts of poly(I:C) provide systems that have a more free poly(I:C)-like nature, therefore masking the effect of the delivery vehicle. Nevertheless, we note that even the less cytotoxic systems may show improved *in vivo* therapeutic efficacy if the PEI-AuNPs provide improved delivery to the tumour.

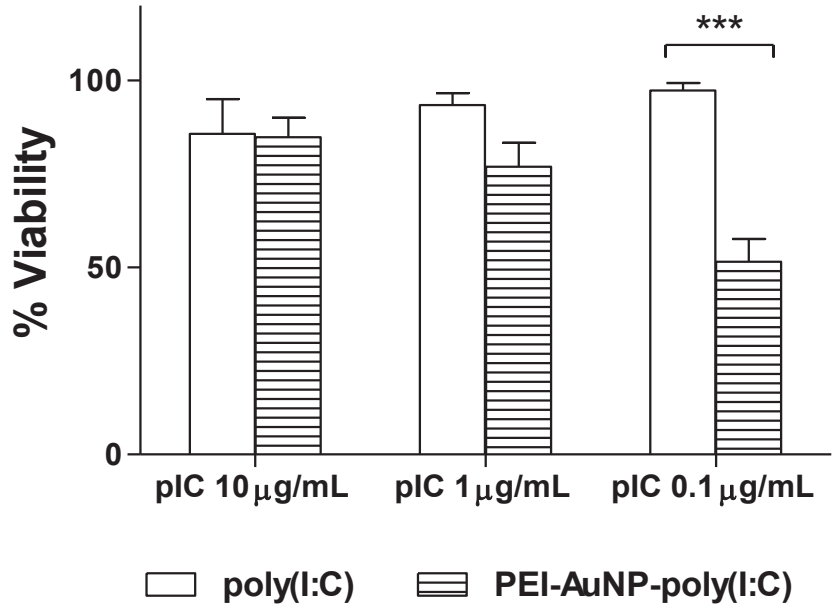

Figure 16. Cytotoxicity of free poly(I:C) and PEI-AuNPs-poly(I:C) in PC-3 cells after 72 h. [poly(I:C)] stated in X-axis; [Au(0)] = 10 μM in all cases.

To investigate the importance of the nanoparticle as drug delivery vehicle, the effect of using free PEI was also evaluated given its known ability to act as a transfection agent by itself. A range of PEI to poly(I:C) ratios were studied but in terms of cell viability none of these systems shows any significant difference compared to the free PEI (Figure 17). Hence, the AuNPs are critical for more effective delivery and cytotoxic

effect of the poly(I:C). This observation is supported by several studies that show the enhanced ability of large DNA molecules to wrap around the curved surface of the nanoparticles through a combination of hydrophobic and electrostatic interactions. Thus the "pre-arranged" curved conformation provided by the PEI-AuNPs might favour the interaction, resulting in a more effective delivery of poly(I:C) to the cells that cannot be achieved with the LMW PEI on its own.

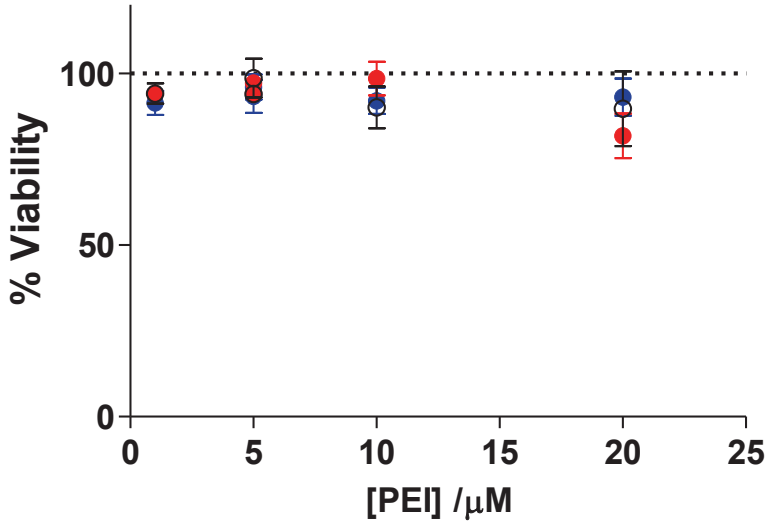

Figure 17. Cytotoxicity of PEI (white circles) and PEI-poly(I:C) at two different poly(I:C) concentrations, 0.1 μg/mL (blue circles) and 1 μg/mL (red circles) in PC-3 cells.

Regarding the possible mechanism behind the cancer cell death, Besch *et al.* already reported that poly(I:C) causes the activation of apoptotic mechanisms mediated not only by TLR-3, but also RIG-I and MDA-5 receptors.[44] To determine if the decrease in cell viability involves an apoptotic pathway, PC-3 cells treated with poly(I:C), PEI-poly(I:C), PEI-AuNP-poly(I:C) and their corresponding controls were stained with a commercially available Annexin V apoptosis kit an analyzed by flow cytometry. These experiments showed that the main population in all the controls as well as for the PEI-poly(I:C) system was made up of live cells (Figure 18). However, the cells treated with the PEI-AuNP-poly(I:C) had an increased population of both apoptotic and late apoptotic/necrotic cells. This indicates that the cancer cell killing effect of poly(I:C) delivered with PEI-AuNPs indeed occurs through an apoptosis mediated mechanism.

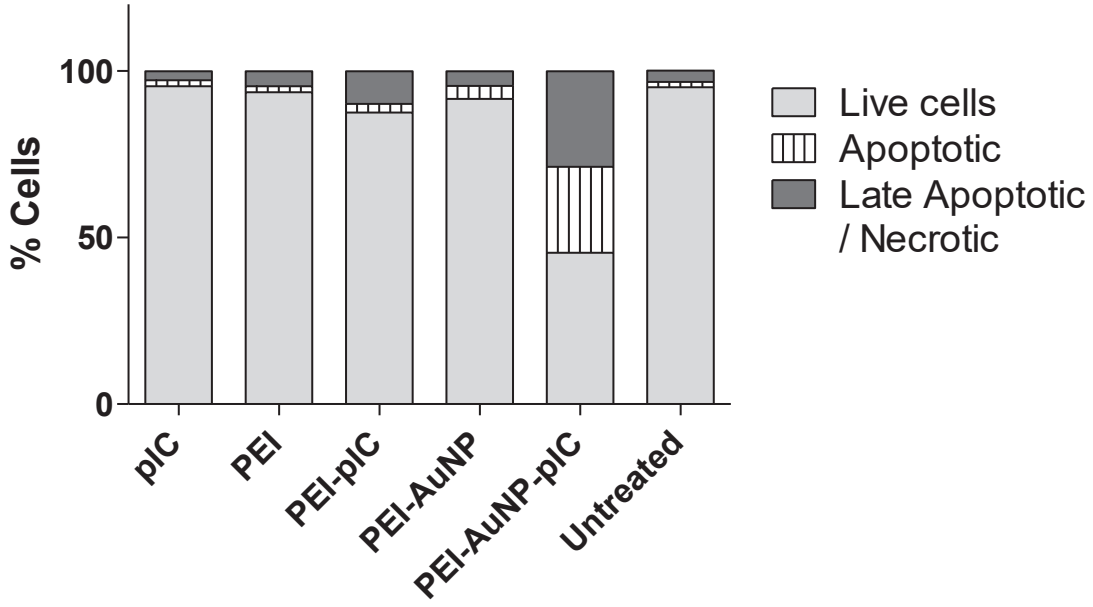

Figure 18. Apoptosis quantification by Annexin V staining in PC-3 cells treated with poly(I:C), PEI, PEI-poly(I:C), PEI-AuNPs and PEI-AuNPs-poly(I:C) in PC-3 cells after 72 h. [poly(I:C)] = 0.1 μg/mL, [PEI] = 1 μM, [Au(0)] = 10 μM.

Even though several different systems with poly(I:C) have already been reported to cause cancer cell death,[25,45] the PEI-AuNP based delivery has not only proved to be effective but more importantly the effect is most pronounced at very low doses of poly(I:C). Next, the potential synergy between the PEI-AuNP and a recently developed peptide-based transfection agent (P21-LK15-8R)[46] to enhance the cancer cell killing activity poly(I:C) was evaluated. This peptide-based structure developed by Gibson *et al.* at the University of Nottingham was selected because it has already demonstrated a significant nucleic acid transfection efficacy. The peptide consists of three components, a short 21-residue peptide (p21), a nucleic acid interaction sequence (LK15) and an 8R sequence. The transfection efficiency of this system is not only comparable to that of the commercial transfection agent Lipofectamine 2000 but most importantly (and unlike Lipofectamine 2000), it is retained even in serum containing environments.

The cytotoxicity of poly(I:C) was examined with the peptide alone and with the combination of both the peptide and the PEI-AuNP. As shown in Figure 19, the

addition of the P21-LK15-8R to the poly(I:C) resulted in a concentration dependent decrease in viability, the opposite behaviour to that observed with the PEI-AuNP. When both transfection systems are used together, although a slightly more cytotoxic effect could be observed at 1 μg/mL, the viability pattern was similar to that of poly(I:C)-P21. This result suggests that rather than interacting in a synergistic way, both components compete and most of the effect due to the PEI-AuNP is presumably inhibited by the formation of stronger P21-LK15-8R/poly (I:C) complexes. Nevertheless, it is important to note that even though P21-LK15-8B is able to act as an efficient transfection agent for poly(I:C) and enhance cancer cell killing, the PEI-AuNP delivery system achieved a similar toxicity with 10-fold less poly(I:C).

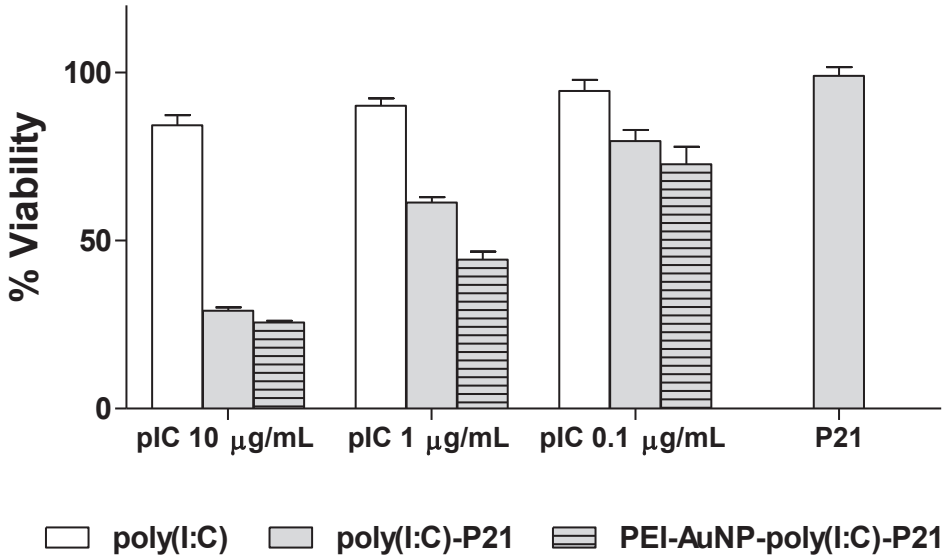

Figure 19. Cytotoxicity of free poly(I:C), combined with P21-LK15-8R at 1 μM and with both P21-LK15-8R and PEI-AuNP ([Au] = 10 μM) in PC-3 cells. Poly(I:C) concentrations shown on the X-axis.

Since poly(I:C) is mainly used as an immunomodulatory agent in immunotherapy, we evaluated next the effect of the PEI-AuNP delivery system towards poly(I:C)-induced the activation of cells of the immune system. For this purpose, the PEI-AuNP-poly(I:C) system was incubated with J774 murine macrophages, and both cytotoxicity and cytokine production were examined. The presence of PEI-AuNPs does induce any significant changes on neither the cytotoxicity nor the

immunostimulatory activity of poly(I:C) in terms of IL-6 cytokine production (Figure 20). Moreover, the poly(I:C) concentration that in combination with PEI-AuNPs led to a significant increase in cancer cell killing ability (0.1 μg/mL) did not induced IL-6 production or cytotoxicity in macrophages.

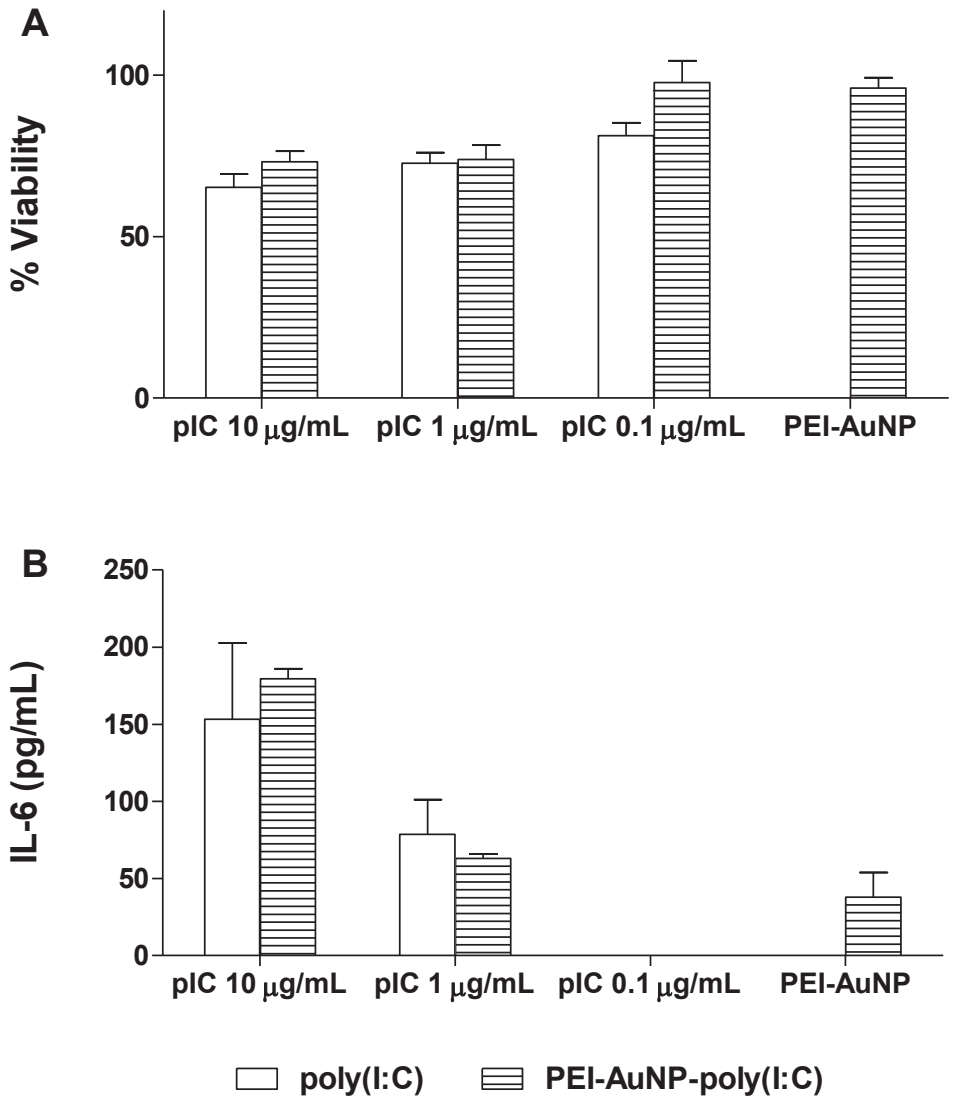

Figure 20. (**A**) Cell viability of free poly(I:C), PEI-AuNP-poly(I:C) and the corresponding PEI-AuNP control ([Au] = 10 μM) in J774 murine macrophages. (**B**) IL-6 cytokine production of J774 macrophages treated with the aforementioned formulations.

To establish the uniqueness of this AuNP based construct to promote cancer cell death, a comparative study was done using PEGylated IONP micelles to deliver poly(I:C) to both PC-3 cancer cells and J774 macrophage cells. These PEGylated micelles were selected because they have already been reported as effective delivery

system for poly(I:C) for enhancing immunostimulatory properties and their size and morphology is similar to that of the PEI-AuNPs.

Summarized in Figure 21 and Figure 22, the results showed that the change of delivery vehicle leads to a totally different behaviour of poly(I:C) in terms of both cytotoxicity and immunostimulatory activity. In the case of PC-3 cells (Figure 21), when the poly(I:C) was delivered with IONPs there is no cytotoxic effect, the cell viability remained constant to that of the IONP itself. Upon the addition of P21-LK15-8R the viability decreased in a concentration dependent manner and was more effective than using P21-LK15-8R alone at the lowest poly(I:C) concentration (0.1 μg/mL) peptide.

The results in the macrophage cell line were similar to those reported by Cobaleda et al.[24] None of the formulations shows any major reduction in cell viability, but the IL-6 cytokine production is drastically improved with the IONP-poly(I:C) system. The addition of P21-LK15-8R however did not improve the enhancement produces by the nanoparticle; while a similar cytokine production can be observed for the highest poly(I:C) concentration (25 μg/mL), the IONP alone is more effective in enhancing the immunostimulatory activity of poly(I:C) at lower concentrations.

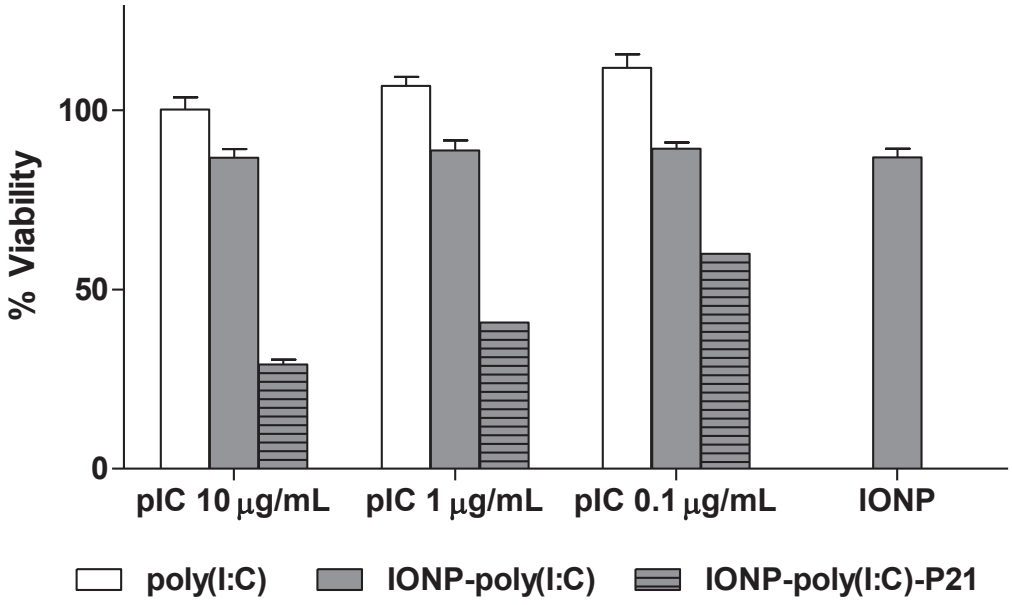

Figure 21. Cytotoxicity of poly(I:C) at 10 μg/mL, 1 μg/mL and 0.1 μg/mL, combined with IONP ([Fe] = 100 μM) and with both P21-LK15-8R (1 μM) and IONP ([Fe] = 100 μM) in PC-3 cells.

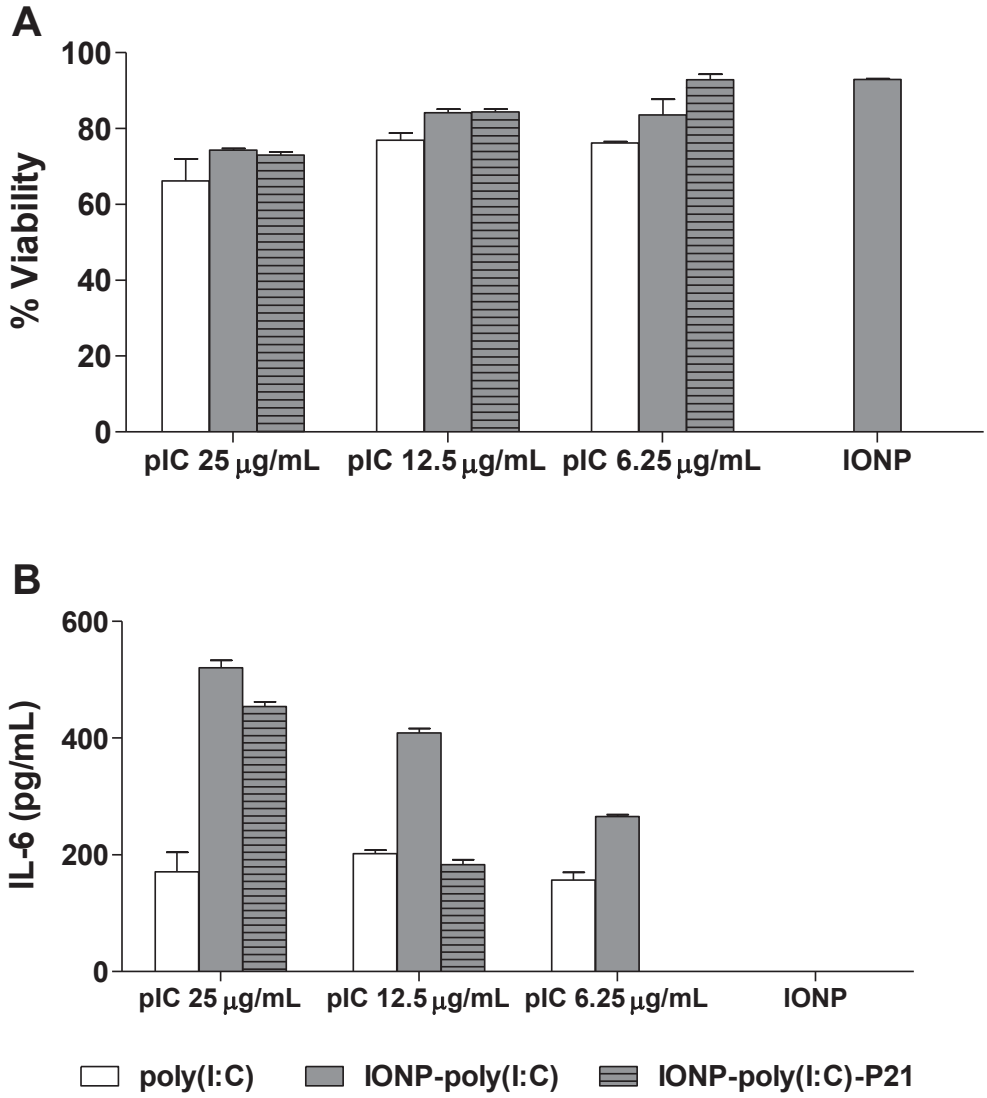

Figure 22. (**A**) Cytotoxicty of poly(I:C) at 25 μg/mL, 12.5 μg/mL and 6.25 μg/mL and in combination with IONP ([Fe] = 100 μM) and both P21-LK15-8R (1 μM) and IONP ([Fe] = 100 μM) in J774 murine macrophages. (**B**) IL-6 cytokine production of J774 macrophages treated with the aforementioned formulations.

2.3 Conclusions

In summary, this chapter describes the facile single-step synthesis and characterization of PEI-coated AuNPs, which due to the positively charged surface provided by the polymer are able to electrostatically interact with the TLR3 agonist poly(I:C) and promote its delivery into prostate cancer cells. The nanocarrier has not only demonstrated to increase the uptake of poly(I:C) in PC-3 cancer cells but also to selectively promote a chemotherapeutic effect (providing enhanced cancer cell killing ability to poly (I:C) rather than enhanced immunostimulation as found in recently reported IONP carriers developed in the group.

In view of the results obtained from the comparative study between the PEI-AuNPs and PEGylated IONP micelles for the delivery of poly(I:C), it becomes clear that poly(I:C) can indeed provide a two-pronged mode of action against cancer, namely chemotherapy and immunotherapy, where any one of them can be selectively enhanced via careful selection of nanoparticles carriers. The specific change of behaviour could be related to the nanocarriers coating or composition causing poly(I:C) to interact differently; such changes may result in poly(I:C) being recognized by different cells and/or receptors that ultimately lead to either immunostimulatory or cytotoxic mechanisms.

The use of a simple and easy to prepare construct such as these PEI coated AuNPs as vehicles for poly(I:C) not only proved to be a new and an effective approach from the delivery point of view, but more importantly this particular system has demonstrated it affects the intracellular behaviour of poly(I:C), selectively enhancing its cancer cell killing ability. Although not investigated, by using this system it may be possible to use the intrinsic properties of AuNPs for both imaging and PTT, opening up a whole range of new possibilities for the further development of more sophisticated PEI-AuNP based theranostic nanoplatforms for simultaneous cancer imaging and therapy.

2.4 Experimental Section

2.4.1 Materials.

All syntheses were carried out with the following commercially available reagents used without further purification. Hydrogen tetrachloroaurate(III) trihydrate (99.99%) and polyethyleneimine (branched, 1.8 kDa, 99%; 36% NH_2, 29% NH and 35% N determined by NMR studies) were purchased from Alfa Aesar. Rhodamine B (≥ 95%), N-hydroxysuccinimide (98%), sulforhodamine B sodium salt and trichloroacetic acid (> 99%) were purchased from Sigma Aldrich. 1-Ethyl-3-[3-dimethylamino porpyl]carbodiimide hydrochloride (EDC) was purchased from Thermo Scientific. Poly(I:C) and poly(I:C)-fluorescein were purchased from Invivogen. BD Cytofix/Cytoperm™ Plus Fixation/Permeabilization Kit and Fc blocking antibody were purchased from BD Biosciences. Anti-TL3 and AlexaFluor488 antibodies were purchased from Abcam. Annexin V/Dead Cell Apoptosis Kit was purchased from Invitrogen.

2.4.2 Synthesis of PEI-coated AuNPs

To prepare the PEI-coated AuNPs, PEI dissolved in water was added to an aqueous solution of $HAuCl_4$ in a 2:1 molar ratio and the mixture was stirred at 90 ºC. This preparation is slightly modified from recent literature preparation, which used high molecular weight PEI.[34,41] In this study PEI-coated AuNPs formed after 2 h were used. Once the reaction mixture was cooled to room temperature, the PEI-AuNPs were purified by passing through a centrifugal filter unit (MWCO 50000; Amicon Ultra-4).

2.4.3 Synthesis of rhodamine-labelled PEI and rhodamine labelled PEI-AuNPs

Rhodamine-labelled PEI was prepared adapting a previously described protocol used for the preparation of fluorescein-labelled PEI.[43] N-hydroxysuccinimide (NHS) (23 mg, 0.2 mmol) and N-(3-dimethylaminopropyl)-N'-ethycarbodiimide hydrochloride

(EDC) (38mg, 0.2mmol) were dissolved in PBS 10 mM pH 6 and stirred for 15 minutes at room temperature. Rhodamine B (4.8 mg, 10 μmol) was added and left to react with magnetic stirring for 2 h at room temperature. Finally an aqueous PEI solution (120 μL, 5 mg/mL) was added to the mixture and allowed to react under magnetic stirring for 2 h at room temperature. Rhodamine labelled PEI-AuNPs were prepared as above using the rhodamine labelled PEI accordingly diluted in water. Any unbound rhodamine B was later removed in the purification step.

2.4.4 Sample preparation

All samples were freshly prepared simply by mixing an aqueous solution of poly(I:C) at the appropriate concentrations with an aqueous solution of PEI or PEI-coated AuNP (concentrations given in the figure captions). For the cell culturing experiments, prior to the incubation with the cancer cells, the samples were left to interact for ca. 30 minutes and then were diluted 1/10 in cell culture medium and directly added to the cells to ensure no loss of reagents. In the studies with PEI-AuNPs, the gold concentration refers to Au(0) determined from the UV-Vis spectrum of the nanoparticle stock solution once purified to remove any excess of reagents. This Au(0) concentration can be directly correlated to the absorbance value at 400 nm.[47]

2.4.5 Cell culture experiments

PC-3 human prostate cancer cell line was obtained from the American Type Tissue Collection (ATCC) and cultured in Ham's F-12K (Kaighn's) medium (Glibco) supplemented with 10% foetal bovine serum (Invitrogen) at 37 ºC under 5% CO_2. Cells were passaged at ~ 70% confluence and a low passage number was maintained using cryopreserved stocks stored in foetal bovine serum supplemented with 10% DMSO.

TLR3 expression. PC-3 cells were trypsinized, resuspended FACS buffer and transferred to cytometry tubes ($5{\cdot}10^5$ cells/tube in 100 μL). Fc receptors were blocked for 10 min at 4 ºC. Cells were fixed and permeabilized for 15 min using a BD Cytofix/Cytoperm fixation and permeabilization kit at 4 ºC. After being washed with BD Perm/wash buffer cells were incubated at 4 ºC for 20 min with the primary anti-TLR3

antibody (10 μg/mL). Cells were then washed with BD Perm/wash buffer and Alexa Fluor 488-labelled secondary antibody (1 μg/mL) was used for staining the primary TLR3 antibody for 30 min at R.T. Finally cells were washed tree times with BD Perm/wash buffer and resuspended in FACS buffer for flow cytometry analysis.

Cell viability studies. Cells were plated at a 3000 cell/well density in 96-well plates and allowed to adhere overnight. All samples were freshly prepared and diluted 1/10 in medium before incubating at 37 ºC using 200 μL of sample per well in triplicate. The cell viability was measured using the sulforhodamine B assay.[48] To determine the viability after 72 h, the cells were fixed by the addition of ice cold 25% trichloroacetic acid (TCA) solution prior to staining with the sulforhodamine dye (SRB) solution (0.4% w/v in 1% glacial acetic acid). The plates were washed with 1% glacial acetic acid, air dried and resuspended in Tris buffer (10 mM, pH 10.5) before reading the absorbance at 550 nm.

Cell imaging. For the live cell microscopy, PC-3 cells were seeded in an Ibidi 18 well μ-Slide at 4000 cell/well density and allowed to adhere overnight in an incubator (37 ºC, 5% CO_2) in Ham's F-12K (Kaighn's) medium. The medium was changed and the nuclei stained with Hoechst 33342 (5 μg/mL) for 5 minutes, washed with sterile PBS 10 mM and incubated with the rhodamine labelled AuNPs and/or FITC labelled poly(I:C) formulations for 2 h. The medium was then removed, cells washed with sterile PBS 10 mM and fresh medium was added prior to image acquisition.

Cellular uptake by flow cytometry. PC-3 cells were plated in 96-well plates (10^5 cell/well) and allowed to adhere overnight in Ham's F-12K (Kaighn's) medium. Fluorescent formulations containing rhodamine labelled PEI-AuNPs or FITC-labelled poly(I:C) were diluted in medium accordingly and added to the cells for 2 h incubation at 37 ºC. After the incubation, the supernatant was removed and cells washed with PBS (10 mM). The adherent cells were trypsinized, transferred to cytometer tubes and washed with PBS (10 mM). Cells were resuspended in a final volume of 200 μL flow cytometry buffer (1% BSA, 0.1% sodium azide in PBS 10 mM) for uptake measurements.

Apoptosis assay. PC-3 cells were plated at 3000 cell/well density in 96-well plates and left to adhere overnight. Cells were then treated with the AuNP-poly(I:C) formulations (10 replicates per sample) at the indicated doses for 72 h. After treatment, apoptosis was assessed by Annexin V staining according to the manufacturer's instruction. Treated and untreated cells were stained with Pacific Blue Annexin V and SYTOX AAdvanced dead cell stain and analyzed by flow cytometry.

2.4.6 Instrumentation

TEM. TEM studies were conducted in a JEOL JEM-2011 electron microscope operating at 200 kV. The samples were prepared by depositing a drop of nanoparticle solution onto a copper specimen grid coated with a holey carbon film and allowing it to dry. For nanoparticle size determination a minimum of 300 particles were measured using the *Image J* software.

UV-Vis and Fluorescence spectroscopy. UV-vis measurements were performed in H_2O using a Varian Cary 5000 spectrophotometer. Absorbance measurements on 96-well plates were carried out on a TECAN Genios Pro 96/384 multifunction microplate reader. Fluorescence emission spectra were recorded with a Horiba Jovin Ibon Fluorolog flurometer.

DLS and ζ-potential. Particle size analysis was performed using a NanoSizer (Malvern Nano-ZS, UK) with 173° scattering angle at 25 ºC. Each sample was measured at least in triplicate. Z-potential measurements were carried out with the same NanoSizer equipment at 25 ºC and a cell drive voltage of 20 V using a Smoluchowski model.

Flow cytometry. All flow cytometry experiments were carried out in a FACS Canto II (BD Bioscience) system, which has an excitation source composed of three lasers: violet (405 nm), blue (488 nm) and red (633 nm). The laser excitation wavelength used for both FITC and rhodamine was 488 nm and the emission filters 530/30 nm and 585/42 nm respectively. The laser excitation wavelength used for SYTOX was 488 nm

and the emission filter 670-735 nm, for Pacific Blue Annexin V the excitation wavelength was 405 nm and the emission filter 425-475 nm. In all measurements cells were electronically gated based on forward and side scatter parameters and the not-singlet events leaved out based on forward area and height parameters. Each analysis represented the acquisition of 10000 cells per sample and data was analyzed with FlowJo LLC software.

Fluorescence microscopy. Live cell fluorescence images were obtained using Zeiss Axio Observer wide field fluorescence microscope (Carl Zeiss, Germany). Both a colibri LED module and a mercury short-arc HXP lamp were used for fluorescence excitation: 365 nm LED excitation for Hoechst staining, 470 nm LED excitation for FITC and HXP lamp for rhodamine B. Fluorescence emission was collected using a high-efficiency multi-band pass colibri filter set which included a 402-488 nm bandpass for Hoechst and 500-557 nm for FITC; rhodamibe B emission was collected using an emission filter with a 570-640 nm bandpass. Brightfield and fluorescence images were collected and processed using AxioVision software.

2.5 References

(1) *World Cancer Report 2014*; Stewart, B. W.; Wild, C. P., Eds.; International Agency for Research on Cancer: Lyon, **2014**.

(2) Shen, M. M.; Abate-Shen, C. *Genes Dev.* **2010**, *24*, 1967.

(3) Akira, S.; Takeda, K. *Nature* **2004**, *4*, 499.

(4) Akira, S.; Uematsu, S.; Takeuchi, O. *Cell* **2006**, *124*, 783.

(5) Zhao, S.; Zhang, Y.; Zhang, Q.; Wang, F.; Zhang, D. *Front. Immunol.* **2014**, *5:352*.

(6) Manna, E. *Arch. Cancer Res.* **2016**, *4*, 3:99.

(7) Saint-Jean, M.; Knol, A. C.; Nguyen, J. M.; Khammari, A.; Dréno, B. *Eur. J. Dermatol.* **2011**, *21*, 899.

(8) Matsumoto, M.; Seya, T. *Adv. Drug Deliv. Rev.* **2008**, *60*, 805.

(9) Tissari, J.; Sirén, J.; Meri, S.; Julkunen, I.; Matikainen, S. *J. Immunol.* **2005**, *174*, 4289.

(10) Yoneyama, M.; Kikuchi, M.; Matsumoto, K.; Imaizumi, T.; Miyagishi, M.; Taira, K.; Foy, E.; Loo, Y. M.; Gale, M.; Akira, S.; Yonehara, S.; Kato, A.; Fujita, T. *J. Immunol.* **2005**, *175*, 2851.

(11) Kawai, T.; Akira, S. *Ann. N. Y. Acad. Sci.* **2008**, *1143*, 1.

(12) Chin, A. I.; Miyahira, A. K.; Covarrubias, A.; Teague, J.; Guo, B.; Dempsey, P. W.; Cheng, G. *Cancer Res.* **2010**, *70*, 2595.

(13) Salaun, B.; Coste, I.; Rissoan, M. C.; Lebecque, S. J.; Renno, T. *J. Immunol.* **2006**, *176*, 4894.

(14) Taura, M.; Fukuda, R.; Suico, M. A.; Eguma, A.; Koga, T.; Shuto, T.; Sato, T.; Morino-Koga, S.; Kai, H. *Cancer Sci.* **2010**, *101*, 1610.

(15) Cheng, Y. S.; Xu, F. *Cancer Biol. Ther.* **2010**, *10*, 1219.

(16) Salaun, B.; Zitvogel, L.; Asselin-Paturel, C.; Morel, Y.; Chemin, K.; Dubois, C.; Massacrier, C.; Conforti, R.; Chenard, M. P.; Sabourin, J. C.; Goubar, A.; Lebecque, S.; Pierres, M.; Rimoldi, D.; Romero, P.; Andre, F. *Cancer Res.* **2011**, *71*, 1607.

(17) Singh, M.; Overwijk, W. W. *Cancer Immunol. Immunother.* **2015**, *64*, 911.

(18) Salazar, A. M.; Erlich, R. B.; Mark, A.; Bhardwaj, N.; Herberman, R. B. *Cancer Immunol. Res.* **2014**, *2*, 720.

(19) Forte, G.; Rega, A.; Morello, S.; Luciano, A.; Arra, C.; Pinto, A.; Sorrentino, R. *J. Immunol.* **2012**, *188*, 5357.

(20) Alexis, F.; Zeng, J.; Shu, W. *Cold Spring Harb. Protoc.* **2006**, DOI:10.1101/pdb.prot4451.

(21) Lungwitz, U.; Breunig, M.; Blunk, T.; Göpferich, A. *Eur. J. Pharm. Biopharm.* **2005**, *60*, 247.

(22) Sonawane, N. D.; Szoka, F. C.; Verkman, A. S. *J. Biol. Chem.* **2003**, *278*, 44826.

(23) Kunath, K.; von Harpe, A.; Fischer, D.; Petersen, H.; Bickel, U.; Voigt, K.; Kissel, T. *J. Control. Release* **2003**, *89*, 113.

(24) Cobaleda-Siles, M.; Henriksen-Lacey, M.; De Angulo, A. R.; Bernecker, A.; Vallejo, V. G.; Szczupak, B.; Llop, J.; Pastor, G.; Plaza-Garcia, S.; Jauregui-Osoro, M.; Meszaros, L. K.; Mareque-Rivas, J. C. *Small* **2014**, *10*, 5054.

(25) Colapicchioni, V.; Palchetti, S.; Pozzi, D.; Marini, E. S.; Riccioli, A.; Ziparo, E.; Papi, M.; Amenitsch, H.; Caracciolo, G. *J. Mater. Chem. B* **2015**, *3*, 7408.

(26) Ultimo, A.; Giménez, C.; Bartovsky, P.; Aznar, E.; Sancenón, F.; Marcos, M. D.; Amorós, P.; Bernardo, A. R.; Martínez-Máñez, R.; Jiménez-Lara, A. M.; Murguía, J. R. *Chemistry* **2016**, *22*, 1582.

(27) Ramani, M.; Mudge, M. C.; Morris, R. T.; Zhang, Y.; Warcholek, S. a; Hurst, M. N.; Riviere, J. E.; DeLong, R. K. *Mol. Pharm.* **2017**, *14*, 614.

(28) Shan, Y.; Luo, T.; Peng, C.; Sheng, R.; Cao, A.; Cao, X.; Shen, M.; Guo, R.; Tomás, H.; Shi, X. *Biomaterials* **2012**, *33*, 3025.

(29) Bishop, C. J.; Tzeng, S. Y.; Green, J. J. *Acta Biomater.* **2015**, *11*, 393.

(30) Yu, F.; Huang, J.; Yu, Y.; Lu, Y.; Chen, Y.; Zhang, H.; Zhou, G.; Sun, Z.; Liu, J.; Sun, D.; Zhang, G.; Zou, H.; Zhong, Y. *J. Biomed. Nanotechnol.* **2016**, *12*, 503.

(31) Thomas, M.; Klibanov, A. M. *Proc. Natl. Acad. Sci. U.S.A.* **2003**, *100*, 9138.

(32) Guo, S.; Huang, Y.; Jiang, Q.; Sun, Y.; Deng, L.; Liang, Z.; Du, Q.; Xing, J.; Zhao, Y.; Wang, P. C.; Dong, A.; Liang, X. J. *ACS Nano* **2010**, *4*, 5505.

(33) Hu, C.; Peng, Q.; Chen, F.; Zhong, Z.; Zhuo, R. *Bioconjug. Chem.* **2010**, *21*, 836.

(34) Song, W. J.; Du, J. Z.; Sun, T. M.; Zhang, P. Z.; Wang, J. *Small* **2010**, *6*, 239.

(35) Cebrián, V.; Martín-Saavedra, F.; Yagüe, C.; Arruebo, M.; Santamaría, J.; Vilaboa, N. *Acta Biomater.* **2011**, *7*, 3645.

(36) Tian, H.; Guo, Z.; Chen, J.; Lin, L.; Xia, J.; Dong, X.; Chen, X. *Adv. Healthcare Mater.* **2012**, *1*, 337.

(37) Tian, Y.; Zhang, Y.; Pan, J.; Lu, N.; Wang, S.; Lu, G. *J. Nanomater. 2015,* DOI:10.1155/2015/720198.

(38) Chanana, M.; Liz-Marzán, L. M. *Nanophotonics* **2012**, *1*, 199.

(39) Note, C.; Kosmella, S.; Koetz, J. *Colloids Surfaces A Physicochem. Eng. Asp.* **2006**, *290*, 150.

(40) Sun, X.; Dong, S.; Wang, E. *Mater. Chem. Phys.* **2006**, *96*, 29.

(41) Sun, X.; Dong, S.; Wang, E. *J. Colloid Interface Sci.* **2005**, *288*, 301.

(42) Veerakumar, P.; Velayudham, M.; Lu, K. L.; Rajagopal, S. *Appl. Catal. A Gen.* **2012**, *439-440*, 197.

(43) Xu, W.; Park, J. Y.; Kattel, K.; Ahmad, M. W.; Bony, B. A.; Heo, W. C.; Jin, S.; Park, J. W.; Chang, Y.; Kim, T. J.; Park, J. A.; Do, J. Y.; Chae, K. S.; Lee, G. H. *RSC Adv.* **2012**, *2*, 10907.

(44) Besch, R.; Poeck, H.; Hohenauer, T.; Senft, D.; Häcker, G.; Berking, C.; Hornung, V.; Endres, S.; Ruzicka, T.; Rothenfusser, S.; Hartmann, G. *J. Clin. Invest.* **2009**, *119*, 2399.

(45) Palchetti, S.; Starace, D.; De Cesaris, P.; Filippini, A.; Ziparo, E.; Riccioli, A. *J. Biol. Chem.* **2015**, *290*, 5470.

(46) Dixon, J. E.; Osman, G.; Morris, G. E.; Markides, H.; Rotherham, M.; Bayoussef, Z.; El Haj, A. J.; Denning, C.; Shakesheff, K. M. *Proc. Natl. Acad. Sci. U.S.A.* **2016**, *113*, E291.

(47) Hendel, T.; Wuithschick, M.; Kettemann, F.; Birnbaum, A.; Rademann, K.; Polte, J. *Anal. Chem.* **2014**, *86*, 11115.

(48) Vichai, V.; Kirtikara, K. *Nat. Protoc.* **2006**, *1*, 1112.

3

PEI-coated AuNPs for outer-sphere interaction-based delivery and activation of a Pt(IV) prodrug

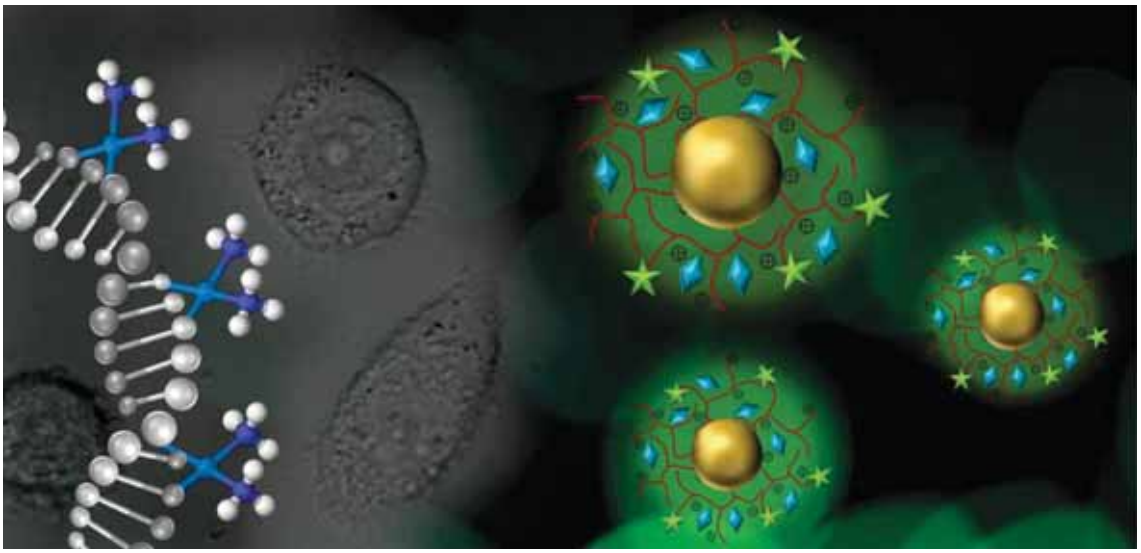

3.1 Introduction

Cisplatin stands as one of the most commonly used and few chemotherapeutic agents with broad efficacy for cancer treatment.[1] Despite its clinical success, there are several limitations to its use, including limited selectivity, development of side effects and resistance mechanisms. In a bid to overcome these issues, a prodrug strategy has been adopted in this work, using inert platinum (IV) prodrugs that can be reduced inside cancer cells to render cytotoxic species (Scheme 1).

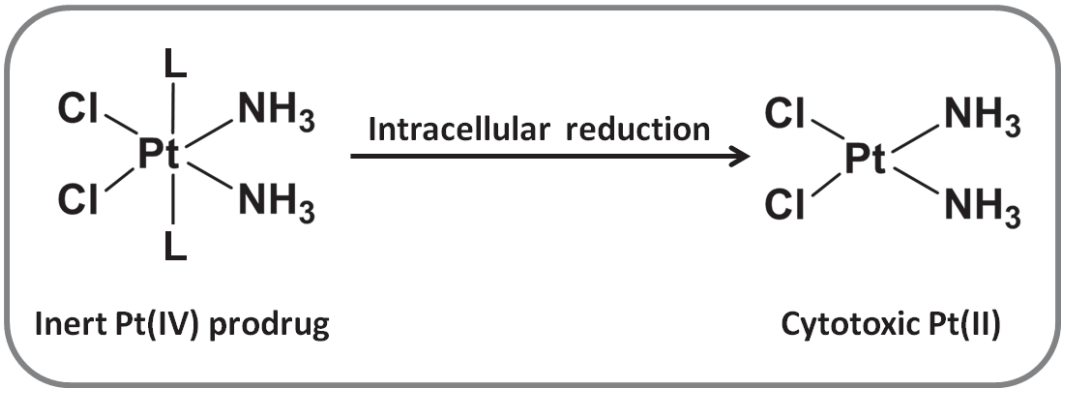

Scheme 1. Prodrug strategy based on the intracellular reduction of inert platinum (IV) prodrugs to generate cytotoxic species.

Although extensive research has already been performed in area of platinum (IV) prodrug research,[2] there is still much room for improvement regarding the efficient delivery and therapeutic efficacy of these compounds. In this regard, apart from the targeting and dual action therapeutic strategies mentioned in the introduction, nanoparticle delivery platforms have also become a very attractive way of enhancing the anticancer efficacy of anticancer platinum prodrugs by providing both active and passive targeting and prolonged bloodstream circulation among other advantages.

Over the past few years several platinum (IV) prodrugs have been attached to nanoplatforms to facilitate their delivery and activation. Many types of nanoparticles have been employed for this purpose, including carbon nanotubes,[3,4] gold nanoparticles[5] and nanorods,[6] polymeric,[7–11] silica[12] and iron oxide nanoparticles,[13,14] up-converting nanomaterials,[15] semiconductor nanocrystals,[16,17] copper sulphide[18]

nanoparticles and silk fibroin nanoparticles.[19] Lippard and co-workers reported various systems based on the encapsulation of a hydrophobic platinum (IV) prodrug in PLGA-PEG nanospheres, also incorporating targeting moieties such as prostate specific membrane aptamer (PSMA) for prostate cancer or RGD targeting peptides for breast cancer (Figure 1). The studies investigating the effectiveness of the delivery system in two different prostate cancer cell lines (PC-3 and LNCaP)[7] as well as the *in vivo* efficacy in both a LNCaP xenograft mouse model of prostate cancer[20] or a highly metastatic human breast carcinoma xenograft model,[21] show that these PLGA-Pt(IV) nanosystems achieve an effect comparable to that of cisplatin but with fewer side effects.

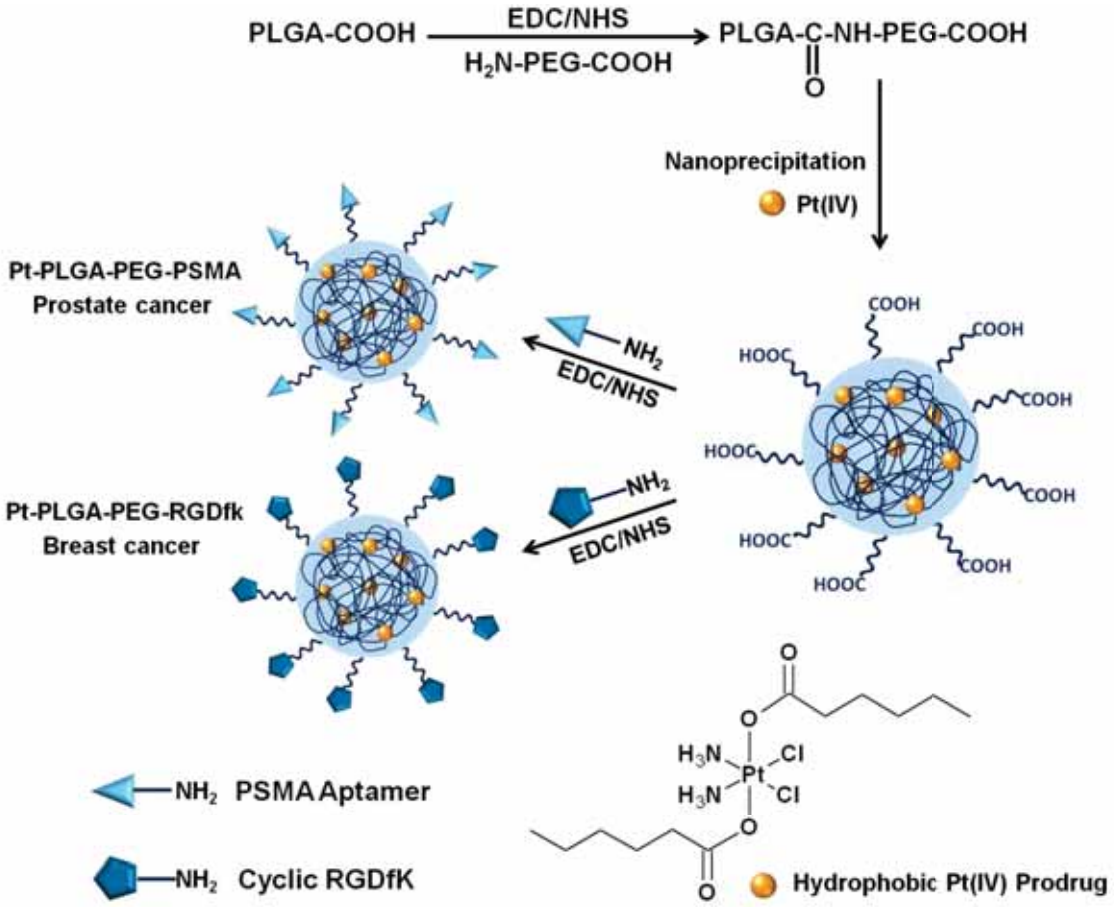

Figure 1. Scheme of the preparation of PMSA aptamer and c(RGDfK) functionalized Pt-PLGA-PEG nanoparticles.

The nanoparticle based delivery of hydrophilic platinum (IV) prodrugs has also been widely studied over the past decade. One of the first examples was reported by Lin and co-workers, who incorporated a succinate derivative platinum (IV) complex into

nanoscale coordination polymer nanoparticles formed with Tb^{3+}, and then stabilized the system by adding a silica shell as well as a RGD peptide for active targeting (Figure 2).[22]

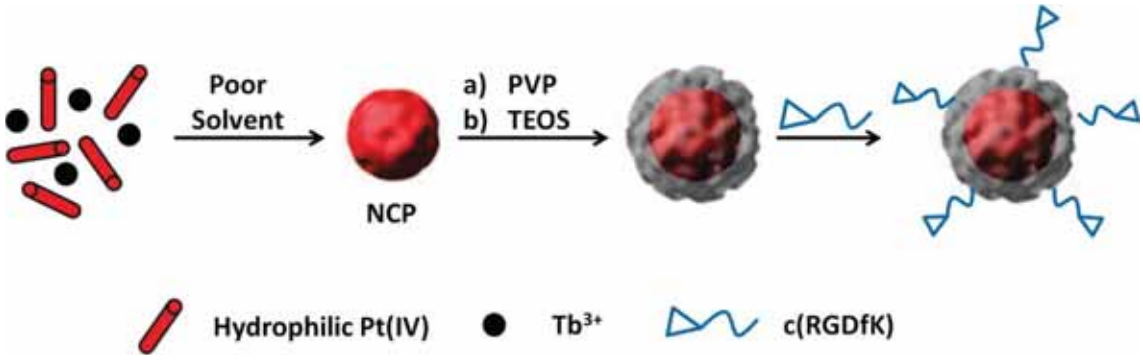

Figure 2. Schematic representation of the formation of platinum loaded nanoscale coordination polymer (NCP) nanoparticles and the incorporation of cyclic RGD for active targeting. Adapted from [22]

Another common approach is the covalent attachment of the prodrug to the nanoparticles; Min *et al.* and Dai *et al.* both reported the conjugation of the platinum (IV) complex to amine terminated PEG ligands on gold nanorods[6] and UCNPs[15] respectively, then achieving the liberation of the drug through the reductive elimination of the axial ligands. Chen *et al.* on the other hand performed a similar conjugation strategy using the free amine groups of gelatine-coated IONPs.[13] In addition to the traditional drug release mechanism based on intracellular reduction, Mareque and co-workers reported a photo-induced activation of a platinum (IV) prodrug through an electron transfer process using quantum dots.[16,17]

While the main strategies used for the nanoparticle based delivery of platinum prodrugs are encapsulation and covalent attachment through the axial ligands, this work is focused on exploiting the supramolecular chemistry of an anionic platinum prodrug to promote outer-sphere interactions with PEI as a novel approach in medicinal inorganic chemistry and nanomedicine. The next sections will examine the nature of the interactions and how they are applied for the delivery of a platinum (IV) prodrug using PEI-coated AuNPs as a novel approach to enhance the therapeutic efficacy in different cancer cell lines.

3.2 Results and Discussion

3.2.1 Synthesis and characterization of Pt-complexes

Given the importance and growing interest in the development of Pt(IV) prodrug based systems, different platinum based complexes have been synthesized for investigating their potential use in combination with nanoparticle based drug delivery systems. The synthetic procedures employed for the preparation of such complexes have already been reported in the literature.

As it was described by Hall *et al.*, the well known Pt(II) drug cisplatin yields the bis-hydroxy Pt(IV) complex (**3**) when subjected to oxidation with hydrogen peroxide.[23] Further treatment of (**3**) with an excess of succinic anhydride leads to the formation of the succinate derivative (**1**)[22] (Scheme 2), a Pt(IV) cisplatin prodrug which can be intracellularly reduced back to cytotoxic Pt(II) species. It is also important to mention that while the parent Pt(II) species are mainly soluble in organic solvents, the subsequent Pt(IV) complexes and specially (**1**) have a more hydrophilic nature, making them more promising for therapeutic applications.

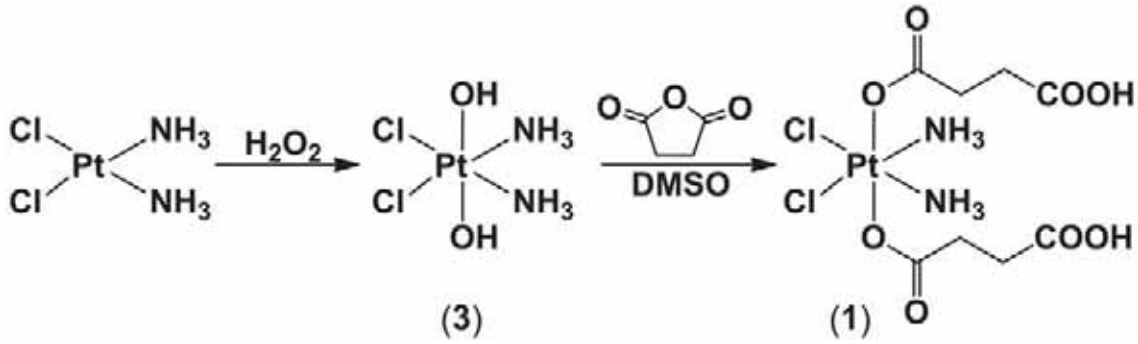

Scheme 2. Reaction scheme for the synthesis of the cisplatin derived Pt(IV) prodrug (**1**).

In order to later study the individual contribution of the different ligands around the platinum centre in the outer sphere interactions, a different Pt(IV) succinate derivative was also synthesized. Starting from another known Pt(II) drug, nedaplatin, a similar procedure leads to the formation of the succinate Pt(IV) complex (**2**) which has a glycolate ligand instead of the two chloro groups (Scheme 3).[24]

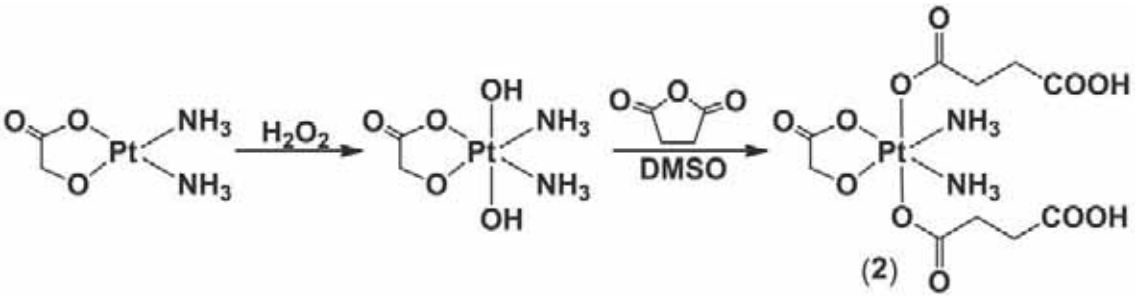

Scheme 3. Reaction scheme for the synthesis of the nedaplatin derived Pt(IV) prodrug (**2**).

The ^{1}H NMR spectrum of cisplatin (Figure 3A) shows the characteristic signal belonging to the protons of the amino groups appearing at high field. As shown in the subsequent spectra, this signal shifts downfield when the platinum centre is oxidized to the bis-hydroxo and then converted to the succinate derivative due to the lower shielding of these protons in each case. The presence of the hydroxyl ligands on (**3**) can be observed in the ^{1}H spectrum where the broad peak corresponding to these groups appears at ca. 10 ppm (Figure 4). The two characteristic triplets arising from the succinate ligands on (**1**) can also be clearly detected in the ^{1}H NMR spectrum (Figure 5), confirming the presence of the axial ligands in the complex. The chemical shift of the triplets from these succinic protons in (**1**) is also dependent on the pH (Figure 6).

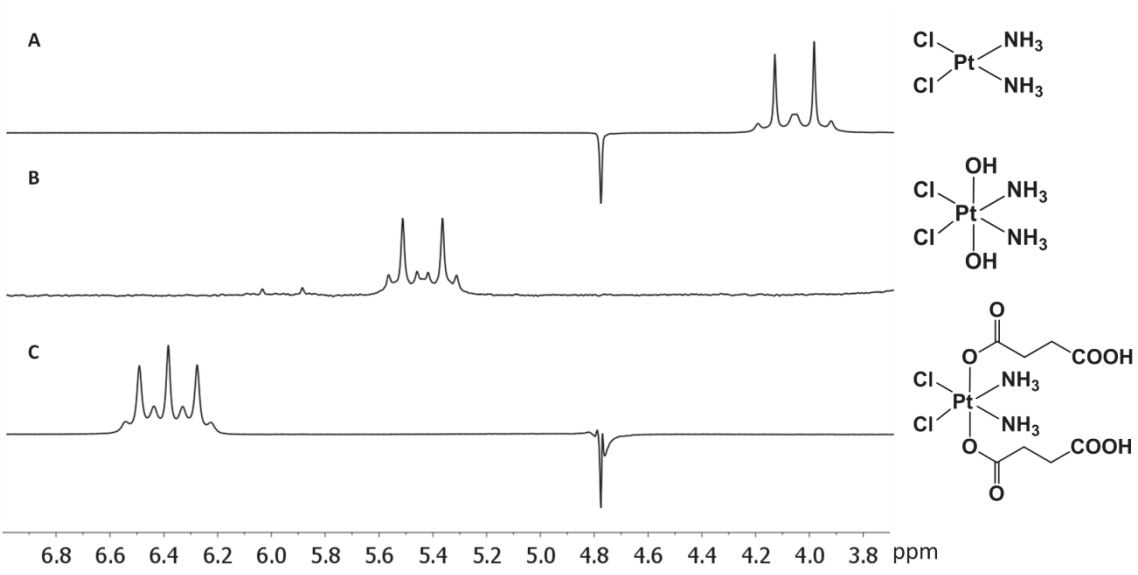

Figure 3. ^{1}H NMR spectra of cisplatin (**A**), (**3**) (**B**) and (**1**) (**C**) in 10% D_2O in H_2O showing the amino peaks.

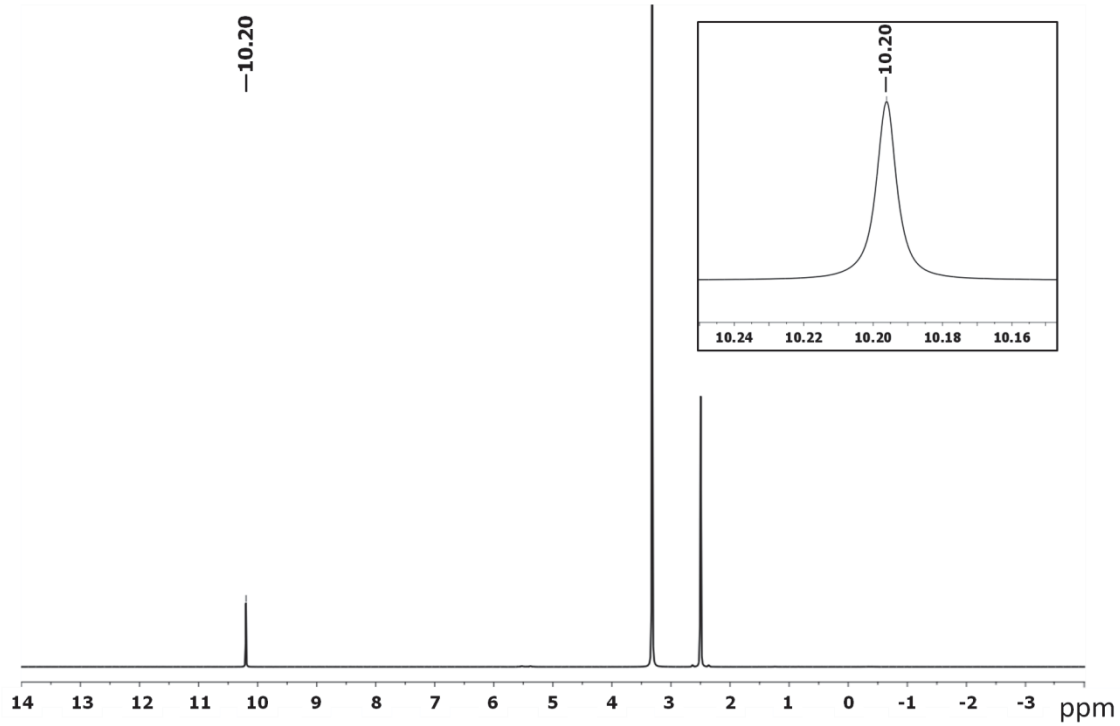

Figure 4. ^{1}H NMR spectrum (**3**) DMSO-d6 and detail of the OH peak (*inset*).

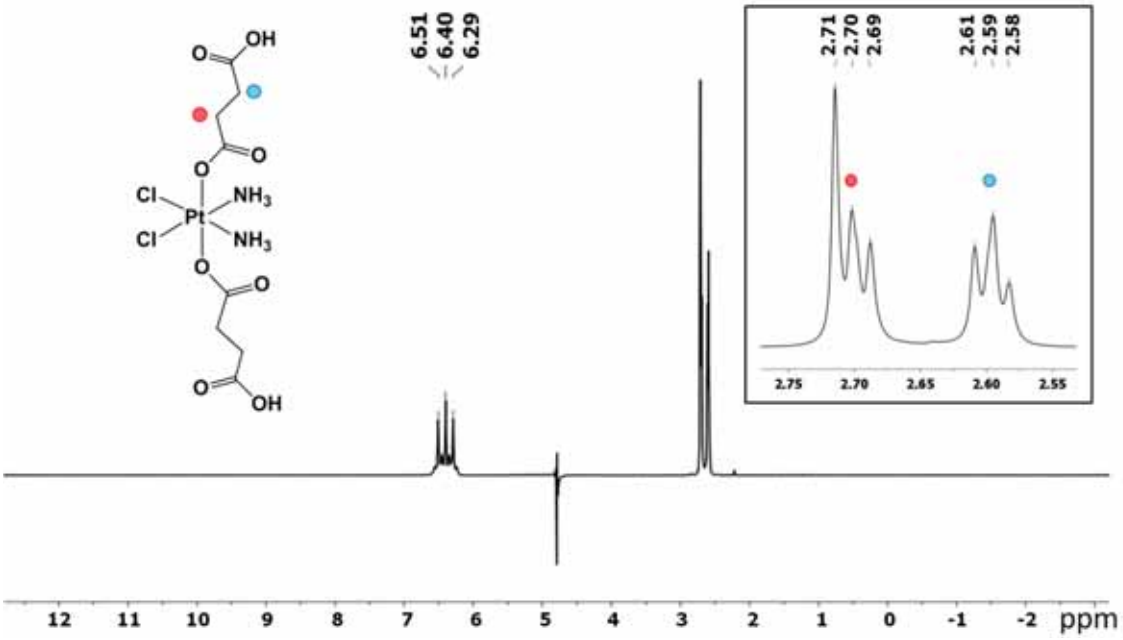

Figure 5. Structure and 1H NMR spectrum of (**1**) in 10% D2O in H2O and detail of the peaks from the succinic protons (*inset*)**.**

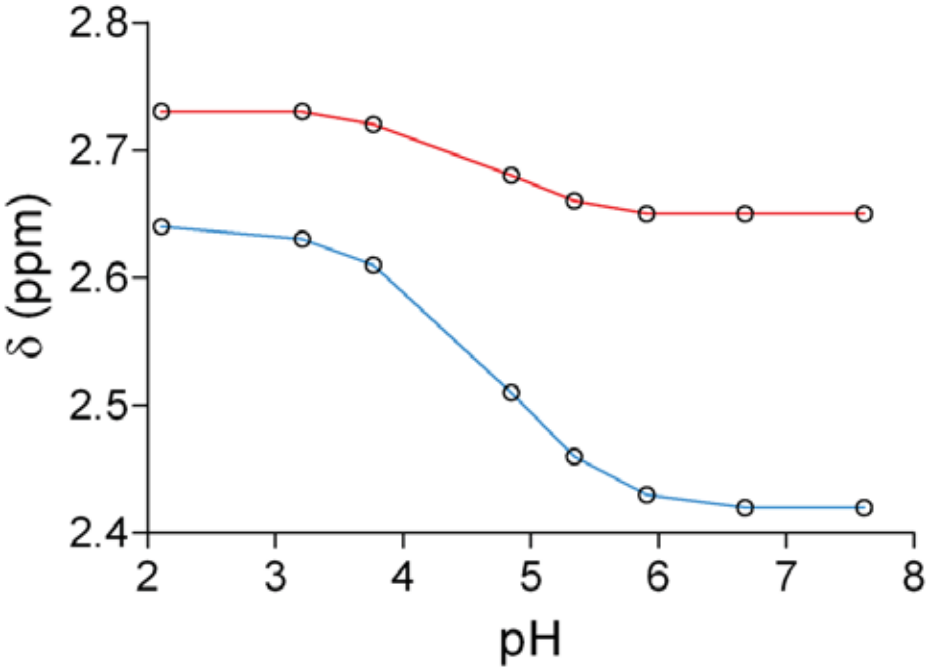

Figure 6. pH dependent variation in the chemical shift of the succinic protons of (**1**)

In the case of the nedaplatin succinate Pt(IV) complex (**2**) the ^{1}H NMR spectrum is characterized by the peaks from the succinate ligands and the singlet corresponding to the glycolic protons (Figure 7).

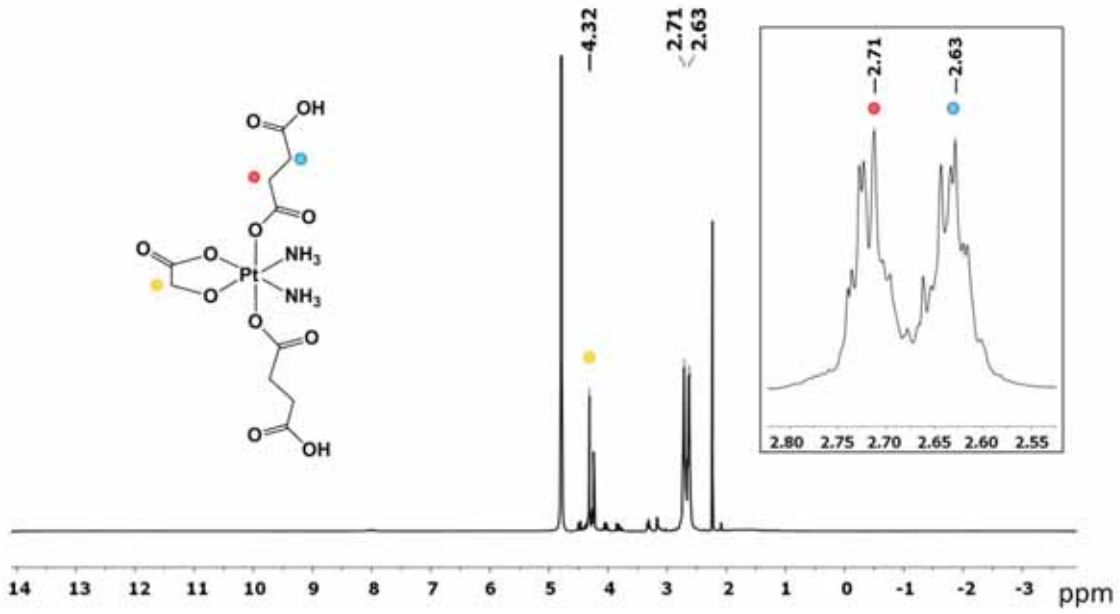

Figure 7. Structure and ^{1}H NMR spectrum of (**2**) in D_2O and detail of the peaks from the succinic protons (*inset*).

3.2.2 Outer sphere interaction between Pt-complexes and PEI

Transition metal complexes can participate in a wide range of outer-sphere or second coordination sphere interactions. Although exploiting these interactions is becoming increasingly useful in a growing number of fields[25–28] it has not been applied to develop more efficient platinum-based drugs.

The previously described platinum (IV) complex (**1**) was selected because apart from being considered a prodrug for the archetypical drug cisplatin, it is stable enough to travel through the bloodstream until it reaches a tumour cell without premature decomposition.[1] Apart from that, it also presents excellent features to participate in multiple non-covalent outer-sphere interactions with PEI as all ligands can contribute to the outer-sphere interaction (Figure 8). In addition to the two carboxylates that give an overall -2 charge at neutral pH to provide strong electrostatic attraction with the positively charged PEI polymer, (**1**) has two *cis*-chloro ligands which have been shown to be excellent hydrogen bond acceptors.[29,30] Additionally, the two amines should have enhanced acidity to act as hydrogen bond donors through coordination to the high valent Pt(IV) centre and N-H●●●Cl-Pt hydrogen bonding.[31,32]

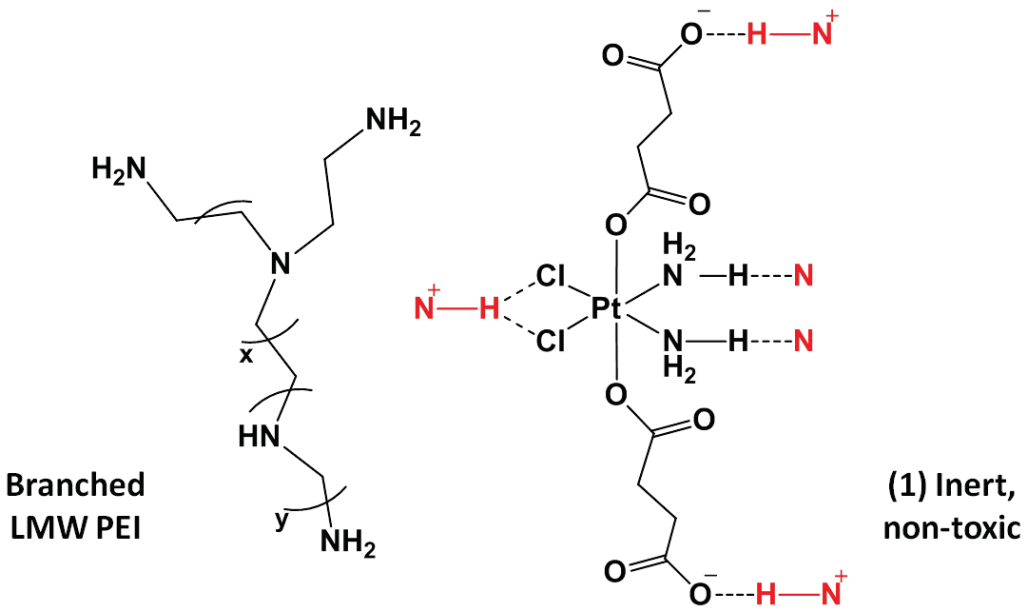

Figure 8. Structure of PEI and (**1**) and the plausible supramolecular synthons involved in the formation of PEI-(**1**) outer-sphere complexes.

In order to evaluate the proposed interaction, NMR studies were carried out in mixtures of (**1**) and PEI with or without the presence of a biologically relevant reducing agent, ascorbate. ^{1}H NMR spectra of the mixtures were recorded at different pH to also determine the stability of the interaction in different conditions.

Consistent with the postulated mechanism of action of (**1**) as a prodrug, addition of ascorbate results in the appearance of a peak due to free succinic acid in a time-dependent manner (Figure 9). Notably, the intensity of this peak is higher in the presence of PEI. When the pH of the solution is adjusted from pH 3-4 to pH 7, the effect of PEI towards promoting the release of succinate is even more pronounced, suggesting that the interactions of (**1**) with PEI are optimum at neutral pH.

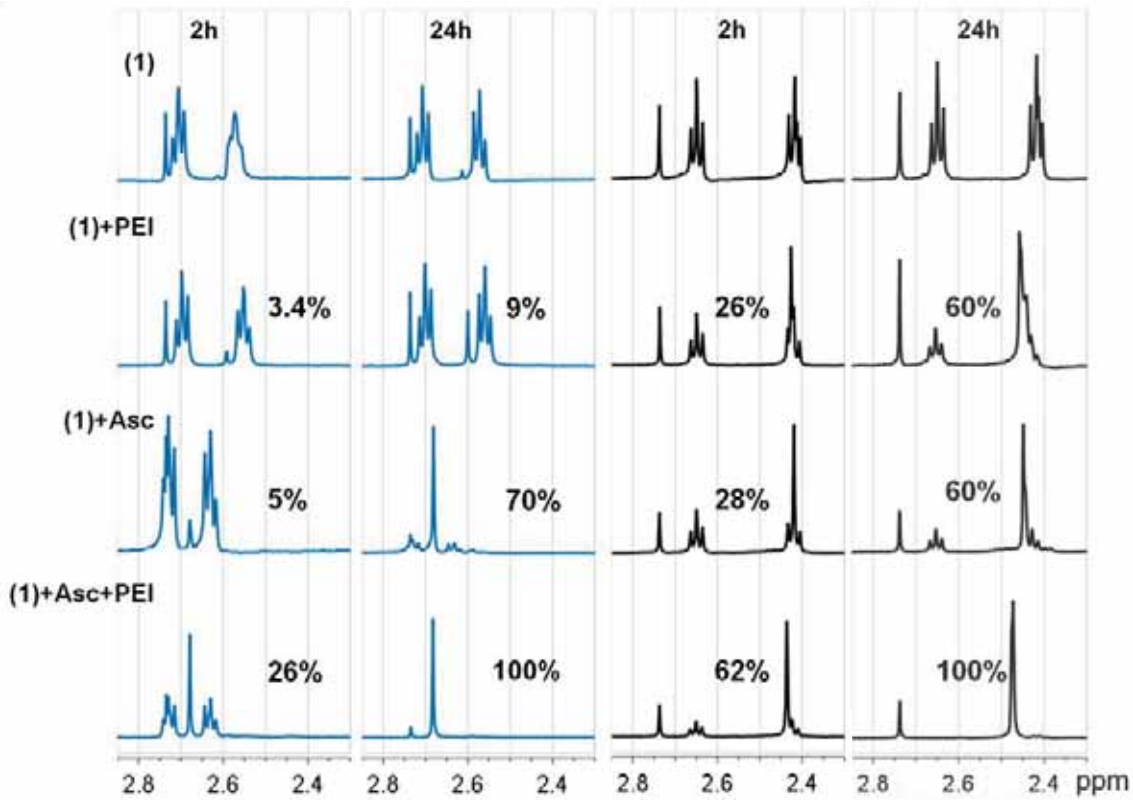

Figure 9. Changes in the ^{1}H NMR spectrum of (**1**) (1 mM) on D_2O at pH 3-4 (blue) and pH 7 (black) in the presence and absence of PEI (10 μM) and ascorbic acid (10 mM).

In view of the pK_a values reported for branched PEI (4.5 for primary, 6.7 for secondary and 11.6 for tertiary amine groups)[33] and succinic acid (4.2 and 5.6) it is obvious that at pH < 4 PEI and (**1**) will exist in their fully protonated forms. At these pH values, the

terminal carboxylates of (**1**) are protonated, and therefore, the neutral Pt(IV) complex interacts less strongly with the cationic PEI. Moreover, it is reasonable to expect that at this pH protonation of the N atoms of the PEI may also be preventing the formation of Pt-NH_3●●●N hydrogen bonding interactions. In contrast, at pH 7 the succinic acid groups of (**1**) are deprotonated and only a fraction of the N atoms are protonated (ca. 35%), making feasible the formation of the different synergistic outer-sphere interactions. As it can be expected from the release of succinic acid and the "proton sponge" properties of PEI, over time the pH of the mixture becomes more acidic (pH 5.5 at 24 h). Although the ability of PEI to promote the efficient internalization and trafficking of drugs by cancer cells is already well known, based on these results PEI as delivery vehicle for Pt(IV) prodrugs can also contribute to the redox-activation process.

Cyclic voltammetry measurements in PBS (pH 7.4) also demonstrate that the interaction with PEI leads to a shift in the reduction potential of (**1**) by as much as +500 mV (Figure 10). This change is not only indicative of the direct influence of multiple H-bonding interactions,[34] but also of the fact the PEI is able to activate the platinum prodrug making it easier to reduce.

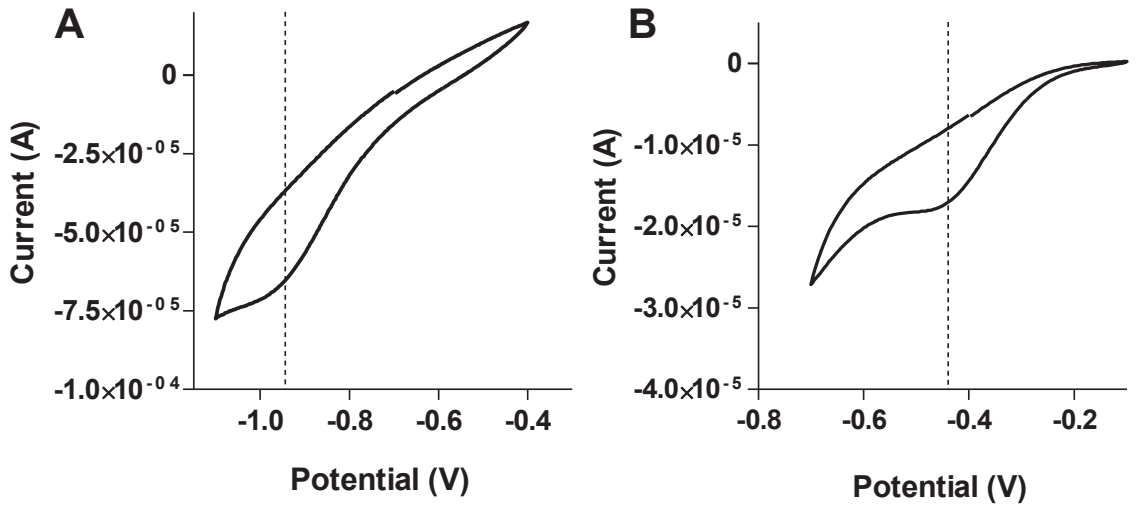

Figure 10. Cyclic voltammograms of (**1**) (**A**) and (**1**) in the presence of PEI (**B**) in PBS 10 mM pH 7.4 (scan rate = 100 mV/s).

To elucidate the oxidation state of the platinum products, XPS measurements

at the Pt 4f region were performed (Figure 11). The spectrum of (**1**) presents peaks at 78.9 ± 0.2 eV ($4f_{5/2}$) and 75.5 ± 0.2 eV ($4f_{7/2}$) but after the addition of ascorbate shows the progressive appearance of new species being generated, with peaks at 76.4 ± 0.3 eV ($4f_{5/2}$) and 73.1 ± 0.3 eV ($4f_{7/2}$) indistinguishable from those of cisplatin.

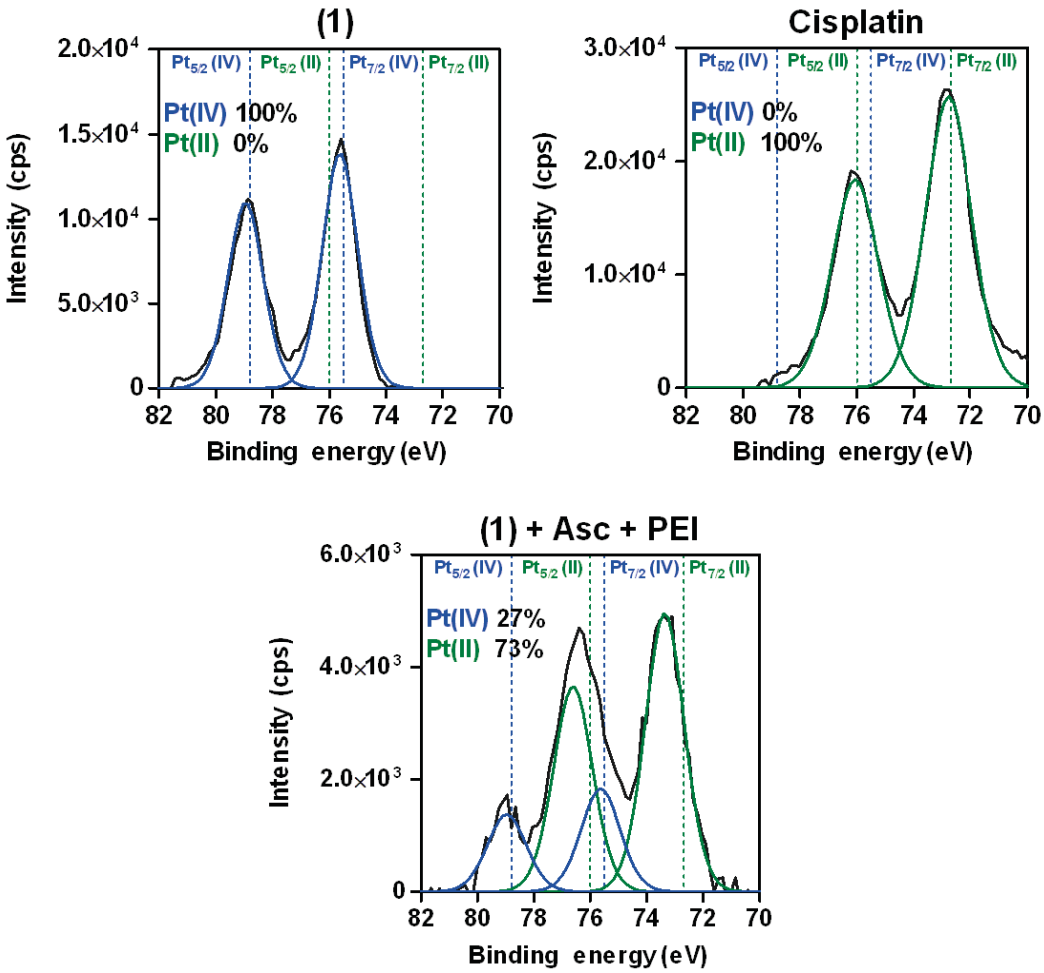

Figure 11. XPS spectra showing the Pt 4f region of (**1**), cisplatin and PEI-(**1**) outer sphere complexes in the presence of ascorbic acid 24 h after mixing in water at pH 7.

Notably, the proportion of Pt(II) species calculated from the XPS data is somewhat lower than it would correspond compared to the amount of free succinate determined by NMR. This results indicate that some succinate can indeed be liberated from (**1**) without reduction. This is an important finding in agreement with recent studies that show how although the design of Pt(IV) prodrugs is based on the assumption that the cytotoxic Pt(II) drug is obtained by clean loss of the two axial ligands, these assumptions need to be reassessed as other products can also be formed.[35]

3.2.3 Interaction between Pt-complexes and PEI-AuNPs

Having analyzed the nature of the interactions between the platinum complex (**1**) and PEI, PEI-coated AuNPs were incorporated to act as delivery vehicles to try to maximize the cancer cell killing ability of the prodrug. Taking advantage of the ability of this LMW PEI not only to form the outer-sphere complex with (**1**) but also to act as the reducing and stabilizing agent for the preparation of AuNPs, PEI-coated AuNPs were prepared for the delivery of (**1**). The use of this nanoparticle based system for the successful delivery of a chemotherapeutic agent, poly(I:C), has already been described in the previous chapter. Employing similar PEI-AuNPs for the delivery and activation of the Pt(IV) prodrug (**1**) will not only prove the versatility of these NPs as drug delivery systems, but also exploit a novel approach taking advantage of outer-sphere interactions between PEI and the platinum prodrug.

The PEI-AuNPs were synthesized similarly to what has already been described in Chapter 2, following a single step reaction between the PEI and an aqueous solution of $HAuCl_4$ at 90 ºC to form stable water soluble PEI-coated AuNPs. The PEI-AuNPs used in this study presented a plasmon band at 521 nm (Figure 12). Transmission electron microscopy studies (TEM) confirmed the non-aggregated and spherical nature of the PEI-AuNPs having in this case a core size of 9.8 ± 1.8 nm (Figure 13).

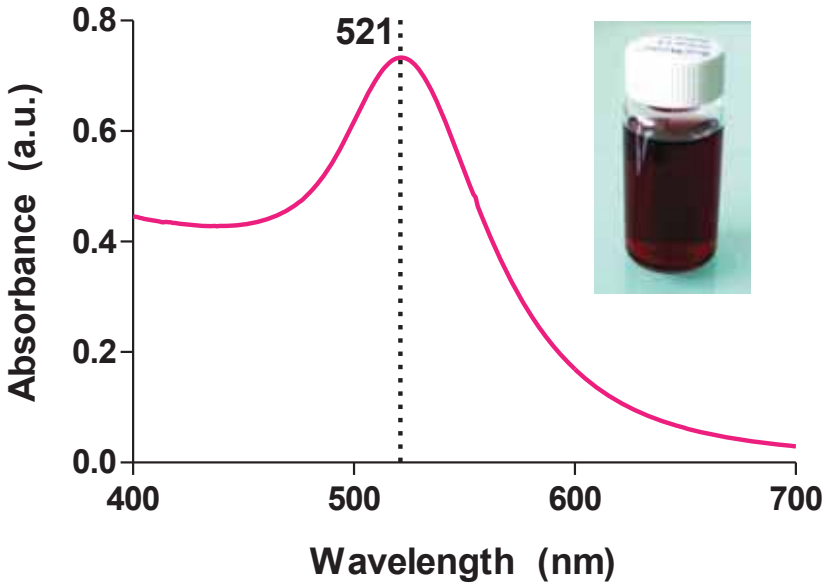

Figure 12. UV-vis spectrum of the synthesized PEI-AuNPs showing the SPR band at 521 nm with a representative photograph of the PEI-AuNPs in water (inset).

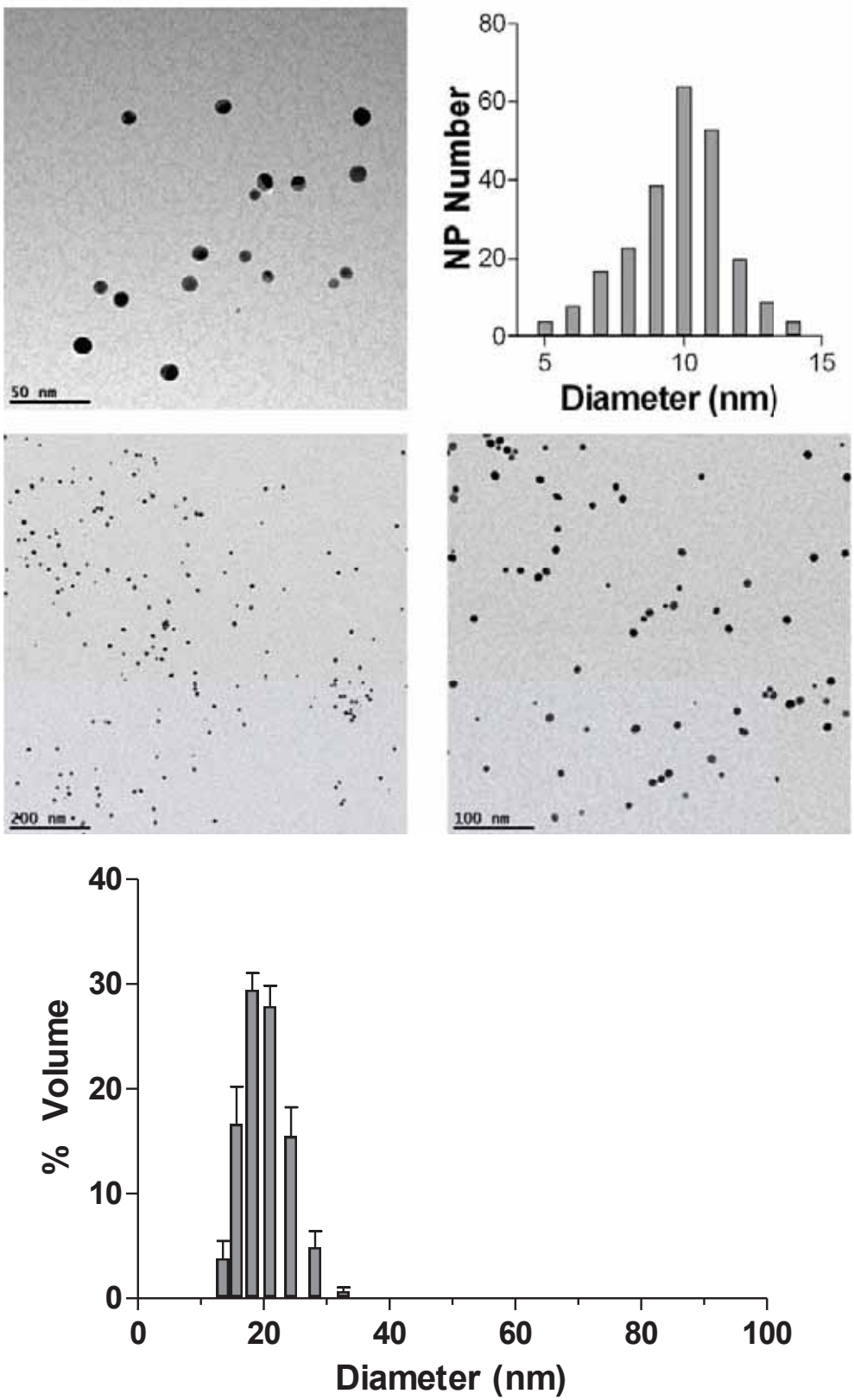

Figure 13. (*top*) Representative low and high magnification TEM images and size distribution histogram of PEI-AuNPs showing an average diameter of 9.8 ± 1.8 nm. (*bottom*) Hydrodynamic diameter of the synthesized PEI-AuNPs.

The hydrodynamic diameter of the PEI-AuNPs in water was measured by dynamic light scattering (DLS). The nanoparticles had an average diameter of 19.9 ± 1.1 nm with relatively narrow size distribution (polydispersity index (PDI) = 0.331 ± 0.035) (Figure 13). The zeta potential studies confirmed the presence of the positively charged PEI on the AuNPs (zeta potential = +34.15 ± 0.48 mV). After the addition of (**1**) to the positively charged nanoparticles (at 100 μM Au and 1 mM Pt), the surface charge of the PEI-AuNPs changed to less positive values (zeta potential= +13.70 ± 0.52 mV) confirming the interaction.

3.2.4 Intracellular delivery studies

3.2.4.1 Synthesis of FITC-labelled PEI-AuNPs

To investigate the cellular internalization behaviour of these PEI-AuNPs, the PEI was modified to incorporate fluorescein isothiocyanate (FITC) as described in previous literature.[36] After the modification, the FITC-labelled PEI was used to synthesize the fluorescent PEI-AuNPs similarly to the non-labelled ones. To confirm the presence of the FITC in the purified PEI-AuNPs, the absorption and fluorescence emission spectra were recorded (Figure 14).

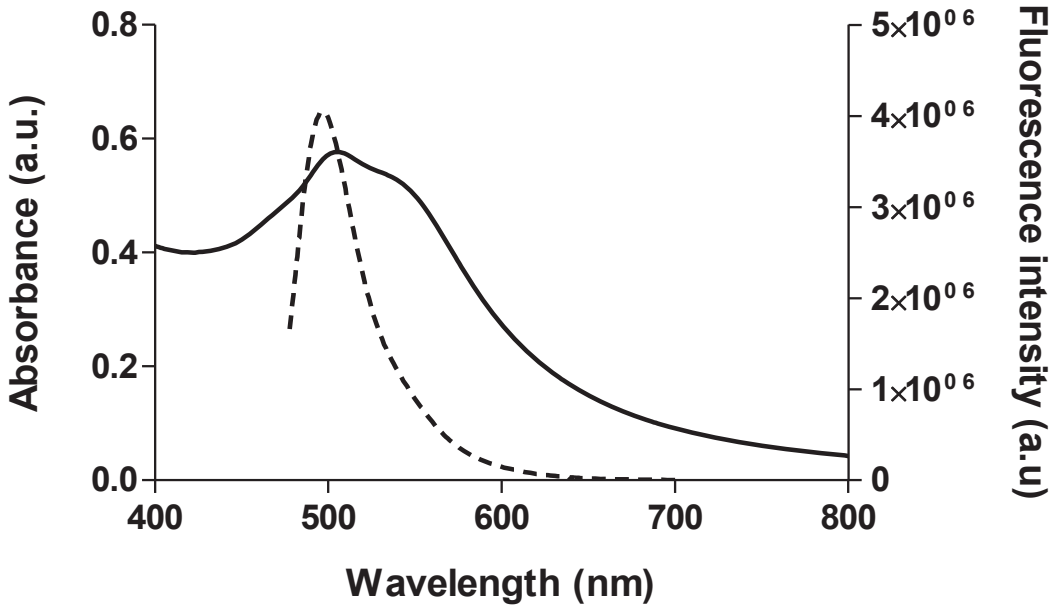

Figure 14. UV-vis absorption (continuous line) and fluorescence emission (dashed line) spectra of the FITC-labelled PEI-AuNPs.

Despite the overlap between the AuNP plasmon band and the absorption spectrum of the fluorophore, the band corresponding to the FITC can be observed at 505 nm in the UV-vis spectrum of the FITC-labelled PEI-AuNPs. The fluorescence emission spectrum of the system also confirms the presence of FITC, hence the effective labelling of the system, showing the characteristic green fluorescence band of the fluorescein.

3.2.5 Flow cytometry and fluorescence microscopy

The fluorescently labelled material was used to study the cellular uptake by PC-3 human prostate cancer cells using both live cell fluorescence microscopy and fluorescence activated cell sorting (FACS) (Figure 15).

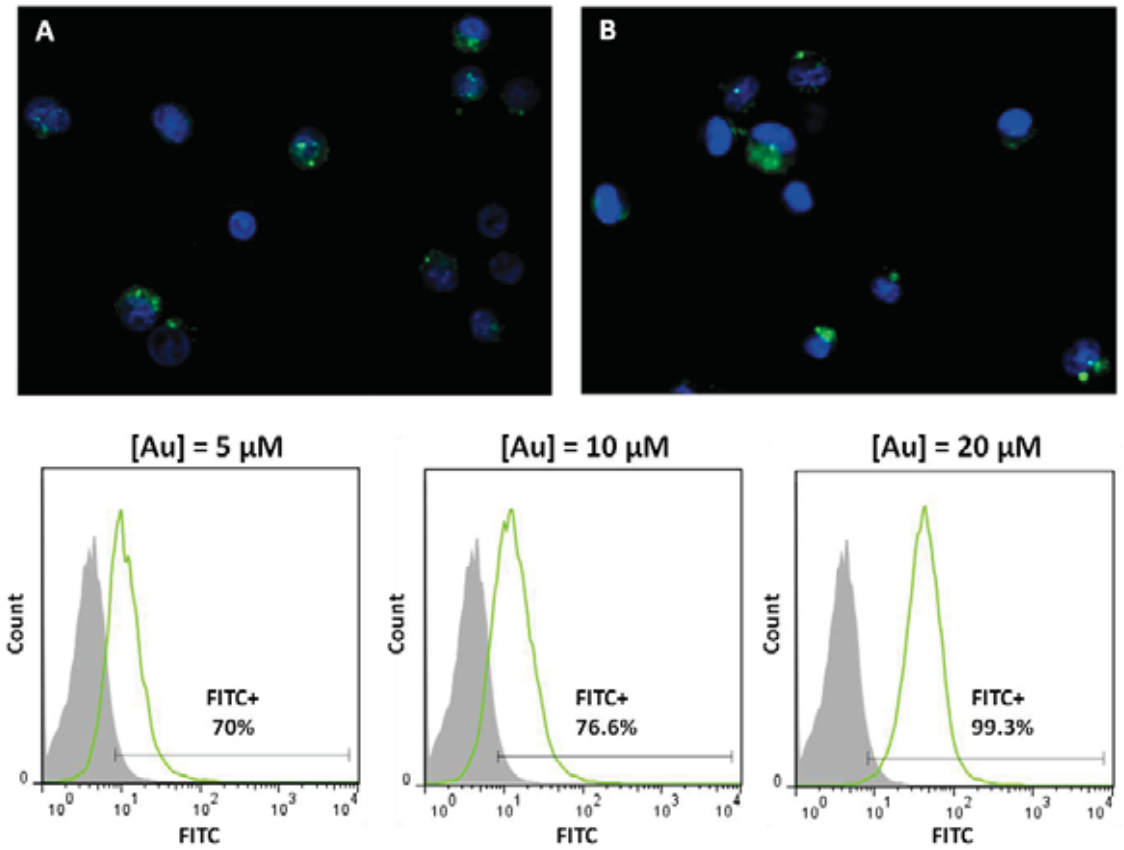

Figure 15. Fluorescence microscopy images taken of live PC-3 cells after 45 min incubation with FITC-PEI-AuNPs (**A**) and FITC-PEI-AuNPs/(**1**) complexes (green) (**B**). The nuclei are stained with Hoechst 33342 (blue). Flow cytometry histograms of PC-3 cells incubated with FITC-PEI-AuNPs for 45 min at different gold concentrations (green line) and non treated controls (solid grey peak).

The uptake of PEI-AuNPs with and without (**1**) can be clearly seen in the live cell fluorescence images, where after 45 min incubation, the green fluorescence due to the FITC appears in the cytoplasmic region of the cells (nuclei stained in blue). FACS experiments also corroborate the rapid uptake of the AuNPs incubated at three different concentrations.

3.2.6 In vitro cell killing efficacy

In vitro studies were carried out to prove the feasibility of using both the non toxic LMW PEI polymer and PEI-coated AuNPs to achieve intracellular delivery and activation of (**1**). The ability of these novel outer-sphere coordination complexes to kill different human cancer cells was studied. Apart from the highly aggressive prostate cancer cell line PC-3, two other clinically relevant cells were selected to test the cancer cell killing efficacy of the system, a cisplatin resistant human breast cancer cell line (MDA-MB231) and the pancreatic cancer cell line PANC-1, a type of cancer known to have a particularly poor prognosis.

3.2.6.1 Cytotoxicity of PEI-Pt outer-sphere complexes

First the cytotoxicity profile of the LMW PEI vehicle was determined in the three cell lines selected (PC-3, MDA-MB231 and PANC-1), and as it can be observed in the graph below (Figure 16) for each cell line there is a wide range of concentrations where the PEI vehicle causes no significant cytotoxicity.

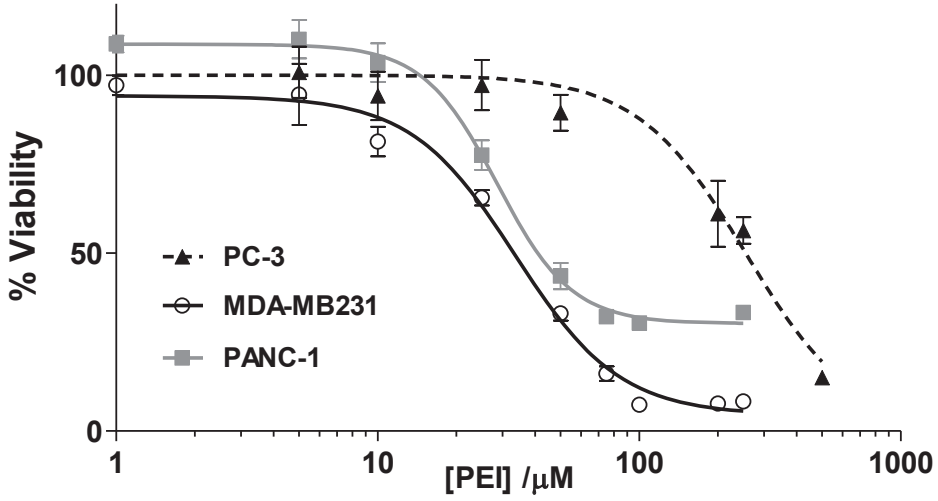

Figure 16. Cytotoxicity profiles PEI PC-3, MDA-MB231 and PANC-1 cell lines.

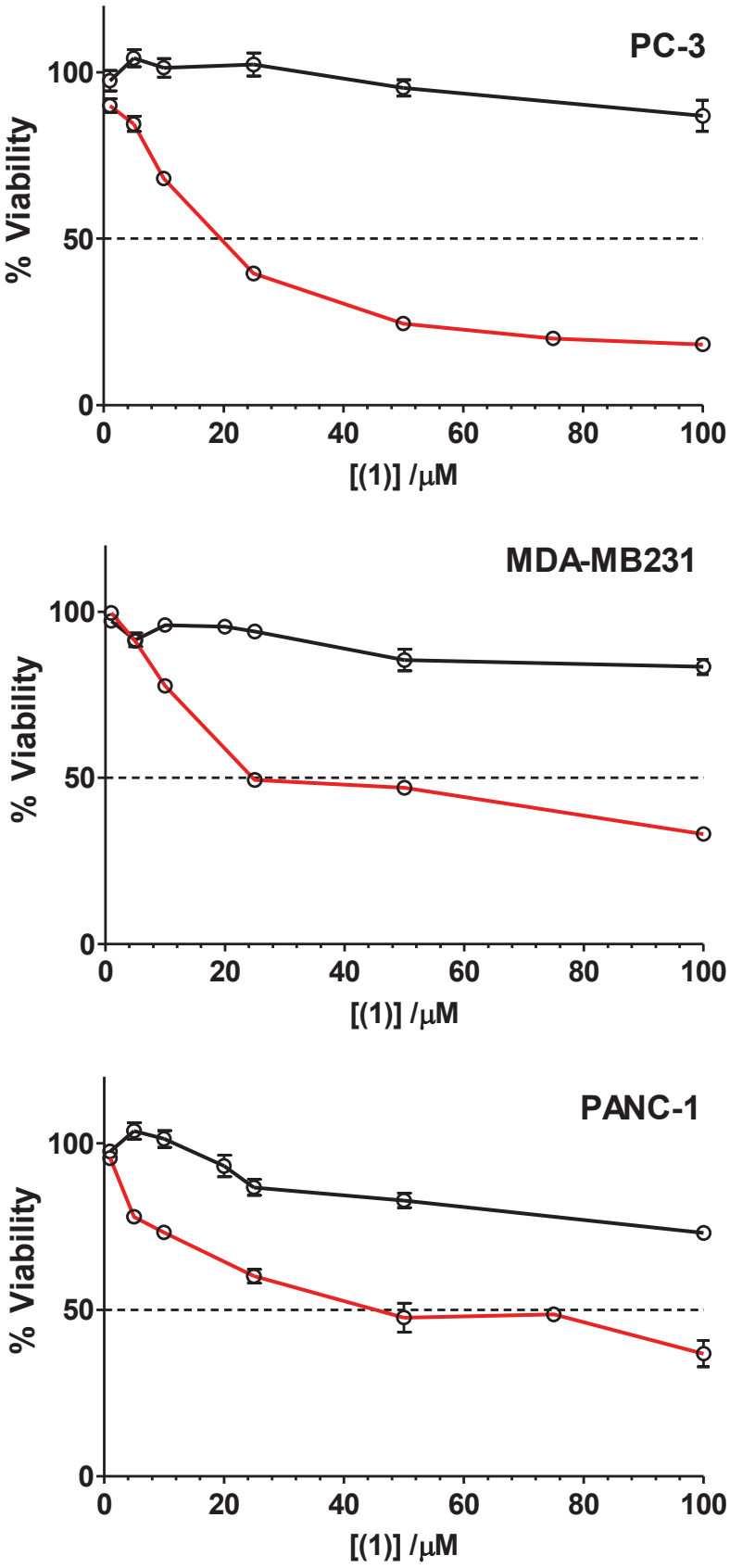

Figure 17. Cytotoxicity profiles of PEI-(**1**) mixtures (red) and (**1**) (black) in PC-3, MDA-MB231 and PANC-1 cell lines ([PEI] = 1 μM).

As well as the LMW PEI, the prodrug (**1**) also proved to be non toxic in all the cell lines over a broad range of concentrations. When combined however, the cell killing ability of the prodrug (**1**) was clearly enhanced in all three human cancer cell lines (Figure 17), indicating the validity of the outer-sphere approach to enhance the cancer cell killing ability of the platinum prodrug (**1**).

To elucidate the relative importance of each of the ligand types present in the inner-sphere of (**1**) towards promoting the outer-sphere interactions with the PEI polymer and the consequent cytotoxicity, two other Pt(IV) complexes, *c,c,t*-$[Pt(NH_3)_2(OCH_2CO_2)(O_2CCH_2CH_2CO_2)_2]^{2-}$ (**2**) and *c,c,t*-$[Pt(NH_3)_2Cl_2(OH)_2]$ (**3**) were also investigated (Figure 18). The nedaplatin derivative (**2**) will help determining the role of the *cis*-chloro ligands, while the neutral complex (**3**) will be used to assess the importance of the negatively charged axial succinate ligands.

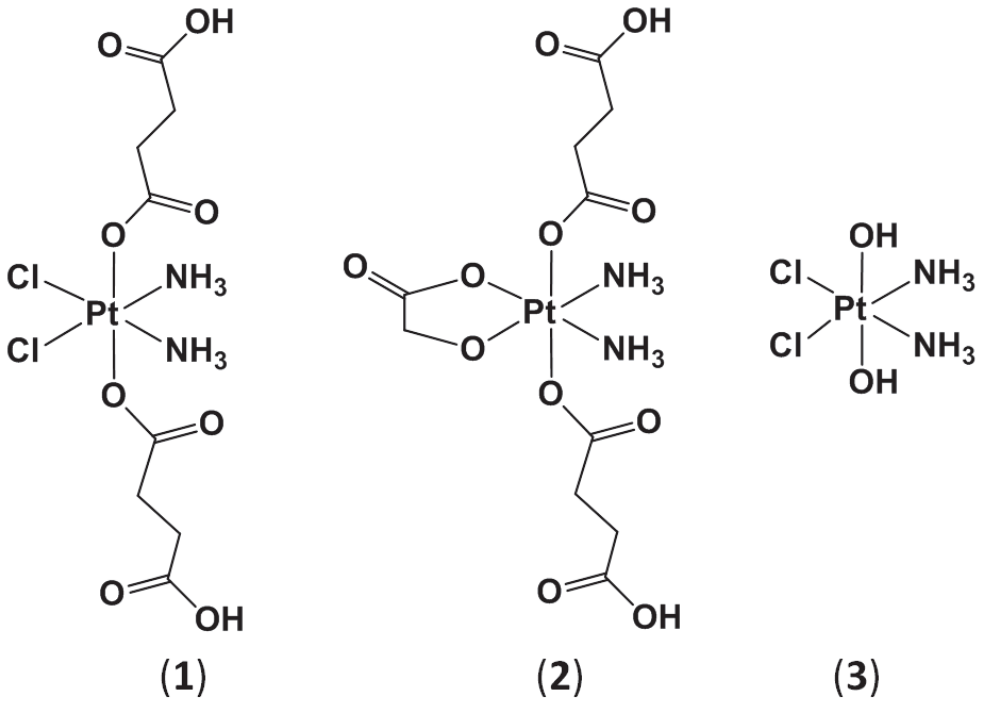

Figure 18. Structures of the platinum complexes (**1**), (**2**) and (**3**).

In contrast to the results with the prodrug (**1**), PEI had no effect on the cancer cell killing ability of the neutral complex (**3**) (Figure 19). In agreement with the NMR studies, this result suggests that the interactions arising from the anionic succinate ligands are crucial for stabilizing the PEI-(**1**) outer-sphere complexes. To elucidate the

importance of the chloro ligands, complex (**2**) was tested in a similar manner. The addition of PEI only increased the cytotoxicity of (**2**) in MDA-MB231 cells and the effect was not as notable as for (**1**). Thus, it becomes clear that interactions with the two *cis*-chloro ligands are also important in promoting the formation of the PEI-(**1**) outer-sphere complexes.

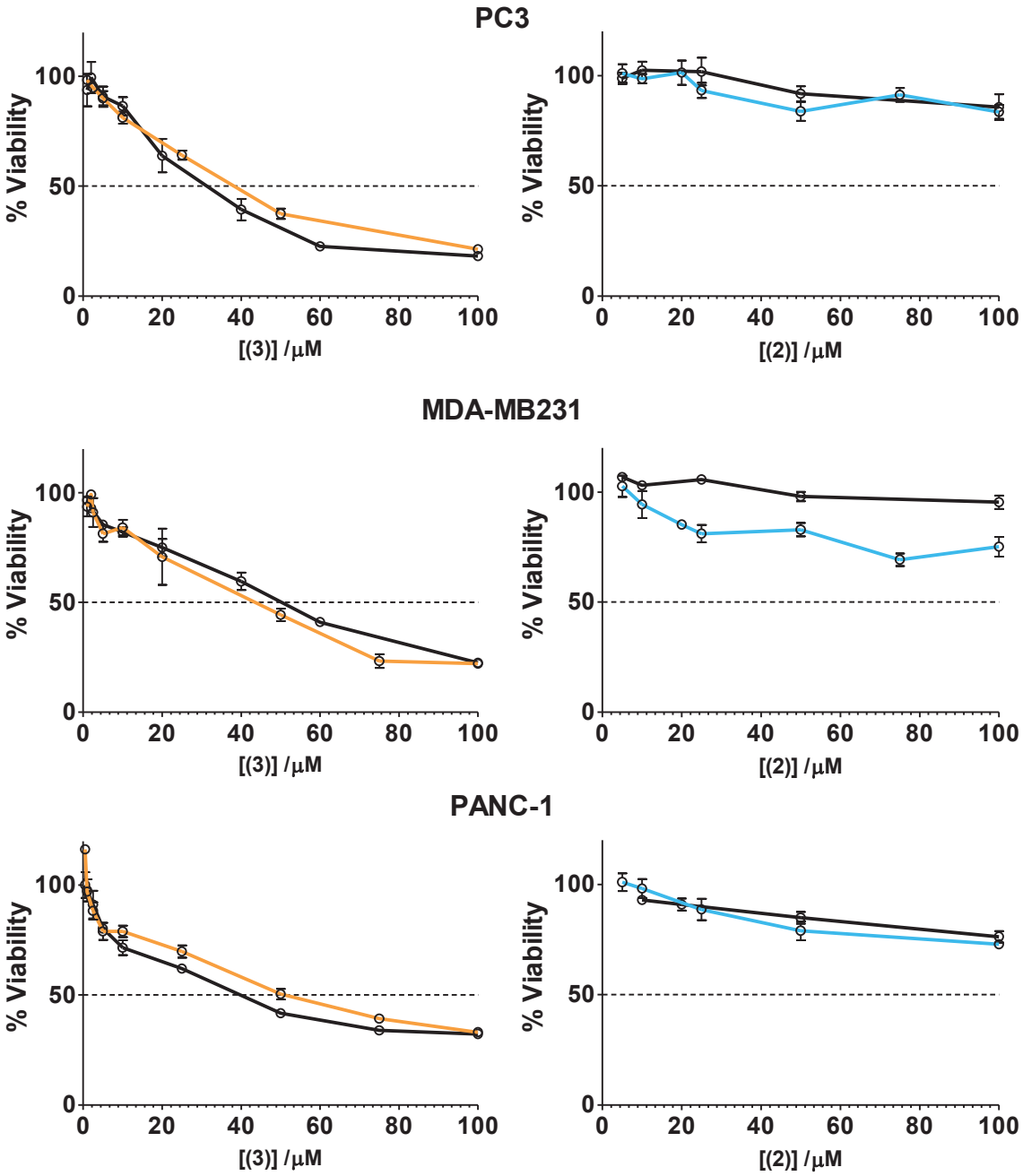

Figure 19. Cytotoxicity profiles of PEI-(**3**) mixtures (orange) and (**3**) (black) in PC-3, MDA-MB231 and PANC-1 cell lines (left column) and cytotoxicity profiles of PEI-(**2**) mixtures (blue) and (**2**) (black) in PC-3, MDA-MB231 and PANC-1 cell lines (right column) ([PEI] = 1 μM).

3.2.6.2 Cytotoxicity of PEI-AuNP-Pt

Having determined that both the chloro and the axial succinate ligands are crucial for the outer-sphere complex to promote cancer cell death, the prodrug (**1**) was selected to take the system a step further by incorporating the AuNP delivery system. The ability of the PEI-AuNPs to deliver and activate the Pt(IV) (**1**) was studied in the aforementioned cancer cell lines. As shown in Figure 20, the efficacy of the outer-sphere complex in the presence of the AuNP is similar to that of the PEI-(**1**) combination in PC-3 cells but increased for both MDA-MB231 and PANC-1 cells lines. These results prove that the PEI-coated AuNPs can be successfully used to enhance the cancer cell-killing ability of the Pt(IV) prodrug (**1**) through outer sphere coordination interactions with the PEI.

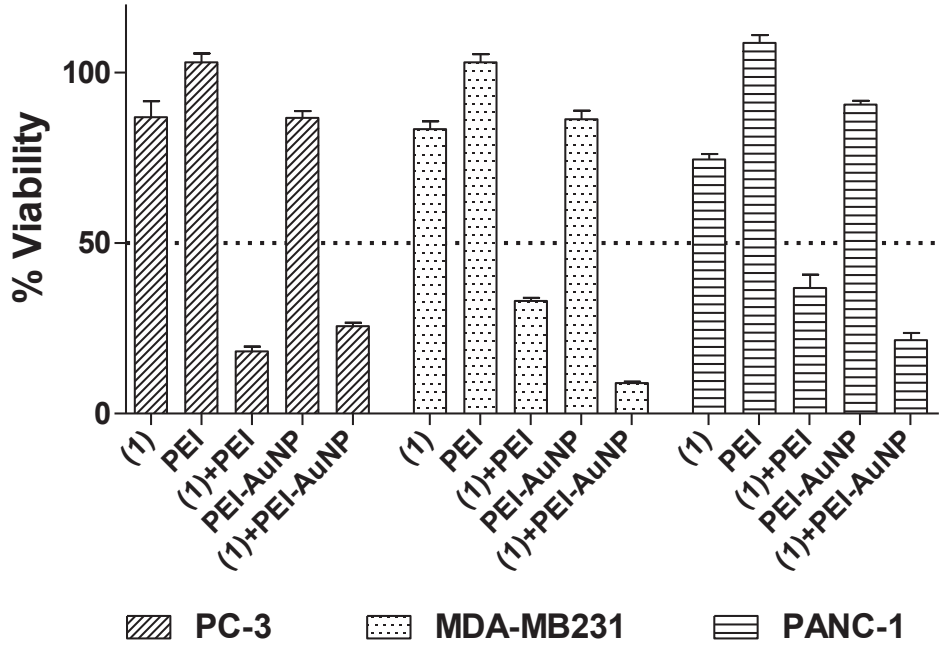

Figure 20. Cytotoxicity of PEI, PEI-AuNPs, PEI-(**1**) and PEI-AuNP-(**1**) outer-sphere complexes in PC-3, MDA-MB231 and PANC-1 cells after 72h. [(**1**)] = 100 μM, [PEI] = 1 μM, [Au(0)] = 10 μM.

3.3 Conclusions

In conclusion, this work demonstrates the applicability of outer-sphere coordination chemistry to promote intracellular delivery and activation of a Pt(IV) prodrug using a non toxic LMW PEI. The PEI-Pt(IV) prodrug outer sphere complex is promoted by interactions with each of the first coordination sphere ligands, and results in more facile reduction to Pt(II), succinate release and significantly enhanced cytotoxicity in several human cancer cell lines.

The significance of these findings lies in the wide range of available PEI-derived compounds and PEI-modified drug delivery vehicles as well as Pt(IV) prodrugs which can be used for tuning and applying successfully this novel outer-sphere coordination chemistry approach for clinical applications. Delivering and activating the Pt(IV) prodrugs with PEI-coated AuNPs in particular, opens up fascinating opportunities to combine synergistically gene therapy with chemotherapy, and chemotherapy with radiotherapy or PTT. Moreover, similarly to in Chapter 2, the incorporation of the AuNP and the already proved suitability of gold based nanomaterials as X-ray and multimodal contrast agents provides the potential for monitoring the efficacy of tumour delivery and the therapeutic response using current clinical molecular imaging approaches.

3.4 Experimental Section

3.4.1 Materials

All syntheses were carried out with the following commercially available reagents used without further purification. Potassium tetrachloroplatinate(II) (99%) was purchased from Precious Metals Online. Polyethyleneimine (branched, 1.8 kDa, 99%; 36% NH_2, 29% NH and 35% N determined by NMR studies) was purchased from Alfa Aesar. Hydrogen tetrachloroaurate(III) trihydrate (99.99%), succinic anhydride (99%), potassium iodide (≥ 99.5%), potassium chloride (≥ 99.0%), silver nitrate (≥ 99.0%), hydrogen peroxide solution 30% (w/w) in H_2O, ammonium hydroxide solution (30-33% NH_3 in H_2O), glycolic acid (99%), L-ascorbic acid (> 99.5%), fluorescenin isothiocyanate (FITC, isomer I), sulforhodamine B sodium salt and trichloroacetic acid (> 99%) were purchased from Sigma Aldrich.

3.4.2 Synthesis of Pt-complexes

Cisplatin was synthesized as described previously.[37] Briefly K_2PtCl_4 (1.5 g, 3.6 mmol) was dissolved in water (15 mL) and KI (2.49 g, 15 mmol) was added and the mixture was stirred at room temperature for 10 minutes. A solution of NH_4OH:H_2O (1:1, 1.2 mL) was added and the mixture was stirred for further 30 minutes. The precipitate ([$Pt(NH_3)_2I_2$]) was filtered, washed and dried (1.15 g, 2.38 mmol, 66.0%). To this complex, $AgNO_3$ (0.79 g, 4.65 mmol) and water (36 mL) were added and the mixture was stirred at 70 ºC for 1 h 30 min. After that the mixture was filtered and the filtrate collected. KCl (0.39 g, 5.23 mmol) was added to the filtrate and stirred at 70 ºC for 1 h. The resulting yellow precipitate, cisplatin, was filtered, washed with cold water and dried (517 mg, 47.9%).

c,c,t-[$Pt(NH_3)_2Cl_2(OH)_2$] (**3**) was prepared as previously described.[23] Briefly a cisplatin suspension (0.18 g, 0.6 mmol) was prepared in water (1.5 mL) and H_2O_2 (9 mL, 30%) added. The mixture was left stirring at 50 ºC for 3 h and then cooled down overnight. The product was filtered and washed with cold water and ethanol and dried (163 mg, 81.3%).

c,c,t-[$Pt(NH_3)_2Cl_2(O_2CCH_2CH_2CO_2H)_2$ (**1**) was prepared as previously described.[22] Briefly *c,c,t*-[$Pt(NH_3)_2Cl_2(OH)_2$] (163 mg, 0.49 mmol) and succinic anhydride (195 mg, 1.95 mmol) were dissolved in DMSO (1 mL) and stirred at 70 ºC for 24 h. After the addition of water (5 mL) the reaction mixture was lyophilized and the resulting solid washed several times with ice cold acetone (172 mg, 65.8%).

c,c,t-[$Pt(NH_3)_2(OCH_2CO_2)(O_2CCH_2CH_2CO_2H)_2$] (**2**) was prepared as previously described.[24] Briefly to a suspension of *c,c,t*-[$Pt(NH_3)_2(OCH_2CO_2)(OH)_2$] (previously synthesized)[24] (0.2 g, 0.59 mmol) in DMF (10 mL) succinic anhydride (0.24 g, 2.4 mmol) was added and left stirring at 70 ºC for 24 h. The product was then lyophilized and washed several times with ice cold acetone (112 mg, 35.4%).

3.4.3 Synthesis PEI-coated AuNPs

PEI-coated AuNPs were prepared and characterized as described in the experimental section of Chapter 2.

3.4.4 Synthesis FITC-labelled PEI and FITC-labelled PEI-AuNPs

FITC-labelled PEI (FITC-PEI) was prepared as described elswhere.[36] An aqueous solution of PEI 1.8 kDa (35 mg, 13.9 μmol, 500 μL) was added to FITC (5 mg, 12.8 μmol) dissolved in 5 mL H_2O:DMSO (1:1). The mixture was stirred overnight in the darkness and later dialyzed against H_2O for 2 days (MWCO 2000 kDa) to remove any unbound FITC until no fluorescence could be detected in the dialysate. The resulting FITC-labelled PEI was then lyophilized. FITC-labelled PEI-AuNPs were prepared as described in the experimental section of Chapter 2 by using the FITC-labelled PEI instead of the normal PEI.

3.4.5 Sample preparation

All samples were freshly prepared simply by mixing an aqueous solution of the protonated Pt(IV) complexes at the appropriate concentrations with an aqueous

solution of PEI or PEI-coated AuNP (concentrations given in the figure captions). For the NMR studies the solvent was D_2O and the pH was adjusted by adding small amounts of NaOH over the pH range 4-8. For the electrochemistry experiments 10 mM PBS pH 7.4 was used to prepare the solutions and the samples were degassed immediately prior to use by bubbling argon through them for at least 30 minutes. For the cell culturing experiments, prior to the incubation with the cancer cells, the samples were left to interact for ca. 30 minutes and then were diluted 1/10 in cell culture medium and directly added to the cells to ensure no loss of reagents. The concentration of Pt(IV) complexes was determined by ICP-MS and the concentration of PEI was calculated taking the average MW of 1.8 kDa. In the studies with PEI-AuNPs, the gold concentration refers to Au(0) determined from the UV-Vis spectrum of the nanoparticle stock solution once purified to remove any excess of reagents. This Au(0) concentration can be directly correlated to the absorbance value at 400 nm.[38]

3.4.6 Cell culture experiments

PC-3 human prostate cancer cell line was obtained from the American Type Tissue Collection (ATCC) and cultured in Ham's F-12K (Kaighn's) medium (Glibco) supplemented with 10% foetal bovine serum (Invitrogen) and 1% penicillin/streptomycin (Invitrogen) at 37 ºC under 5% CO_2. Cells were passaged at ~70% confluence and a low passage number was maintained using cryopreserved stocks stored in foetal bovine serum supplemented with 10% DMSO (Sigma Aldrich). MDA-MB231 human breast cancer cell line and PANC-1 human pancreatic carcinoma cell line were obtained from ATCC and European Collection of Cell Cultures (ECACC) respectively and were cultured in RMPI medium 1640 (Lonza) with 10% foetal bovine serum (Invitrogen), 1% L-glutamine and 1% penicilin/streptomycin (Invitrogen) at 37 ºC under 5% CO_2. Cells were passaged at ~70% confluence and a low passage number was maintained using cryopreserved stocks stored in foetal bovine serum supplemented with 10% DMSO.

Cell viability studies. The cell viability was measured using the sulforhodamine B assay.[39] For cell viability measurements, PC-3, MDA-MB231 and PANC-1 cells were

pated at 2000 cell/well density on 96-well plates and allowed to adhere overnight. All the formulations were diluted 1/10 in medium and incubated at 37 ºC using 200 µL of sample per well in quintuplets. After 72 h, the cells were fixed by the addition of ice cold 25% trichloroacetic acid (TCA) solution prior to staining with the SRB dye solution (0.4% w/v in 1% glacial acetic acid). The plates were washed with 1% glacial acetic acid, air-dried and resuspended in Tris buffer (10 mM, pH 10.5) before reading the absorbance at 550 nm. Curve fitting and interpolation of the IC_{50} values was carried out using GraphPad Prism 4 software.

Cell imaging. PC-3 cells were seeded in an Ibidi 18 well µ-Slide at 4000 cell/well density and allowed to adhere overnight in an incubator (37 ºC, 5% CO_2) in Ham's F-12K (Kaighn's) medium. The medium was changed and the nuclei were stained with Hoechst 33342 (1 µg/mL) for 5 minutes, washed with sterile PBS 10 mM and incubated with the FITC containing nanoparticle formulations for 45 minutes. The medium was them removed, cells washed with sterile PBS 10 mM and fresh medium was added. The cells were visualized using a Zeiss Axio Observer wide field fluorescence images were collected and processed using Axio Vision software.

Cellular uptake by flow cytometry. PC-3 cells were trypsinized and collected into cytometer tubes ($1x10^5$ cells/tube). The cells were centrifuged (1000 rpm, 5 min, 4 ºC) in order to discard the media and the pellet was resuspended in the formulations diluted in cell culture media (200 µL/tube). After 45 minutes of incubation at 37 ºC, the cells were centrifuged (1000 rpm, 5 min, 4 ºC) and washed once with cold PBS 10 mM. Finally the cell pellet was resuspended in 0.4 mL cold cytometer buffer (1% bovine serum albumin (BSA) and 0.1% sodium azide in PBS 10 mM). Cells were kept on ice until the analysis. The cellular uptake of the different formulations was measured using FACS Canto II (BD Bioscience) and the data was analyzed with FlowJo, LCC software. PC-3 cells were electronically gated based on forward area and height scatter parameters. The laser excitation wavelength used for FITC was 488 nm and the emission filter 530/30 nm. Each analysis represented the acquisition of 10000 cells per sample.

3.4.7 Instrumentation

NMR studies. ^{1}H NMR spectra were recorded on a Bruker Avance 500 NMR spectrometer at 298 K. Data processing was carried out using Mnova software.^{1}H NMR spectra for (**1**), (**2**) and (**3**) were recorded in 10% D_2O in H_2O for characterization and in D_2O with in combination with PEI and ascorbic acid; in all cases the chemical shifts were expressed relative to the water peak at 4.8 ppm.

XPS measurements. XPS experiments were performed in a SPECS Sage HR 100 spectrometer with a non-monochromatic X-ray source (Magnesium Kα line of 1253.6 eV energy and 250 W), placed perpendicular to the analyzer axis and calibrated using the $3d_{5/2}$ line of Ag with a full width at half maximum (FWHM) of 1.1 eV. The selected resolution for the spectra was 15 eV of Pass Energy and 0.15 eV/step for the detailed spectra of the Pt 4f peaks. The deconvolution of the Pt 4f peaks was carried out at 36 s of X-ray exposure. The deconvolution allowed to estimate the ratio of the Pt(II) and Pt(IV) states. All measurements were made in an ultra high vacuum (UHV) chamber at a pressure below $5 \cdot 10^{-8}$ mbar. In the fittings Gaussian-Lorentzian functions were used, where the FWHM of all the peaks were constrained while the peak positions and areas were set free.

Electrochemical studies. Cyclic voltammetry measurements were performed with an Autolab PGSTAT 128N (Metrohm Autolab B.B., The Netherlands) using disposable screen-pronted electrodes and an Ag/AgCl reference electrode onto a ceramic substrate (DRP-110, DropSens, Spain).

TEM. TEM studies were conducted in a JEOL JEM-2011 electron microscope operating at 200 kV. The samples were prepared by depositing a drop of nanoparticle solution onto a copper specimen grid coated with a holey carbon film and allowing it to dry. For nanoparticle size determination a minimum of 300 particles were measured using the *Image J* software.

UV-Vis and Fluorescence spectroscopy. UV-vis measurements were performed in H_2O using a Varian Cary 5000 spectrophotometer. Absorbance measurements on

96-well plates were carried out on a TECAN Genios Pro 96/384 multifunction microplate reader. Fluorescence emission spectra were recorded with a Horiba Jovin Ibon Fluorolog fluorometer.

DLS and ζ-potential. Particle size analysis was performed using a NanoSizer (Malvern Nano-ZS, UK) with 173° scattering angle at 25 ºC. Each sample was measured at least in triplicate. Z-potential measurements were carried out with the same NanoSizer equipment at 25 ºC and a cell drive voltage of 20 V using a Smoluchowski model.

Flow cytometry. All flow cytometry experiments were carried out in a FACS Canto II (BD Bioscience) system, which has an excitation source composed of three lasers: violet (405 nm), blue (488 nm) and red (633 nm). The laser excitation wavelength used for FITC was 488 nm and the emission filter 530/30 nm. In all measurements cells were electronically gated based on forward and side scatter parameters and the not-singlet events leaved out based on forward area and height parameters. Each analysis represented the acquisition of 10000 cells per sample and data was analyzed with FlowJo LLC software.

Fluorescence microscopy. Live cell fluorescence images were obtained using Zeiss Axio Observer wide field fluorescence microscope (Carl Zeiss, Germany). A colibri LED module was used for fluorescence excitation: 365 nm excitation for Hoechst staining and 470 nm excitation for FITC. Fluorescence emission was collected using a high-efficiency multi-band pass colibri filter set which included a 402-488 nm bandpass for Hoechst and 500-557 nm for FITC. Brightfield and fluorescence images were collected and processed using AxioVision software.

3.5 References

(1) Graf, N.; Lippard, S. J. *Adv. Drug Deliv. Rev.* **2012**, *64*, 993.

(2) Hall, M. D.; Hambley, T. W. *Coord. Chem. Rev.* **2002**, *232*, 49.

(3) Feazell, R. P.; Nakayama-Ratchford, N.; Dai, H.; Lippard, S. J. *J. Am. Chem. Soc.* **2007**, *129*, 8438.

(4) Dhar, S.; Liu, Z.; Thomale, J.; Dai, H.; Lippard, S. J. *J. Am. Chem. Soc.* **2008**, *130*, 11467.

(5) Dhar, S.; Daniel, W. L.; Giljohann, D. A.; Mirkin, C. A.; Lippard. *J. Am. Chem. Soc.* **2009**, *131*, 14652.

(6) Min, Y.; Mao, C.; Xu, D.; Wang, J.; Liu, Y. *Chem. Commun.* **2010**, *46*, 8424.

(7) Dhar, S.; Gu, F. X.; Langer, R.; Farokhzad, O. C.; Lippard, S. J. *Proc. Natl. Acad. Sci. U.S.A.* **2008**, *105*, 17356.

(8) Aryal, S.; Hu, C. J.; Zhang, L. *ACS Nano* **2010**, *4*, 251.

(9) Poon, C.; He, C.; Liu, D.; Lu, K.; Lin, W. *J. Control. Release* **2015**, *201*, 90.

(10) He, C.; Liu, D.; Lin, W. *ACS Nano* **2015**, *9*, 991.

(11) He, C.; Liu, D.; Lin, W. *Biomaterials* **2015**, *36*, 124.

(12) Ravera, M.; Gabano, E.; Zanellato, I.; Perin, E.; Arrais, A.; Osella, D. *Dalton Trans.* **2016**, *45*, 17233.

(13) Cheng, Z.; Dai, Y.; Kang, X.; Li, C.; Huang, S.; Lian, H.; Hou, Z.; Ma, P.; Lin, J. *Biomaterials* **2014**, *35*, 6359.

(14) Hernández-Gil, J.; Cobaleda-Siles, M.; Zabaleta, A.; Salassa, L.; Calvo, J.; Mareque-Rivas, J. C. *Adv. Healthcare Mater.* **2015**, *4*, 1034.

(15) Dai, Y.; Kang, X.; Yang, D.; Li, X.; Zhang, X.; Li, C.; Hou, Z.; Cheng, Z.; Ma, P.; Lin, J. *Adv. Healthcare Mater.* **2013**, *22*, 562.

(16) Gómez Blanco, N.; Maldonado, C. R.; Mareque-Rivas, J. C. *Chem. Commun.* **2009**, 5257.

(17) Maldonado, C. R.; Gómez-Blanco, N.; Jauregui-Osoro, M.; Brunton, V. G.; Yate, L.; Mareque-Rivas, J. C. *Chem. Commun.* **2013**, *49*, 3985.

(18) Bi, H.; Dai, Y.; Xu, J.; Lv, R.; He, F.; Gai, S.; Yang, D.; Yang, P. *J. Mater. Chem. B* **2016**, *4*, 5938.

(19) Lozano-Pérez, A. A.; Gil, A. L.; Pérez, S. a.; Cutillas, N.; Meyer, H.; Pedreño, M.; D. Aznar-Cervantes, S.; Janiak, C.; Cenis, J. L.; Ruiz, J. *Dalt. Trans.* **2015**, *44*, 13513.

(20) Dhar, S.; Kolishetti, N.; Lippard, S. J.; Farokhzad, O. C. *Proc. Natl. Acad. Sci. U.S.A.* **2011**, *108*, 1850.

(21) Graf, N.; Bielenberg, D. R.; Kolishetti, N.; Muus, C.; Banyard, J.; Farokhzad, O. C.; Lippard, S. J. *ACS Nano* **2012**, *6*, 4530.

(22) Rieter, W. J.; Pott, K. M.; Taylor, K. M. L.; Lin, W. *J. Am. Chem. Soc.* **2008**, *130*, 11584.

(23) Hall, M. D.; Dillon, C. T.; Zhang, M.; Beale, P.; Cai, Z.; Lai, B.; Stampfl, A. P. J.; Hambley, T. W. *J. Biol. Inorg. Chem.* **2003**, *8*, 726.

(24) Gramatica, P.; Papa, E.; Luini, M.; Monti, E.; Gariboldi, M. B.; Ravera, M.; Gabano, E.; Gaviglio, L.; Osella, D. *J. Biol. Inorg. Chem.* **2010**, *15*, 1157.

(25) Turkington, J. R.; Bailey, P. J.; Love, J. B.; Wilson, a M.; Tasker, P. A. *Chem. Commun.* **2013**, *49*, 1891.

(26) Pordea, A.; Creusa, M.; Panek, J.; Duboc, C.; Mathis, D.; Novic, M.; Ward, T. R. *J. Am. Chem. Soc.* **2008**, *130*, 8085.

(27) Boersma, A. J.; Feringa, B. L.; Roelfes, G. *Angew. Chem. Int. Ed.* **2009**, *48*, 3346.

(28) Dutta, A.; Lense, S.; Hou, J.; Engelhard, M. H.; Roberts, J. a S.; Shaw, W. J. *J. Am. Chem. Soc.* **2013**, *135*, 18490.

(29) Mareque-Rivas, J. C.; Brammer, L. *Inorg. Chem.* **1998**, *37*, 4756.

(30) Brammer, L.; Swearingen, J. K.; Bruton, E. A.; Sherwood, P. *Proc. Natl. Acad. Sci. U.S.A.* **2002**, *99*, 4956.

(31) Natale, D.; Mareque-Rivas, J. C. *Chem. Commun.* **2008**, 425.

(32) Metteau, L.; Simon Parsons, A.; Mareque-Rivas, J. C. *Inorg. Chem.* **2006**, *45*, 6601.

(33) Demadis, K. D.; Paspalaki, M.; Theodorou, J. *Ind. Eng. Chem. Res.* **2011**, *50*, 5873.

(34) Lin, I. J.; Gebel, E. B.; Machonkin, T. E.; Westler, W. M.; Markley, J. L. *Proc. Natl. Acad. Sci. U.S.A.* **2005**, *102*, 14581.

(35) Wexselblatt, E.; Gibson, D. *J. Inorg. Biochem.* **2012**, *117*, 220.

(36) Pinheiro, P. C.; Daniel-da-Silva, A. L.; Tavares, D. S.; Calatayud, M. P.; Goya, G. F.; Trindade, T. *Materials* **2013**, *6*, 3213.

(37) Dhara, S. C. *Indian J. Chem.* **1970**, *8*, 193.

(38) Hendel, T.; Wuithschick, M.; Kettemann, F.; Birnbaum, A.; Rademann, K.; Polte, J. *Anal. Chem.* **2014**, *86*, 11115.

(39) Vichai, V.; Kirtikara, K. *Nat. Protoc.* **2006**, *1*, 1112.

4

Iron oxide-filled Pt(IV) prodrug-modified PEG-phospholipid micelles: proof-of-concept study in an aggressive murine model of melanoma

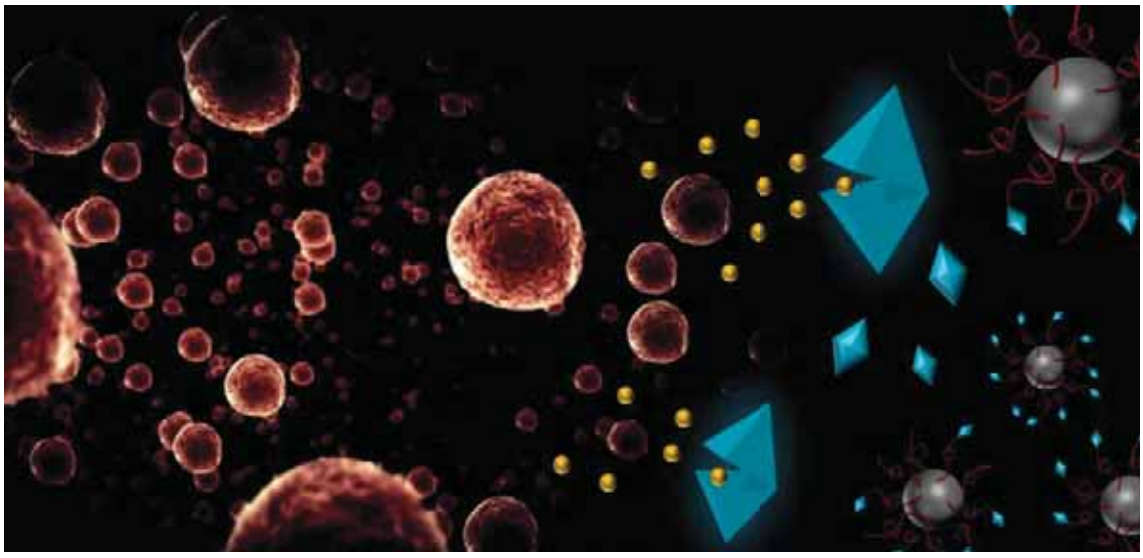

4.1 Introduction

Metastatic melanoma is one of the most aggressive and challenging types of cancer to treat, with a 5 year survival rate between 5-19%.[1] Surgery, radiation and systemic treatments are used for treatment of curable melanoma and remain as the main treatment options in the management of patients with metastatic disease. However, one of the main causes behind the low survival rate is the notoriously resistant nature of melanoma to chemotherapy. Approved over 3 decades ago, dacarbazine continues to be the standard chemotherapeutic drug against melanoma.[2]

Despite being the main treatment for a wide variety of cancers, the contribution of cisplatin towards melanoma has been somewhat limited. Platinum derivatives including cisplatin and carboplatin have a moderate antitumour effect, but similarly to the use of dacarbazine, they are limited by low response rates.[2] Hence, the majority of the research has been oriented towards combined therapy using platinum derived drugs together with immunotherapy, gene therapy and different small molecules in search for a synergistic effect.[3–6] Kubo *et al*. for example reported the combined use of cisplatin, interferon-β and IL-2 for tumour growth inhibition in a B16-F1 murine melanoma model.[7]

The main limitation of traditional chemotherapeutics and combined approaches relates to their poor penetration into the tumour and lymph nodes involved in metastatic processes. With up to 80% of melanomas resulting in metastatic spread through the lymph nodes,[8] the traditional intravenous administration of anticancer drugs is not able to provide sufficient lymphatic accumulation. Current clinical options towards treatment of lymph node metastases frequently involve complete lymph node dissection, a procedure associated with complications such as lymphatic oedema or infection and prolonged hospitalization.[9] Therefore, the development of chemotherapeutic agents capable of efficiently accumulating in the tumour and lymph nodes could potentially lead to more successful treatment of the metastatic disease.

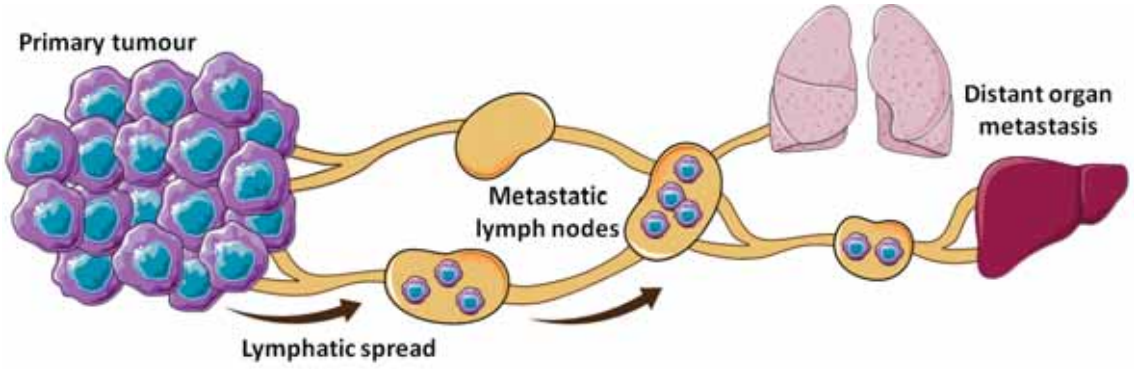

Figure 1. Lymphatic spread of the melanoma tumour cells from the primary location to the draining lymph nodes and the ultimate formation of distant organ metastases.

Nanomedicine stands out as a particularly intriguing approach to assist in the lymphatic delivery and tumour accumulation of anticancer drugs. Due to their size and unique features, nanoparticles can not only be designed to target tumour tissue but also to selectively accumulate in lymph nodes and traffic through the lymphatic system.[10,11] Subcutaneous administration of nanocarriers has already shown great potential for lymphatic delivery of anticancer drugs.[12] Many different preparations have been explored for the treatment of melanoma, including liposomes, polymer nanoparticles and inorganic nanoparticles delivering various anticancer drugs.[13,14]

Zhang *et al*. for example prepared paclitaxel loaded Pluronic (F123 and F127) polymeric micelles for the treatment of a pulmonary metastatic melanoma mouse model (B16-F10).[15] With such preparation, the authors were able to prolong the blood circulation time and tumour accumulation of the drug as well as an improved therapeutic effect compared to Taxol. A similar strategy based on polymeric nanoparticles was reported by Talelli *et al.*, who developed a covalent encapsulation of doxorubicin into cross-linked polymer micelles.[16] A biodegradable block copolymer was used to form the micelles in which a methacrylamide derivative of doxorubicin was covalently incorporated through free radical polymerization. Designed to release the drug payload in acidic conditions, this construct demonstrated its enhanced therapeutic efficacy compared to free doxorubicin in the same murine melanoma model (B16-F10).

Nanocarriers for the delivery of platinum based drugs against melanoma have also been reported over the last few years. For example, Yang *et al*. developed a hyaluronan-conjugated cisplatin system which shows improved antitumour efficacy in a murine melanoma model compared to standard cisplatin treatment.[17] Tao and co-workers on the other hand described the covalent attachment of cisplatin to poly-*N*-isopropylacrylamide (PNIPAM) and polyethyleneglycol (PEG) coated AuNPs.[18] This pH-sensitive construct showed enhanced cytotoxicity in A875 melanoma cells due to the liberation of the drug under the acidic conditions of the intracellular environment. In a more recent example Cabral *et al*. developed a platinum (II) drug loaded polymeric micelle construct that were able to target and fight lymph node metastases following systemic administration.[19] The authors explored the therapeutic efficacy of the system in a highly aggressive metastatic melanoma mouse model (B16-F10) and highlighted the importance of the size of the nanocarrier, which played a key role in achieving an improved therapeutic efficacy compared to the free drug and even the clinically used doxorubicin-loaded liposome preparation (Doxil).[19]

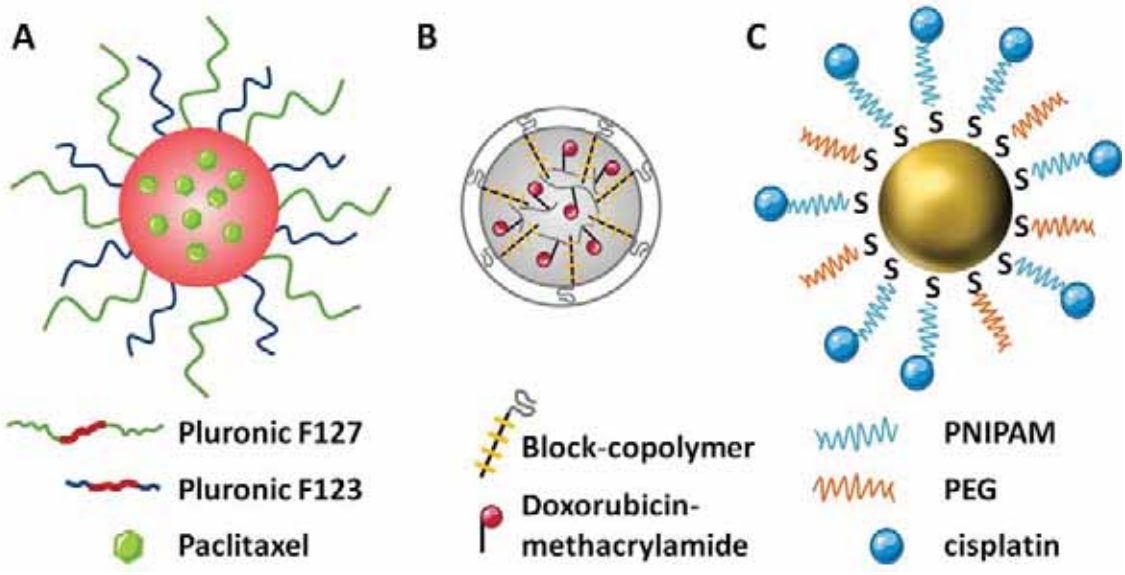

Figure 2. Schematic representation of three nanoparticle based delivery vehicles for the treatment of melanoma. (**A**) Paclitaxel loaded polymeric micelle,[15] (**B**) cross-linked block-copolymer micelles with covalently entrapped doxorubicin[16] and (**C**) PNIPAM and PEG coated AuNPs for the delivery of cisplatin.[18]

Beyond their role as drug delivery vehicles, nanoparticles can also be conceived to function as contrast agents for diverse imaging modalities for early detection of tumours and metastases, as well as real time tracking of the drug and its therapeutic efficacy. Particularly interesting is the possibility of not only selectively delivering anticancer agents to the tumour and lymphatic system but also being able to non-invasively visualize these areas of interest. Indeed, the early detection of metastases in the lymph nodes is a key aspect for improving the therapeutic outcome of melanoma. In this regard, recent efforts have been focussed on the design of nanoparticles that able to accumulate and traffic through the lymphatic system also incorporate capabilities for high resolution and sensitive imaging.

Lim *et al.* reported a thermally cross-linked superparamagnetic IONP system for MRI contrast enhancement and its applicability for the detection of metastatic lymph nodes in a melanoma mouse model (B16-F1).[20] Mareque-Rivas and co-workers described the use of IONP-filled PEG-phospholipid micelles for lymphatic delivery of immunostimulatory drugs and multimodal MRI/SPECT imaging. This system initially took advantage of the intrinsic nature of the IONPs as MRI contrast agents and incorporated ^{99m}Tc as a radioisotope for SPECT imaging.[21] ^{67}Ga radiolabelling of a similar IONP-based system was reported for image tracked lymphatic delivery of an antigen/adjuvant combination against melanoma.[22]

Based on the successful lymphatic delivery of IONP-based micelles, their excellent imaging capabilities as well as the potential of platinum based drugs and prodrugs against melanoma, this work focused on investigating the properties of IONP-filled PEG-phospholipid micelle nanocarriers to deliver of a cisplatin platinum (IV) prodrug for the treatment of melanoma.

4.2 Results and Discussion

4.2.1 Synthesis and characterization of PEG-Pt

Adopting the Pt(IV) prodrug approach, the inert Pt(IV) prodrug *cis,cis,trans*-$[Pt(NH_3)_2Cl_2(O_2CCH_2CH_2CO_2H)_2]$ (**1**) was selected for attachment and delivery using water soluble IONPs micelles using a protocol previously described by the group.[23] This prodrug is capable of releasing cytotoxic Pt(II) species upon intracellular reduction inside tumour cells.[24] Its use in combination with a nanoparticle based delivery system was expected to facilitate prodrug delivery to the area of interest (i.e. tumour and tumour draining lymph nodes). The use of dicyclohexylcarbodiimide (DCC) coupling chemistry allows the conjugation of the prodrug to the amine end group of a commercially available PEGylated phospholipid (PEG-NH_2). Following the reaction, any unbound (**1**) is removed via dialysis and the purified phospholipid (PEG-Pt) (Figure 3) recovered by freeze-drying. Adding an excess of (**1**) in the reaction ensures that only one of the axial ligands on the Pt(IV) complex reacts with the phospholipid molecule, minimizing unwanted side products.

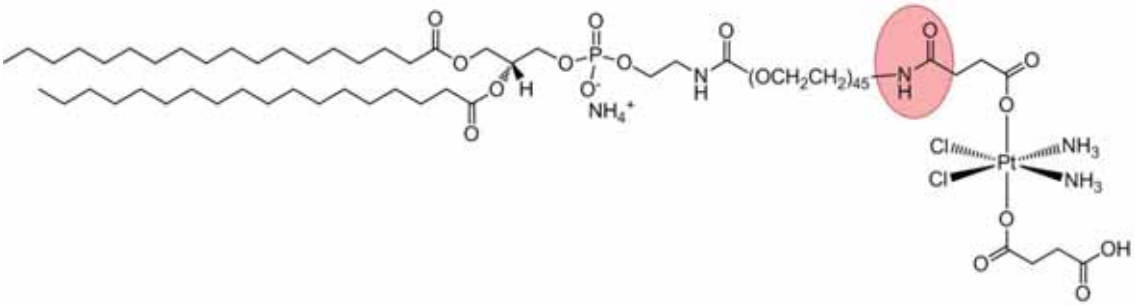

Figure 3. Structure of the Pt-modified PEGylated phospholipid (PEG-Pt). The amide bond is highlighted in red.

The characterization of the final product by UPLC-MS (Figure 4) reflects a change in the retention time compared to the initial PEG-NH_2, indicating a change in polarity, hence in the structure. The lower retention time of the Pt(IV)-modified phospholipid indeed suggests a more polar nature of the compound, resulting in less affinity for the stationary phase (reverse phase column, apolar).

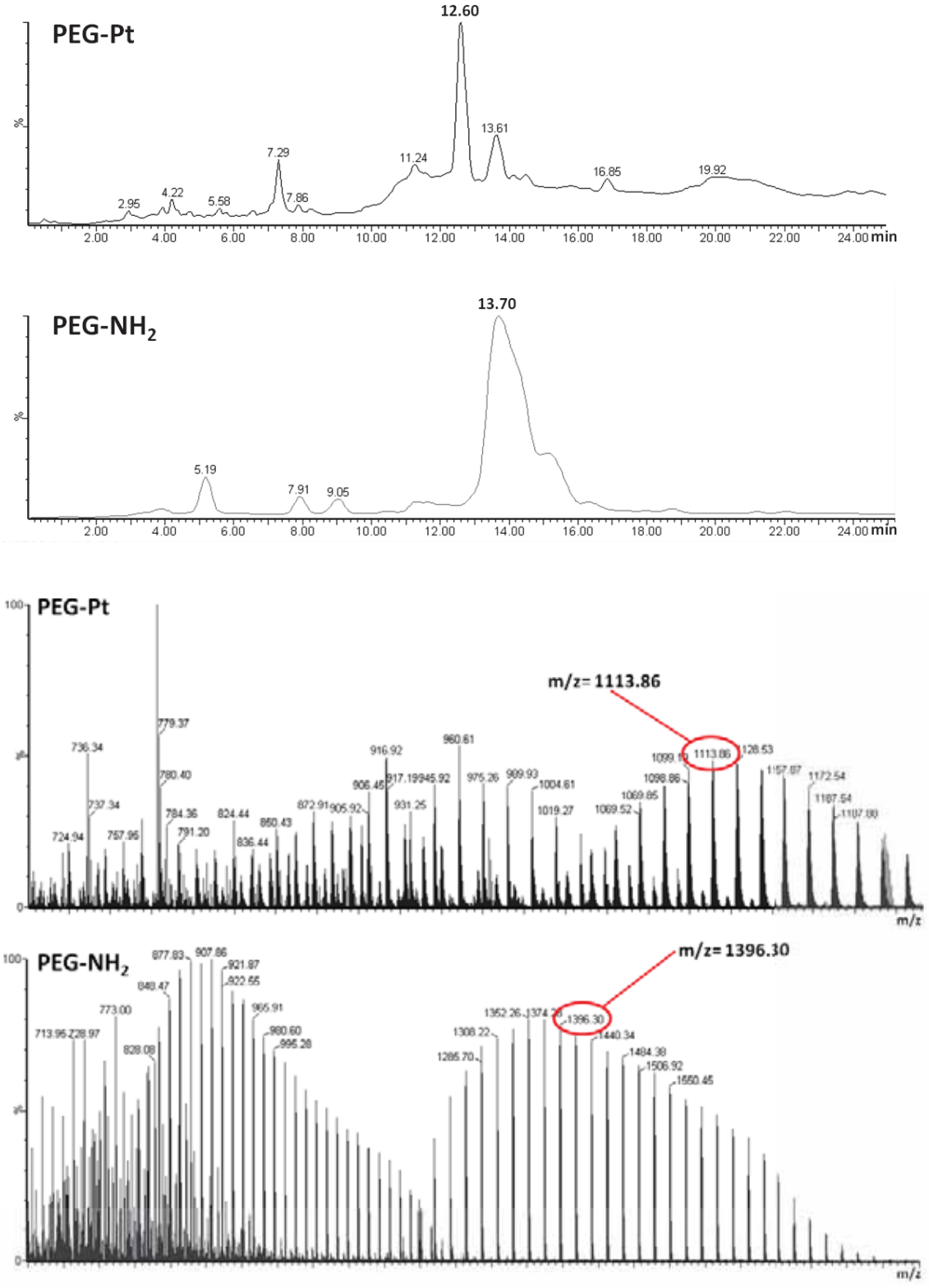

Figure 4. Typical chromatograms obtained for the PEG-Pt final product and the initial PEG-NH_2 as a control (*top*). Positive ESI-MS m/z spectra of the parent PEG-NH_2 (control) and the PEG-Pt product (*bottom*): m/z for $[PEG\text{-}NH_2+H^+ +NH_4^+]^{2+}$ ($C_{132}H_{267}N_3O_{54}P$) expected = 1395.74, found = 1396.30; m/z for $[PEG\text{-}Pt+2H^+ +3NH_4^+]^{3+}$ ($C_{140}H_{289}N_7O_{61}PPtCl_2$) expected = 1114.89, found = 1113.86.

The ESI-MS spectrum in Figure 4 indicates a successful incorporation of the prodrug, showing an isotopic pattern in accordance with PEG-containing polymers and an experimental m/z value (1113.86) very close to the expected one (1113.33). The ^{1}H NMR spectrum also agrees with the formation of PEG-Pt as new peaks due to the Pt(IV) prodrug's succinate ligands are present at ca. 2.5 ppm (Figure 5).

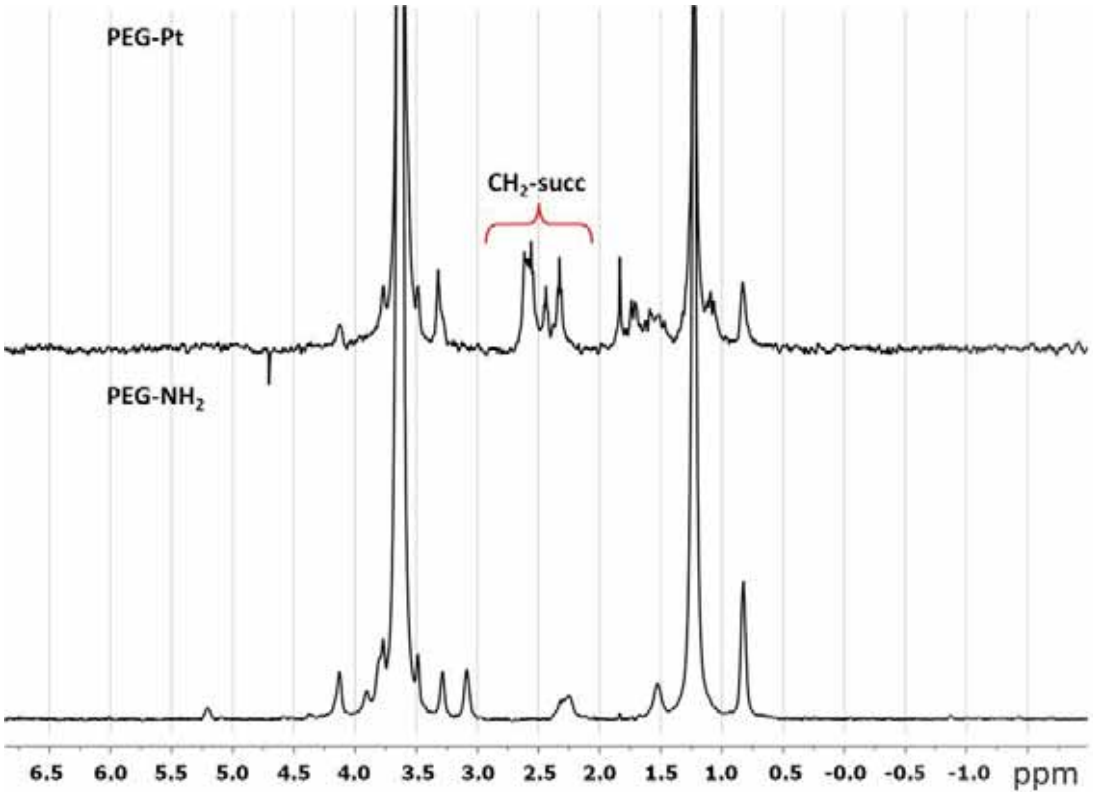

Figure 5. ^{1}H-NMR spectra of PEG-Pt and unmodified PEG-NH_2 in D_2O (water suppression).

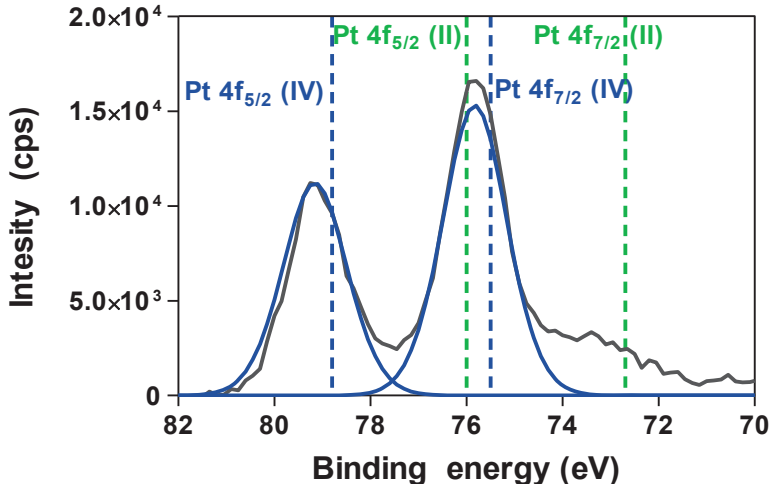

Figure 6. XPS spectrum of PEG-Pt showing the expected binding energy of the Pt 4f regions for Pt(II) (green) and Pt(IV) species (blue).

XPS analysis of the Pt 4f region also confirms that the oxidation state of the platinum centre remains as Pt(IV) even following the conjugation (Figure 6). In accordance with the literature data for Pt(IV) species, the characteristic Pt($4f_{7/2}$) and Pt($4f_{5/2}$) appear at 75.5 eV and 78.8 eV respectively while any peaks corresponding the Pt(II) oxidation state (at 72.7 eV and 76.1 eV) are absent.

4.2.2 Synthesis and characterization of IONPs and water soluble IONP micelles

Hydrophobic IONPs were prepared by thermal decomposition of an iron (III) precursor using oleylamine and oleic acid as surfactants and 1,2-hexadecanediol as the reducing agent. Adjusting the experimental conditions, the shape and morphology of the resulting particles was controlled to obtain spherical 6-7 nm IONPs.[25] The TEM characterization of the synthesized nanoparticles (Figure 7) shows monodisperse and spherical IONPs with a mean core diameter of 6.6 ± 0.9 nm.

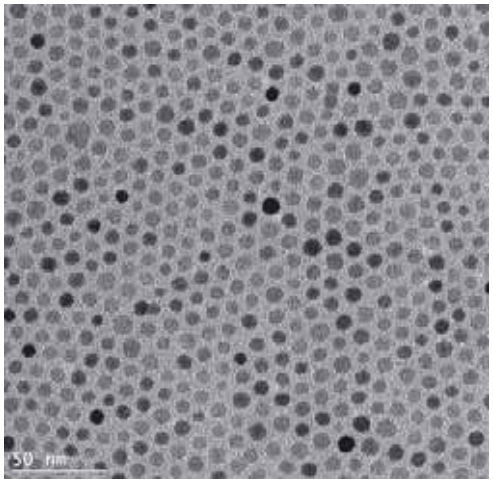

Figure 7. Representative TEM image of the hydrophobic IONPs used for the micelle preparation.

IONPs prepared by thermal decomposition methods result in hydrophobic materials that need further modification to achieve the water solubility required for biomedical applications. Among the many different polymers and ligands that impart water solubility and biocompatibility to hydrophobic IONPs, polyethyeneglygol (PEG) and its derivatives represent a very interesting alternative and have indeed been

widely used.[26] PEG polymers have low toxicity and immunogenicity and several PEGylated products have been approved by the FDA (Food and Drug Administration) for clinical use.[27] PEGylated phospholipids in particular offer a great scaffold for further chemical modification through their terminal functional groups, allowing the incorporation of different moieties such as the prodrug described above. The use of this kind of commercially available PEGylated phospholipids to form micelles encapsulating nanoparticles and other kinds of hydrophobic molecules has been reported in different biomedical applications.[28]

In this work the intercalation of the amphiphilic PEGylated phospholipids between the oleic acid chains on the surface of the nanoparticles leads to the formation of stable and water soluble micelles based on a modification of the lipid hydration method previously used by the group.[29] Any free phospholipid can then be eliminated by ultracentrifugation, leading to purified micelles that are stable in either water or saline solution. The covalent attachment of the platinum (IV) prodrug to the PEGylated phospholipid allows the formation of prodrug-loaded water soluble IONP micelles following the same lipid hydration strategy. In order to compare the Pt(IV) prodrug-loaded system against a prodrug-free control, the commercially available methoxy terminated phospholipid (PEG-OMe) was used to prepare unloaded micelles in a similar manner.

The characterization and comparison between the loaded and unloaded micelles (Figure 8) shows the presence of small aggregates in both cases, with a slightly higher hydrodynamic diameter for the Pt-loaded micelles. The fact that the system is constituted of small aggregates not larger than 100 nm is highly desirable in this case. Indeed, it has already been described that this is the ideal size range for a subcutaneously injected nanocarriers to be able to enter the lymphatic system.[30] Too large nanoparticles are mainly stuck in the injection site, while too small system will mostly be absorbed by the capillary network and go into systemic circulation. Nanocarriers between 10 and 100 nm on the other hand, maybe able to enter and traffic through the lymphatic system reaching the tumour site and draining lymph nodes, being able to potentially fight metastasis.

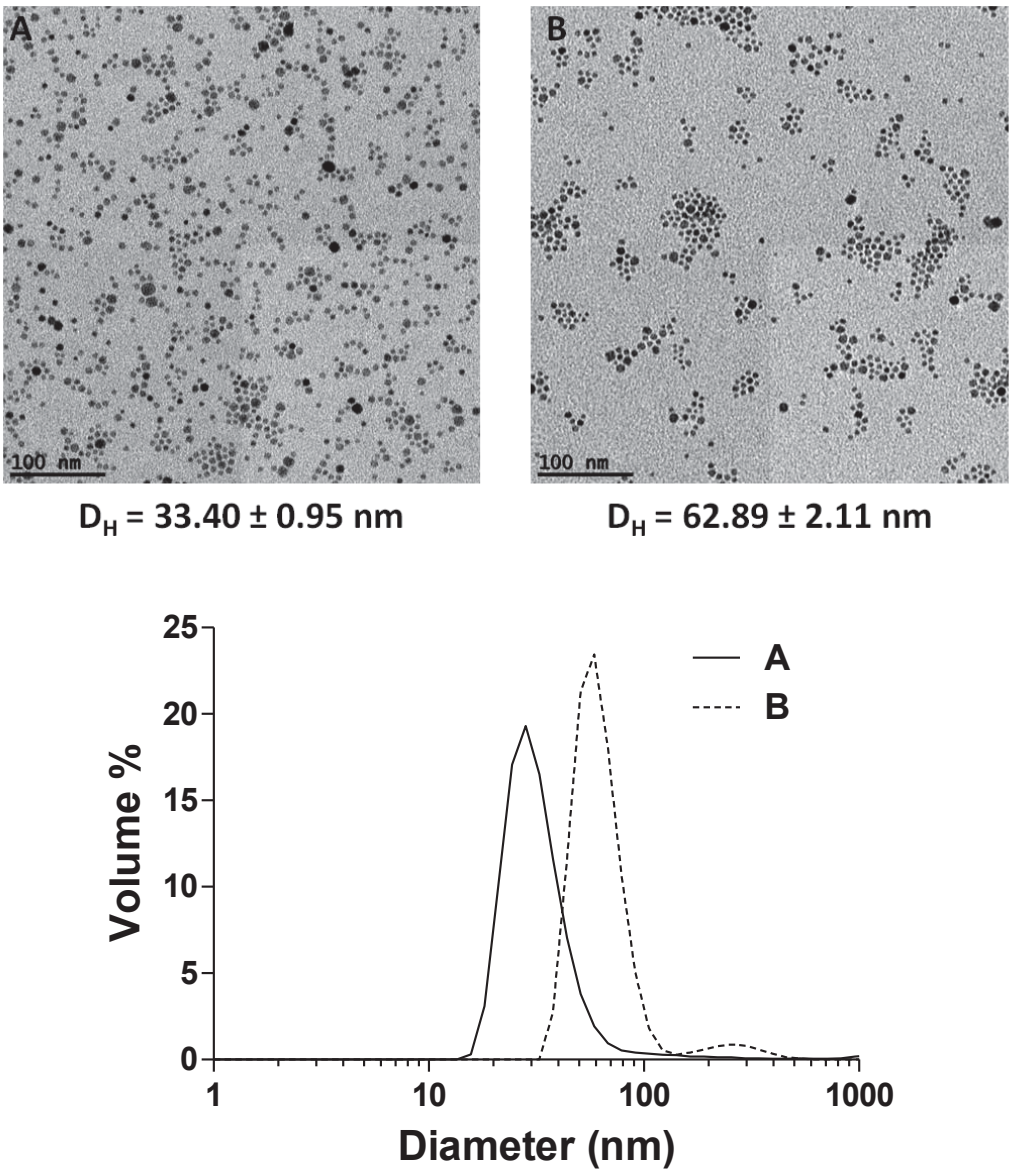

Figure 8. Representative TEM images and DLS size distribution of control (**A**) and Pt-loaded (**B**) micelles.

The change in zeta potential from -15.1 ± 2.1 mV to -26.9 ± 1.9 mV also reflects the attachment of the prodrug, where the carboxylate group of (**1**) provides a negative charge. In order to determine the loading capacity of the system, ICP-AES and ICP-MS analysis were performed to measure the iron and platinum content, resulting in an average of 150 molecules of (**1**) per IONP. Using a representative example with an iron oxide core of 6.6 nm in diameter and a [Fe]/[Pt] ratio of 40 (in mM), the following calculations can be performed to determine the approximate number of prodrug molecules per nanoparticle.

Assuming a completely spherical nanoparticle and the known density of magnetite structure, the mass per nanoparticle can be determined:

$$V_{IONP} = 4/3 \cdot (D/2)^3 \cdot \pi = 1.505 \cdot 10^{-25}\ m^3$$

$$\rho(Fe_3O_4) = 5.17 \cdot 10^6\ g \cdot m^3$$

$$m = \rho(Fe_3O_4) \cdot V_{IONP} = 7.783 \cdot 10^{-19}\ g$$

Taking the molecular weight and the general formula of the iron oxide, the moles and atoms of iron can be determined. Together with the ICP results this data can be used to obtain an estimated nanoparticle concentration ([IONP]) and hence the approximate number of platinum molecules per IONP:

$$n_{Fe} = m \cdot MW\ (Fe_3O_4) \cdot 3 = 1.009 \cdot 10^{-20}\ mol$$

$$Fe_{atoms} = n_{Fe} \cdot N_A = 6076\ atoms$$

$$[IONP] = [Fe] / Fe_{atoms} = 1.79\ \mu M$$

$$[Pt] / [IONP] = 179\ Pt\ molecules / IONP$$

Fluorescently labelled micelles were also prepared in a similar way but with the addition of a commercially available rhodamine labelled phospholipid to the preparation. Figure 9 shows how the the incorporation of the rhodamine phospholipid does not affect the size or the ζ-potential of the micelles. From the UV-Vis and fluorescence spectra the absorption (λ = 570 nm) and emission (λ = 589 nm) peaks corresponding to the rhodamine can be easily identified (Figure 10).

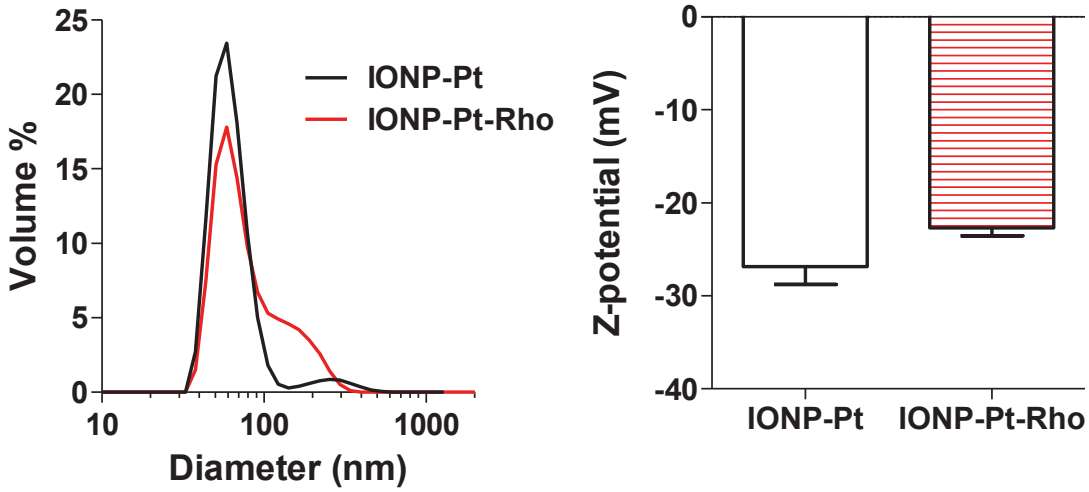

Figure 9. Representation of the size distribution and ζ-potential of normal platinum loaded IONP micelles (black) and rhodamine-labelled IONP-Pt micelles (red).

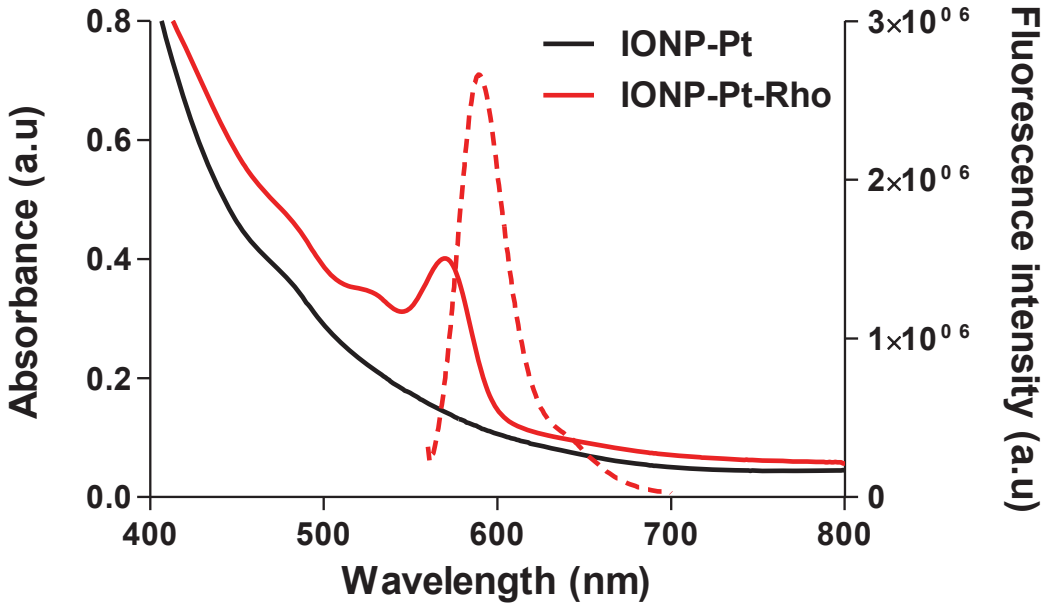

Figure 10. UV-Vis absorption (continuous line) and fluorescence spectra (dashed line) of the unlabelled micelles (black) and the rhodamine-labelled IONP micelles (red).

4.2.3 In vitro cell killing ability

To study the cancer cell killing ability of the system *in vitro*, a sub-line of a highly aggressive and notoriously difficult to treat metastatic melanoma cell line (B16-F10) was selected. The specific sub-line used in this case (B16-F10-OVA) has been engineered to express the full-length ovalbumin model antigen and although the expression of ovalbumin is not relevant for these studies it serves a purpose for the future combination of chemo and immunotherapy. In addition, this type of murine tumour cell line is widely used in research as a model for skin cancers and is indeed one of the most effective in terms of metastasis related research.[31,32]

4.2.3.1 Cellular uptake studies

The internalization of the Pt-loaded micelles was studied in B16-F10-OVA cells by both flow cytometry and live cell fluorescence microscopy (Figure 11). The incubation of the rhodamine labelled IONP-Pt micelles with B16-F10-OVA cells for 2 h and the later analysis by flow cytometry showed an efficient uptake of the NPs by the tumour cells. To gain further information on their intracellular localization, live cell

fluorescence images were also acquired at the same time-point, confirming the uptake of the micelles which localize in the cytoplasm.

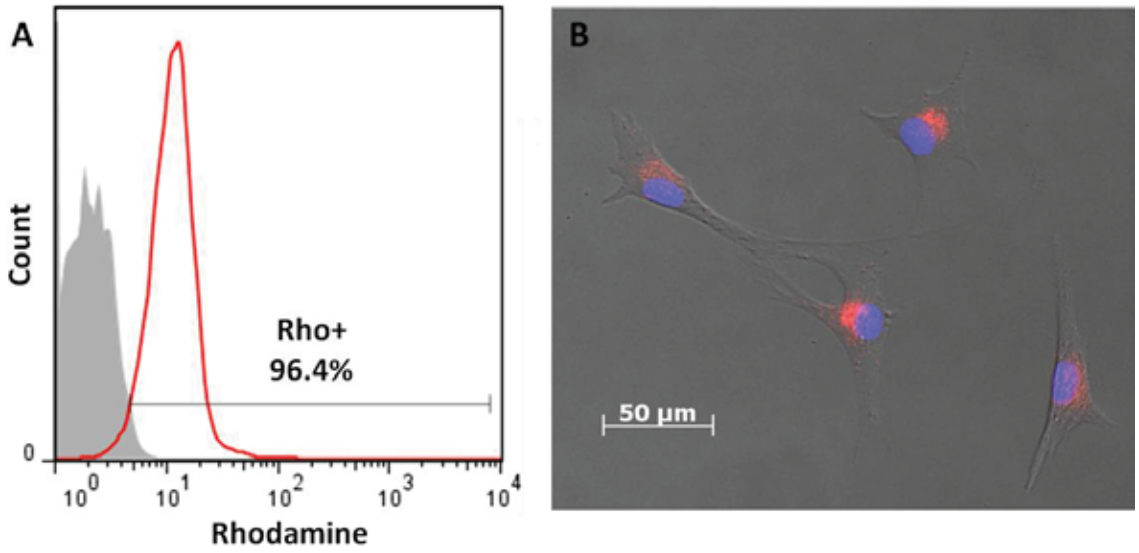

Figure 11. (**A**) Flow cytometry histograms of B16-F10-OVA cells after 2 h incubation with rhodamine-labelled Pt-loaded IONPs (red line) and non treated cells (solid grey peak). (**B**) Overlay of brigthfield and fluorescence microscopy images of live B16-F10-OVA cells after 2 h incubation with the aforementioned formulation (red). Nuclei are stained with Hoechst 33342 (blue).

4.2.3.2 In vitro cytotoxicity studies

To be able to compare between slightly different preparations for all the experiments regarding IONP micelles the concentrations refer to the iron or platinum contents determined by ICP. First the potential toxicity of the vehicle itself was assessed testing a range of different concentrations of unloaded IONP micelles. Figure 12 shows that the IONP micelles do not produce any significant decrease in cell viability in a wide range of iron concentration even after 72 h of incubation.

Accordingly, to evaluate the effect of the Pt(IV) prodrug the platinum loaded micelles were tested keeping the iron concentration at a non-toxic level. As the Pt/Fe ratio slightly varies between preparations, these studies refer to platinum concentration rather than iron.

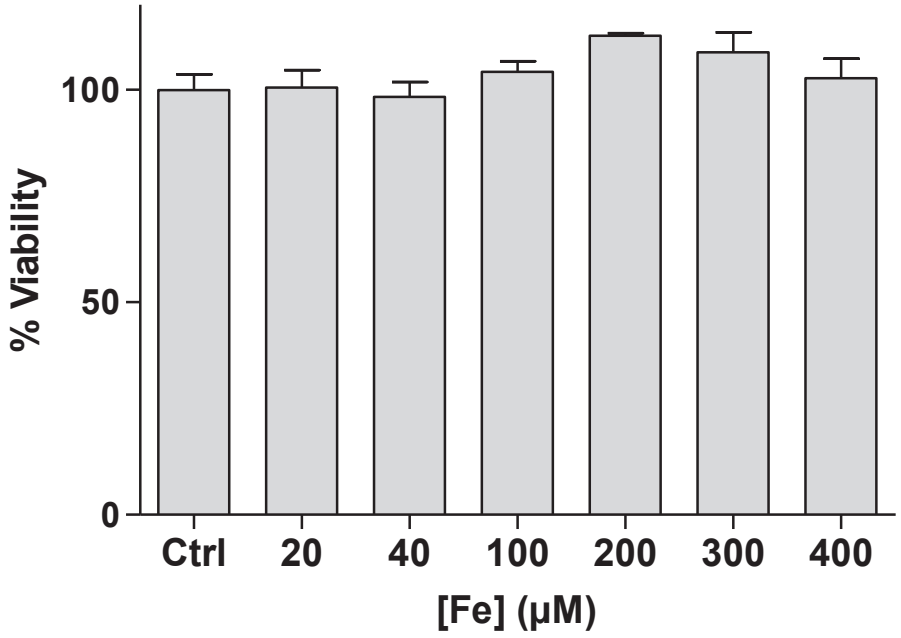

Figure 12. Cytotoxicity profile of the unloaded IONP control micelles in B16-F10-OVA cells (72 h incubation).

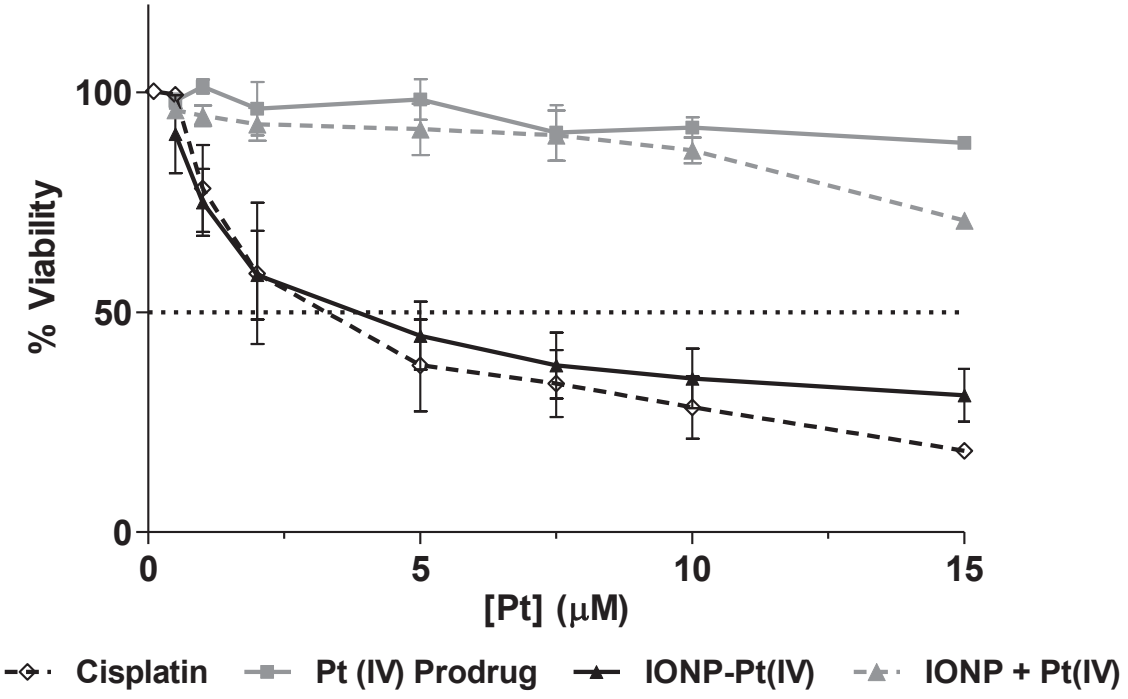

Figure 13. Cytotoxicity profiles of cisplatin, (**1**), Pt-loaded IONP micelles and a mixture of unloaded IONP micelles and (**1**) in B16-F10-OVA cells after 72 h incubation.

The platinum loaded micelles were compared with the Pt(IV) prodrug alone and cisplatin at similar Pt concentrations. Figure 13 shows the cell viability curves for each of these three systems after 72 h incubation with B16-F10-OVA cells, where a clear increase on the cancer cell killing ability of (**1**) can be observed when is delivered by the IONP-filled PEG-phospholipid micelles compared to the prodrug alone. Remarkably, using this delivery vehicle the prodrug (**1**) is able to achieve an *in vitro* cytotoxic effect comparable to cisplatin. Importantly, the simple mixture of unloaded IONP micelles and (**1**) does not render any significant cytotoxic effect, corroborating that the covalent attachment of the prodrug is essential for a successful delivery and cytotoxic effect.

4.2.4 Nuclear imaging: SPECT

In addition to studying the *in vitro* internalization and cancer cell killing ability of the system, the assessment of its *in vivo* trafficking is also very important for the development of new drug delivery systems. For this purpose, nuclear imaging techniques such as PET and SPECT represent a non-invasive, rapid and effective tool to study the biodistribution and pharmacokinetics. Compared to imaging techniques like MRI or CT, one of the major advantages of using nuclear imaging relies on their high sensitivity, allowing the detection of extremely low amounts of radiotracers.

4.2.4.1 Radiolabelling of the IONP-Pt with ^{67}Gallium

Following a previously reported protocol that exploits the similarity between Ga^{3+} and Fe^{3+} ions,[22] the gamma emitting radionuclide ^{67}Ga was used to radiolabel the IONP micelles for SPECT imaging. This approach allowed the direct binding of Ga^{3+} ions without the need of additional steps to incorporate traditional organic metal chelator groups. Commercially available ^{67}Ga citrate was first converted into ^{67}Ga chloride and then incubated with the IONP micelles to achieve the radiolabelling.

As shown in Figure 14 this protocol yielded very efficient radiolabelling of the platinum-loaded micelles with results comparable to those previously described.[22]

More importantly however, the radiolabelled system showed an excellent radiochemical integrity. Even in the presence of a large excess the current "gold standard" Ga^{3+} chelator DOTA (1,4,7,10-tetraazacyclododecane-1,4,7,10-tetraacetic acid) (ca. 10^6 mol DOTA per mol IONP), over 80% of the initial activity is retained.

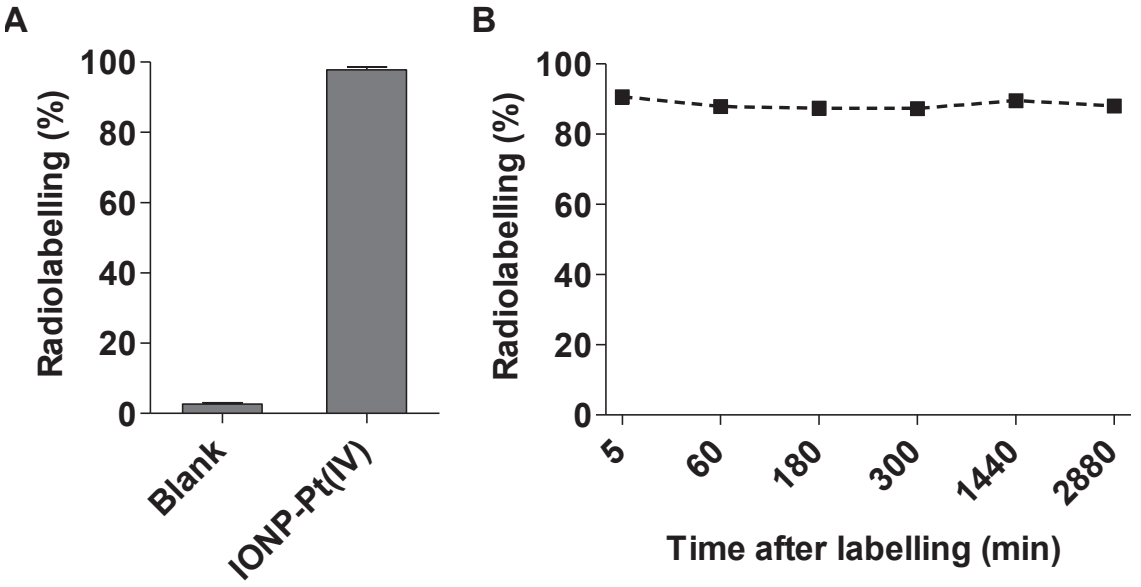

Figure 14. (**A**) ^{67}Ga radiolabelling efficiency of platinum-loaded IONP micelles and (**B**) stability profile of the radiolabelling in presence of large excess of competitor chelating ligand DOTA (ca. 10^6 mol DOTA per mol IONP).

4.2.4.2 Biodistribution and in vivo trafficking

As mentioned previously, tumour metastases not only spread through the circulation but also through the lymphatic system, where the draining lymph nodes are the most common sites of metastasis.[33] For this reason the ^{67}Ga-labelled IONP-Pt micelles were used to monitor the *in vivo* trafficking of the system in tumour bearing mice. Similarly to the *in vitro* studies, the highly aggressive B16-F10-OVA murine melanoma tumour model was used and the radiolabelled system was tracked using SPECT/CT at 3, 24 and 48h after the subcutaneous injection in the peritumoural region.

Despite the intense signal still present at the site of injection, clear accumulation in the tumour and right inguinal lymph nodes can be observed 3 h after the subcutaneous injection of the IONP-Pt(IV) micelles (Figure 15). Notably, the presence of a strong

signal in the right axillary lymph node proves a successful lymphatic trafficking of the nanoparticles to distant sites. A similar biodistribution pattern is observed 24 h post-injection, with a clear signal appearing in both the tumour and the aforementioned lymph nodes. After 48 h on the other hand, most of the remaining activity is in the tumour. *Ex vivo* SPETC images of the different organs confirm the *in vivo* observations (Figure 16).

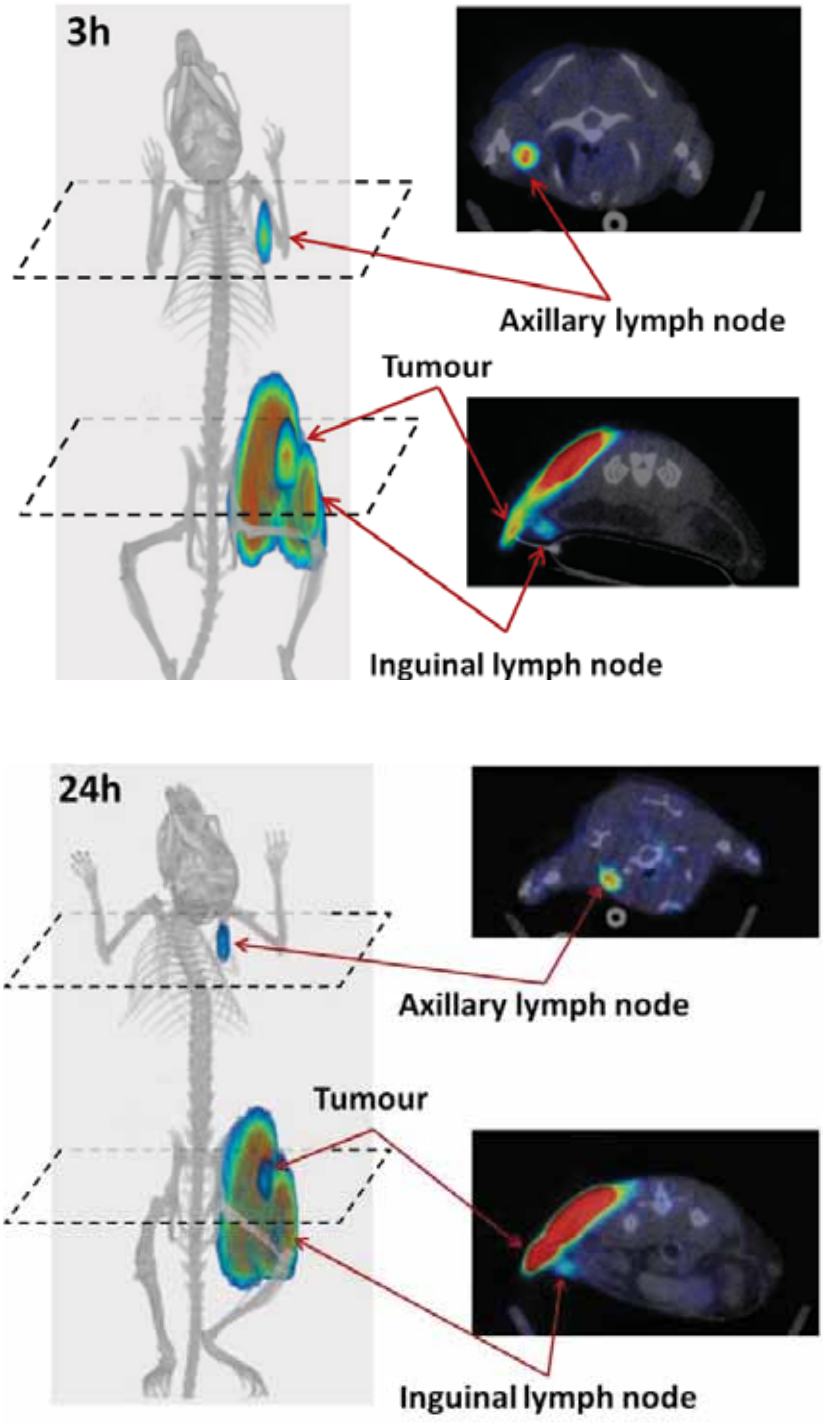

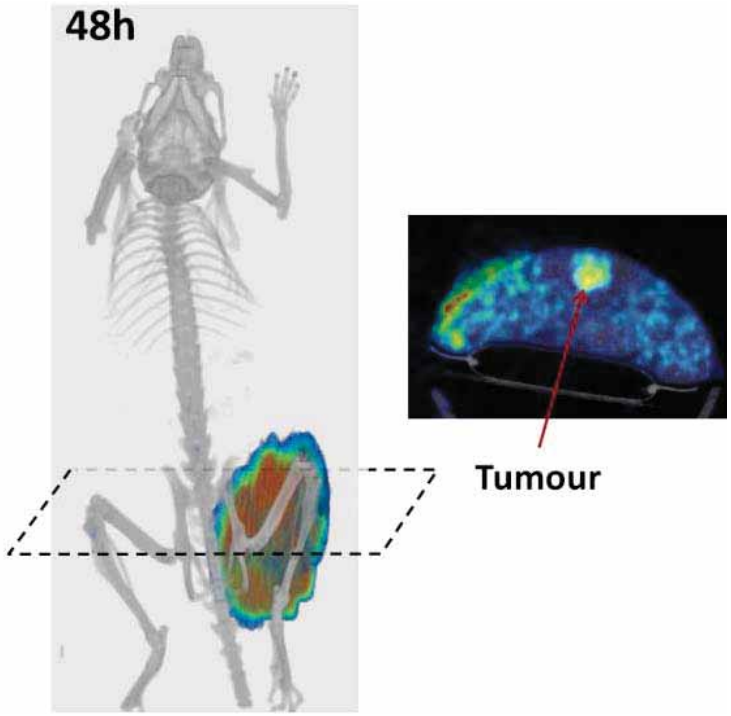

Figure 15. SPECT/CT images 3, 24 and 48 h post injection. Detail of the signal intensity in the tumour area and the inguinal and axillary lymph nodes.

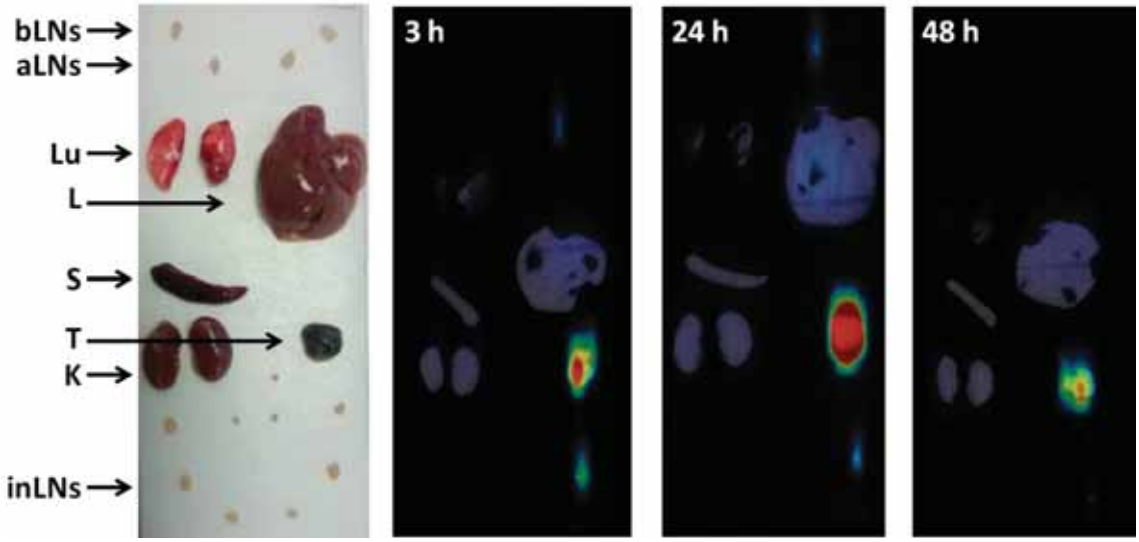

Figure 16. Ex vivo images at 3, 24 and 48h showing the photograph of the selected organs and the corresponding SPECT images bLN: brachial LN; aLN: axillary LN; Lu: lungs; L: liver; S: spleen; T: tumour; K: kidneys; inLN: inguinal LN; iLN: iliac LN; (R): right side; (L): left side.

Gamma-counter analysis of the activity of the organs of interest is also in accordance with the SPECT images. As shown in Figure 17 the radiolabelled system preferentially accumulates in the tumour rather than other organs such as spleen, kidneys or liver. With regards to the lymph nodes, gamma counter results of the activity per lymph node clearly indicate a rapid accumulation in the right side lymph nodes, mainly the inguinal close to the site of injection but also the distant axillary lymph node and a slight signal in the inguinal as well.

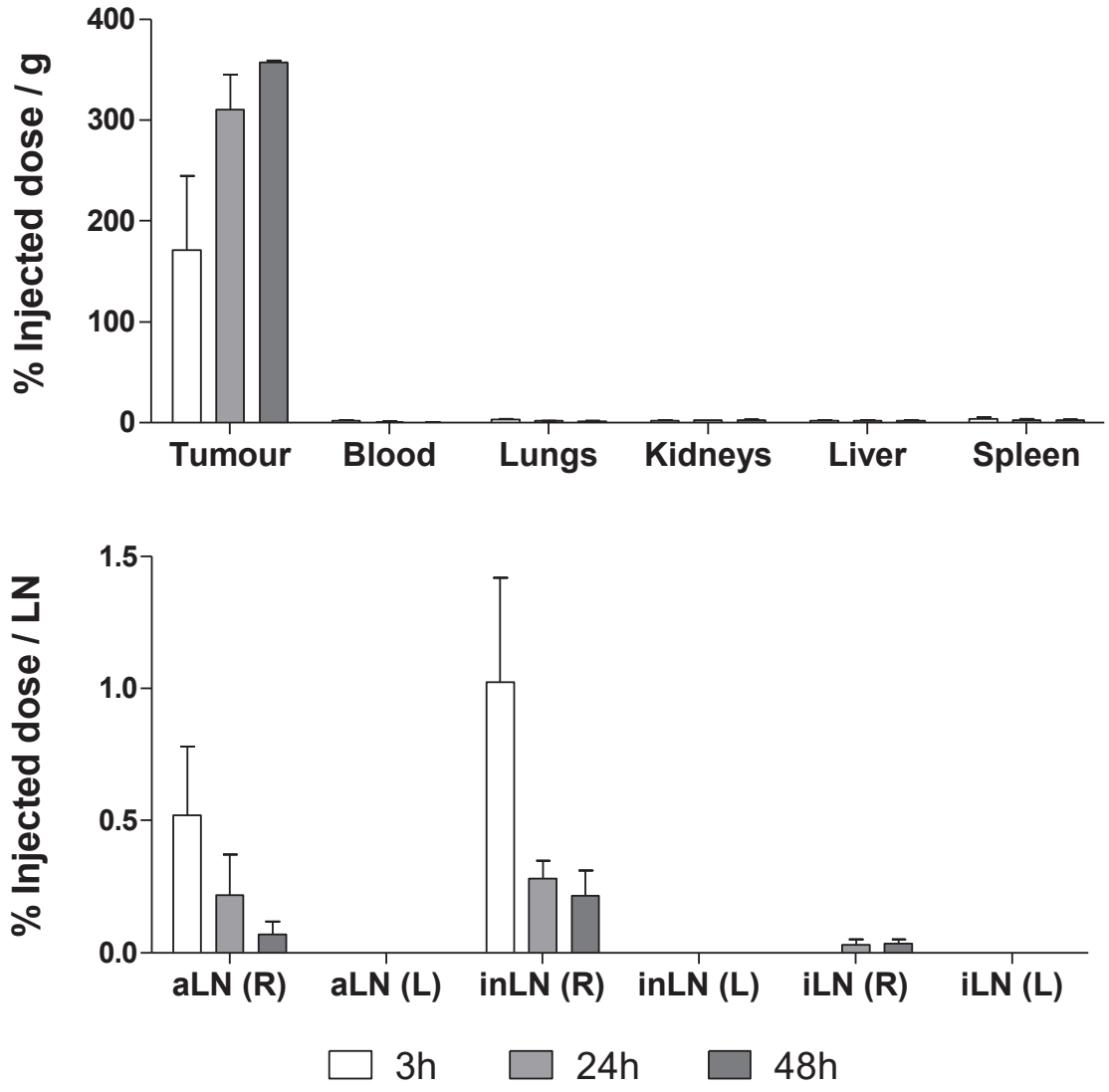

Figure 17. (*top*) Ex vivo gamma-counter analysis of the selected organs at 3, 24 and 48 h. Biodistribution expressed as percentage of injected dose per gram of tissue. (*bottom*) Ex vivo gamma-counter analysis of the selected lymph nodes at 3, 24 and 48 h. Biodistribution expressed as percentage of injected dose per gram lymph node. (R): Right side, (L): left side.

These results corroborate the ability of the nanocarrier to accumulate in the tumour area. Moreover, it is also able to enter and traffic through the lymphatic system where not only they reach the inguinal lymph nodes proximal to the site of injection but also have the capacity to migrate to the distant axillary lymph nodes directly connected via lymphatic vessels.[34]

4.2.5 In vivo therapeutic efficacy

Encouraged by the enhanced *in vitro* cancer cell killing ability of the system as well as the efficient cellular uptake and accumulation in the tumour and tumour draining lymph nodes, the *in vivo* therapeutic efficacy of the IONP-Pt was assessed next.

As an initial approach to determine if the presence of the IONP-Pt system would impact the development of the tumour, the treatment and the B16-F10 OVA cells were subcutaneously co-injected into the right back side of the mice. The administered platinum content was fixed to 0.55 mg per kilogram of animal weight as a single therapeutic dose. Throughout the experiment body weight and tumour size were monitored as indicators of the toxicity and efficacy of the therapy. In all cases the iron content was kept within the authorized doses for similar NPs (e.g. ferumoxytol).

As shown in Figure 18 both cisplatin and IONP-Pt(IV) significantly inhibited tumour growth compared to the administration of the prodrug. Remarkably, the platinum-loaded nanoparticle proved to be even more effective than cisplatin. While none of the formulations had an effect on the body weight, the tumour growth inhibition led to a significantly enhanced survival rate of mice treated with IONP-Pt(IV) (Figure 19), with all mice living over 10 more days than the control group and the group treated with the prodrug alone.

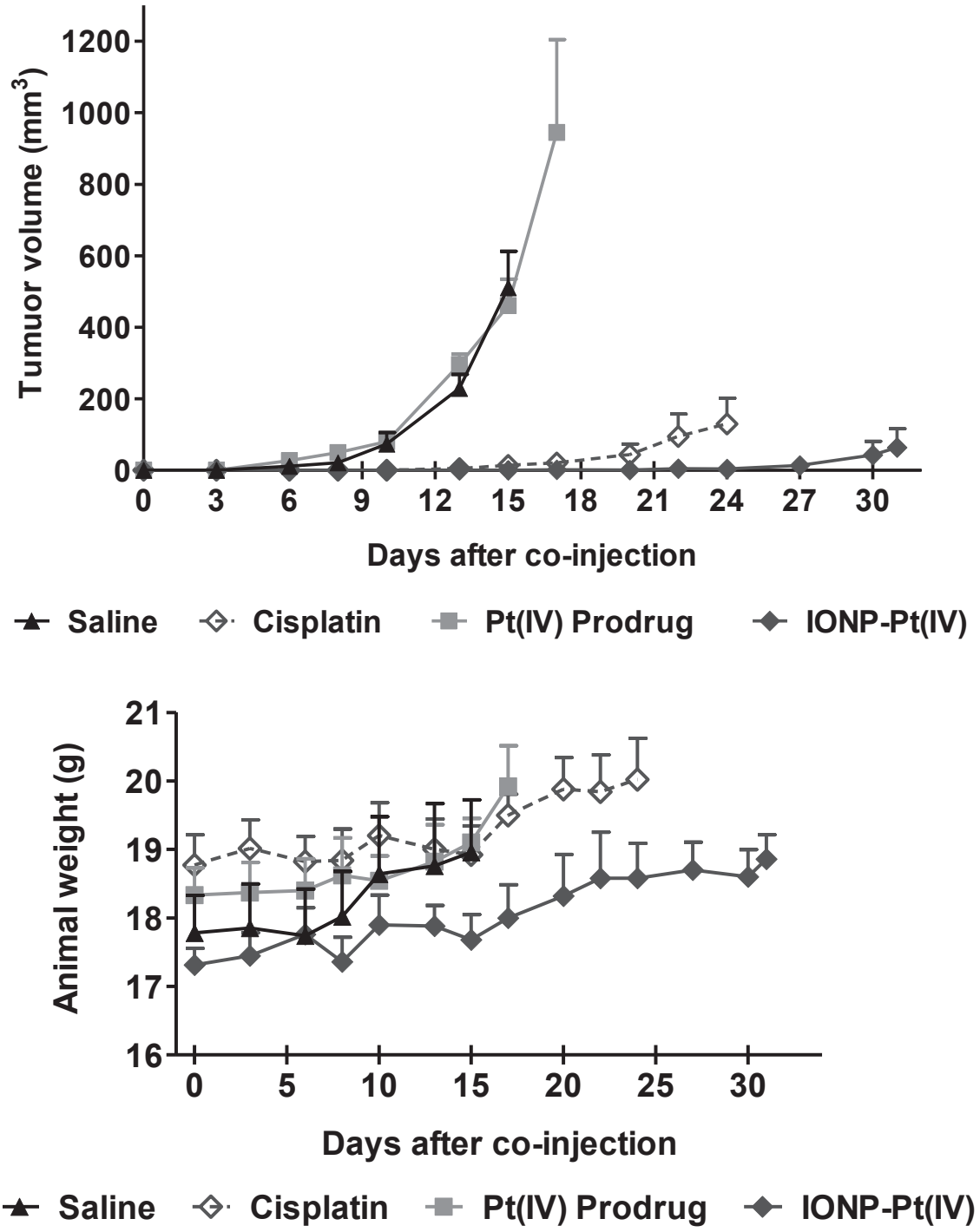

Figure 18. (*top*) Effect of cisplatin, Pt(IV) prodrug and Pt-loaded IONPs (all at 0.55 mg Pt/kg) on the growth of tumours after subcutaneous co-injection with B16-F10 OVA cells in C57BL/6 mice. Mean values and standard errors of the mean are represented (n = 5 for each group). (*bottom*) Animal weigh of C57BL/6 mice co-injected aforementioned formulations and B16-F10 OVA cells. Mean values and standard errors of the mean are represented (n = 5 for each group).

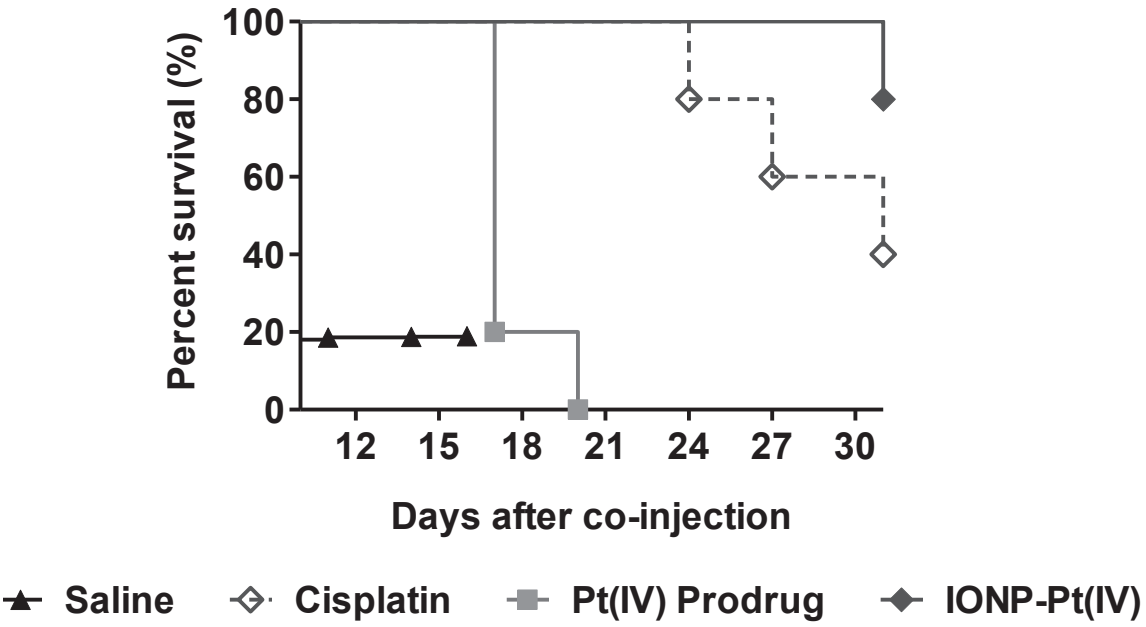

Figure 19. Survival curves of C57BL/6 mice co-injected with cisplatin, Pt(IV) prodrug or Pt-loaded IONPs (all at 0.55 mg Pt/kg) and B16-F10 OVA cells.

Following the promising results obtained with the co-injection the efficacy of the platinum-loaded nanocarrier was assessed in tumour bearing mice. To develop the tumour, the B16-F10-OVA cells were injected into the right back side of the mice and left to grow for 7 days before starting the treatment. Based on the literature about similar therapeutic efficacy studies,[35] the administration of a total of 3 doses (one every three days) was selected as the treatment strategy. Similarly to the previous experiment, regarding body weight and tumour size were monitored throughout the treatment as indicators of the toxicity and efficacy of the therapy. The platinum loaded IONP micelles and the corresponding Pt(IV) and cisplatin controls were then subcutaneously injected in the peritumoural region fixing the Pt dose to 0.24 mg per kilogram of animal weight in all cases.

In addition, a commercially available TGF-*β* inhibitor, LY364947 was incorporated to the treatment as a way to maximize the efficacy (Figure 20). When administered at a low dose, this small molecule has been described to inhibit the TGF-*β* type I receptor (T*β*R-I) and hence alter the tumour microenvironment to enhance the EPR effect, increasing the chances of the system to penetrate in the tumour area.[36,37]

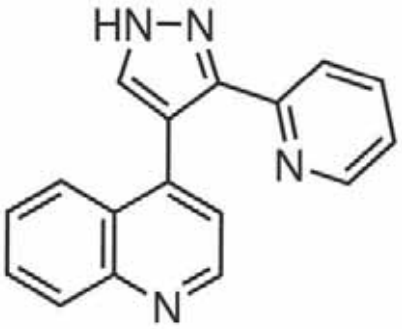

Figure 20. Chemical structure of the commercially available TGF-*β* inhibitor LY364947.

As it can be observed from the tumour volume progression in Figure 21 the IONP-Pt micelles slightly delayed the tumour growth compared to the prodrug alone and even cisplatin. When administered in combination with the TGF-*β* inhibitor however (referred to as INH in the figure), the development of the tumour was suppressed up to 10 days after the final dose. Moreover, the fact that no significant weight loss was detected suggests a good tolerance of the treatment. Most importantly the IONP-Pt system was more efficient with regards to survival than the prodrug and cisplatin, resulting in mice living up to 35 days, a very encouraging outcome for further development of the system towards the treatment of melanoma.

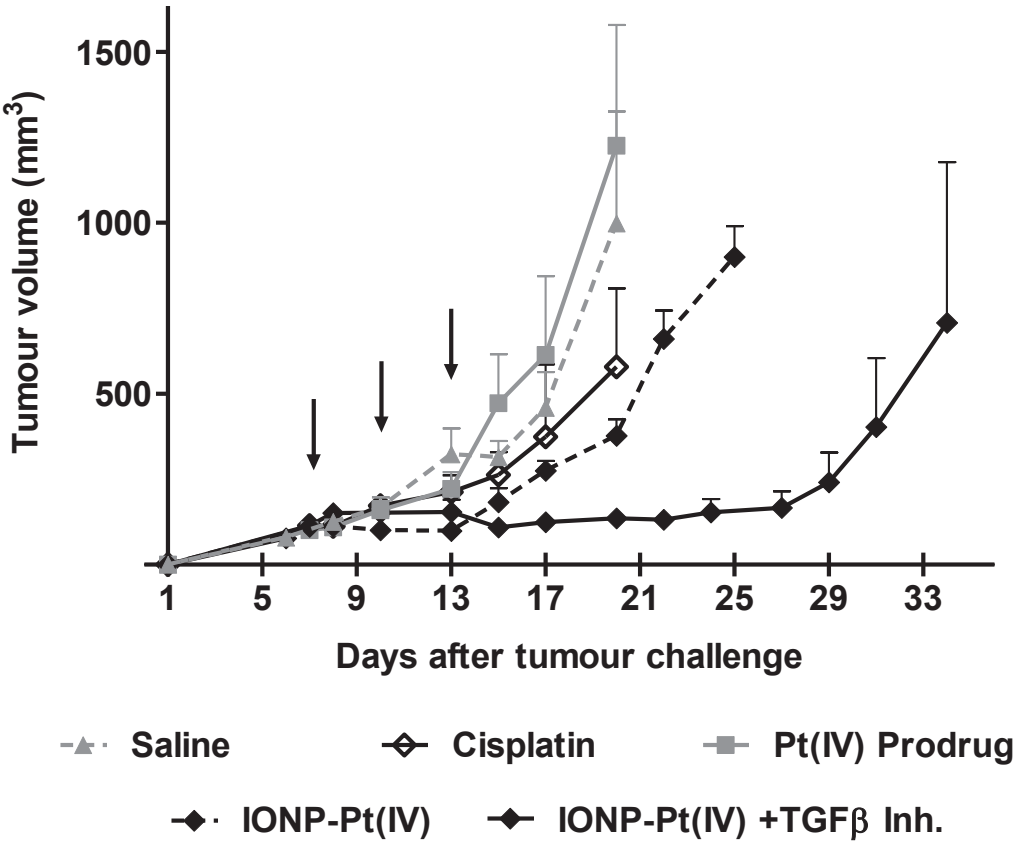

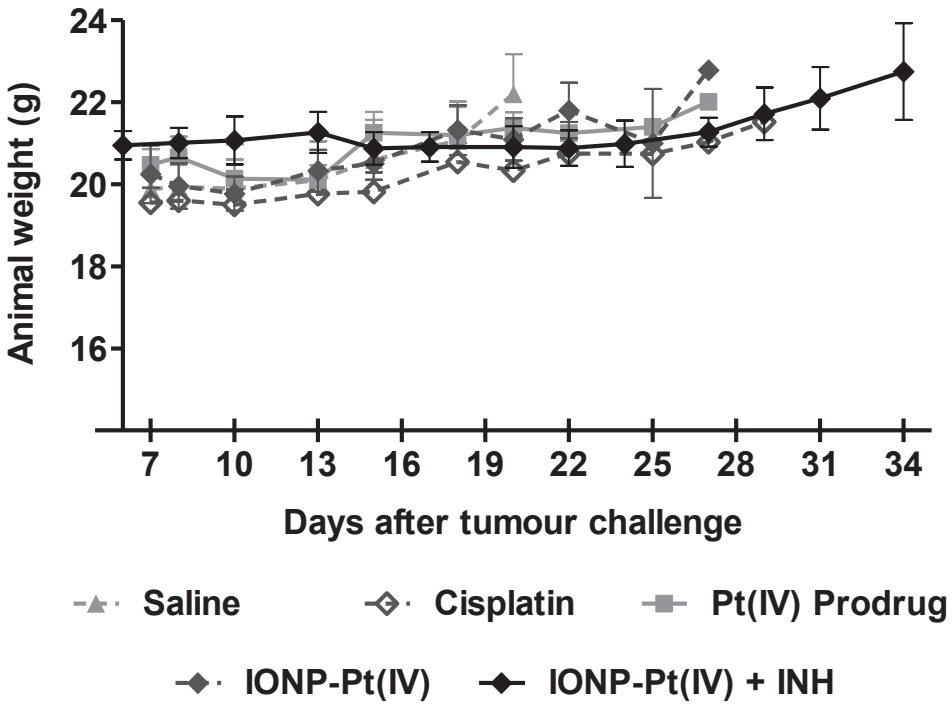

Figure 21. Effect of cisplatin, Pt(IV) prodrug and Pt-loaded IONPs (with and without TGF-*β* inhibitor) (all at 0.24 mg Pt/kg per dose) on the growth of tumours inoculated in C57BL/6 mice. Three doses of each formulation were administered every three days (marked with arrows) by subcutaneous peritumoural injection. Mean values and standard errors of the mean are represented (n = 5 for each group). Animal weight for tumour bearing mice treated with the aforementioned formulations.

These results are very promising from the therapeutic point of view as the prodrug delivered with the IONP micelles is not only better than the prodrug alone, but also more effective than cisplatin. Compared to several other recent nanocarriers developed for platinum based anticancer therapy vivo, not only is this construct is less complex, but also it is able to achieve major tumour growth inhibition with lower doses of Pt. Similar in vivo antitumour studies report platinum doses ranging from 0.65 to 1.2 mg Pt/kg for intratumoural administration[38,39] and up to 4-5 mg Pt/kg for intravenous or intraperitoneal injections.[40–46]

In addition, taking into account the highly aggressive nature of the tumour model selected for these studies, the administered dosage scheme (a dose every three days and a total of three doses) is able to achieve a remarkable tumour growth suppression

for over two weeks following the last administration. In a very similar experimental setup by Farokhzad *et al*. 5-fold larger platinum doses are administered close to the tumour area in a prostate cancer xenograft model twice a week for over 5 weeks.[38] Despite the sustained administration and in contrast to the results with the IONP-Pt system, the treatments failed to delay the tumour growth but only produced a slower but steady growth of the tumour (Figure 22).

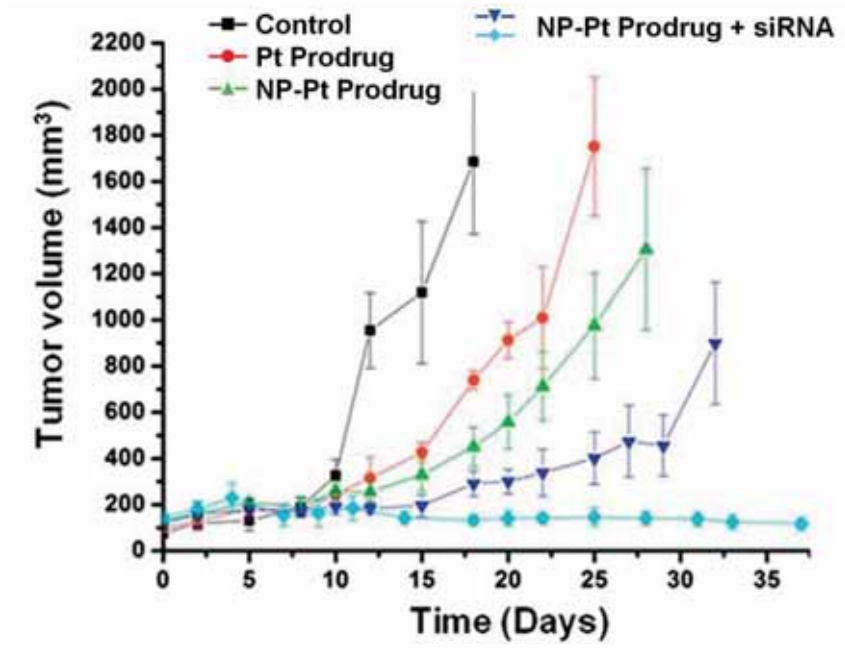

Figure 22. Tumour growth progression of LNCaP prostate cancer xenograft model treated with a platinum prodrug containing nanoparticles. Adapted from [38]

The improvement of the therapeutic efficiency of the system in the presence of the TGF-*β* inhibitor is quite remarkable, however it might not only be related to an increased uptake provoked the change in the permeability of the tumour microenvironment. TGF-*β* also plays an important role within the immune system, being indeed one of the immunosuppressive factors known to be secreted by tumour cells and that might among other aspects be involved in the ability of melanomas to evade immunotherapeutic approaches.[47] Described in several studies, this cytokine has been described to cause a reduction in the activity of T lymphocytes and natural killer cells while producing an increase of regulatory T lymphocytes, therefore producing a deleterious effect over the immune response.[48-50] Therefore, the administration of a

TGF-*β* inhibitor would help counteract the immunosuppressive effect of the cytokine and enhance the immune responses.[51-52]

Although the platinum-loaded IONP micelles are designed for improving the chemotherapy, it is important to note that the hydrophobic nature of the IONP cores may also add an immunotherapeutic contribution to the system. Once injected *in vivo* the micelle structures are subjected to degradation over time, leading to the release of the hydrophobic IONP cores. Hydrophobic moieties or motifs have indeed been proposed to belong to an ancient family of DAMPs. Described by Seong and Matzinger,[53] these hydrophobic portions which are often protected, act as universal DAMPs when they become exposed and are able to activate the innate immune system through interaction with TLRs. In this case, the micelle structure provides a stealth immunostimulatory component that only becomes active once the system has degraded *in vivo*.

Therefore, the notably improved antitumour therapeutic efficacy of the IONP-Pt system showed in Figure 21 is most likely a combination of different contributions including the chemotherapeutic effect of the platinum prodrug, the immunostimulatory activity of the hydrophobic IONP cores and the effect of the TGF-*β* inhibitor in enhancing this immune response.

4.3 Conclusions

This chapter has focused on the use of a covalent strategy to attach a platinum (IV) prodrug to PEG-phospholipids which then were used to prepare water soluble IONP-filled micelles, and testing the efficacy of these construct in an aggressive murine melanoma model. This simple construct fulfils many of the requirements for a successful drug delivery system for the treatment of metastatic melanoma. *In vitro* results indicate a rapid internalization of the system by cancer cells as well as an enhanced cytotoxicity of the prodrug when delivered with the micelle nanocarrier. Moreover, the size of the small micelle aggregates falls within the optimum range for lymphatic trafficking, a key aspect for the potential application against lymph node mediated metastatic spread.

The use of a chelator-free strategy to incorporate ^{67}Ga as a radiolabel allowed the use of highly sensitive nuclear imaging to track the biodistribution of the nanocarrier *in vivo*. SPECT images following the subcutaneous administration of the system indeed show the accumulation of the prodrug-loaded IONP micelles in the tumour as well as the effective uptake by the lymphatic system with migration to draining and distant lymph nodes. The *in vivo* therapeutic efficacy experiments have also led to promising results and made clear that the system has the potential to produce a strong therapeutic effect against metastatic melanoma.

Moreover, in view of the results, the promising antitumour effect of the system might be due to a combination of different contributions. In addition to the chemotherapeutic effect given by the platinum prodrug, the intrinsically hydrophobic nature also provides the construct with a stealth immunostimulatory component. Finally, the use of a TGF-*β* inhibitor might not only serve as a way to enhance the penetration of the micelles into the tumour, but also reinforce the antitumour immune responses.

In conclusion, this system can serve as the starting point for developing novel chemo-immunotherapeutic constructs for melanoma that integrates different treatment modalities and imaging capabilities in a simple construct.

4.4 Experimental Section

4.4.1 Materials

All syntheses were carried out with the following commercially available reagents used without further purification. Chloroform (water 0.005%) was purchased from LABSCAN, dimethylsulfoxide (≥ 99.5%) was purchased from Panreac. 1,2-dipalmitoyl-*sn*-glycero-3-phosphoethanolamine-N-[methoxy(polyethylene glycol)-2000] (ammonium salt) (PEG-OMe), 1,2-distearoyl-*sn*-glycero-3-phosphoethanolamine-N-[amino(polyethylene glycol)-2000] (ammonium salt) (PEG-NH_2) and 1,2-dipalmitoyl-*sn*-glycero-3-phosphoethanolamine-N-(lissaminerhodamine B sulfonyl) (Rho-PS) were purchased from Avanti Polar Lipids. 4-(dimethylamino)pyridine (99%), *N,N'*-dicyclohexylcarbodiimide (99%), LY364947, sulforhodamine B sodium salt and trichloroacetic acid (> 99%) were purchased from Sigma.

Cisplatin and *cis,trans*-$[Pt(NH_3)_2Cl_2(O_2CCH_2CH_2CO_2H)_2]$ (**1**) were prepared as described in chapter 3. Hydrophobic IONPs were prepared by Dr. N. Gómez Blanco following a previously described protocol.[25]

4.4.2 Synthesis of PEG-Pt

In a typical reaction, *cis,cis,trans*-$[Pt(NH_3)_2Cl_2(O_2CCH_2CH_2CO_2H)_2]$ (**1**) (9.6 mg, 18.0 μmol), dicyclohexylcarbodiimide (DCC) (3.7 mg, 18.0 μmol) and 4-(dimethylamino) pyridine (1.0 mg, 7.2 μmol) were dissolved in DMSO (130 μL). This solution containing the activated platinum (IV) complex was added to a DMSO solution of PEG-NH_2 (10 mg, 3.6 μmol, 170 μL). The resulting mixture was allowed to react at room temperature for 72 h under continuous stirring and protected from the light. Water was then added to the reaction mixture and the solution was centrifuged to remove the insoluble material. The supernatant was filtered (0.45 μm) and dialyzed in a Slide-A-Lyzer dialysis cassette (Thermo Scientific, MW cut-off 2000 Da) against water. Finally the dialyzed product (PEG-Pt) was lyophilized and stored in a stock solution of 10 mg/mL in 2:1 $CHCl_3$:MeOH.

4.4.3 Synthesis of water soluble IONP micelles

For the control micelles, hydrophobic Fe_3O_4 nanoparticles (0.5 mg) and PEG-OMe (1 mg) were dissolved in chloroform (500 μL). The solvent was allowed to evaporate overnight at room temperature. Any remaining solvent was removed under vacuum. The dried residue was heated in a water bath at 80 ºC for 30 s and rehydrated in 1 mL of nanopure water. The solution was centrifuged at 7300 × g for 5 minutes. The pellet was discarded and the supernatant was filtered (0.45 μm). To eliminate the free PEG, the solution was ultracentrifuged (369000 x g, 45 min, three cycles). The final pellet was resuspended in a known volume of nanopure water or saline 0.9% solution. The purified micelles were stored at room temperature.

For the platinum-loaded micelles, all the synthesis and purification steps were performed in darkness. Hydrophobic Fe_3O_4 nanoparticles (0.5 mg) and PEG-Pt (100 μL of a 10 mg/mL solution on 1:2 MeOH:$CHCl_3$) were dissolved in chloroform (to a final volume of 500 μL). The solvent was allowed to evaporate overnight at room temperature. Any remaining solvent was removed under vacuum. The dried residue was heated in a water bath at 80 ºC for 30 s, after which 1 mL of nanopure water was added. The solution was transferred to a microtube and centrifuged at 1800 x g for 3 minutes. The pellet was discarded and the supernatant was filtered (0.45 μm). To eliminate the free PEG, the solution was ultracentrifuged (140000 x g, 30 min, three cycles). The final pellet was resuspended in a known volume of nanopure water or saline 0.9% solution and stored at room temperature.

Fluorescent micelles were prepared as above by introducing a commercial rhodamine labelled phospholipid into the mixture prior to the solvent evaporation (15 μL from a 2 mg/mL solution).

For ICP analysis, acid digestion of sample aliquots was carried out in concentrated HNO_3. Prior to the measurements digested samples were diluted in nanopure water to a final acid concentration of 1-2%.

4.4.4 Cell culture experiments

The B16-F10-OVA melanoma cell line was a gift from Dr. P. Sarobe (Centre for Applied Medical Research (CIMA), University of Navarra). Cells were cultured in RMPI 1640 (Lonza) supplemented with 10% foetal bovine serum (FBS), 1% penicillin/streptomycin and L-Glutamine (all from Glibco®) and maintained in a humidified atmosphere of 5% CO_2 at 37 ºC. For cytotoxicity studies cells were seeded (1000 cells/well in complete RPMI medium) in 96-well plates (100 μL/well) and allowed to adhere overnight. The samples to be tested were accordingly diluted in media and added directly to the cells (100 μL/well), in triplicate. After 72 h incubation at 37 ºC, cell viability was measured using MTT assay. Briefly, 100 μL/well of MTT reagent (0.25 mg/mL in RPMI 1640) was added after the removal of the supernatants. Cells were incubated at 37 ºC for 1 h after which the medium was removed and the lysis solution added (DMSO, 200 μL/well). The absorbance was measured at 550 nm and the data represented as cell viability compared to the untreated control wells.

Cell imaging. B16-F10-OVA cells were plated in an ibidi 15 well angiogenesis μ-Slide at a density of 4000 cells/well and allowed to adhere overnight in the presence of complete RPMI 1640 medium. Then, the medium was removed and fresh medium containing the rhodamine labelled Pt-loaded IONP micelles was added and incubated for 2 h. Nuclei were stained with Hoechst 33342 (5 μg/mL in RPMI medium) for 5 minutes. After the nuclear staining the cells were washed twice with PBS (10 mM) and fresh medium was added prior to image acquisition.

Cellular uptake by flow cytometry. B16-F10-OVA cells were plated in 96-well plates (10^5 cell/well) and allowed to adhere overnight in complete RMPI 1640 medium. Fluorescent formulations containing rhodamine labelled Pt-loaded IONP were diluted in medium accordingly and added to the cells at a final concentration of 1 mM Fe for 2 h incubation at 37 ºC. The supernatant was removed and cells washed with PBS (10 mM). The adherent cells were transferred to cytometer tubes and washed with PBS (10 mM). Cells were resuspended in a final volume of 200 μL of flow cytometry buffer (1% BSA, 0.1% sodium azide in PBS 10 mM) and analyzed by flow cytometry.

4.4.5 Labelling of the Pt-loaded IONP micelles with ^{67}Ga

^{67}Ga was purchased as a citrate solution from Molypharma (Spain) (specific activity = 1.4 TBq/μmol), and converted to $^{67}GaCl_3$ following a previously reported method. Briefly, the gallium citrate solution was passed through a light silica column cartridge (Sep-Pak, Waters) to selectively retain the radiometal. The cartridge was washed with ultrapure water (10 mL) and ^{67}Ga was finally eluded with HCl 0.1 M. The eluate was collected in different 100μL fractions, and only those containing maximum activity concentration were used in subsequent labelling experiments. The eluded $^{67}GaCl_3$ solution (100 μL, c.a. 37 MBq) was then mixed with 50 μL of a Pt-loaded IONP micelle solution and diluted to a final volume of 350 μL in acetate buffer (pH = 3.8 ± 0.1). After a 30 minute incubation at 70 ºC, the reaction crude was cooled down to room temperature and the labelled IONPs were separated via centrifugal filtration (6708 x g, 10 min) using AmiconUltracel 100k (MWCO 100 kDa) centrifugal devices (Merck) and washed twice with saline solution. The retentate was recovered from the filter by the addition of saline solution (100 μL). The total radioactivity in the filtrated and retentates was measured in a CRC-25R dose calibrator (Capintec, USA) in order to determine the incorporation efficiency.

For stability studies, one batch of ^{67}Ga-IONP-Pt micelles was fractions in different aliquots and incubated in the presence of the chelating agent DOTA (10^6 mol DOTA per NP mol) at 37 ºC. At different time points, the samples were filtered to separate the IONPs from the ^{67}Ga complexed to DOTA and the radioactivity in the retentate and filtrate was measured in a 2470 WIZARD2 Automatic Gamma Counter (PerkinElmer). The dissociation of ^{67}Ga from the radiolabelled micelles was calculated (expressed in percentage) at each time point as the ratio between the amount of radioactivity on the filter and the starting radioactivity.

4.4.6 In vivo experiments

Tumour inoculation. C57BL/6 mice (6-8 weeks old) were used for all *in vivo* experiments. B16-F10-OVA cells were used for the tumour inoculation and were

previously cultured similarly to what described for the *in vitro* experiments. Prior to injecting *in vivo*, cells were tested for mycoplasma using the commercially available MYCOALERT Mycoplasma Detection Kit (Lonza). For tumour inoculation 300,000 cell/mouse were dissolved in Corning® Matrigel® Basement Membrane Matrix High Concentration diluted in PSB 10 mM (1:4 PBS:Matrigel®). All the material (tips, pipettes, syringes and storage vials) and the cell suspension in Matrigel® were kept in ice until use. The suspension was then loaded in a syringe and 100 µL/mouse injected into the right back side of the animals using a 23 G needle. Animals were monitored for tumour growth using an electronic digital calliper 779A series (Starrett) until the tumour size was appropriate to start the therapy or SPECT/CT Imaging (~ 100 mm^3, ~ 7 days from tumour inoculation).

Biodistribution SPECT/CT studies. C57BL/6 mice (6-8 weeks old) were injected with ^{67}Ga-IONP-Pt micelles in saline solution subcutaneously in the peritumoural region (110 µL, 15.69 MBq, 2.7 mg Fe/kg, 0.24 mg Pt/kg). With the mice under isofluorane anaesthesia (1.5-2% in oxygen), whole body SPECT/CT scans were acquired at 3 h, 24 h and 48 h post-injection. With the full ring detector, 360° data was acquired by rotating the collimator 45° (45 steps, 1°/step). Data was collected in an energy acquisition window from 125-150 keV to 84-102 keV and acquisition times from 60 min (80 s/step) to 45 min (60 s/step). During image acquisition, mice were kept normothermic using a heating blanket (Homeothermic Blanket Control Unit; Bruker BioSpin GmbH, Karlsruhe, Germany). After each SPECT scan, CT acquisitions were performed to provide anatomical information on each animal. The CT acquisition consisted of 220 views in 0.88° increments around the animal with 16 ms exposure per view. The X-ray tube settings were 70 kV and 32 mA. SPECT/CT images were acquired using the eXplore speCZT CT preclinical imaging system (GE Healthcare, USA).

The system combines SPECT and CT on one gantry, allowing co-registration of the SPECT and CT data sets without additional post-processing. The SPECT scanner uses a stationary, full ring of CZT detectors and interchangeable rotating cylindrical collimators. An 8-slit collimator was used with a field of view of 32 and 78 mm in the transaxial and axial directions, respectively. The SPECT images were reconstructed

using the OSEM iterative algorithm (5 and 15 subsets, 3 and 5 iterations) into 128 x 128 x 32 array with a voxel size of 0.4 x 0.4 x 2.46 mm, and were not corrected for scatter and attenuation. The CT images were reconstructed using a cone beam filtered back-projection Feldkamp algorithm into 437 x 437 x 523 array with a voxel size of 0.2 x 0.2 x 0.2 mm. At the end of the scanning procedure, the mice were culled by cervical dislocation and organs of interest removed for further *ex vivo* SPECT/CT imaging under the same conditions of the *in vivo* images. Analysis of the injected dose percentage per organ was performed by measuring their activity with a WIZARD^{2}2470 Automatic Gamma Counter (PerkinElmer).

In vivo therapeutic efficacy. For the co-injection experiment both the B16-F10 OVA cells (300,000 cell/mouse) and the corresponding samples were injected into the right back side of the mice. For the experiment in tumour bearing mice, the theapy started roughly 1 week after the tumour inoculation (Day 0), when the tumour size reached ~ 100 mm^3. The corresponding doses were injected on days 7, 10 and 13 in the subcutaneous peritumoural region (~ 2 cm away from the tumour). In each case, 1 h prior to sample administration, TGF-*β* inhibitor LY364947 (1 mg/kg) was administered by intraperitoneal injection (for the groups without TGF-*β* inhibitor, saline solution was similarly injected). All samples were prepared in saline solution (0.9% NaCl) with the a similar platinum concentration for all the groups (the injected iron concentration never exceeded 5 mg Fe/Kg). Similarly to the tumour inoculation step, animals were monitored for tumour growth using an electronic digital calliper 779A series (Starrett). Results of tumour volume, animal weight and survival rate are expressed as mean ± SEM (n = 5).

4.4.7 Instrumentation

HPLC-MS. Liquid chromatography was performed on an ACQUITY UPLC system (Waters, Milford, USA) with a conditioned autosampler at room temperature. The separation was carried out on an ACQUITY UPLC BEH C18 column (100 mm x 2.1 mm i.d., 1.7 μm). The column temperature was maintained at 40 ºC. The analysis was achieved using 100mM ammonium formate H_2O/MeOH as the mobile phase with a

flow rate of 0.3 mL/min. The injection volume was 5 μL. A Waters LCT-ToF premier Spectrometer (Waters, Milford, USA) was connected to the UPLC system via an electrospray ionization (ESI) interface. The ESI source was operated in W-optics positive ionization scan mode with the capillary voltage at 2.5 kV. The temperature source and desolvation was set at 120 ºC. The cone and desolvation gas flows were 50 L/h and 600 L/h, respectively. The instrument was calibrated over a 50-4000 m/z range before each measurement using a standard NaI solution (1 μM). All data collected in the centroid mode was processed using Masslynx software (Waters, Mildord, USA).

NMR studies. ^{1}H NMR spectra were recorded on a Bruker Avance 500 NMR spectrometer at 298 K. Data processing was carried out using Mnova software. ^{1}H NMR spectra were recorded in D_2O and the chemical shifts were expressed relative to the water peak at 4.8 ppm.

XPS measurements. XPS experiments were performed in a SPECS Sage HR 100 spectrometer with a non-monochromatic X-ray source (Magnesium Kα line of 1253.6 eV energy and 250 W), placed perpendicular to the analyzer axis and calibrated using the $3d_{5/2}$ line of Ag with a full width at half maximum (FWHM) of 1.1 eV. The selected resolution for the spectra was 15 eV of Pass Energy and 0.15 eV/step for the detailed spectra of the Pt 4f peaks. The deconvolution of the Pt 4f peaks was carried out at 36 s of X-ray exposure. The deconvolution allowed to estimate the ratio of the Pt(II) and Pt(IV) states. All measurements were made in an ultra high vacuum (UHV) chamber at a pressure below $5 \cdot 10^{-8}$ mbar. In the fittings Gaussian-Lorentzian functions were used, where the FWHM of all the peaks were constrained while the peak positions and areas were set free.

TEM. TEM studies were conducted in a JEOL JEM-2011 electron microscope operating at 200 kV. The samples were prepared by depositing a drop of nanoparticle solution onto a copper specimen grid coated with a holey carbon film and allowing it to dry. For nanoparticle size determination a minimum of 300 particles were measured using the *Image J* software.

ICP-MS. ICP-MS measurements were performed by the SGIker analytical facility of

the University of the Basque Country (EHU/UPV, Leioa, Spain). ICP-AES measurements were carried out using a Perking Elmer optima 5300 DV (Perkin Elmer, Santa Clara, USA) employing an RF forward power of 1400 W, with argon gas flows of 15, 0.2 and 0.75 L/min for plasma, auxiliary and nebulizer flows respectively. Using a peristaltic pump sample solutions were taken up into a Gem Top Cross-Flow nebulizer and Scotts spray chamber at a rate of 1.5 mL/min. The instrument was operated in axial mode. To measure the iron content three wavelengths (238.024, 239.562, 259.939 nm) were selected and analyzed in a fully quant mode (three points per unit wavelength). A range of calibration standards were prepared using single element 1000 mg/L stock solutions (Fisher Scientific UK LDT) and Merk multi element standard (ICP Multi element standard solution VICertiPUR®) was used as a reference standard.

ICP-MS studies were performed on an Agilent 7700x ICP-MS (Agilent Technologies, Palo Alto, USA) with a MicroMist micro-uptake glass concentric nebulizer (Glass Expansion, West Melbourne, Victoria, Australia) and RF power of 1550 W with gas flows of 15 and 1.05 L/min for plasma an carrier respectively. To measure the platinum content three isotopic masses (m/z 194, 195 and 195) were selected and analyzed in spectrum mode (three points per unit point/mass and 200 ms integration time). In order to reduce MO^+ formation in the plasma, the spray chamber was peltier cooled at 2 ºC. A standard quartz torch with 2.5 mm internal diameter injector was used. Finally, standard nickel cones (sample and skimmer) were used. The optimization of the ICP-MS conditions was achieved by adjusting the torch position sand tuning for reducing oxide and doubly charged ion formation with a standard tuning solution containing 1.0 µg/L of ^{7}Li, ^{24}Mg, ^{59}Co, ^{89}Y, ^{140}Ce and ^{205}Tl in 1% HNO_3. This equipment includes a collision cell (He gas, ORS3 system, Agilent Technologies) to discriminate spectral interferences with high performance.

UV-Vis and Fluorescence spectroscopy. UV-vis measurements were performed in H_2O using a Varian Cary 5000 spectrophotometer. Absorbance measurements on 96-well plates were carried out on a TECAN Genios Pro 96/384 multifunction microplate reader. Fluorescence emission spectra were recorded with a Horiba Jovin Ibon Fluorolog fluorometer.

DLS and ζ-potential. Particle size analysis was performed using a NanoSizer (Malvern Nano-ZS, UK) with 173° scattering angle at 25 ºC. Each sample was measured at least in triplicate. Z-potential measurements were carried out with the same NanoSizer equipment at 25 ºC and a cell drive voltage of 20 V using a Smoluchowski model.

Flow cytometry. All flow cytometry experiments were carried out in a FACS Canto II (BD Bioscience) system, which has an excitation source composed of three lasers: violet (405 nm), blue (488 nm) and red (633 nm). The laser excitation wavelength used for rhodamine B was 488 nm and the emission filter 585/42 nm. In all measurements cells were electronically gated based on forward and side scatter parameters and the not-singlet events leaved out based on forward area and height parameters. Each analysis represented the acquisition of 10000 cells per sample and data was analyzed with FlowJo LLC software.

Fluorescence microscopy. Live cell fluorescence images were obtained using Zeiss Axio Observer wide field fluorescence microscope (Carl Zeiss, Germany). For Hoechst staining a colibri LED module was used for fluorescence excitation at 365 nm and Fluorescence emission was collected using a high-efficiency multi-band pass colibri filter set which included a 402-488 nm bandpass. A mercury short-arc HXP lamp was used for the excitation of rhodamine B and the fluorescent emission was collected using an emission filter with a 570-640 nm bandpass. Brightfield and fluorescence images were collected and processed using AxioVision software.

4.5 References

(1) Melanoma of the Skin - Cancer Stat Facts https://seer.cancer.gov/statfacts/html/melan.html (accessed May 4, 2017).

(2) Arvin, S.; Chapman, P. B. *Hematol. Oncol. Clin. North Am.* **2009**, *23*, 583.

(3) Kirchner, H. H.; Atzpodien, J.; Poliwoda, H. *Med. Klin.* **1996**, *91 Suppl 3*, 44.

(4) Daponte, A.; Ascierto, P. A.; Gravina, A.; Melucci, M.; Scala, S.; Ottaiano, A.; Simeone, E.; Palmieri, G.; Comella, G. *Anticancer Res.* **2005**, *25*, 1441.

(5) Zupi, G.; Scarsella, M.; Semple, S. C.; Mottolese, M.; Natali, P. G.; Leonetti, C. *Clin. Cancer Res.* **2005**, *11*, 1990.

(6) Pandha, H. S.; Heinemann, L.; Simpson, G. R.; Melcher, A.; Prestwich, R.; Errington, F.; Coffey, M.; Harrington, K. J.; Morgan, R. *Clin. Cancer Res.* **2009**, *15*, 6158.

(7) Kubo, H.; Matsumoto, K.; Funahashi, M.; Takagi, H.; Kitajima, Y.; Taniguchi, S.; Saida, T. *Melanoma Res.* **2000**, *10*, 223.

(8) Alitalo, A.; Detmar, M. *Oncogene* **2012**, *31*, 4499.

(9) Ahmed, A.; Sadadcharam, G.; Huisma, F.; Fogarty, K.; Mushtaque, M.; Shafiq, A.; Redmond, P. *ISRN Surg.* **2013**, *2013*, 382138.

(10) Rao, D. A.; Forrest, M. L.; Alani, A. W. G.; Kwon, G. S.; Robinson, J. R. *J. Pharm. Sci.* **2010**, *99*, 2018.

(11) Darwis, Y.; Ali Khan, A.; Mudassir, J.; Mohtar, N. *Int. J. Nanomedicine* **2013**, *8*, 2733.

(12) McLennan, D. N.; Porter, C. J. H.; Charman, S. a. *Drug Discov. Today Technol.* **2005**, *2*, 89.

(13) Rigon, R. B.; Oyafuso, M. H.; Fujimura, A. T.; Gonçalez, M. L.; Do Prado, A. H.; Gremião, M. P. D.; Chorilli, M. *Biomed Res. Int.* **2015**, *2015*, 16.

(14) Li, J.; Wang, Y.; Liang, R.; An, X.; Wang, K.; Shen, G.; Tu, Y.; Zhu, J.; Tao, J. *Nanomedicine: Nanotech., Biol. Med.* **2015**, *11*, 769.

(15) Zhang, W.; Shi, Y.; Chen, Y.; Hao, J.; Sha, X.; Fang, X. *Biomaterials* **2011**, *32*, 5934.

(16) Talelli, M.; Iman, M.; Varkouhi, A. K.; Rijcken, C. J. F.; Schiffelers, R. M.; Etrych, T.; Ulbrich, K.; van Nostrum, C. F.; Lammers, T.; Storm, G.; Hennink, W. E. *Biomaterials* **2010**, *31*, 7797.

(17) Yang, Q.; Aires, D. J.; Cai, S.; Fraga, G. R.; Zhang, D.; Li, C. Z.; Forrest, M. L. *J. Drugs Dermatol.* **2014**, *13*, 283.

(18) Xiao, M.; Liang, R.; Deng, R.; Dong, L.; Yi, S.; Zhu, J.; Tao, J. *J. Control. Release* **2013**, *172*, e44.

(19) Cabral, H.; Makino, J.; Matsumoto, Y.; Mi, P.; Wu, H.; Nomoto, T. *ACS Nano* **2015**, 4957.

(20) Lim, S. W.; Kim, H. W.; Jun, H. Y.; Park, S. H.; Yoon, K. H.; Kim, H.S.; Jon, S.; Yu, M. K.; Juhng, S. K. *Acad. Radiol.* **2011**, *18*, 504.

(21) Cobaleda-Siles, M.; Henriksen-Lacey, M.; De Angulo, A. R.; Bernecker, A.; Vallejo, V. G.; Szczupak, B.; Llop, J.; Pastor, G.; Plaza-Garcia, S.; Jauregui-Osoro, M.; Meszaros, L. K.; Mareque-Rivas, J. C. *Small* **2014**, *10*, 5054.

(22) Ruiz-De-Angulo, A.; Zabaleta, A.; Gómez-Vallejo, V.; Llop, J.; Mareque-Rivas, J. C. *ACS Nano* **2016**, *10*, 1602.

(23) Hernández-Gil, J.; Cobaleda-Siles, M.; Zabaleta, A.; Salassa, L.; Calvo, J.; Mareque-Rivas, J. C. *Adv. Healthcare Mater.* **2015**, *4*, 1034.

(24) Graf, N.; Lippard, S. J. *Adv. Drug Deliv. Rev.* **2012**, *64*, 993.

(25) Sun, S.; Zeng, H.; Robinson, D. B.; Raous, S.; Rice, P. M.; Wang, S. X.; Li, G. *J. Am. Chem. Soc.* **2004**, *126*, 273.

(26) Barrow, M.; Taylor, A.; Murray, P.; Rosseinsky, M. J.; Adams, D. J. *Chem. Soc. Rev.* **2015**, *44*, 6733.

(27) Mishra, P.; Nayak, B.; Dey, R. K. *Asian J. Pharm. Sci.* **2016**, *11*, 337.

(28) Weingart, J.; Vabbilisetty, P.; Sun, X.-L. *Adv. Colloid Interface Sci.* **2013**, *197-198*, 68.

(29) Gómez Blanco, N.; Jauregui-Osoro, M.; Cobaleda-Siles, M.; Maldonado, C. R.; Henriksen-Lacey, M.; Padro, D.; Clark, S.; Mareque-Rivas, J. C. *Chem. Commun.* **2012**, *48*, 4211.

(30) Xie, Y.; Bagby, T. R.; Cohen, M. S.; Forrest, M. L. *Expert Opin. Drug Deliv.* **2009**, *6*, 785.

(31) Kuzu, O. F.; Nguyen, F. D.; Noory, M. a; Sharma, A. *Cancer Growth Metastasis* **2015**, *8*, 81.

(32) Herlyn, M.; Fukunaga-Kalabis, M. *J. Invest. Dermatol.* **2010**, *130*, 911.

(33) Stacker, S. A.; Williams, S. P.; Karnezis, T.; Shayan, R.; Fox, S. B.; Achen, M. G. *Nat. Rev. Cancer* **2014**, *14*, 159.

(34) Harrell, M. I.; Iritani, B. M.; Ruddell, A. *J. Immunol. Methods* **2008**, *332*, 170.

(35) Kang, T. H.; Mao, C. P.; Lee, S. Y.; Chen, A.; Lee, J. H.; Kim, T. W.; Alvarez, R. D.; Roden, R. B. S.; Pardoll, D.; Hung, C. F.; Wu, T. C. *Cancer Res.* **2013**, *73*, 2493.

(36) Zuo, Z. Q.; Chen, K. G.; Yu, X. Y.; Zhao, G.; Shen, S.; Cao, Z. T.; Luo, Y. L.; Wang, Y. C.; Wang, J. *Biomaterials* **2016**, *82*, 48.

(37) Kano, M. R.; Bae, Y.; Iwata, C.; Morishita, Y.; Yashiro, M.; Oka, M.; Fujii, T.; Komuro, A.; Kiyono, K.; Kaminishi, M.; Hirakawa, K.; Ouchi, Y.; Nishiyama, N.; Kataoka, K.; Miyazono, K. *Proc. Natl. Acad. Sci. U.S.A.* **2007**, *104*, 3460.

(38) Xu, X.; Xie, K.; Zhang, X. Q.; Pridgen, E. M.; Park, G. Y.; Cui, D. S.; Shi, J.; Wu, J.; Kantoff, P. W.; Lippard, S. J.; Langer, R.; Walker, G. C.; Farokhzad, O. C. *Proc. Natl. Acad. Sci. U.S.A.* **2013**, *110*, 18638.

(39) He, C.; Liu, D.; Lin, W. *Biomaterials* **2015**, *36*, 124.

(40) Mattheolabakis, G.; Taoufik, E.; Haralambous, S.; Roberts, M. L.; Avgoustakis, K. *Eur. J. Pharm. Biopharm.* **2009**, *71*, 190.

(41) Dhar, S.; Kolishetti, N.; Lippard, S. J.; Farokhzad, O. C. *Proc. Natl. Acad. Sci. U.S.A.* **2011**, *108*, 1850.

(42) Graf, N.; Bielenberg, D. R.; Kolishetti, N.; Muus, C.; Banyard, J.; Farokhzad, O. C.; Lippard, S. J. *ACS Nano* **2012**, *6*, 4530.

(43) Pichler, V.; Mayr, J.; Heffeter, P.; Dömötör, O.; Enyedy, É. a; Hermann, G.; Groza, D.; Köllensperger, G.; Galanksi, M.; Berger, W.; Keppler, B. K.; Kowol, C. R. *Chem. Commun.* **2013**, *49*, 2249.

(44) Poon, C.; He, C.; Liu, D.; Lu, K.; Lin, W. *J. Control. Release* **2015**, *201*, 90.

(45) He, C.; Poon, C.; Chan, C.; Yamada, S. D.; Lin, W. *J. Am. Chem. Soc.* **2016**, *138*, 6010.

(46) Poon, C.; Duan, X.; Chan, C.; Han, W.; Lin, W. *Mol. Pharm.* **2016**, *13*, 3665.

(47) Gorelik, L.; Flavell, R. A. *Nature Med.* **2001**, *7*, 1118.

(48) Smyth, M. J.; Teng, M. W.; Swann, J.; Kyparissoudis, K.; Godfrey, D. I.; Haykawa, Y. *J. Immunol.* **2006**, *176*, 1582.

(49) Wrzesinski, S. H.; Wan, Y. Y.; Flavell, R. A. *Clin. Cancer Res.* **2007**, *13*, 5262.

(50) Liu, V. C.; Wong L. Y.; Jang, T.; Shah, A. H.; Park, I.; Yang, X.; Zhang, Q.; Lonning, S.; Teicher, B. A.; Lee, C. *J. Immunol.* **2007**, *178*, 2883.

(51) Kano, M. R.; Bae, Y.; Iwata, C.; Morishita, Y.; Yashiro, M.; Oka, M.; Fujii, T.; Komuro, A.; Kiyono, K.; Kaminishi, M.; Hirakawa, K.; Ouchi, Y.; Nishiyama, N.; Kataoka, K.; Miyazono, K. *Proc. Natl. Acad. Sci. U.S.A.* **2007**, *104*, 3460.

(52) Park, J.; Wrzesinski, S. H.; Sterm, E.; Look, M.; Criscione, J.; Ragheb, R.; Jay, S. M.; Demento, S. L.; Agawu, A.; Limon, P. L.; Ferrandino, A. F.; Gonzalez, D.; Habermann, A.; Flavell, R. A.; Fahmy, T. M. *Nat. Mater.* **2012**, *11*, 895.

(53) Seong, S. Y.; Matzinger, P. *Nat. Rev.* **2004**, *4*, 469.

Conclusions

- During this thesis, two water soluble and biocompatible nanoparticle delivery systems based on iron oxide and gold nanoparticles have been synthesized and characterized.

- Following a prodrug approach, cisplatin and nedaplatin platinum (IV) prodrugs have been synthesized.

- The loading of both platinum based prodrugs and dsRNA into the different delivery platforms was achieved through the use of different strategies. The AuNP-PEI-Pt(IV) system has been based on outer-sphere interactions while the incorporation of poly(I:C) to the AuNP-PEI was achieved through electrostatic interactions. Finally, a covalent attachment strategy was selected in the case of IONP-Pt(IV) constructs.

- For all three systems, fluorescent labelling was incorporated and their intracellular uptake followed by live cell fluorescence microscopy and flow cytometry.

- *In vitro* cytotoxicity experiments were performed in different relevant cancer cell lines to assess the functionality of the systems. Overall, the use of PEI coated AuNPs resulted in an increased cytotoxic activity of both poly(I:C) and the platinum (IV) prodrug in human prostate cancer cells as well as breast and pancreatic cells in the case of the prodrug. The delivery of a Pt(IV) prodrug with IONP-filled micelles also increased the cytotoxic effect of the prodrug in an aggressive metastatic melanoma cell line.

- Notably, the use of AuNPs preferentially promoted the cytotoxic effect of poly(I:C) while its delivery with IONPs increased the immunostimulatory activity.

- For the IONP-Pt(IV) construct, a chelate free radiolabelling strategy allowed the incorporation of ^{67}Ga radioisotopes and thus the visualization of the biodistribution *in vivo* in tumour bearing mice through SPECT/CT. The system successfully accumulated in the tumour area and also entered the lymphatic system reaching draining lymph nodes.

- Finally, the *in vivo* therapeutic efficacy was also studied for IONP-Pt(IV) and promising results were obtained. Initially, the co-injection of tumour cells with the appropriate samples lead to a therapeutic effect slightly better than cisplatin and a great improve in animal survival. A therapeutic treatment in tumour bearing mice led to the hypothesis that the system consists of both chemo and immunotherapeutic components with produce a combined effect that is notably enhanced in the presence of a TGF-*β* inhibitor.

Overall this PhD thesis has not only been focused on the preparation of biocompatible nanoparticle based delivery vehicles for cancer therapy, but has also demonstrated the versatility of these systems to deliver different cytotoxic payloads. *In vitro* studies carried out in relevant cancer cell lines prove the therapeutic potential of all constructs and although *in vivo* experiments were only carried out for one of the systems, very promising results were obtained. Beyond using the nanoparticles as delivery systems or imaging platforms, this work also highlights the possibility of using the nanoparticles as stealth immunotherapeutic agents to reach a combination therapy.

Future work will involve more in depth *in vitro* and *in vivo* studies to investigate the role of the immune system in the therapeutic effect of the IONP-Pt(IV) construct as well as the development of the animal tumour model of prostate cancer (PC-3) to be able to explore the *in vivo* efficacy of PEI-AuNP based constructs.